

UNCLASSIFIED

AD NUMBER: AD0884490

LIMITATION CHANGES

TO:

Approved for public release; distribution is unlimited.

FROM:

Distribution authorized to U.S. Gov't. agencies only; Test and Evaluation; 1 Jun 1971. Other requests shall be referred to the Air Force Weapons Lab, Attn: LR, Kirtland AFB, NM 87117.

AUTHORITY

AFWL ltr, 4 MAR 1975

THIS REPORT HAS BEEN DELIMITED  
AND CLEARED FOR PUBLIC RELEASE  
UNDER DOD DIRECTIVE 5200.20 AND  
NO RESTRICTIONS ARE IMPOSED UPON  
ITS USE AND DISCLOSURE.

DISTRIBUTION STATEMENT A

APPROVED FOR PUBLIC RELEASE,  
DISTRIBUTION UNLIMITED.

LRD-71-1

1  
93

**LASER DIVISION DIGEST  
SPRING 1971**

**AD884490**



June 1971

**DDC  
RECEIVED  
JUN 10 1971  
REGULATED  
C**

**AIR FORCE WEAPONS LABORATORY  
Air Force Systems Command  
Kirtland Air Force Base  
New Mexico**

**AD No. DDC FILE COPY**

Each transmittal of this document outside the agencies of the U. S. Government must have prior approval of AFWL (LR) , Kirtland AFB, NM, 87117.

LRD-71-1

LASER DIVISION DIGEST

Spring 1971

Each transmittal of this document outside the agencies of the U. S. Government must have prior approval of AFWL (LR), Kirtland AFB, NM 87117. Distribution is limited because of the technology discussed in the report.

ACQUISITION FOR			
CFSTI	WRITE SECTION <input type="checkbox"/>		
DOC	DIFF SECTION <input checked="" type="checkbox"/>		
UNANNOUNCED	<input type="checkbox"/>		
JUSTIFICATION			
BY			
DISTRIBUTION AVAILABILITY CODES			
DIST.	AVAIL.	and/or	SPECIAL
3			

AIR FORCE WEAPONS LABORATORY  
Air Force Systems Command  
Kirtland Air Force Base  
New Mexico 87117

When US Government drawings, specifications, or other data are used for any purpose other than a definitely related Government procurement operation, the Government thereby incurs no responsibility nor any obligation whatsoever, and the fact that the Government may have formulated, furnished, or in any way supplied the said drawings, specifications, or other data, is not to be regarded by implication or otherwise, as in any manner licensing the holder or any other person or corporation, or conveying any rights or permission to manufacture, use, or sell any patented invention that may in any way be related thereto.

This report is made available for study with the understanding that proprietary interests in and relating thereto will not be impaired. In case of apparent conflict or any other questions between the Government's rights and those of others, notify the Judge Advocate, Air Force Systems Command, Andrews Air Force Base, Washington, DC 20331.

DO NOT RETURN THIS COPY. RETAIN OR DESTROY.

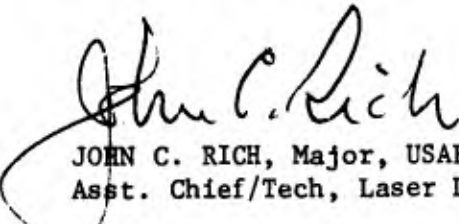
FOREWORD


This digest contains the results of theoretical and experimental research work carried on within the Laser Division of the Air Force Weapons Laboratory during the six months ending 1 May 1971.

The contributions in this digest generally represent the highlights of recent work, reported in a concise, timely manner. More complete technical reports and journal articles written during this time period are abstracted herein.

The work reported has been performed under the Air Force Advanced Development Program 644A, Project 3326 of Exploratory Development Program 62601F, ARPA Order 313, or ARPA Order 1256.

The Laser Division Digest is published semiannually in the Spring and Fall of each year. The Digest is compiled and edited by Major John C. Rich (LR).

  
JOHN C. RICH, Major, USAF  
Asst. Chief/Tech, Laser Division

  
DONALD L. LAMBERSON, Colonel, USAF  
Chief, Laser Division

ABSTRACT

(Distribution Limitation Statement No. 3

This digest covers the unclassified high-energy laser research performed at the Air Force Weapons Laboratory during the 6 months ending 1 May 1971. This report includes individual technical contributions in the specific areas of laser systems and devices, optics, optical systems, propagation, and laser effects.

## CONTENTS

<u>Section</u>		<u>Page</u>
I	LASER SYSTEMS AND DEVICES	1
	Nd:GLASS AMPLIFIER DRIVEN BY A Nd:YAG OSCILLATOR ---- C. R. Jones	2
	Q-SWITCHING WITH DIMETHYL SULFOXIDE AND OTHER ORGANIC LIQUIDS ---- P. Sivgals	8
	A METHOD OF OBTAINING PARTICLE-FREE OPTICAL SURFACES ---- P. Sivgals	13
II	OPTICS	15
	ACOUSTIC BEAM-SPLITTER FOR INFRARED LASERS ---- G. H. Nickel, G. M. Goodfellow, D. F. Terwilliger, and D. A. Holmes	16
	DIFFRACTION OF AN UNAPERTURED FOCUSED HERMITE GAUSSIAN BEAM BY A MOVING SINUSOIDAL PHASE GRATING ---- J. E. Korka and D. A. Holmes	27
	PHOTON POPULATION DECAY IN A FABRY-PEROT CAVITY ---- D. A. Holmes	31
	PARAMETRIC STUDY OF APERTURED FOCUSED GAUSSIAN BEAMS ---- D. A. Holmes, J. E. Korka, and P. V. Avizonis	37
	POWER PROFILES FOR APERTURED FOCUSED GAUSSIAN BEAMS ---- D. A. Holmes, J. E. Korka, and P. V. Avizonis	55
	COMPARISON OF FAR-FIELD IRRADIANCES FOR AXICON AND CASSEGRAIN TRANSMITTERS ---- D. A. Holmes, M. L. Bernabe, and R. R. Selleck	61
	ON-AXIS FOCAL PLANE INTENSITY VARIATIONS DUE TO TELESCOPE MIRROR MOTION ---- C. DeHainaut, J. E. Korka, and L. Sher	72
	AN IMAGING TECHNIQUE FOR BEAM FORMING AND POWER REMOVAL ---- D. A. Maier, J. E. Korka, and R. R. Selleck	77
	A REGENERATIVE RING AMPLIFIER FOR A CHEMICAL LASER ---- John A. Love III	83

**Preceding page blank**



## CONTENTS (cont'd)

<u>Section</u>	<u>Page</u>
TELESCOPIC AMPLIFIER ---- D. A. Holmes, P. V. Avizonis, J. A. Love, and J. E. Korka	92
GAUSSIAN BEAM PROPAGATION THROUGH A DIELECTRIC PLATE ---- D. A. Holmes	103
REFLECTANCE CALCULATIONS FOR LOSSLESS MULTILAYER DIELECTRIC STACKS ---- J. E. Korka, M. L. Bernabe, and D. A. Holmes	107
TRANSMISSION THROUGH LASER WINDOWS FOR COHERENT AND INCOHERENT RADIATION ----John Loomis	119
III OPTICAL SYSTEMS	129
POINTING AND TRACKING SIMULATION AND DESIGN ---- Robert J. Johnson	130
IV PROPAGATION	153
GEOMETRIC OPTICS OF THERMAL BLOOMING IN GASES: I ---- P. V. Avizonis, C. B. Hogge, R. R. Butts, and J. R. Kenemuth	154
A GEOMETRICAL OPTICS TREATMENT OF THERMAL BLOOMING ---- C. B. Hogge and R. R. Butts	182
EXPERIMENTAL INVESTIGATION OF THERMAL BENDING ---- W. L. Visinsky	192
PROBLEMS ASSOCIATED WITH PROPAGATION IN AN AERODYNAMIC ENVIRONMENT ---- W. L. Visinsky and C. B. Hogge	205
PROPAGATION THROUGH A SHOCK WAVE ---- W. L. Visinsky	209
MODELING PROPAGATION THROUGH TURBULENT BOUNDARY LAYERS BY THIN RANDOM PHASE SCREENS ---- C. B. Hogge and W. L. Visinsky	211
TURBULENCE DEGRADATION OF FOCUSED GAUSSIAN BEAMS ---- C. B. Hogge	220
COMPUTER SIMULATION OF BOUNDARY LAYER TURBULENCE ---- C. B. Hogge and W. L. Visinsky	243

## CONTENTS (cont'd)

<u>Section</u>	<u>Page</u>
PROPAGATION IN EXTREME TURBULENCE ---- C. B. Hogge and W. L. Visinsky	248
LASER BEAM PROPAGATION THROUGH JET EXHAUSTS ---- K. G. Gilbert, C. B. Hogge, and W. L. Visinsky	257
CO <sub>2</sub> LASER AIR BREAKDOWN CALCULATIONS ---- G. H. Canavan and S. D. Rockwood	258
INTERACTION OF HIGH-INTENSITY LASERS WITH OPTICALLY THIN AEROSOLS ---- P. E. Nielsen and G. H. Canavan	265
HYDRODYNAMIC CALCULATIONS OF LASER INTERACTION WITH ATMOSPHERIC AEROSOLS ---- P. E. Nielsen and G. H. Canavan	273
V LASER EFFECTS	283
THREE-MICRON LASER WINDOW ABSORPTION COEFFICIENTS ---- K. G. Gilbert	284
UNSTEADY-STATE HEATING OF A FINITE DISC BY LASER RADIATION ---- W. T. Laughlin and J. S. Shaberman	291

## Nd:GLASS AMPLIFIER DRIVEN BY A Nd:YAG OSCILLATOR

C. R. Jones

### Introduction

The Solid State Laser Branch at the Air Force Weapons Laboratory is developing a high-average-power, high-peak-power laser system. The oscillator and amplifiers comprising such a device may be constructed on the basis of the liquid-cooled, segmented-laser concept using neodymium-doped glass material. Unfortunately, the development of a segmented-glass laser oscillator has met with considerable difficulty because of undetermined optical problems associated with the disc geometry.

A chain of disc-laser amplifiers driven by a Nd:YAG oscillator may provide a suitable alternative configuration for the high-average-power system. At best, the price for such a modification would be the addition of another disc amplifier of 10 to 20 dB optical gain to compensate for the typically low-energy output ( $\sim 0.1$  joule) of Nd:YAG laser oscillators. However, it is possible that association of a Nd:YAG oscillator with Nd:glass amplifiers may be impractical because of low gain in the amplifiers. This reduced gain could arise from a mismatch between the peaks of the Nd:glass and Nd:YAG fluorescence spectra in the  $\lambda = 1.06\mu$  region. A more dramatic gain decrease, however, could arise from the linewidth difference in the  $1.06\mu$  emission spectra of the two materials: The spectrally narrow Nd:YAG pulse may simply burn a hole in the broad, inhomogeneous gain profile of Nd:glass. It is the purpose of this paper to report the results of an investigation undertaken to determine the magnitude of the gain reduction due to the above phenomena.

### Experiment

The experiment involved the comparison of the gain experienced by a pulse emitted from a Nd:YAG oscillator in passing through a Nd:glass amplifier with the gain of a Nd:glass-oscillator pulse passing through the same amplifier. Both oscillators, Q-switched with rotating mirrors, produced Nd:YAG and Nd:glass pulse durations of 20 and 50 nanoseconds respectively. Two Nd:glass amplifiers preceding the test amplifier were necessary in order to boost the approximately

50-millijoule Nd:YAG pulse to the maximum 5-joule level before entering the test amplifier. The set-up of the experiment is otherwise similar to that described in some detail elsewhere\* (in which one preamplifier was used). Care was taken to ensure that the amplifier chain did not self-oscillate, a phenomena which limited the Nd:YAG pulse input energy to about 5 joules. All of the Nd:glass was Owens-Illinois, Inc., ED-2 laser glass. It is significant that no optical damage within the test amplifier rod could be visually detected even though the output end of this amplifier experienced giant-pulse flux densities in excess of 15 joules/cm<sup>2</sup>.

### Results and Discussion

The results of the experiment are summarized with the data plotted in Figures 1, 2, and 3. In each graph the numerical gain of the test amplifiers is plotted as a function of the capacitor-bank energy discharged into the amplifier flashlamps. Each plot is the gain characteristic of the amplifier for one particular energy density of the input laser pulse. This input energy was changed by changing the pumping level on the two preamplifiers. The oscillator flashlamp energy was held constant to ensure that the intensity profile of the input laser pulse remained the same for all data points.

Figure 1 illustrates the small-signal-gain behavior of the amplifier and clearly indicates that there is a small spectral mismatch between the Nd:YAG emission and the Nd:glass fluorescence peak. Reportedly, other laser glasses have even greater mismatches with Nd:YAG. The small-signal input data would not be affected by hole-burning effects since insignificant energy is swept out of the amplifier by the pulse (that is, in fact, the definition of small-signal gain).

The gain curves of Figures 2 and 3 are in the transition region between small-signal gain and saturated gain. Since, the saturation parameter (which is the inverse of the gain storage coefficient) for ED-2 laser glass is about 7 joules/cm<sup>2</sup>, these data would exhibit any significant energy depletion effects in the amplifier. The fact that there is less separation between the Nd:YAG and Nd:glass gain curves than in the small-signal case indicates that hole-burning is an insignificant process for pulses of 20 nanoseconds or greater duration.

---

\*Jones, C. R., Avizonis, P. V., and Sivgals, P., Behavior of Neodymium-Glass Laser Amplifiers, AFWL-TR-70-150, 1970.

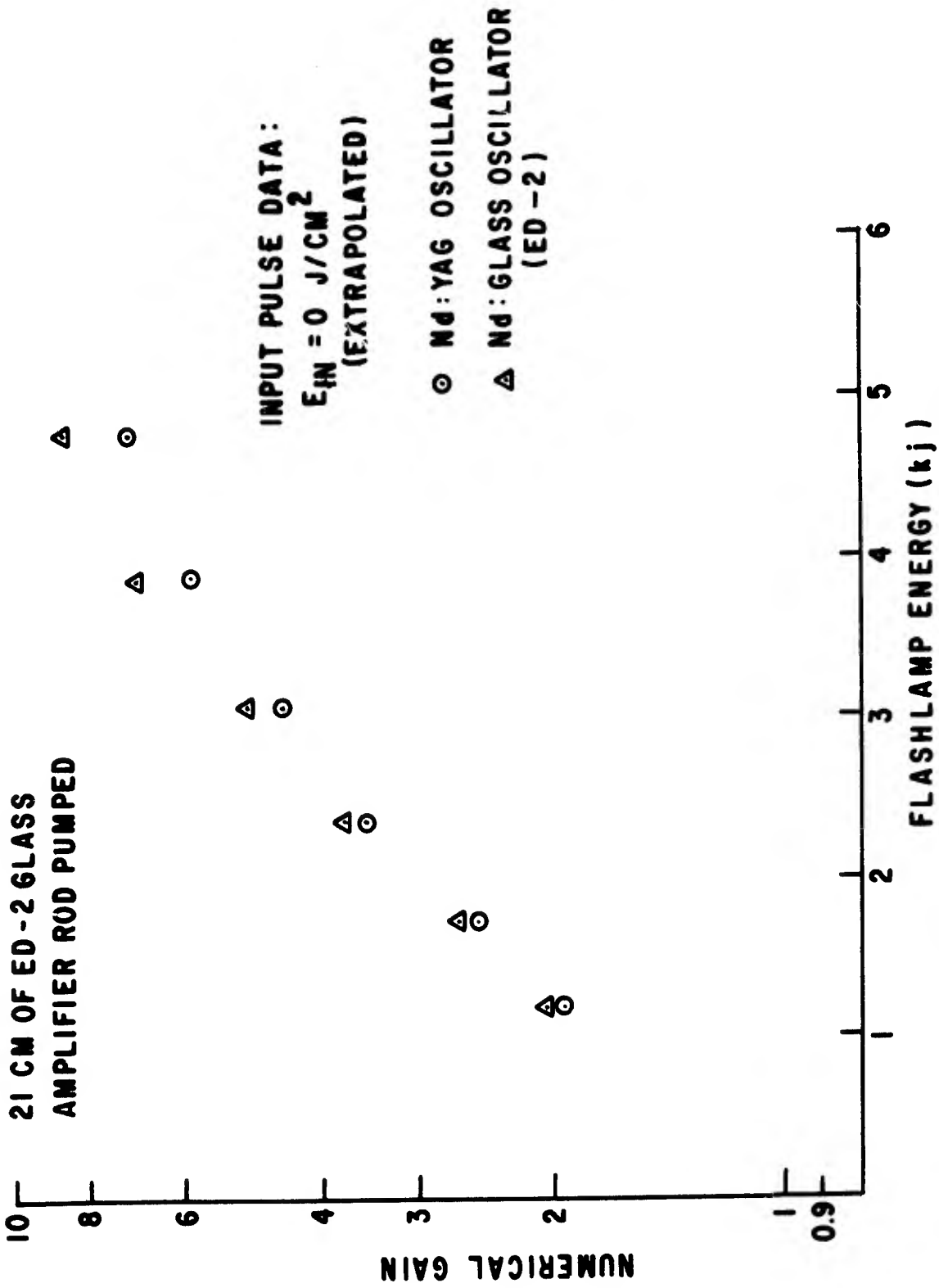


Figure 1. Numerical gain as a function of flashlamp input energy. Small-signal gain.

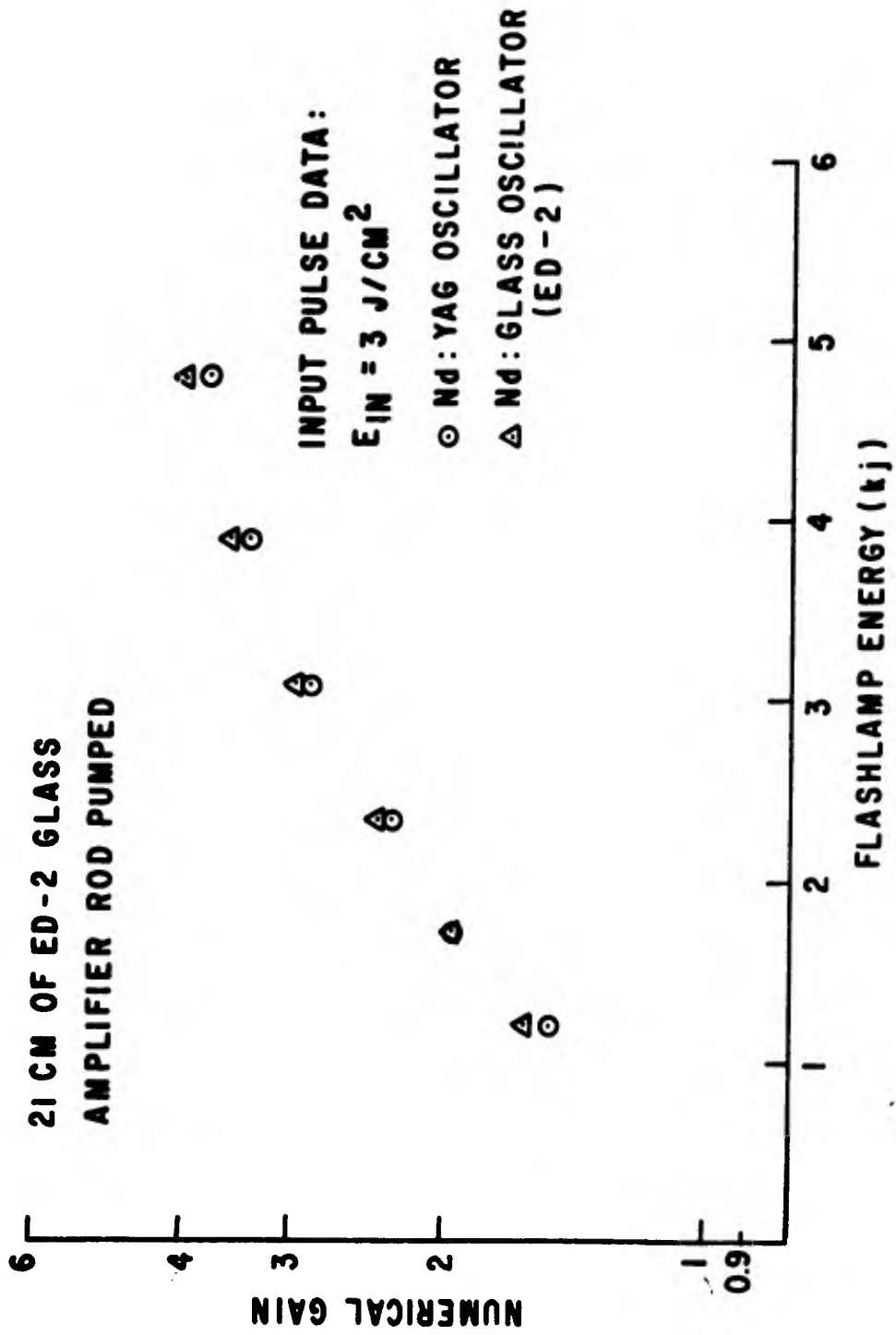


Figure 2. Numerical gain as a function of flashlamp input energy.  $E_{in} = 3 \text{ joules/cm}^2$ .

21 CM OF ED-2 GLASS  
AMPLIFIER ROD PUMPED

INPUT PULSE DATA:  
 $E_{in} = 6 \text{ J/CM}^2$

○ Nd:YAG OSCILLATOR

△ Nd:GLASS OSCILLATOR  
(ED-2)

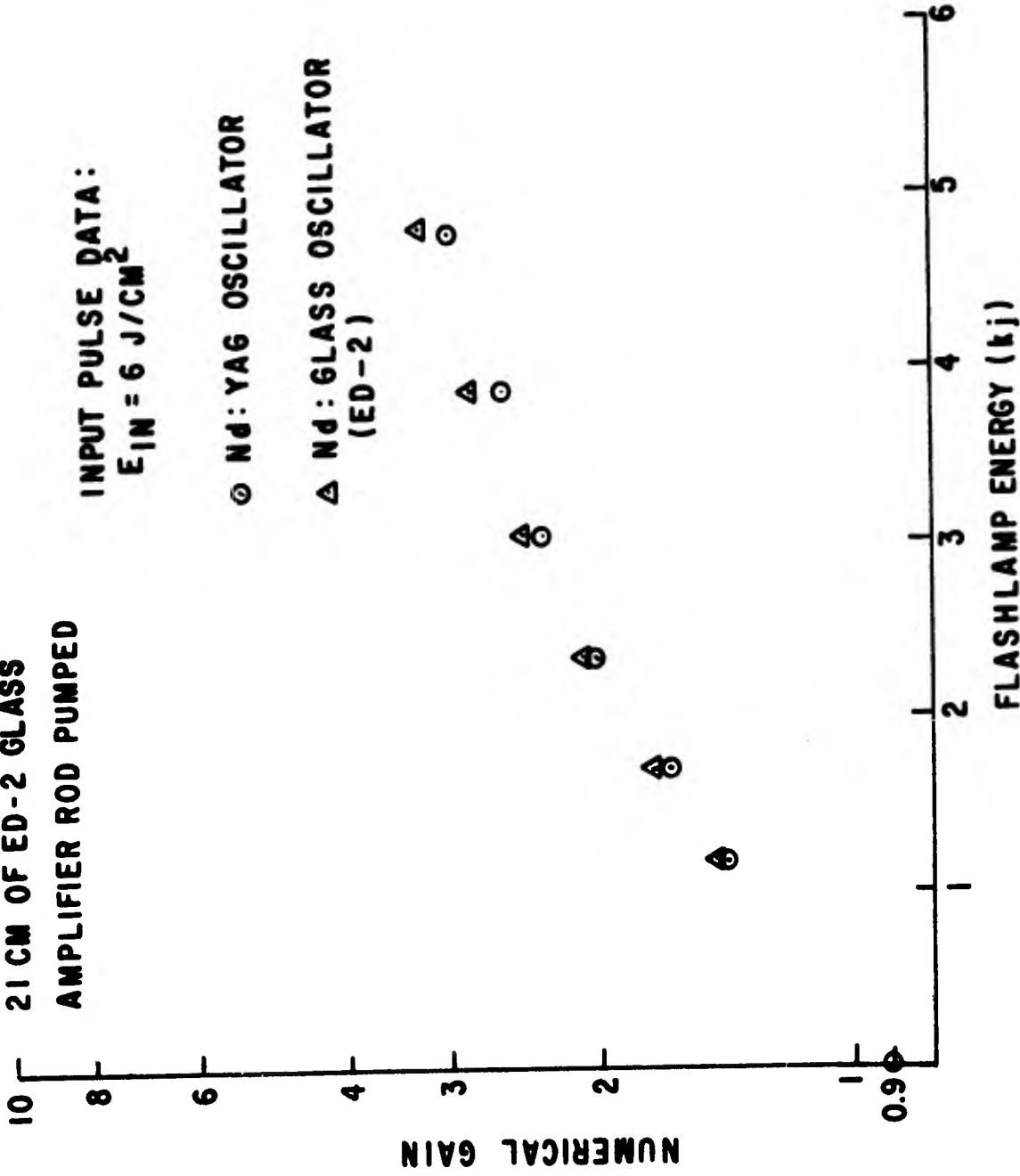


Figure 3. Numerical gain as a function of flashlamp input energy.  $E_{in} = 6 \text{ joules/cm}^2$ .

Apparently, cross-relaxation (energy transfer between Nd ions) rates in ED-2 glass are great enough to negate hole-burning effects on this time scale. The lower limit to this excitation transfer rate constant is, then, about  $10^{-13}$   $\text{cm}^3/\text{sec}$  (ED-2 has a nominal Nd density of  $3 \times 10^{20} \text{ cm}^{-3}$ ). The actual rate constant is probably much larger than this since such relaxation processes commonly occur on picosecond time scales.

### Conclusions

The data clearly demonstrate that Nd:YAG pulses are amplified by ED-2 laser glass only slightly less efficiently than pulses from an ED-2 glass oscillator. This small decrease in gain arises primarily from the spectral mismatch between the Nd:YAG laser emission wavelength and the Nd:glass gain profile peak.

It appears, then, that it is feasible to drive an ED-2 glass amplifier chain with a Nd:YAG oscillator. Hole-burning effects in the power amplifiers should be insignificant.

### Acknowledgements

The author acknowledges the fine technical effort of SSgt Tom Adams, who very competently set up the laser system and took the data. The helpful discussions with Capt Peter Sivgals and technical assistance of MSgt Ted Ledbetter were indispensable to the completion of this experiment.



Q-SWITCHING WITH DIMETHYL SULFOXIDE  
AND OTHER ORGANIC LIQUIDS

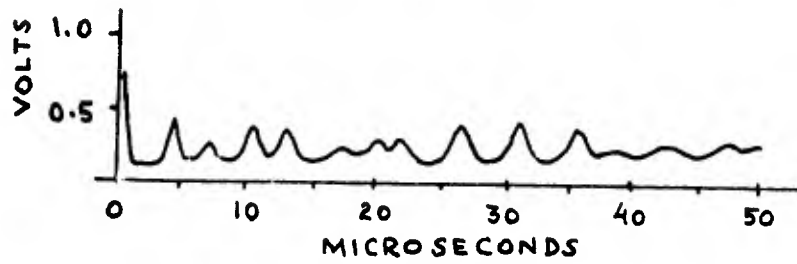
P. Sivgals

During our search for a cooling fluid which would more closely match the index of refraction of glass, an interesting phenomenon was observed when an axial gradient laser (AGL) was filled with dimethyl sulfoxide (DMSO). When the AGL was used as a normal-mode oscillator with flat mirrors, the burn pattern on polaroid film showed very pronounced filamentary lasing, i.e., many intense spots within the lasing aperture. The time-resolved photographs of the output pulse train (Figure 1) showed that considerably fewer pulses were produced and the pulses that were produced had a shorter width and a higher amplitude, i.e., pulse sharpening effect. Further experiments showed conclusively that this effect was produced by the liquid itself and occurred only when the liquid was within the laser resonator.

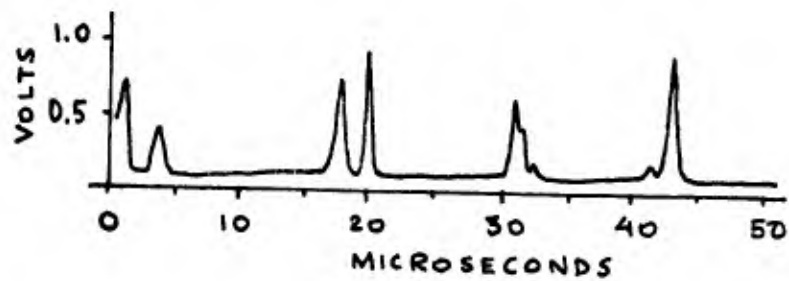
Similar pulse sharpening effects and filamentary lasing was observed when the DMSO cell was placed within the normal-mode Nd:YAG oscillator. However, when the YAG oscillator was Q-switched with a rotating mirror, the giant output pulse was identical in amplitude and width (20 ns) with or without the DMSO cell.

Literature search revealed that pulse sharpening was previously observed by T. Katzenstein<sup>1</sup> with other liquids such as acetone, benzene, and methanol. S. V. Gaponov et al.,<sup>2</sup> of the Soviet Union, have gone a step further and have produced Q-switched pulses by intentionally misaligning the flat mirrors. We have repeated Gaponov's experiment with acetone and DMSO and have obtained a single giant pulse with duration of 20 nanoseconds and energy of about 0.7 joules. The active element was a Nd:glass rod 3/8 by 6-1/2 inches pumped approximately three times above the threshold energy. Filamentary lasing was still observed and the beam divergence was in excess of 20 milliradians.

Instead of flat mirrors, a hemispherical resonator was set up using a one meter radius of curvature back mirror and a 35 percent reflective flat dielectric as an output mirror. One of the properties of this type of a resonator is that the laser output is relatively insensitive to the mirror alignment. When the



(a) Without DMSO



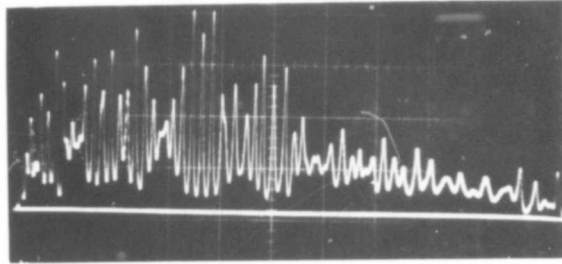
(b) With DMSO

Figure 1. Normal Mode Laser Output

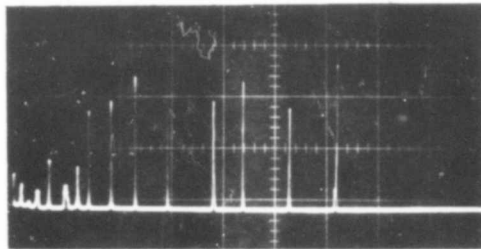
acetone-filled optical cell was introduced into the hemispherical resonator, pulse sharpening was immediately obvious on a time-resolved photograph of the output pulse train. When the output mirror was misaligned by about 7.5 milliradians, a single giant pulse was again obtained. Figure 2 shows the output from a hemispherical resonator with and without the liquid cell. Figure 3 shows the integrated output with acetone cell within the resonator before and after mirror misalignment. Note that a single giant pulse is obtained after mirror misalignment.

#### REFERENCES

1. Katzenstein, J., Magyar, G., and Selden, A. C., "Laser Q-Switching by Organic Solvents," Opto-Electronics, 1, pp. 13-19, 1969.
2. Gaponov, S. V., Goncharov, A. G., Kraftmakher, G. A., and Khanin, Ya. I., "Obtaining a Giant Pulse in a Solid-State Laser with the Aid of Organic Solvents," ZhETF Pis. Red., 11, pp. 370-373, 1970.

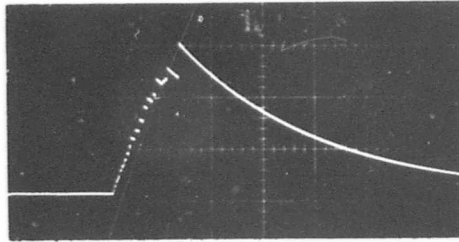


(a) Without DMSO

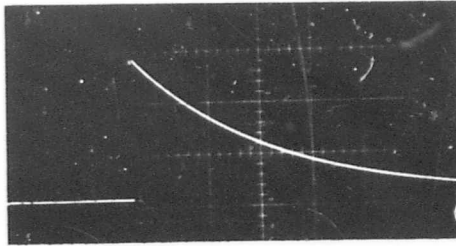


(b) With DMSO

Figure 2. Output from Hemispherical Resonator  
Time Scale: 20  $\mu$ s/cm



(a) Mirrors Aligned



(b) Mirrors Misaligned

Figure 3. Integrated Output from Hemispherical Resonator with DMSO Cell

## A METHOD OF OBTAINING PARTICLE-FREE OPTICAL SURFACES

P. Sivgals

In many applications clean, particle-free optical surfaces are highly desirable to reduce scattering losses and, in high-power lasers, to decrease the probability of damage to the surface. For example, in the axial gradient laser, as many as 120 optical glass surfaces are encountered by the laser pulse in a single amplifier stage, thus surface scattering may be a significant fraction of the total losses.

When a glass surface is examined with a 100-power microscope, surface contamination is clearly visible as the surface is illuminated with an ordinary microscope light at near grazing incidence angle. The position, angle, and focus of the illuminating source should be adjusted to obtain the maximum contrast between the dark background and the scattered light. We have observed a great number of optical glass surfaces in this manner (glass discs, mirrors, beam splitters, etc.) and have found that the particle density is at least  $10^4$  per square centimeter and often several orders of magnitude higher; this is true even after the surface is carefully cleaned using conventional cleaning techniques, such as ultrasonic agitation in detergent solution, chromic acid bath, distilled water rinse, ultrasonic agitation in distilled water with a final rinse in pure ethanol, and ultrasonic agitation in ethanol. In addition, many acids and bases were used as vapor degreasing technique in various organic solvents. All of these methods failed to remove most of the particle contamination except for the large 5 to 10  $\mu\text{m}$  size particles. The largest particles measured were approximately 1 to 2  $\mu\text{m}$  in diameter with most of the scattering centers in the submicron diameter range. The vast majority of these scattering centers were found to be on the surface rather than any defect in the surface itself because after another cleaning (or wiping) the particle distribution around a reference mark, such as a scratch, could be completely rearranged. It is believed that electrostatic attraction between the particles and the glass is the force that holds the particles on the surface.

As suggested by Dr. A. H. Guenther of this Laboratory, the replicating tape cleaning method was tried. In this method the optical surface is wetted with clean reagent-grade acetone or methyl acetate and an actyl cellulose film (tape) is carefully placed on the top of the glass surface so that a bond is formed between the wet film and the glass. After the cellulose film dries completely, it is peeled off the glass surface. The particle contamination previously observed is almost entirely removed, leaving a very clean surface. Of course, the glass surface must be chemically clean prior to the use of the replicating tape. A thick replicating tape is recommended because it is easier to peel off the surface. The only disadvantage of this method is that it will leave some of the cellulose film around the edges of the optical surface. Also, if the cellulose is not completely hardened when peeled off, some of the cellulose may be left on the surface.

In addition to cleaning the surface, the optical element may be completely encased in the cellulose for storage. This will protect the element from scratches, dust, fingerprints, and other contamination while in storage.

SECTION II

OPTICS



## ACOUSTIC BEAM-SPLITTER FOR INFRARED LASERS

G. H. Nickel, G. M. Goodfellow, D. F. Terwilliger, and D. A. Holmes

### Introduction

For high-power continuous-wave lasers, especially of the molecular type operating in the infrared, beam-splitters that do not undergo thermo-optical deformations are not available; but they are required if both phase and amplitude of laser beams are to be examined.

To address this problem, a technique is described which appears promising and employs a diffraction grating of ultrasonic waves in the air path across a laser beam. The phase grating created in this manner has a grating spacing equal to the acoustic wavelength, and the phase modulation depends on the grating "thickness" (width along the laser beam path), the relative compression in the sound waves, and the variation of the index of refraction with density. This principle, discovered 40 years ago by Brillouin, has been used to slew laser beams rapidly in information retrieval systems.

The principal difficulties in establishing an acoustic diffraction grating in air have been noted by Richardson<sup>1</sup>. First, the coupling of sound waves from ultrasonic transducers into a gas is very poor; and second, because the density of a gas is very low, the change in the index of refraction in an acoustical grating is very small for a gas when compared with solids or liquids. Also, there can be a problem with multiple diffraction if the grating "thickness" is too great. Balancing these drawbacks are the facts that extremely high-power densities are envisioned for laser beams (or else more conventional techniques would be used), and that current IR detectors can detect very low levels of radiation. Hence, a very small beam-splitting fraction can be tolerated. The system to be described produced a very high signal-to-noise ratio with a mercury-cadmium-telluride (MCT) detector used in conjunction with a lock-in amplifier.

## Theory

An explanation of the use of an air-acoustic diffraction grating as a CO<sub>2</sub> laser beam-splitter can begin with a description of the ultrasonic transducers. The transducers are constructed of PZT ceramic materials which have a piezoelectric coefficient of typically 3 Å/volt. Thus, application of 100 volts peak-to-peak to the transducer will produce a peak-to-peak surface displacement of about  $3 \times 10^{-6}$  cm. Since the motion is sinusoidal with radian frequency  $2\pi \times 10^6$ /sec, for 1 MHz, the peak-to-peak velocity variation is about 20 cm/sec, giving an rms velocity of approximately 7 cm/sec. As pointed out by Landau<sup>2</sup>, the case of acoustic radiation whose dimension is large compared to the wavelength is easily treated by assuming that the sound wave particle velocity  $v_p$  equals the normal surface velocity of the radiator. Hence, the energy in the sound wave is  $\rho(v_p)^2$  ergs/cm<sup>3</sup>; the acoustic power is  $\rho c(v_p)^2$  ergs/cm<sup>2</sup>/sec; and the density variation in the wave is about  $\delta\rho/\rho \approx v_p/c$ . The resulting index of refraction change is then

$$\delta n \approx 3 \times 10^{-4} \frac{\delta\rho}{\rho} \approx 3 \times 10^{-4} \frac{v_p}{c} \approx \frac{3 \times 10^{-4} \times 20}{3 \times 10^4} \approx 2 \times 10^{-7}$$

The peak-to-peak phase modulation  $\delta\phi$  is just the total phase across the acoustic grating times the fractional change in index of refraction,

$$\delta\phi = \frac{\delta n}{n} 2\pi \frac{L}{10.6\mu} \approx 10^{-3} \text{ for } L = 1 \text{ cm}$$

As developed by Goodman<sup>3</sup>, the power in the  $n$ th order diffracted uniform beam is proportional to

$$J_n \left( \frac{\phi}{2} \right)^2$$

Therefore, the beam-splitting fraction  $F$  can be defined as

$$F = \left[ \frac{J_1 \left( \frac{\phi}{2} \right)}{J_0 \left( \frac{\phi}{2} \right)} \right]^2$$

In the case of a very small argument,  $J_n(x) \sim x^n$ , and thus one has the relation

$$F = \left( \frac{\phi}{2} \right)^2$$

The diffraction angle can be calculated from the transmission grating relation,  $\sin \theta = n\lambda/d$ , where  $n$  is the order number,  $\lambda$  is the laser wavelength, and  $d$  is the grating spacing. The grating spacing  $d$  for the acoustic grating is defined  $d = c/v$ , where  $c$  is the velocity of sound in the medium, and  $v$  is the frequency at which the transducer is driven. Therefore, for the first order diffracted beam, one has  $\sin \theta = \lambda v/c$ .

To ascertain if there may be distortions upon the diffracted laser beam due to the phase grating, the interaction of an optical wave with an acoustical wave is developed in the sense of the diffraction theory. The Fresnel diffraction integral is used to calculate diffracted fields created when a free Gaussian beam propagates through a sinusoidal phase grating that is translating perpendicular to the direction of propagation of the optical beam. It is assumed that the grating does not aperture the Gaussian beam.

Considering that the Gaussian beam is propagating in the positive  $z$  direction, we take the  $z = 0$  plane as the integration surface for the Fresnel diffraction integral. The transverse coordinates in the  $z = 0$  plane are taken as  $(\xi, \eta)$ . The wave amplitude in the  $z = 0$  plane, normalized to beam power  $P$ , is taken as

$$v(\xi, \eta) = (2P/\pi w^2)^{1/2} \exp [-(\xi^2 + \eta^2)(1/w^2 + i\pi/\lambda R)] \\ \cdot \exp \left\{ 2\pi \Delta i \cos \left( 2\pi v [\xi - Vt] + \phi \right) \right\} \exp (-i\omega t) \quad (1)$$

In equation (1),  $w$  is the beam spot size and  $R$  is the beam phase radius of curvature in the  $x = 0$  plane. When  $R > 0$ , then the beam is considered to be focused at the point  $z = R$ . The amplitude of the phase shift in wavelength units induced by the phase grating is  $\Delta$ . The peak-to-peak phase variation  $\phi$  is simply equal to  $4\pi\Delta$ . The spatial period of the phase is  $1/v$  in the  $\xi$  direction and the grating is considered to be moving in the positive  $\xi$  direction with velocity  $V$ . A constant arbitrary phase factor is denoted by  $\phi$  and the field  $v(\xi, \eta)$  is oscillating at the angular frequency  $\omega$ .

Defining  $x$  and  $y$  coordinates with  $x$  corresponding to  $\xi$  and  $y$  corresponding to  $\eta$ , the diffracted field is taken as  $u(x, y, z)$ . For  $z > 0$ , the Fresnel diffraction integral gives

$$u(x,y,z) = \exp [2\pi iz/\lambda + i\pi(x^2+y^2)/\lambda z] / (i\lambda z) \iint_{-\infty}^{\infty} d\xi d\eta v(\xi, \eta) \cdot \exp [i\pi(\xi^2+\eta^2)/\lambda z] \exp [-2\pi i(\xi x + \eta y)/\lambda z] \quad (2)$$

To evaluate the integral in equation (2), we use the identity

$$\exp [i\delta \cos \theta] = \sum_{q=-\infty}^{+\infty} i^q J_q(\delta) \exp (iq\theta) \quad (3)$$

With the help of the identity equation (3), we substitute equation (1) into equation (2) and obtain

$$\begin{aligned} u(x,y,z) = & -i \left( 2P/\pi w^2(z) \right)^{1/2} \exp \left[ 2\pi iz/\lambda - i \tan^{-1} \left\{ \pi(z-R)w^2/\lambda Rz \right\} \right] \\ & \cdot \exp \left[ - \left( y/w(z) \right)^2 + i\pi y^2/\lambda R(z) \right] \\ & \cdot \sum_{q=-\infty}^{+\infty} i^q J_q(2\pi\Delta) \exp \left[ iq\phi - i(\omega + 2\pi q\nu V)t \right] \\ & \cdot \exp \left[ - (z - q\nu\lambda z)^2/w^2(z) \right] \\ & \cdot \exp \left[ i(\pi/\lambda z) \left( x^2 - \{x - q\nu\lambda z\}^2 \{1 - z/R(z)\} \right) \right] \end{aligned} \quad (4)$$

where

$$w^2(z) = w^2 \left\{ (1-z/R)^2 + (\lambda z/\pi w^2)^2 \right\} \quad (5)$$

and

$$R(z) = - \left( R w^2(z)/w^2 \right) / \left\{ 1 - (z/R) - R z \lambda^2/\pi^2 w^4 \right\} \quad (6)$$

The irradiance of the diffracted field is taken (in the scalar wave approximation) as

$$I(x,y,z) = |u(x,y,z)|^2 \quad (7)$$

The various diffracted orders will not "overlap" when

$$v\lambda z \gg w(z) \quad (8)$$

In the approximation of equation (8), we have

$$I(x, y, z) \approx \left[ 2P/\pi w^2(z) \right] \exp \left[ -2 \left( y/w(z) \right)^2 \right] \cdot \sum_{q=-\infty}^{\infty} J_q^2(2\pi\Delta) \exp \left[ -2(x - qv\lambda z)^2/w^2(z) \right] \quad (9)$$

Examination of equation (9) clearly shows that the transmitted beam (zero order)  $q = 0$  is not distorted by the phase grating and remains Gaussian. This is so because  $J_0(2\pi\Delta) \approx 1$  for small arguments, which is the case here. The 1st order diffracted beam ( $q = \pm 1$ ) has no distortion either, as

$$J_{\pm 1}^2(2\pi\Delta) \approx 4\pi^2\Delta^2$$

for very small arguments and equation (9) becomes,

$$I_{\pm 1}(x, y, z) \approx \left[ 8\pi\Delta^2 P/w^2(z) \right] \exp \left[ -2 y/w(z)^2 - 2(x \pm \lambda z)^2/w^2(z) \right] \quad (10)$$

where the second term in the exponential (x-plane) indicates a displacement of  $\pm\lambda z$  from  $x$  due to 1st order diffraction.

### Experimental Procedure

The transducers are fabricated from PZT-5 with electrodes on front and back surfaces, and are mounted in a 1-inch brass cylinder as shown in Figure 1. Each transducer is 3/4-inch in diameter, and is nominally resonant at 1 MHz. Two transducers are used in this experiment: one as a receiver mounted in a fixed position, the other as a transmitter mounted in a two-axis translation mount to facilitate alignment for parallelism and separation.

Optimization of experimental technique led to the arrangement shown in Figure 2. The transducer is 100 percent square wave modulated, thus diffracting the beam at a 1-kHz rate so that the detector output can be applied to the PAR Model 121 lock-in amplifier. Two immediate advantages are realized when using the lock-in amplifier. First, its increased signal-to-noise ratio can be exploited;

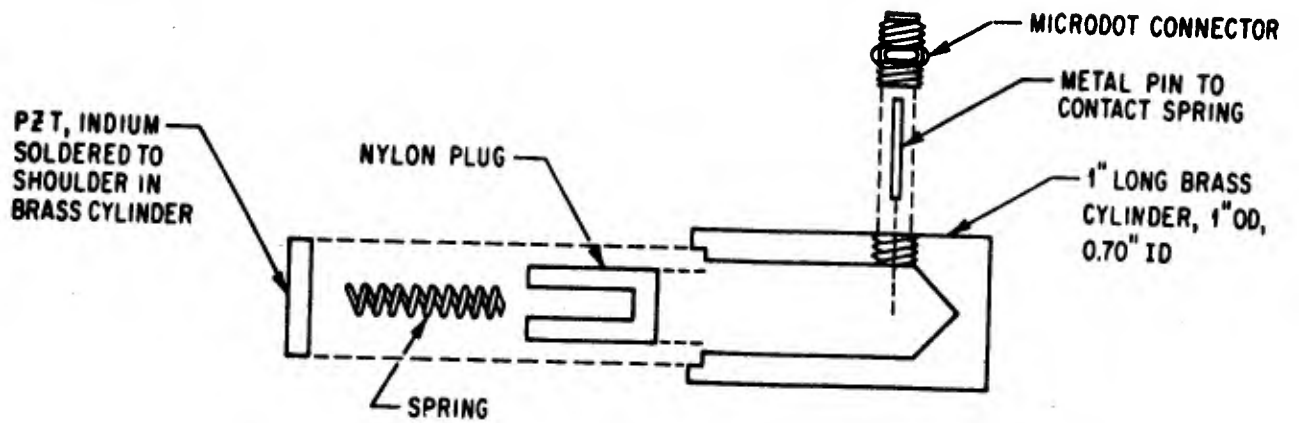


Figure 1. Transducer and Mount

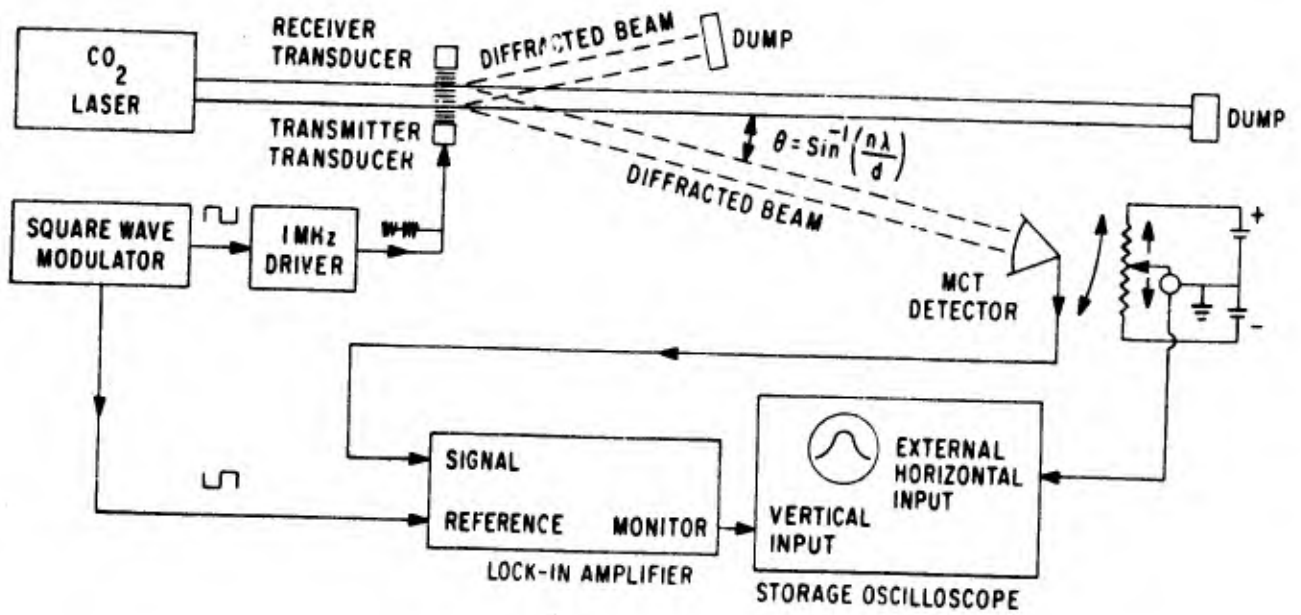


Figure 2. Block Diagram of the Experimental Arrangement

and second, this method ensures that the output response is due only to the diffracted beam rather than to spurious signals or side lobes of the main beam.

Angular position of the detector is determined with a voltage from a battery and potentiometer which is applied to the external horizontal input of a Tektronix Model 549 storage oscilloscope. Thus, lateral movement of the detector produces a horizontal trace on the oscilloscope. Consequently, as the detector is swept across the path of the diffracted beam, the beam profile can be stored for observation, photographs, and/or comparison.

The detector is mounted vertically and cooled with liquid nitrogen. A gold mirror reflects the horizontal diffracted beam up into the end-looking MCT detector.

The electronics used to drive the transducer consists of a modified amateur radio transmitter and a modulator circuit as shown in Figure 3. A 6146B oscillator tube, in conjunction with a 1-MHz crystal, generates the RF driving power. A pi-type network matches the 4-kohm oscillator output impedance to the 300 ohm impedance of the transducer. Negative pulses from the variable-rate pulse generator (GE-22 and 2N3642 transistors) are used to toggle the SF7473N J-K flip-flop integrated circuit. The nominal 1-kHz square wave output of the J-K flip flop provides the reference signal to the lock-in amplifier while simultaneously switching the GE-12 transistor. The 6146B oscillator is cathode-keyed through this switching action, providing square wave modulation of the transducer for phase locking in the PAR Model 121.

Oscilloscope traces of the diffracted beam profiles for Gaussian and donut modes are shown in Figure 4. The signal disappears when the transducer is turned off and/or when the laser beam is blocked, indicating that the system is not just seeing a spurious reflection. The importance of chopping the transducer drive instead of the laser beam is that the very low intensity wings of the main beam, which are not necessarily negligible in comparison to the diffracted beam, are rejected by the lock-in amplifier. (Of course, a beam chopper would have violated the basic premise that no solid material intersects the beam.)

In this experiment, the main beam was about 16 watts, having an  $e^{-2}$  diameter of 1.2 cm at the transducers, spreading to 1.9 cm at the detector position, about 2 m down the beam. The driver produced about 120 volts peak-to-peak,

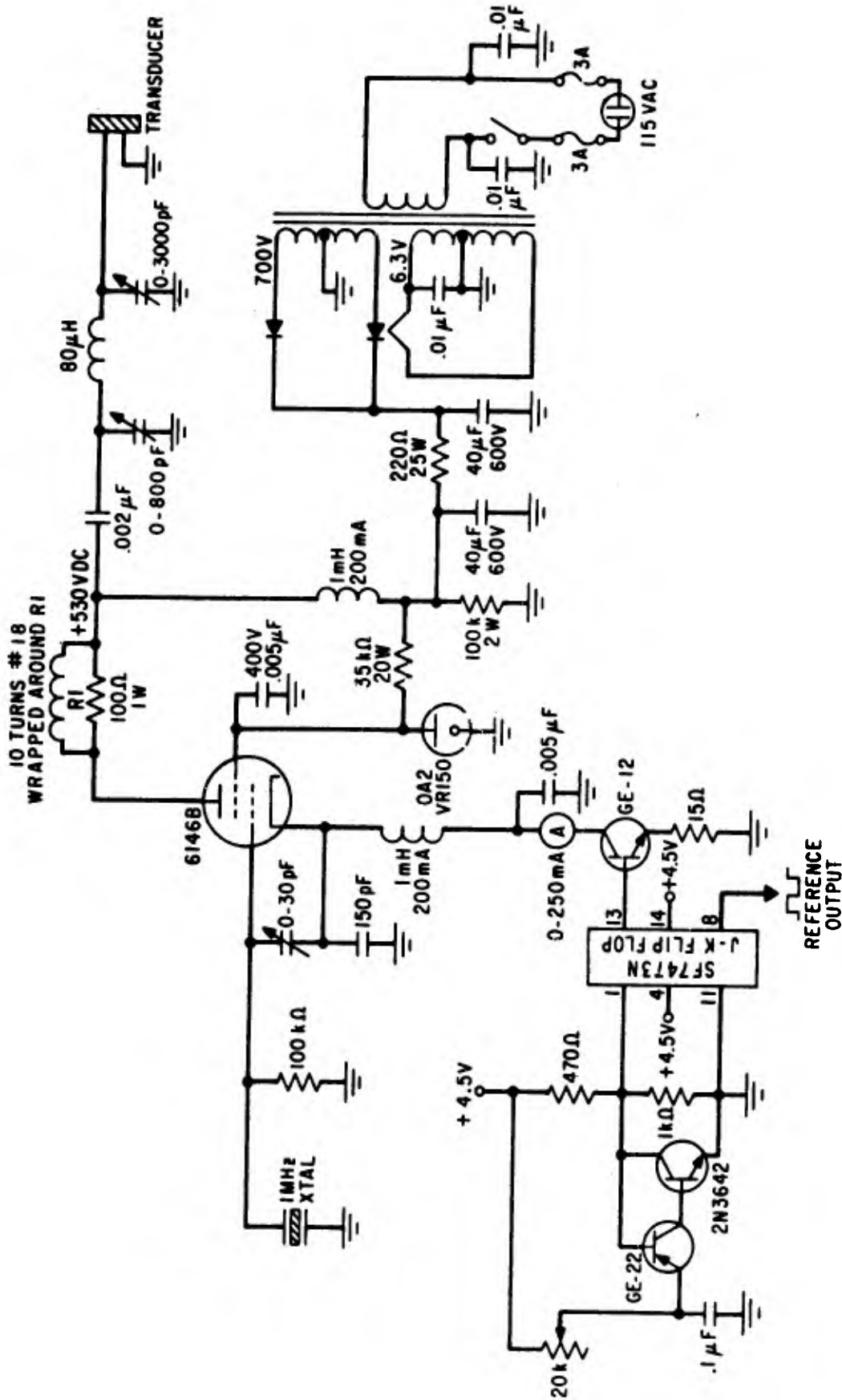
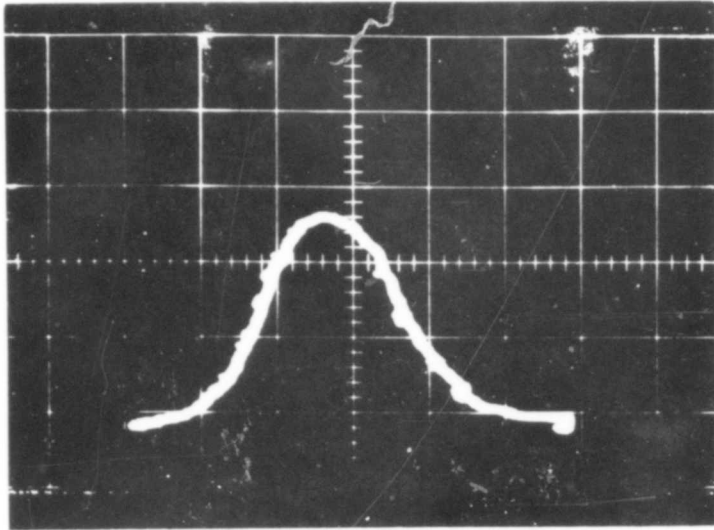
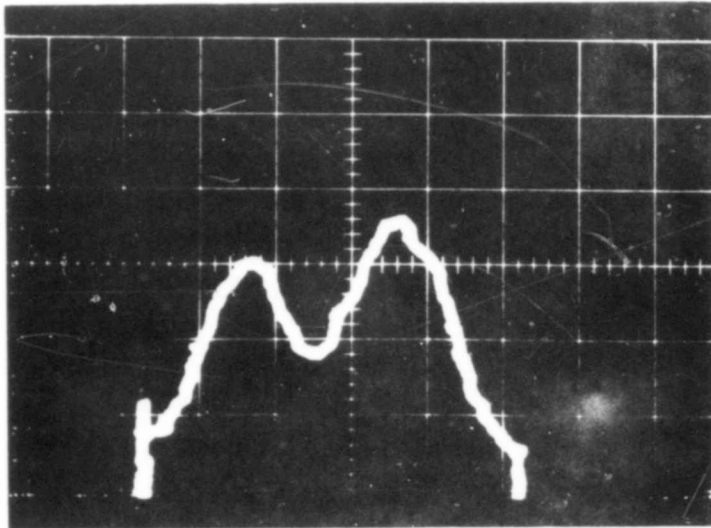


Figure 3. Transducer Modulator and Driver Circuit





(a) A Laser Operating in the Gaussian Mode



(b) A Laser Operating in the Donut Mode

Figure 4. Profiles of the Diffracted Beam

corresponding to about 5 watts at a 50 percent duty cycle, or 2-1/2 watts average power delivered to the transducer. This provided about 1/4 watt of acoustic power.

Some care had to be taken to shield the transducers from air currents since blowing across the acoustic cavity causes the output to vary considerably. It has been suggested that the use of a modulating frequency much higher than any frequencies normally found in air turbulence should minimize this problem.

The beam-splitting fraction is  $F \approx (\phi/2)^2 \approx 10^{-7}$  in the present case, since the square wave modulation makes the average beam-splitting fraction 1/2 of the peak value. Since the original beam had a peak intensity of  $\sim 5$  watts/cm<sup>2</sup>, the diffracted beam could be expected to have 1/2  $\mu$ watt/cm<sup>2</sup> intensity. This seems to be reasonable in view of the advertised  $D^*$  of MCT detectors of  $\sim 10^{10}$ . Using a bandwidth of 100 Hz and a detector size of 1 mm<sup>2</sup>, one needs a power of  $10^{-10}$  watts to give a signal-to-noise ratio of unity. Since this is falling on a detector area of  $10^{-2}$  cm<sup>2</sup>, the threshold intensity is  $10^{-8}$  watts/cm<sup>2</sup>. This gives a signal-to-noise ratio of about 50 in the peak intensity region, which seems to be a reasonable value, at least in terms of orders of magnitude. Lacking a more accurate value of the diffracted power, the beam-splitting fraction of  $10^{-7}$  is probably close. The diffraction angle for this experiment was calculated to be about 1.8° for  $\lambda$  of 10.6 microns,  $\nu$  of 1 MHz, and  $c$  of  $3.35 \times 10^4$  cm/sec in air. This angle agreed with experimental results.

### Discussion

It should be possible to use a 1/4-wave matching plate to increase the acoustic power coupled into the air by about one order of magnitude. Also, there are transducer materials that can be driven at considerably higher power levels than the PZT-5 used in these prototype experiments. Thus, a diffracted power density on the order of milliwatts/cm<sup>2</sup> instead of  $\mu$ watts/cm<sup>2</sup> could be expected.

On the other hand, the problem of acoustic wave attenuation becomes more important as the diameter of the laser beam increases. Richardson shows an  $e^{-1}$  attenuation length at 1 MHz to be about 50 cm in argon, and somewhat less in air. The principal offender in air is water vapor, so the gaseous medium should be controlled in any event, and argon might as well be used. The attenuation effect can be minimized by using appropriately-phased opposed transducers.

Another possible problem area involves the grating thickness, or width of the acoustic waves along the laser beam. Multiple diffraction occurs if this distance exceeds  $\lambda_s/\lambda_{IR}$  where  $\lambda_s$  is the grating spacing, or sound wavelength, and  $\lambda_{IR}$  is the light wavelength. This maximum thickness is about 1 cm in this case ( $\lambda_s = 365 \mu$ , measured). It may not be that the multiple diffraction is at all important in this application, since the amount diffracted is so very small that second order effects are many orders of magnitude less than the first order diffracted beam.

Using a flowing argon atmosphere, or at least dry air or  $N_2$ , one should be able to extend this method to handle a 10-cm beam rather easily. For these large systems, it may be necessary to design an acoustic cavity in much the same manner that optical cavities are currently designed. It may also require special processing of the output data in order to counter effects of acoustic beam attenuation.

#### Summary

A method for noninterference sampling of high power  $CO_2$  laser beams has been described. The technique employs an ultrasonic diffraction grating generated in the air path across a laser beam. A very small fraction ( $\sim 10^{-6}$ ) of the main beam is diffracted through a small angle ( $\sim 2^\circ$ ) on either side. Profiles of Gaussian and donut modes from low power  $CO_2$  lasers have been obtained with the acoustic beam-splitter.

#### REFERENCES

1. Richardson, E. G., Ultrasonic Physics, Elsevier Publishing Company, Amsterdam, 1952.
2. Landau, L. D., and Lifshitz, E. M., Fluid Mechanics, Pergamon Press, London, 1959.
3. Goodman, Joseph W., Introduction to Fourier Optics, McGraw-Hill Book Company, San Francisco, 1968.

DIFFRACTION OF AN UNAPERTURED FOCUSED HERMITE GAUSSIAN  
BEAM BY A MOVING SINUSOIDAL PHASE GRATING\*

J. E. Korka and D. A. Holmes

Consider that the Hermite Gaussian beam is propagating in the positive  $z$  direction and we take the  $z = 0$  plane as the integration surface for the Fresnel diffraction integral. The transverse coordinates in the  $Z = 0$  plane are taken as  $(\xi, \eta)$ . The wave amplitude in the  $z = 0$  plane, normalized to beam power  $P$ , is taken as

$$\begin{aligned}
 v_{nm}(\xi, \eta) = & (2P/\pi w^2)^{1/2} \exp [-(\xi^2 + \eta^2)(1/w^2 + i\pi/\lambda R)] \\
 & \cdot H_n(\sqrt{2}\xi/w) H_m(\sqrt{2}\eta/w) \\
 & \cdot \exp \left\{ 2\pi\Delta i \cos \left( 2\pi\nu[\xi - Vt] + \phi \right) \right\} \exp(-i\omega t)
 \end{aligned} \tag{1}$$

In equation (1)  $w$  is the beam spot size and  $R$  is the beam phase radius of curvature in the  $z = 0$  plane. When  $R > 0$ , then the beam is considered to be focused at the point  $z = R$ . The amplitude of the phase shift induced by the phase grating is  $\Delta$ . The spatial period of the phase is  $1/\nu$  in the  $\xi$ -direction and the grating is considered to be moving in the positive  $\xi$ -direction with velocity  $V$ . A constant arbitrary phase factor is denoted by  $\phi$  and the field  $v_{nm}(\xi, \eta)$  is oscillating at the angular frequency  $\omega$ .

We now define  $x$  and  $y$  coordinates with  $x$  corresponding to  $\xi$  and  $y$  corresponding to  $\eta$ . The diffracted field is taken as  $u_{nm}(x, y, z)$ . For  $z > 0$ , the Fresnel diffraction integral gives

$$\begin{aligned}
 u_{nm}(x, y, z) = & \left[ \exp 2\pi iz/\lambda + i\pi(x^2 + y^2)/\lambda z \right] / (i\lambda z) \\
 & \cdot \int_{-\infty}^{\infty} \int_{-\infty}^{\infty} d\xi d\eta v_{nm}(\xi, \eta) \exp [i\pi(\xi^2 + \eta^2)/\lambda z] \cdot \exp [-2\pi i(\xi x + \eta y)/\lambda z]
 \end{aligned} \tag{2}$$

---

\*The December 1970 Laser Division Digest contains an article by D. A. Holmes on "Diffraction of an Unapertured Focused Gaussian Beam by a Moving Sinusoidal Phase Grating." This paper is an extension of that paper and considers a general Hermite Gaussian beam.

To evaluate the integral in equation (2) we use the identity

$$\exp [i\delta \cos \theta] = \sum_{q=-\infty}^{+\infty} i^q J_q(\delta) \exp(iq\theta) \quad (3)$$

With the help of the identity equation (3) we substitute equation (1) into equation (2) and obtain

$$\begin{aligned} u_{nm}(x,y,z) = & -i \left( 2P/\pi w^2(z) \right)^{1/2} \exp \left[ 2\pi i z/\lambda - i \tan^{-1} \left\{ \pi(z-R)w^2/\lambda R z \right\} \right] \\ & \cdot \exp \left[ - \left( y/w(z) \right)^2 + i\pi y^2/\lambda R(z) \right] \\ & \cdot \sum_{q=-\infty}^{+\infty} i^q J_q(2\pi\Delta) \exp \left[ iq\phi - i(\omega + 2\pi q\nu V)t \right] \cdot \exp \left[ - (x - q\nu\lambda z)^2/w^2(z) \right] \\ & \cdot \exp \left[ i(\pi/\lambda z) \left( x^2 - \{x - q\nu\lambda z\}^2 \{1 - z/R(z)\} \right) \right] \\ & \cdot \left[ w^2 \left\{ (1 - z/R)^2 - \lambda z/\pi w^2 \right\}^2/w^2(z) - 2i\lambda z(1 - z/R/\pi w^2) \right]^{(n+m)/2} \\ & \cdot H_n \left( -\sqrt{2}(x - q\nu\lambda z)/w(z) \right) \cdot H_m \left( -\sqrt{2}y/w(z) \right) \end{aligned} \quad (4)$$

where

$$w^2(z) = w^2 \left\{ (1 - z/R)^2 + (\lambda z/\pi w^2)^2 \right\} \quad (5)$$

and

$$R(z) = - \left( R w^2(z)/w^2 \right) / \left\{ 1 - z/R - R z \lambda^2/\pi^2 w^4 \right\} \quad (6)$$

The irradiance of the diffracted field is taken (in the scalar wave approximation) as

$$I(x,y,z) = |u(x,y,z)|^2 \quad (7)$$

The various diffracted orders will not "overlap" when

$$\nu\lambda z \gg w(z) \quad (8)$$

In the approximation of equation (8) we have

$$\begin{aligned}
I(x,y,z) = & [2P/\pi w^2(z)] \exp[-2(y/w(z))^2] \\
& \cdot \sum_{q=-\infty}^{+\infty} J_q^2(2\pi\Delta) \exp[-2(x-qv\lambda z)^2/w^2(z)] \\
& \cdot \left\{ w^2 \left[ (1-z/R)^2 - \lambda z/\pi w^2 \right]^2 / w^2(z) - 2i\lambda z(1-z/R)/\pi w^2 \right\}^{n+m} \\
& \cdot \left\{ H_n \left( -\sqrt{2}y/w(z) \right) \right\}^2 \cdot \left\{ H_m \left( -\sqrt{2}(x-qv\lambda z)/w(z) \right) \right\}^2
\end{aligned} \tag{9}$$

An arbitrary wave  $\Psi$  in the  $z = 0$  plane can be expressed as a sum over the Hermite modes given by

$$\Psi(\xi, \eta, z=0) = \sum_{n=0}^{\infty} \sum_{m=0}^{\infty} A_{nm} v_{nm} \tag{10}$$

The diffracted field of this wave in the  $z = z_0$  plane is then given by

$$\Psi(x,y,z=z_0) = \sum_{n=0}^{\infty} \sum_{m=0}^{\infty} A_{nm} u_{nm}(x,y,z=z_0) \tag{11}$$

In order for the grating to be useful as a sampling tool, we must show that an arbitrary wave is only scaled in the diffracted orders. For the  $q = 1$  and  $q = 0$  orders we must show that

$$\Psi(x + v\lambda z, y, z=z_0)_{q=1} = K \Psi(x, y, z=z_0)_{q=0} \tag{12}$$

where  $K$  is a complex constant. If we compare the amplitude functions we see that

$$u_{nm}(x + v\lambda z, y, z=z_0)_{q=1} = K'(x) u_{nm}(x, y, z=z_0)_{q=0} \tag{13}$$

where

$$\begin{aligned}
K'(x) = & i J_1(2\pi\Delta) \exp(i\phi - 2\pi i v \lambda z_0) / J_0(2\pi\Delta) \\
& \cdot \exp \left[ (i\pi/\lambda z_0) \left( 2v\lambda z_0 x + (v\lambda z_0)^2 \right) \left( 1 - z_0/R(z_0) \right) \right]
\end{aligned} \tag{14}$$

Using equation (11) for the  $q = 1$  case and equation (13) we can show that

$$\Psi(x-v\lambda z, y, z=z_0)_{q=1} = \sum_{n=0}^{\infty} \sum_{m=0}^{\infty} A_{nm} u_{nm}(x-v\lambda z, y, z=z_0)_{q=1} \quad (15)$$

$$= \sum_{n=0}^{\infty} \sum_{m=0}^{\infty} A_{nm} K'(x) u_{nm}(x, y, z=z_0)_{q=0}$$

$$= K'(x) \Psi(x, y, z=z_0)_{q=0} \quad (16)$$

Thus we see that the first order mode is just a scaled sample of the zero order, except for the phase term linear in  $x$ . This linear term can be explained when one realizes that the observation plane (the  $z=z_0$  plane) is not normal to the propagation direction for any order except the zero order. Therefore this grating may be useful if one can correct for the linear phase shift term.

If one is interested in intensity, we take the absolute square of equation (16) and get

$$I(x-v\lambda z, y, z=z_0)_{q=1} = K I(x, y, z=z_0)_{q=0} \quad (17)$$

where  $K = [J_1(2\pi\Delta)/J_0(2\pi\Delta)]^2$ .

Thus we see that for the intensity profile the grating is useful since it produces a scaled profile in the first order.

## PHOTON POPULATION DECAY IN A FABRY-PEROT CAVITY

D. A. Holmes

The concept of a decay time of a photon in an optical cavity is often used in the analytical description of laser devices.<sup>1,2\*</sup> Assume, at time  $t = 0$ , that  $N_0$  monochromatic photons reside inside a passive optical cavity such as that shown in Figure 1. The usual approximation for the photon population at later times is given by<sup>3</sup>

$$N(t) \approx N_0 e^{-t/t_c} \quad (1)$$

where the decay time  $t_c$  is commonly written as

$$t_c = -2nl/c \ln(R_1 R_2) \quad (2)$$

When the exponential approximation (equation (1)) is valid, the average time  $\langle t \rangle$  that a photon spends in the cavity is simply equal to  $t_c$ .

It is the purpose of this work to give the exact expressions for the photon population  $N(t)$  and the average time  $\langle t \rangle$ , using the idealized model described in Figure 1. The initial conditions will be specified by photon distributions  $f_R(x)$  and  $f_L(x)$ , where  $f_R(x)$  distributes the photons which are traveling to the right at time  $t = 0$  and  $f_L(x)$  distributes the photons which are traveling to the left at time  $t = 0$ . The initial population is thus given by

$$N_0 = \int_0^l f_R(x) dx + \int_0^l f_L(x) dx \quad (3)$$

We first discuss the photon population  $N(t)$ . The population can be constructed by observing the distributions as they travel with speed  $v = c/n$  and undergo successive partial reflections at the end reflectors. For  $m$  an even integer and  $(m-1)l \leq vt \leq ml$ , the population is

---

\*Many additional references can be found in references 1 and 2.



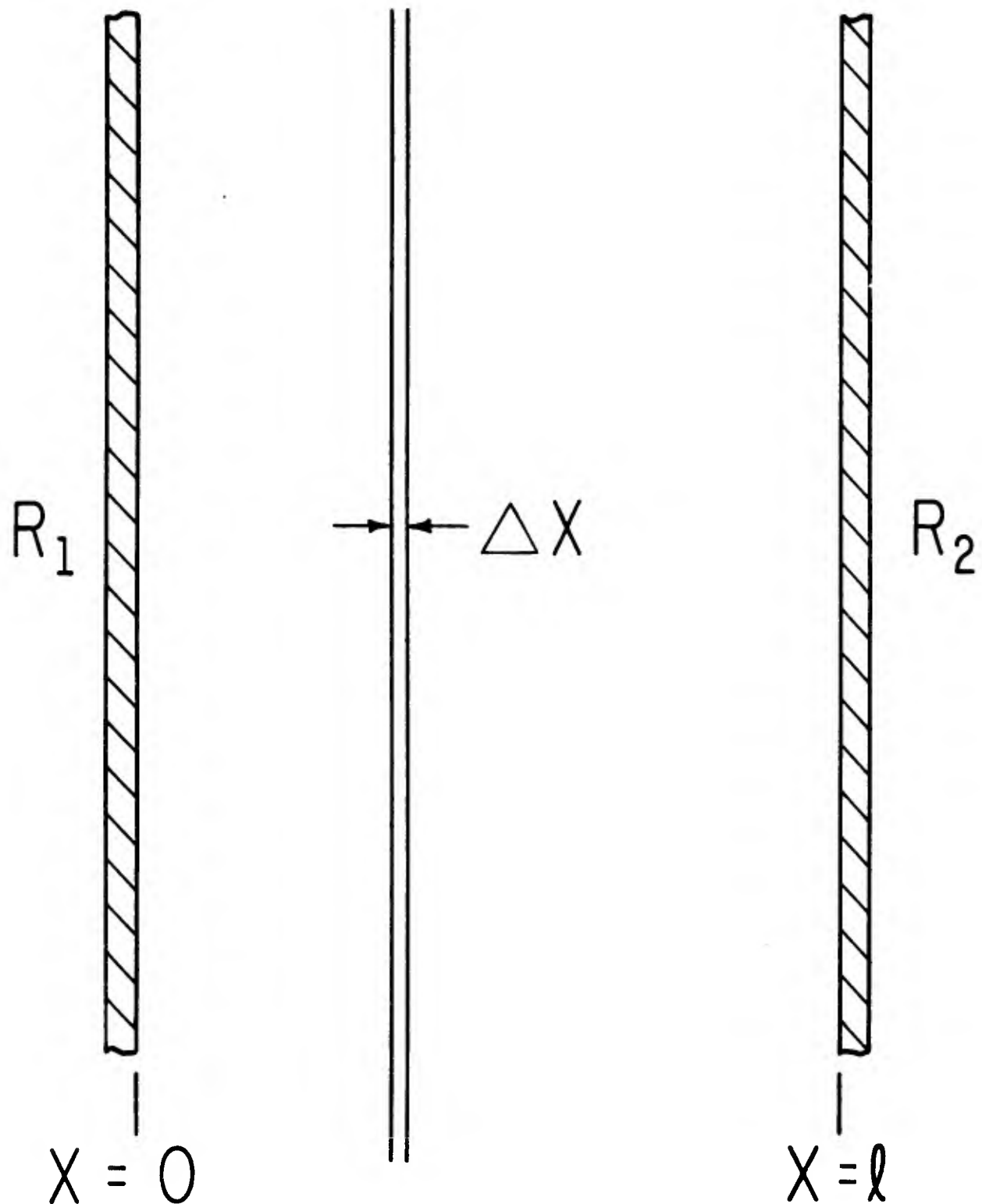


Figure 1. A parallel-plate (Fabry-Perot) optical cavity with infinite mirrors. The intensity (or power) reflectance of the left mirror is  $R_1$  while that for the right mirror is  $R_2$ . For time  $t \geq 0$ , the medium between the mirrors ( $0 \leq x \leq l$ ) is assumed to be lossless, homogeneous and isotropic with refractive index  $n$ . At time  $t = 0$ ,  $N_0$  identical photons exist in the cavity, all of which are traveling parallel to the  $x$ -axis. The only way a photon can escape the cavity is via transmission through one of the end mirrors.

$$\begin{aligned}
N(t) = & \frac{(R_1 R_2)^{\frac{m}{2}}}{R_1} \left[ \int_0^{m\ell - vt} f_R(x) dx + R_1 \int_{m\ell - vt}^{\ell} f_R(x) dx \right] \\
& + \frac{(R_1 R_2)^{\frac{m}{2}}}{R_2} \left[ R_2 \int_0^{vt - (m-1)\ell} f_L(x) dx + \int_{vt - (m-1)\ell}^{\ell} f_L(x) dx \right] \quad (4)
\end{aligned}$$

For  $m$  an odd integer and  $(m-1)\ell < vt < m\ell$ , we have

$$\begin{aligned}
N(t) = & (R_1 R_2)^{\frac{m-1}{2}} \left[ \int_0^{m\ell - vt} f_R(x) dx + R_2 \int_{m\ell - vt}^{\ell} f_R(x) dx \right] \\
& + (R_1 R_2)^{\frac{m-1}{2}} \left[ R_1 \int_0^{vt - (m-1)\ell} f_L(x) dx + \int_{vt - (m-1)\ell}^{\ell} f_L(x) dx \right] \quad (5)
\end{aligned}$$

The exact solutions (equations (4) and (5)) bear little resemblance to the approximation (equation (1)), however, for certain discrete values of  $t$ , the exact and the approximate solutions are identical. When  $vt = m\ell$  ( $m$  even), equation (4) gives

$$N\left(\frac{m\ell}{v}\right) = N_0 (R_1 R_2)^{\frac{m}{2}} \quad (6)$$

which is identical to the result obtained by using equations (1) and (2), hence, the approximate form (equation (1)) does provide an estimate of the gross time-dependent behavior of  $N(t)$ .

The exact and approximate solutions can be used to obtain the photon loss rate. For  $m$  an even integer and  $(m-1)\ell \leq vt \leq m\ell$ , we have

$$-\frac{dN(t)}{dt} = \left[ \frac{(R_1 R_2)^{\frac{m}{2}}}{R_1} \right] (1-R_1) v f_R(m\ell - vt) + \left[ \frac{(R_1 R_2)^{\frac{m}{2}}}{R_2} \right] (1-R_2) v f_L(vt - m\ell + \ell) \quad (7)$$

For  $m$  an odd integer and  $(m-1)\ell \leq vt \leq m\ell$ , we have

$$-\frac{dN(t)}{dt} = \left(R_1 R_2\right)^{\frac{m-1}{2}} (1-R_2)^v f_R(\ell-vt) + \left(R_1 R_2\right)^{\frac{m-1}{2}} (1-R_1)^v f_L(vt-m\ell+\ell) \quad (8)$$

From equations (1) and (2) we obtain

$$-\frac{dN(t)}{dt} \approx \left(R_1 R_2\right)^{\frac{vt}{2\ell}} / \tau_c \quad (9)$$

For arbitrary initial distributions and reflectivities, it is certainly not clear that equation (9) represents a valid approximation to equations (7) and (8). When  $R_1$  and  $R_2$  are close to unity, however, it can be argued qualitatively that equation (9) is representative of the gross behavior of the photon loss rate because the change in  $N(t)$  is small over a cavity transit time.

Now we discuss the average cavity time  $\langle t \rangle$ . Using equations (7) and (8) and the definition

$$\langle t \rangle = \int_0^{\infty} dt \left( \frac{-1}{N_0} \cdot \frac{dN(t)}{dt} \right) t \quad (10)$$

we obtain

$$\langle t \rangle = \left(1/N_0\right) \int_0^{\ell} \left[ \tau_R(x) f_R(x) + \tau_L(x) f_L(x) \right] dx \quad (11)$$

where

$$\tau_R(x) = \frac{\ell-x}{v} + \frac{\ell}{v} \cdot \frac{R_2(1+R_1)}{1-R_1 R_2} \quad (12)$$

$$\tau_L(x) = \frac{x}{v} + \frac{\ell}{v} \cdot \frac{R_1(1+R_2)}{1-R_1 R_2} \quad (13)$$

An alternative derivation of  $\langle t \rangle$ , which is perhaps more simple and direct, is as follows. Consider an infinitesimal slab  $\Delta x$  located at position  $x$ . This slab contains  $f_L(x) \Delta x$  photons moving toward the left with speed  $v = c/n$  at time  $t = 0$ . The average time  $\tau_L(x)$  that these photons remain within the cavity is given by

$$\begin{aligned} \tau_L(x) = & \sum_{i=0}^{\infty} (1-R_1)(R_1R_2)^i (x+2i\ell)/v \\ & + \sum_{i=0}^{\infty} (1-R_2)R_1(R_1R_2)^i (x+\ell+2i\ell)/v \end{aligned} \quad (14)$$

Evaluation of the sums in equation (14) yields equation (13). A similar procedure is used to obtain  $\tau_R(x)$  and averaging over the initial photon distributions yields the final formula (equation (11)). In general,  $\langle t \rangle$  depends upon the initial distributions, except for the special case  $f_R(x) = f_L(x)$ .

A physical interpretation of equation (11) can be realized by considering the following conceptual experiment. Suppose we have a very large number of identical empty cavities of the type shown in Figure 1. At time  $t = 0$ , a single photon is created in each cavity, subject to the constraint that it can only travel parallel to the x-axis. For each cavity, the probability that its photon lies between  $x$  and  $x + \Delta x$  and is moving toward the left at time  $t = 0$  is  $(f_L(x)/N_0)\Delta x$ . The probability that a photon (moving toward the left at  $t = 0$ ) leaves the cavity at  $t = \frac{x}{v}$  is  $(1-R_1)$ , the probability that it leaves the cavity at  $t = (x+\ell)/v$  is  $(1-R_2)R_1$ , and so on. Photons initially moving toward the right are considered in a similar manner. Suppose that the time each photon disappears from its cavity is measured. If these disappearance times are averaged, then the resultant average will approach  $\langle t \rangle$  as given by equation (11) as the number of cavities becomes infinite.

To consider a specific example, let us assume the following analytical forms:

$$f_R(x) = g_R e^{\alpha x}, \quad f_L(x) = g_L e^{\alpha(\ell-x)} \quad (15)$$

where  $g_R$ ,  $g_L$  and  $\alpha$  are arbitrary constants. Using equation (15) in equation (11), we obtain

$$\langle t \rangle = \frac{1}{\alpha v} \cdot \frac{e^{\alpha\ell} - \alpha\ell - 1}{e^{\alpha\ell} - 1} + \frac{\ell}{c} \cdot \frac{R_2(1+R_1)g_R + R_1(1+R_2)g_L}{(1+R_1R_2)(g_R+g_L)} \quad (16)$$

A case of physical interest occurs when

$$R_1R_2e^{2\alpha\ell} = 1 \text{ and } g_R/g_L = (R_1/R_2)^{1/2} \quad (17)$$

Conditions (equation (17)) thus simulate a laser, operating at threshold prior to time zero, whose gain  $\alpha$  suddenly drops to zero at  $t = 0$ . Under these conditions  $\langle t \rangle = t_c$ ; in addition, equations (1) and (9) are exact.

It is a pleasure to acknowledge several helpful discussions with Dr. P. V. Avizonis.

#### REFERENCES

1. Smith, W. V., and Sorokin, P. P., The Laser, McGraw-Hill Book Company, New York, p. 71, 1966.
2. Lengyel, B. A., Introduction to Laser Physics, John Wiley and Sons, New York, p. 237, 1966.
3. Schawlow, A. L., and Townes, C. H., "Infrared and Optical Masers," Phys. Rev., 112, pp. 1940-1949, December 1958.

## PARAMETRIC STUDY OF APERTURED FOCUSED GAUSSIAN BEAMS

D. A. Holmes, J. E. Korka, and P. V. Avizonis

### Introduction

Diffraction of Gaussian beams by circular apertures has been the subject of several recent papers.<sup>1,2,3,4</sup> In the present paper, we would like to consider some additional features of apertured and focused Gaussian beams. To use a simple analytical approach we assume that the focusing element is an ideal lens and that the wave-field magnitude is Gaussian over the lens. Simple kinds of phase distortion are introduced and the subsequent changes in the nature of the focused beam are discussed. Numerical illustrations have been prepared using generalized dimensionless coordinates.

### Diffraction Formulation

To set up the problem, we define an  $(r, \theta, z)$  cylindrical coordinate system. The ideal thin lens is assumed to lie in the  $z = 0$  plane while the output beam travels in the positive  $z$  direction. The focusing problem will be handled by postulating a convergent Gaussian beam diffracted by an annular aperture in the  $z = 0$  plane. The transmitting portion of the annular aperture occupies the region  $a \leq r \leq b$ . The diffraction calculations are applicable to the region  $z > 0$  and are subject to the usual restrictions governing the use of Fresnel diffraction integrals in the scalar wave approximation.<sup>5</sup>

The aperture field is taken as

$$v(r) = v_0 \exp \left[ -(r/w)^2 - (i\pi r^2/\lambda R) - i\phi \right] \quad (1)$$

In the sense of geometrical optics, the beam is focused at a point on the  $z$ -axis a distance  $R$  from the  $z = 0$  plane, hence, the plane  $z = R$  is called the focal plane. The focal range  $R$  is taken to be positive which implies a time variation given by  $\exp[-i\omega t]$ . In equation (1),  $w$  is the beam spot size<sup>6</sup> at the aperture,  $\lambda$  is the vacuum wavelength, and  $\phi$  is a phase distortion which we shall restrict to be a function of  $r$  only.

For convenience in later calculations, we shall assume that  $v_0$  is a real constant and is normalized so that total power  $P_0$  is always transmitted by the aperture. In the scalar wave approximation, we can then always determine  $v_0$  by the relation

$$P_0 = 2\pi \int_a^b dr r |v(r)|^2 \quad (2)$$

When  $v(r)$  is given by equation (1) we have

$$v_0^2 = (2P_0/\pi w^2) / \left[ \exp(-2(a/w)^2) - \exp(-2(b/w)^2) \right] \quad (3)$$

Using the Fresnel diffraction integral,<sup>5</sup> we write the scalar wave complex amplitude of the diffracted beam in the cylindrical coordinate system as

$$u(r, z) = (2\pi/\lambda z) \int_a^b d\rho \rho v(\rho) J_0(2\pi\rho r/\lambda z) \exp[i\pi\rho^2/\lambda z] \quad (4)$$

where we have omitted a phase factor on the right hand side of

$$-i \exp[i2\pi z/\lambda + i\pi r^2/\lambda z]$$

The irradiance of the diffracted beam is taken simply as  $I(r, z) = |u(r, z)|^2$ . In any plane  $z = \text{constant}$ , the power passing through a circle of radius  $r$  centered on the  $z$ -axis is given by

$$P(r, z) = 2\pi \int_0^r d\rho \rho |u(\rho, z)|^2 \quad (5)$$

#### On-Axis Irradiance for Ideal Beams

We now assume  $\phi = 0$  in equation (1) and  $r = 0$  in equation (4). With these restrictions  $I(0, z)$  can be written as

$$I(0, z) = v_0^2 \text{ NUM/DEN} \quad (6)$$

where

$$\begin{aligned} \text{NUM} &= \left[ \exp\left(-\frac{a^2}{w^2}\right) - \exp\left(-\frac{b^2}{w^2}\right) \right]^2 \\ &\quad + 4 \exp\left[-\frac{a^2 + b^2}{w^2}\right] \sin^2 \left[ \pi(b^2 - a^2)(z-R)/2\lambda zR \right] \\ \text{DEN} &= (\lambda z/\pi w^2)^2 + (z-R)^2/R^2 \end{aligned}$$

It is commonly assumed that  $I(0, z)$  is symmetrical<sup>7</sup> about the point  $z = R$  but inspection of equation (6) reveals that this is not generally the case.

There is an optimization problem that one can readily solve using equation (6). We first consider that  $z$  is fixed at a constant value  $z_0$  and that  $R$  is variable. In this case  $I(0, z_0)$  is regarded as a function of  $R$  and there exists an optimum value of  $R$  which maximizes  $I(0, z_0)$ . This optimum value is simply  $R = z_0$ . Physically, this means that an on-axis detector located at an arbitrary fixed location  $z_0$  will receive the largest signal when the beam is focused such that  $R = z_0$ . This is true regardless of the values of  $a$ ,  $b$ , and  $w$ . If now the beam focus is fixed at  $R = z_0$  and the on-axis detector is physically moved along the  $z$ -axis toward the aperture, it is generally found that the detector signal will first increase, then pass through a maximum and then decrease.

For fixed  $a$ ,  $b$ ,  $P_0$ , and  $\lambda$ , the focal point irradiance is maximized for  $w \rightarrow \infty$ , i.e., the case of uniform illumination. The analytical proof of this maximization is not difficult, but will not be given here; numerical illustrations will demonstrate this fact later. The focal point irradiance is defined as  $I_f = I(0, R)$  and is given by

$$I_f = \frac{2\pi w^2 P_0 \exp\left[\frac{b^2 - a^2}{w^2}\right] - 1}{(\lambda R)^2 \exp\left[\frac{b^2 - a^2}{w^2}\right] + 1} \quad (7)$$

The maximum value of  $I_f$  is given by

$$\lim_{w \rightarrow \infty} I_f = \pi(b^2 - a^2)P_0/(\lambda R)^2$$

We now define the dimensionless parameters

$$\alpha = a/b \quad (8a)$$

and

$$\beta = b/w \quad (8b)$$



Using equation (8) and rearranging equation (7) we get

$$\frac{(\lambda R)^2 I_f}{\pi b^2 P_0} = \frac{(2/\beta^2) \{ \exp[\beta^2(1-\alpha^2)] - 1 \}}{\exp[\beta^2(1-\alpha^2)] + 1} \quad (9)$$

In Figure 1 we have plotted equation (9) as a function of  $\beta$ , with  $\alpha$  as a changing parameter, to illustrate how the focal point irradiance is influenced by truncation and central obscuration of the focused Gaussian beam. There are two points of interest for this figure. First, for relatively large  $\alpha$  values, the focal plane irradiance is insensitive to large changes in  $\beta$ . Secondly, to efficiently utilize the transmitting aperture (i.e., maintain largest possible value of  $I_f$ ), one should confine  $\beta$  to the range  $0 \leq \beta \leq 1$ .

Diffraction of a Gaussian beam by a circular, opaque disk with no outer truncation can be accommodated by equation (6). This case occurs when  $b \rightarrow \infty$  and it is then found that equation (6) reduced to

$$I(0, z) = \frac{2P_0 / \pi w^2}{(\lambda z / \pi w^2)^2 + (z - R)^2 / R^2} \quad (10)$$

Note that equation (10) is independent of  $a$ . The on-axis irradiance (equation (10)) is, in fact, the result for the free [ $a = 0$ ,  $b = \infty$ ] Gaussian of power  $P_0$ . It is important to note that this result applies for fields normalized such that power  $P_0$  is always transmitted past the aperture plane. The similar problem of an opaque disk illuminated by a uniform field is discussed by Stone.<sup>8</sup>

To illustrate the behavior of equation (6), a set of dimensionless quantities is defined as

$$\gamma = \pi b^2 / \lambda R \quad (11a)$$

$$\zeta = z / R \quad (11b)$$

and

$$\bar{I}(0, \zeta) = I(0, z) / I_f \quad (11c)$$

In Figure 2, we have plotted the normalized irradiance  $\bar{I}(0, \zeta)$  as a function of the normalized distance  $\zeta$  with  $\alpha$ ,  $\beta$ , and  $\gamma$  as changing parameters. For large values of  $\gamma$ , the curves become more symmetrical about the point  $\zeta = 1$ ,

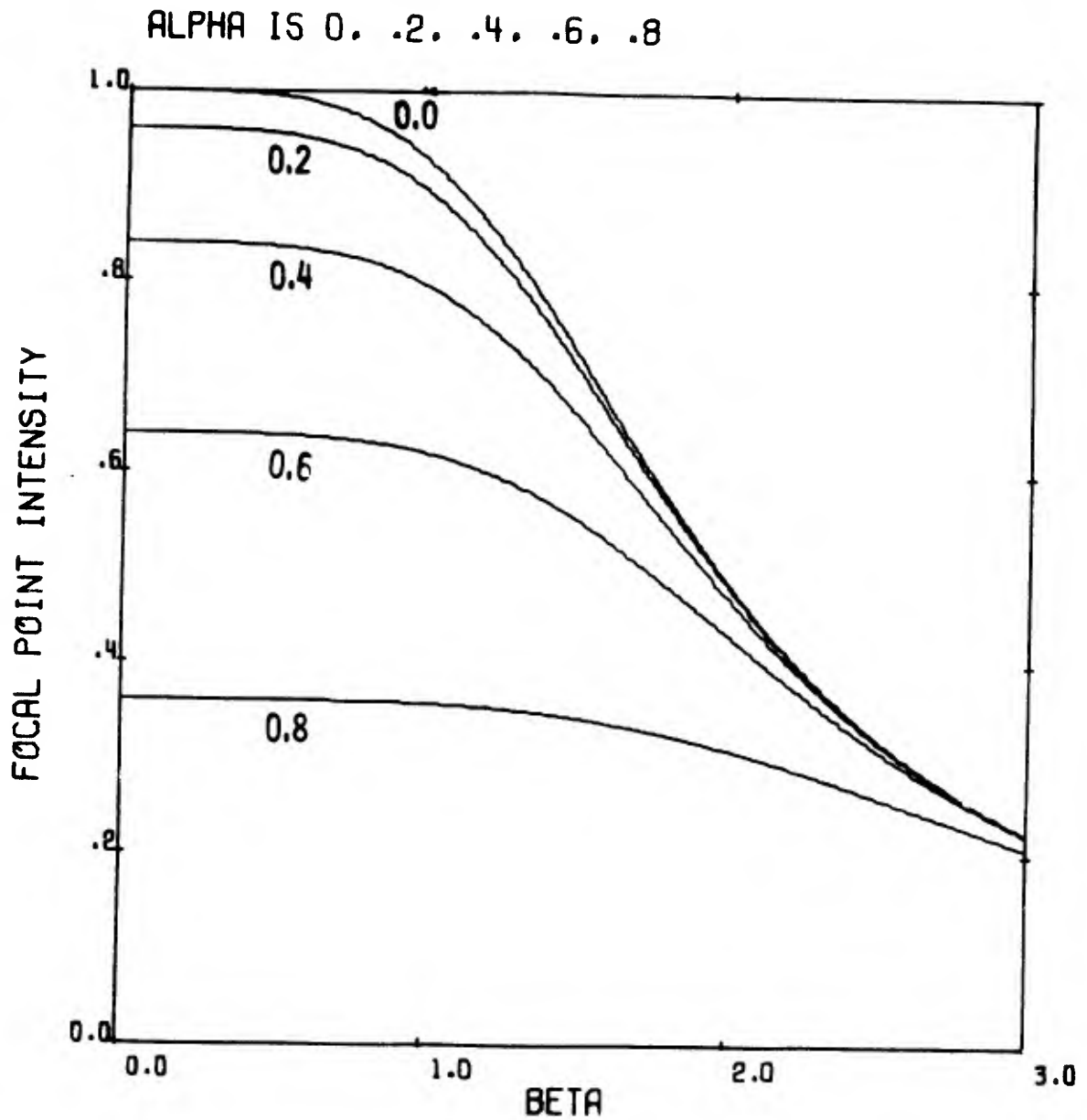


Figure 1. Normalized focal point irradiance  $(\lambda R)^2 I_f / \pi b^2 P_0$  versus  $b/w$  with  $a/b$  as a changing parameter. The curves are labeled with the value  $\alpha$ . For all values of  $\alpha$ , the curves show that the focal point irradiance is maximized for  $\beta \rightarrow 0$  or  $w \rightarrow \infty$ .

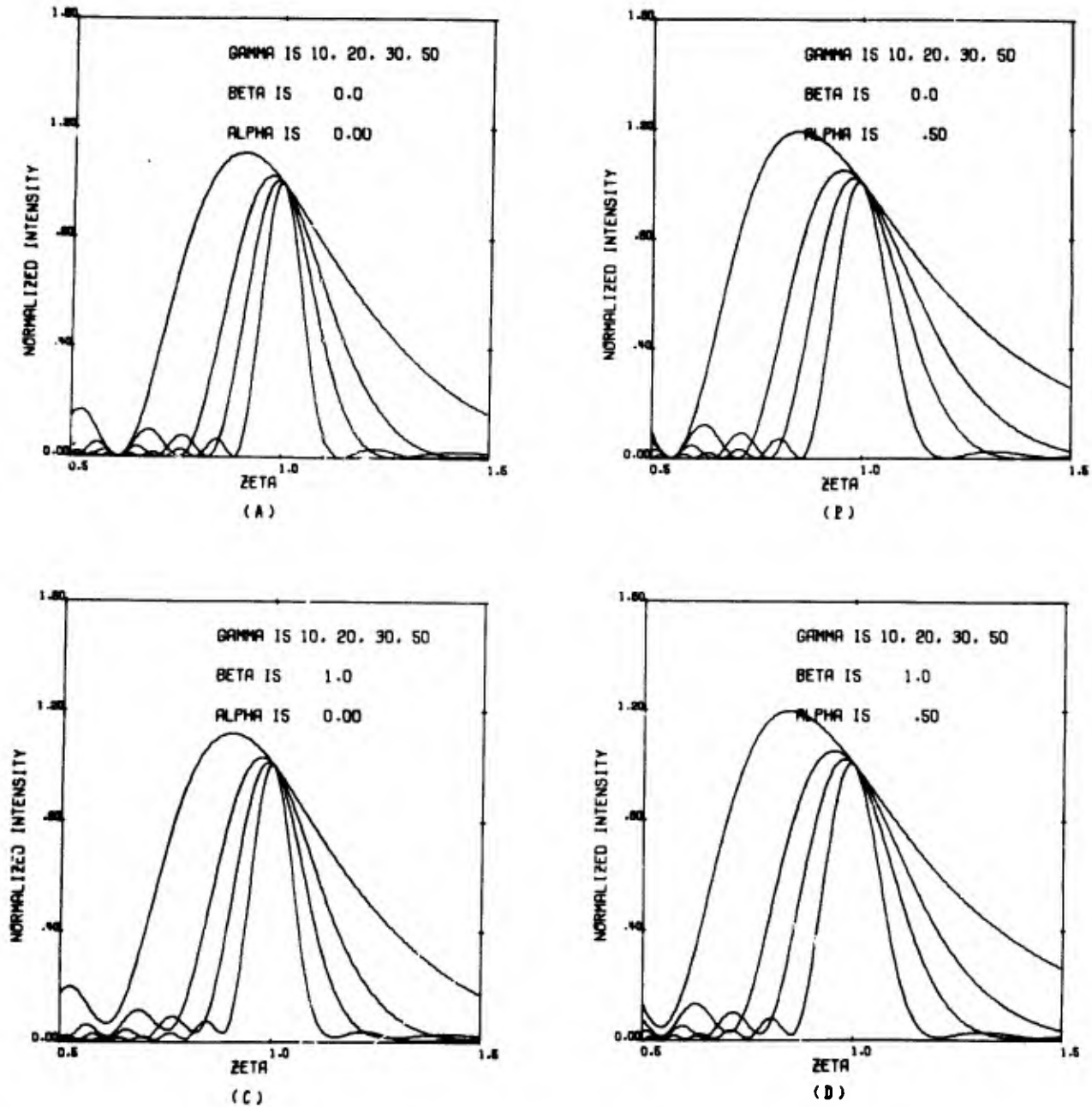


Figure 2. Normalized on-axis irradiance  $\bar{I}(0, \zeta)$  as a function of normalized distance  $\zeta$  from the aperture with  $\alpha$ ,  $\beta$ , and  $\gamma$  as changing parameters. For each figure, the curves sharpen as  $\gamma$  increases. Note that, by comparing (a) with (c) and (b) with (d), the change from  $\beta = 0$  to  $\beta = 1$  does not greatly change the general shape of the on-axis irradiance curves; this behavior is indicated in Figure 1. The  $\beta = 0$  solution for  $\bar{I}(0, \zeta)$  is

$$\bar{I}(0, \zeta) = (1/\zeta^2) \text{sinc}^2[\gamma(1-\alpha^2)(\zeta-1)/2\zeta]$$

which shows clearly that  $\bar{I}(0, \zeta)$  becomes a more sharply peaked function of  $\zeta$  as  $\gamma$  increases.

approaching the behavior predicted by Born and Wolf.<sup>7</sup> Large  $\gamma$  systems are not unusual in optical systems used at visible wavelengths. However, small  $\gamma$  values can easily characterize long focal length infrared systems, e.g., for  $R = 100\pi\text{cm}$ ,  $\lambda = 10\mu\text{m}$  and  $b = 1\text{ cm}$ , we find that  $\gamma = 10$ , for which the irradiance distributions are distinctly unsymmetrical about the geometrical focus. This could certainly be the case for laboratory type optical setups. Again, in general, there is not much dependence upon  $\beta$  for values of 0 to 1, as expected from previous section considerations, and Figure 1. Also, it is clear from Figure 2 that the maximum on-axis intensity does not occur at the focal point, especially for small  $\gamma$ , but is displaced substantially to  $\zeta < 1$ .

### Irradiance Distributions Near the Focus

It is convenient now to transform equation (4) to a function of the dimensionless parameters and coordinates defined in equations (8) and (11) and

$$\xi = 2rb/\lambda R \quad (12)$$

with a new integration variable  $x = \rho/b$ . Using equation (1) in equation (4), the transformation yields

$$u(\xi, \zeta) = \frac{2\gamma v_0}{\zeta} \int_{\alpha}^1 J_0(\pi\xi x/\zeta) \exp[-(\beta x)^2 - ix^2\gamma(\zeta-1)/\zeta - i\phi] x dx \quad (13)$$

The amplitude  $v_0$  cannot be expressed in terms of the dimensionless parameters; therefore, it is convenient to normalize equation (13) to the nonaberrated, ( $\phi = 0$ ), focal point amplitude.

$$\bar{u}(\xi, \zeta) = \frac{\int_{\alpha}^1 J_0(\pi\xi x/\zeta) \exp[-(\beta x)^2 - ix^2\gamma(\zeta-1)/\zeta - i\phi] x dx}{(\zeta/2\beta^2) [\exp(-\alpha^2\beta^2) - \exp(-\beta^2)]} \quad (14)$$

The normalized irradiance is given simply by

$$\bar{I}(\xi, \zeta) = |\bar{u}(\xi, \zeta)|^2 = |u(\xi, \zeta)|^2 / I_f \quad (15)$$

where the normalization is such that  $\bar{I}(0, 1) = 1$ .

We have prepared several three-dimensional plots which illustrate the behavior of equation (15); these are shown in Figure 3.

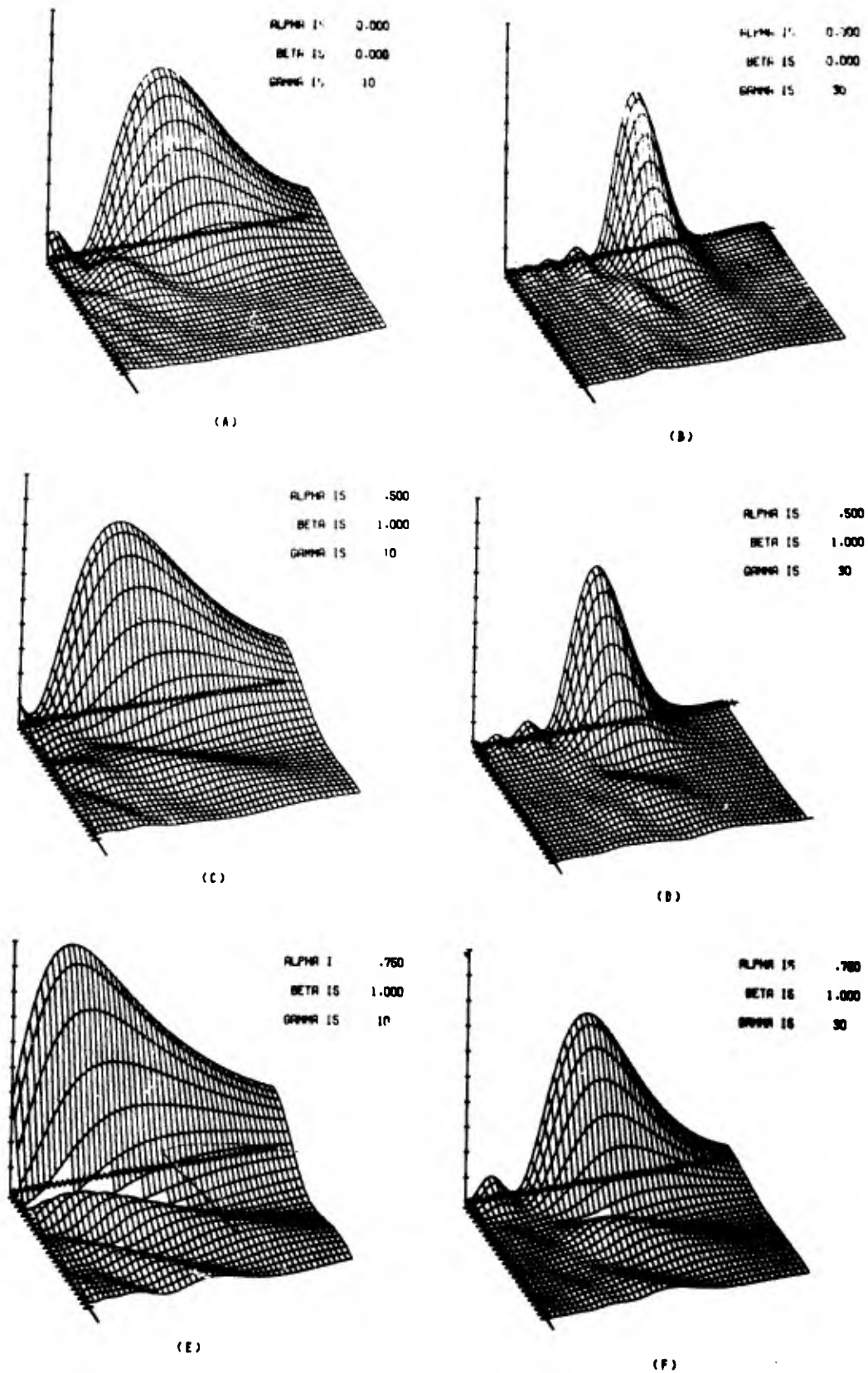


Figure 3. The  $\bar{I}(\xi, \zeta)$  surface. The normalized irradiance is plotted on the vertical axis. The  $(\xi, \zeta, \bar{I}(\xi, \zeta))$  coordinate axis form a right hand coordinate system. The axes cover the ranges  $0 \leq \bar{I}(\xi, \zeta) \leq 1.6$ ,  $0 \leq \xi \leq 2.5$ , and  $0.5 \leq \zeta \leq 1.5$ . In each figure,  $\phi = 0$ .

### Power Distributions Near the Focus

We define the normalized power as,

$$\bar{P}(\xi, \zeta) = P(r, z)/P_0$$

where  $P(r, z)$  is the integrated intensity from 0 to  $r$  and is defined in equation (5). Using equations (5) and (15), we obtain

$$\bar{P}(\xi, \zeta) = (\pi/\beta)^2 \frac{\exp(-\alpha^2\beta^2) - \exp(-\beta^2)}{\exp(-\alpha^2\beta^2) + \exp(-\beta^2)} \int_0^\xi \eta \bar{I}(\eta, \zeta) d\eta \quad (16)$$

We have prepared three dimensional plots of the normalized power corresponding to those of Figure 3; these are shown in Figure 4 and apply for ideal beams,  $\phi = 0$ .

In Figure 5, we show predictions of equation (16) when  $\zeta = 1$  and  $\phi = 0$ . The focal plane (or far field) power profiles shown in Figures 5a and 5b may be considered as generalizations of Figure 8.13 on page 397 of Born and Wolf.<sup>7</sup> From Figures 5a and 5b, it is possible to derive the approximate formula

$$\bar{P}(\xi, 1) \approx 1.25(\xi - 0.14) \quad (17)$$

which is a very good approximation over the ranges  $0.3 \leq \xi \leq 0.7$  and  $0 \leq \beta \leq 1$  with  $\alpha = 0$ . Figures 5c, d, e, and f are quite useful in evaluating the focal plane power as a function of beam truncation and obscuration.

We shall now assume  $\phi = 0$  and  $\zeta = 1$  and show that equation (16) implies that energy is conserved, in spite of the many approximations that are used to obtain the Fresnel diffraction integral in the form given by equation (4). Conservation of energy requires that

$$\lim_{\xi \rightarrow \infty} \bar{P}(\xi, 1) = 1 \quad (18)$$

To show that equation (18) is satisfied, we shall write equation (16) in the following form

$$\bar{P}(\xi, 1) = f_1(\alpha, \beta) f_2(\xi, \alpha, \beta) \quad (19)$$

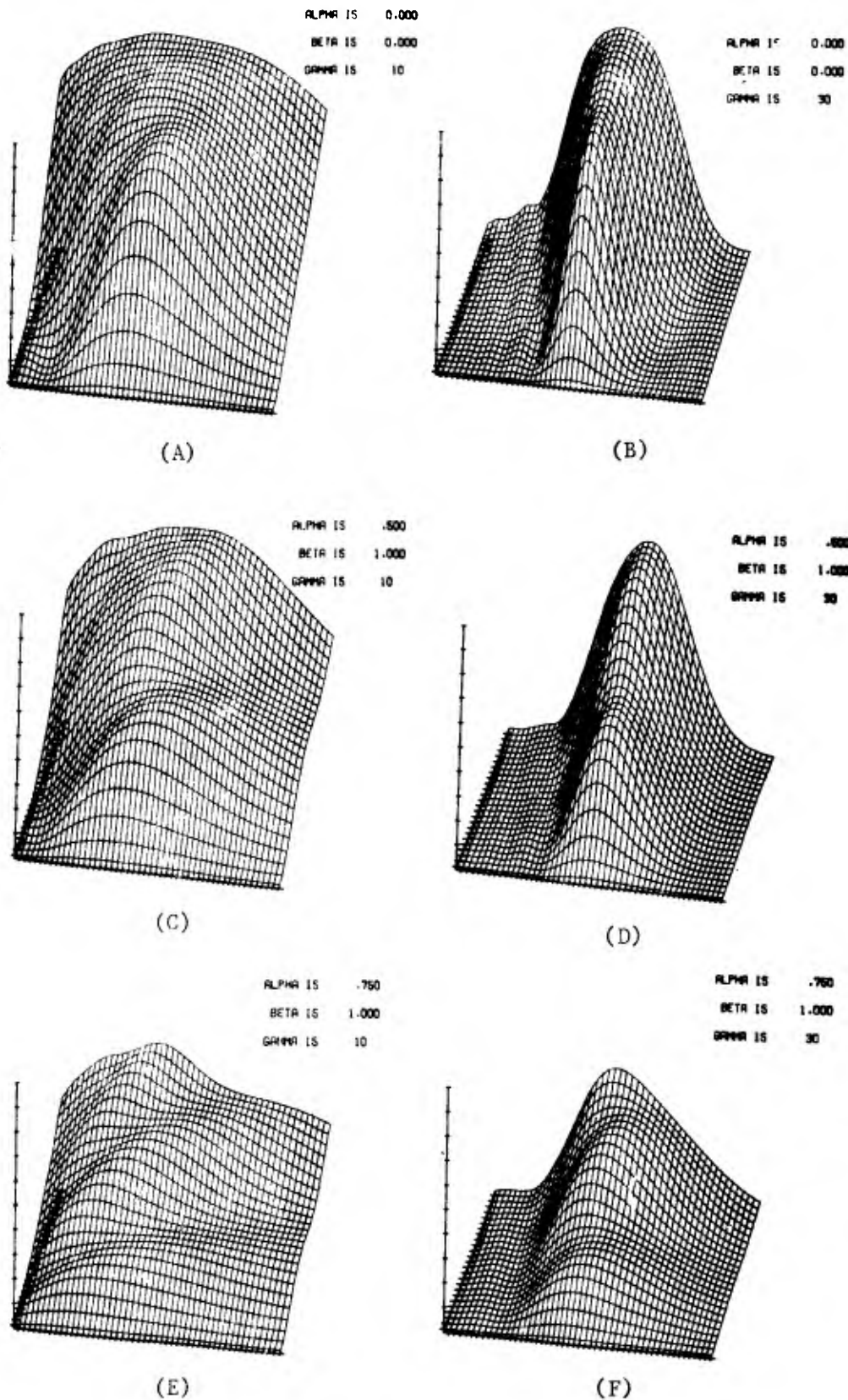


Figure 4. The  $\bar{P}(\xi, \zeta)$  surface. Each plot here corresponds to a plot in Figure 3. The normalized power is plotted on the vertical axis. The  $(\xi, \zeta, \bar{P}(\xi, \zeta))$  coordinate axes form a left hand coordinate system. The axes cover the ranges  $0 \leq \bar{P}(\xi, \zeta) \leq 1$ ,  $0 \leq \xi \leq 2.5$  and  $0.5 \leq \zeta \leq 1.5$ . In each case,  $\phi = 0$ .

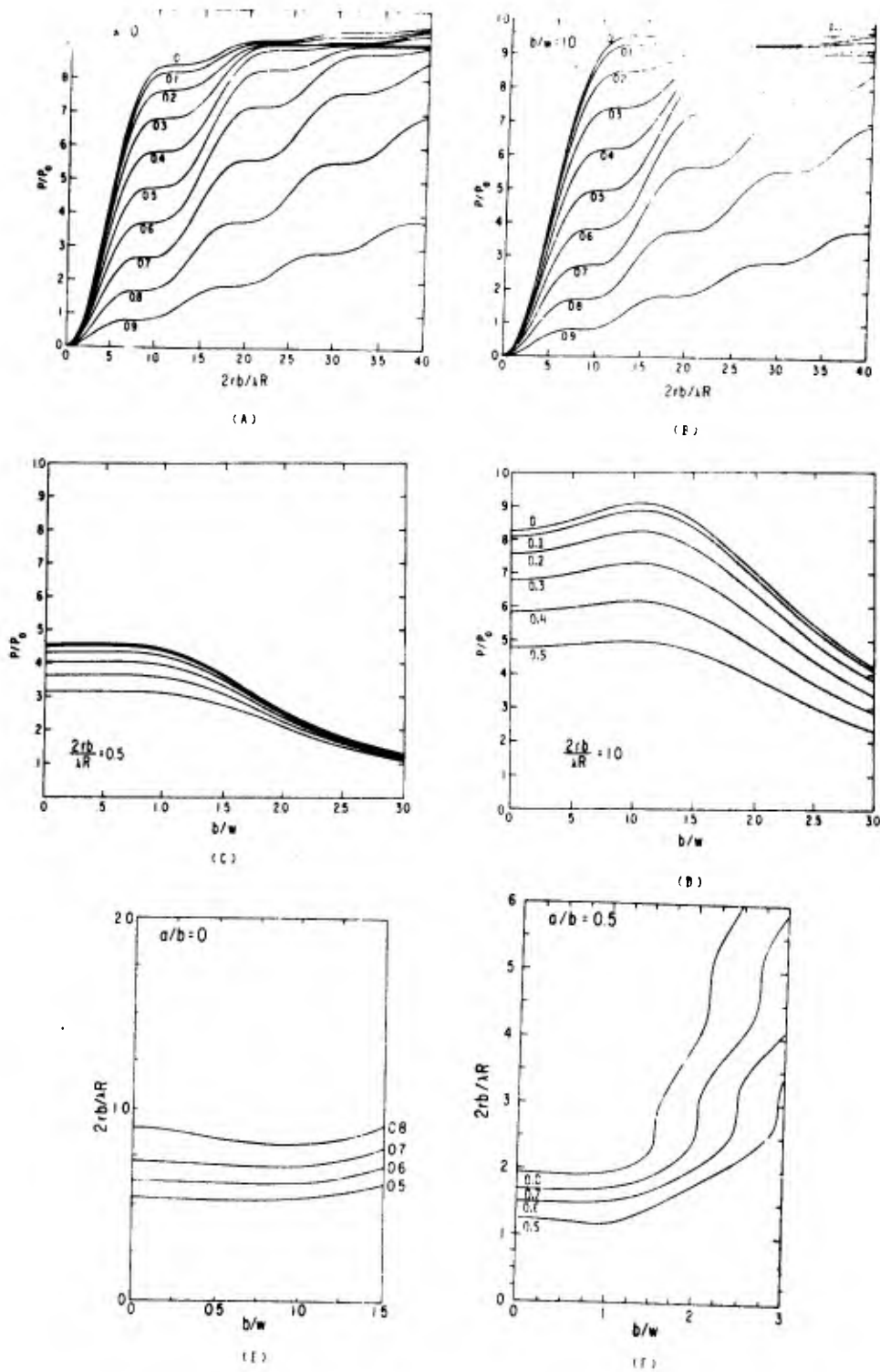


Figure 5. Focal plane profiles. In (a) and (b) we show  $\bar{P}(\xi, 1)$  as a function of  $\xi$  with  $\alpha$  and  $\beta$  as changing parameters. Each curve is labeled by the corresponding value of  $\alpha$ . In (a),  $\beta = 0$  and in (b),  $\beta = 1$ . In (c) and (d), we show the normalized power as a function of  $\beta$  for selected values of  $\xi$  and  $\alpha$ . In (d), the curves are labeled by the corresponding value of  $\alpha$ ; the curves in (c) correspond to the same values of  $\alpha$ . In (e) and (f) we show constant power loci; each curve is labeled by the corresponding constant value of normalized power. Graphs (e) and (f) would be useful for quickly estimating the required radius for a focal plane aperture that is to transmit, say 50 percent of the total focal plane power.



where

$$f_1(\alpha, \beta) = (2\beta)^2 \left[ \exp(-2\alpha^2\beta^2) - \exp(-2\beta^2) \right]^{-1} \quad (20a)$$

$$f_2(\xi, \alpha, \beta) = \int_0^{\pi\xi} y dy \left\{ \int_{\alpha}^1 dx x J_0(yx) \exp(-\beta^2 x^2) \right\}^2 \quad (20b)$$

By taking the limit as  $\xi \rightarrow \infty$  in equation (20b) and by rearranging the order of integration, we can obtain

$$\lim_{\xi \rightarrow \infty} f_2 = \int_{\alpha}^1 d\eta \eta \exp[-(\beta\eta)^2] \int_{\alpha}^1 d\sigma \sigma \exp[-(\beta\sigma)^2] \int_0^{\infty} d\rho \rho J_0(\rho\eta) J_0(\rho\sigma) \quad (21)$$

Now we use the following identity

$$\int_0^{\infty} d\rho \rho J_0(\rho\eta) J_0(\rho\sigma) = \delta(\sigma-\eta)/\sigma \quad (22)$$

Substituting equation (22) into equation (21) and then performing the integration over  $\sigma$  we obtain

$$\lim_{\xi \rightarrow \infty} f_2 = \int_{\alpha}^1 d\eta \eta \exp[-2(\beta\eta)^2] = 1/f_1 \quad (23)$$

and thus equation (18) is exactly satisfied. All of the approximations used to obtain equation (19) exactly balance; a similar compensation of approximations is discussed by Stone.<sup>9</sup>

### Phase Aberrations

In this section we consider the effects owing to the phase distortion term  $\phi$ . We shall limit the discussion to only two simple analytical expressions for  $\phi$ , a Gaussian distortion and a cosinusoidal distortion. The Gaussian distortion is of the form

$$\phi = (2\pi\Delta) \exp(-2(r/w)^2) \quad (24)$$

$\Delta$  is simply defined as the peak value of the phase distortion in number of wavelengths. One motivation for assuming  $\phi$  of the form (equation (24)) is to provide a simple, though perhaps crude, model of the effects owing to beam heating of any mirror surfaces that may be used to reflect the beam prior to the aperture. Every mirror in the optical train before the aperture, absorbs a small fraction of the beam power. This small fraction is not insignificant, however, because the absorbed energy is converted to heat near the surface of the mirror and this heat forces dimensional changes in the mirror surface. The simplest possible model is to postulate that each mirror expands in a direction normal to its reflecting surface by an amount proportional to the local beam irradiance. Thus a normally plane mirror surface will become a convex Gaussian surface when subjected to a Gaussian local irradiance distribution.

By neglecting near field diffraction between mirrors, one then arrives at the Gaussian phase term as given in equation (24). Such a phase distortion can be visualized approximately as consisting of two significant components: a quadratic term in  $r$  plus a more complex function. By a straightforward expansion of the exponential we find that

$$\phi = (2\pi\Delta) \left[ 1 - 2(r/w)^2 + \text{higher order terms} \right] \quad (25)$$

The quadratic term merely contributes to an effective change in focus. The new focal distance is  $R$  where

$$1/R = 1/R - 4\Delta\lambda/w^2 \quad (26)$$

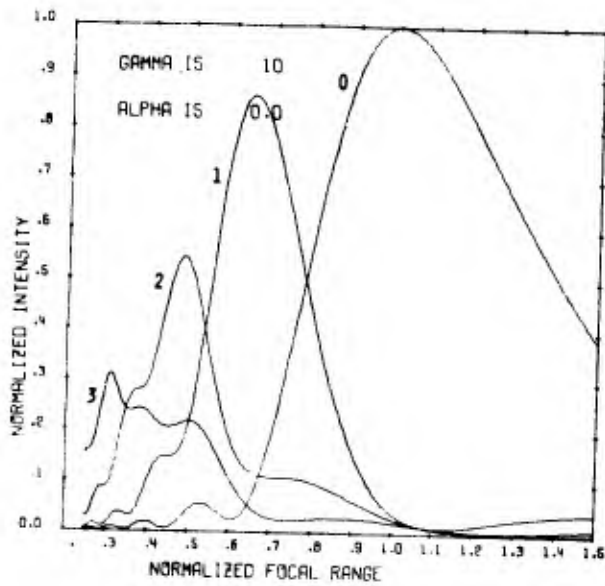
The higher order terms contribute to a degradation of the irradiance at the new focal point.

As an aid to understanding the implications of the Gaussian aberration (equation (24)), we have prepared the curves in Figure 6, which are based on the formulas

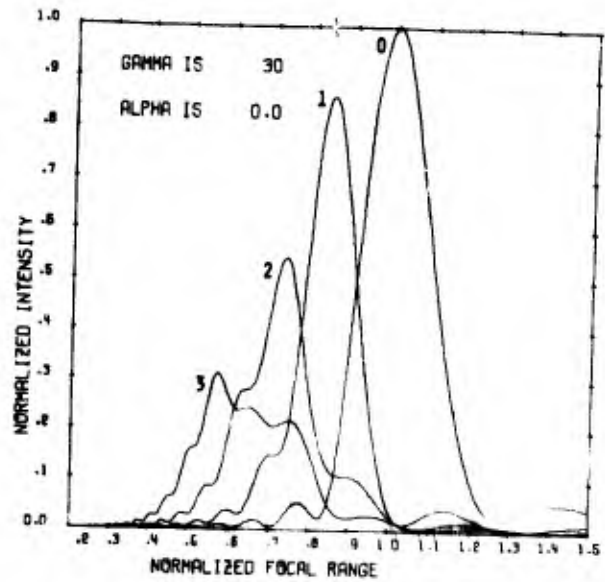
$$\bar{u}(R/z) = 2\beta^2 \int_{\alpha}^1 dx \, x \, g(x, R/z) \exp \left[ -(\beta x)^2 - 2\pi i \Delta \exp(-2\beta^2 x^2) \right] \quad (27)$$

$$g(x, R/z) = \frac{\exp \left[ i x^2 \gamma' (1-R/z) / (R/z) \right]}{\exp[-\alpha^2 \beta^2] - \exp[-\beta^2]} \quad (28a)$$

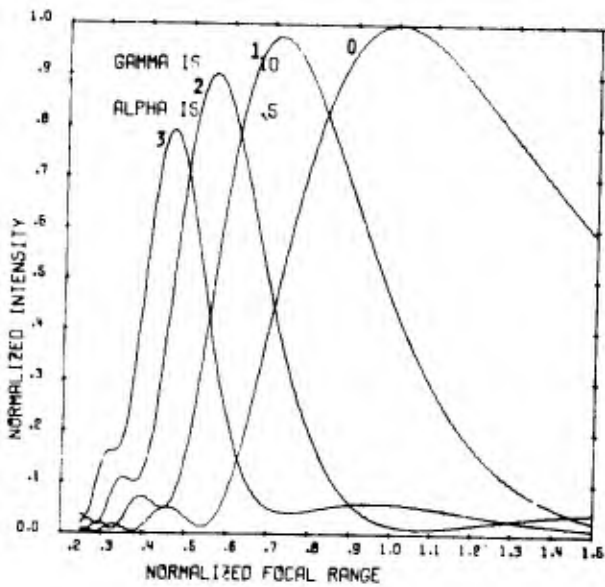
$$\gamma' = \pi b^2 / \lambda z \quad (28b)$$



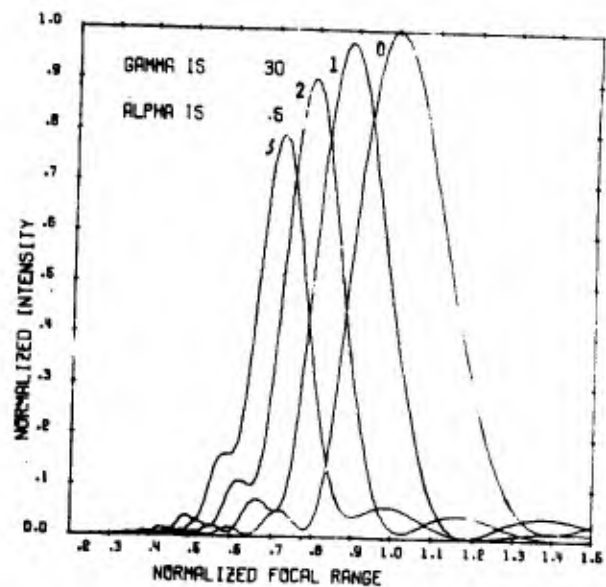
(A)



(B)



(C)



(D)

Figure 6.  $\bar{I}(R/z) = |\bar{u}(R/z)|^2$  versus  $R/z$ , calculated from equations (27) and (28) with  $\gamma'$  and  $\alpha$  as changing parameters. For all graphs we have  $\beta = 1$ . Each curve is labeled by the corresponding value of  $\Delta$ . The  $\Delta = 0$  curves peak at  $R/z = 1$  as was discussed in the text. For  $0 \leq \Delta \leq 1$ , it is seen that a change of the system will restore most of the peak irradiance at a fixed receiver site. The Gaussian phase distortion is thus seen to contain a significant change-of-focus component.

Equations (27) and (28) are obtained by returning to equation (4), setting  $r = 0$ , considering  $z$  as a constant, and reformulating the normalized wave amplitude as a function of the normalized focal range  $R/z$ . It is interesting to note in Figure 6 that for non-zero values of  $\alpha$ , the effect of phase distortion is minimized. The physical reason for this is that a substantial part of the phase distortion is blocked out by the central obscuration.

Now we consider the case when phase distortion is a sinusoidal function of  $r$  given by

$$\phi = 2\pi\delta \cos(2\pi r/T) \quad (29)$$

where  $T$  specifies the spatial period of the sinusoidal phase distortion.

One of the reasons for choosing to examine equation (29) is that, in an approximate way, equation (29) does have connection with physical reality. For example, consider a water cooled mirror with circular, equally spaced coolant channels behind the reflecting surface. When the surface of the mirror is loaded with a nearly uniform heat input, one would expect surface deformations that depend on radius in a nearly periodic manner while possessing aximuthal symmetry. Such a physical situation is roughly approximated by the phase distortion (equation (29)).

To put equation (29) in the dimensionless form required by equation (14), we set

$$\phi = 2\pi\delta \cos(2\pi\nu x) \quad (30)$$

where  $\nu = b/T$ . A numerical illustration, shown as Figure 7, depicts the influence of equation (30). It should be noted that the location of the peak in the on-axis irradiance moves closer to the aperture as the values of  $\delta$  run from  $+1/4$  to  $-1/4$ . This shows that, for  $\nu = 1$ , the sinusoidal phase aberration contains a large change-of-focus component. For  $\nu = 5$ , we found that the plots of irradiance for  $\delta = +1/4$  appeared very much the same as for  $\delta = -1/4$ , indicating that, for  $\nu = 5$ , the change of focus component in the phase aberration is negligible.

When  $\nu$  is an integer and  $\alpha = \beta = 0$ , it is possible to derive a relatively simple expression for the focal point irradiance. By using the identity

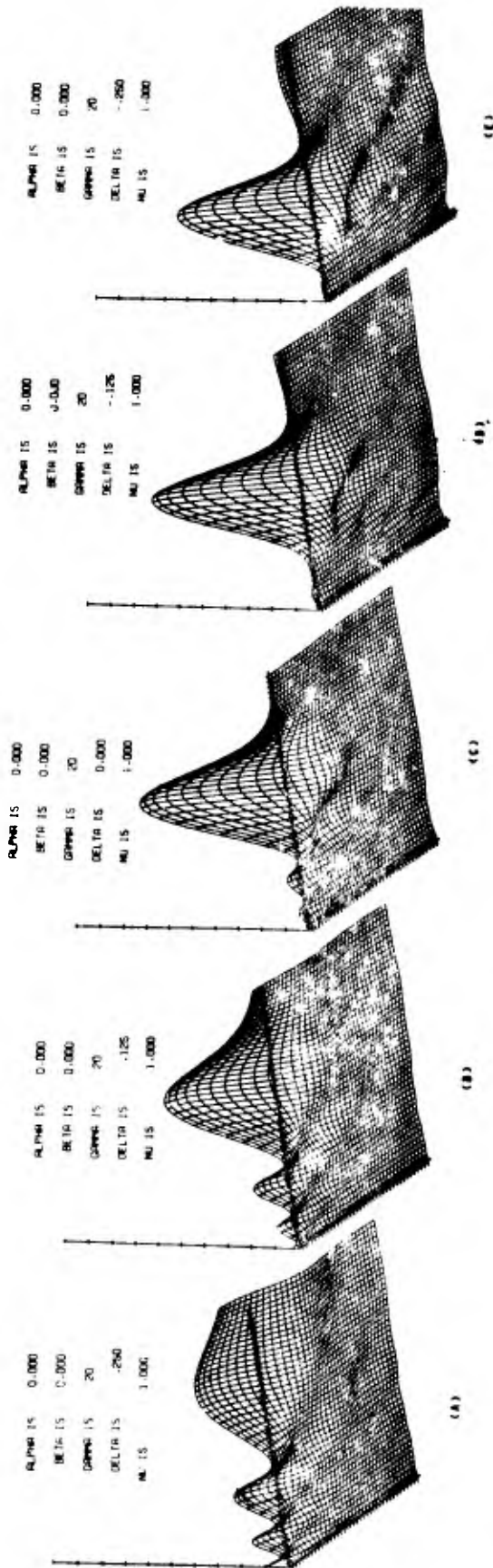


Figure 7. The  $\bar{I}(\xi, \zeta)$  surface for a sinusoidal phase distortion in the aperture field. The parameter that changes is  $\delta$ , for all graphs  $\alpha = \beta = 0$ ,  $\gamma = 20$  and  $\nu = 1$ . The right hand coordinate system axes are identified as in Figure 3 except that we now have  $0 < \xi < 3.0$ . Note that the  $\bar{I}(\xi, \zeta)$  surface contours depend strongly upon the sign of  $\delta$ . This is because of the low value of the frequency  $\nu$ ; for small values of  $\nu$ , the sinusoidal phase distortion contains a significant change of focus component. For  $\nu = 5$  the change of focus component is almost negligible and the  $\bar{I}(\xi, \zeta)$  surface contours (not shown here) are virtually independent of the sign of the parameter  $\delta$ .

$$\exp[iz\cos\theta] = \sum_{k=-\infty}^{+\infty} i^k J_k(z) \exp[ik\theta] \quad (31)$$

equation (14) reduces to

$$\bar{u}(0,1) = J_0(2\pi\delta) \quad (32)$$

It is noticed that equation (32) is independent of the (integer) value of  $\nu = b/T$ . In Figure 8, we have plotted  $\bar{I}(0,1)$  as a function of  $\delta$  for various values of  $\alpha$  and  $\beta$  and for  $\nu = 1$ . The point here is that the focal point intensity does not appear to be significantly affected by changes in  $\alpha$  or  $\beta$ . The transverse irradiance distributions are strong functions of  $\nu$  even though the focal point irradiance is relatively insensitive to the precise (integer) value of  $\nu$ .

#### REFERENCES

1. Buck, A. L., "The Radiation Patterns of a Truncated Gaussian Aperture Distribution," Proc. IEEE, 55, p. 448, 1967.
2. Campbell, J. P., and DeShazer, L. G., "Near Fields of Truncated-Gaussian Apertures," J. Opt. Soc. Am., 59, p. 1427, 1969.
3. Olaofe, G. O., "Diffraction by Gaussian Apertures," J. Opt. Soc. Am., 60, p. 1654, 1970.
4. Schell, R. G., and Tyras, G., "Irradiance from an Aperture with a Truncated-Gaussian Field Distribution," J. Opt. Soc. Am., 61, p. 31, 1971.
5. Goodman, J. W., Introduction to Fourier Optics, McGraw-Hill, New York, Chapter 4, 1968.
6. Kogelnik, H., and Li, T., "Laser Beams and REsonators," Appl. Opt., 5, p. 1550, 1966.
7. Born, M., and Wolf, E., Principles of Optics, First Edition, p. 439, Pergamon Press, New York, 1959.
8. Stone, J. M., Radiation and Optics, p. 205-206, McGraw-Hill, New York, 1963.
9. Stone, J. M., Radiation and Optics, p. 184 (problem 9-3), McGraw-Hill, New York, 1963.

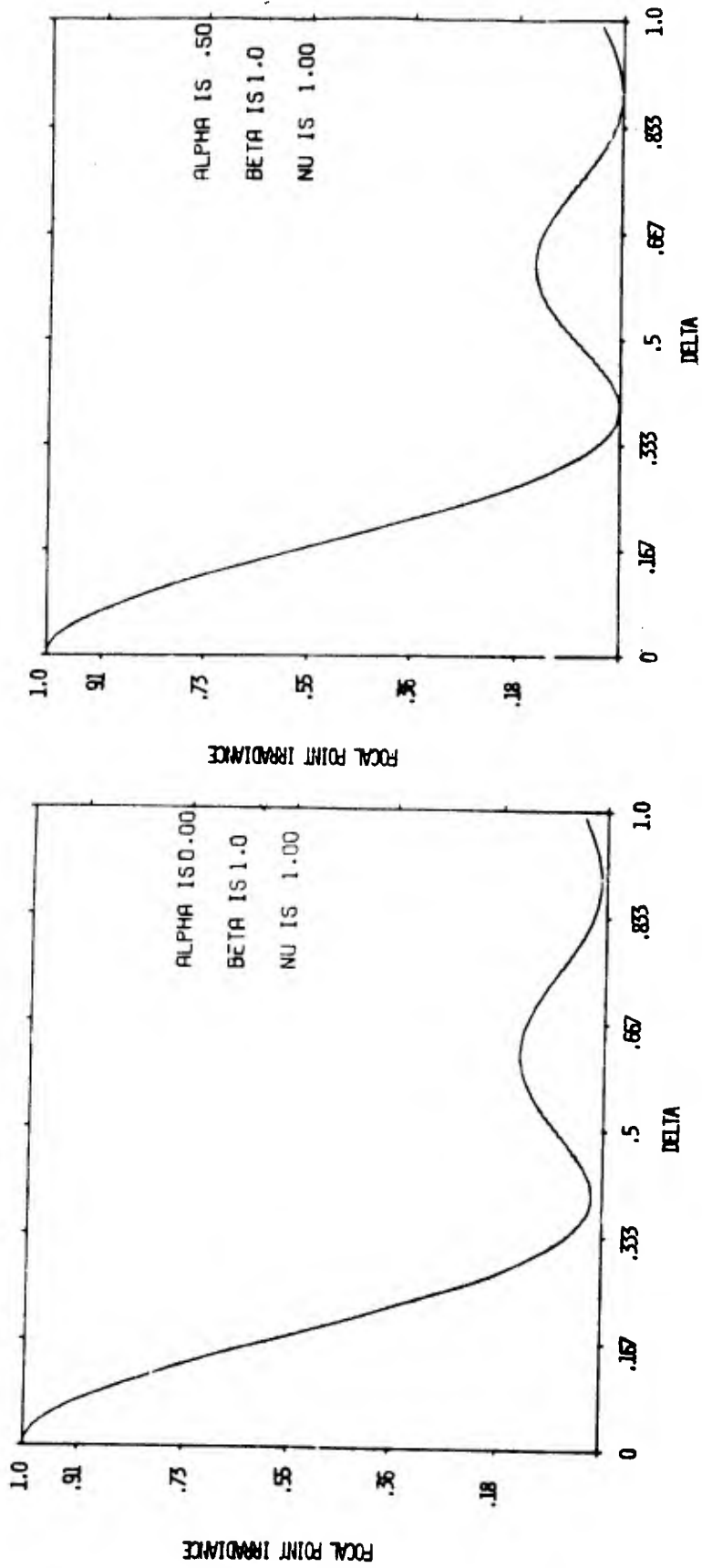


Figure 8. Focal point irradiance  $\bar{I}(0,1)$  as a function of the sinusoidal phase amplitude  $\delta$ . Neither of the curves departs greatly from the  $\alpha = \beta = 0$  curve, which goes as  $J_0^2(2\pi\delta)$ .

## POWER PROFILES FOR APERTURED FOCUSED GAUSSIAN BEAMS

D. A. Holmes, J. E. Korka, and P. V. Avizonis

This note is an extension of "Parametric Study of Apertured Focused Gaussian Beams" which was published by us in the Laser Division Digest of December 1970. In the previous note, we showed that the normalized irradiance distribution in the vicinity of the focus is given by

$$\bar{I}(\xi, \zeta) = |u(\xi, \zeta)|^2$$

where

$$\bar{u}(\xi, \zeta) = \frac{\int_{\alpha}^1 J_0(\pi \xi x / \zeta) \exp\left[-(\beta x)^2 - i x^2 \gamma (\zeta - 1) / \zeta\right] x dx}{(\zeta / 2\beta^2) \left[\exp(-\alpha^2 \beta^2) - \exp(-\beta^2)\right]} \quad (1)$$

and

$$\alpha = a/b$$

$$\beta = b/w$$

$$\gamma = \pi b^2 / \lambda R$$

$$\zeta = z/R$$

$$\xi = 2rb/\lambda R$$

As before, the symbols are defined as follows:

- a Inside radius of annular aperture
- b Outside radius of annular aperture
- r, z Cylindrical coordinates
- w Spot size of Gaussian aperture field
- $\lambda$  Vacuum wavelength
- R Radius of curvature of aperture field phase front
- $P_0$  Power transmitted through aperture



In any plane  $z = \text{constant}$ , the beam power passing through a circle of radius  $r$ , centered on the  $z$  axis, is denoted by  $P(r,z)$ . We shall now transform this power to be a function of the dimensionless coordinates  $\xi$  and  $\zeta$  and define the dimensionless power  $p(\xi,\zeta)$  as follows

$$p(\xi,\zeta) = P(\xi,\zeta)/P_0 \quad (2)$$

We see that  $0 \leq p(\xi,\zeta) \leq 1$ . By integrating  $\bar{I}(\xi,\zeta)$ , we can obtain

$$p(\xi,\zeta) = (\pi/\beta)^2 \frac{\exp[-\alpha^2\beta^2] - \exp[-\beta^2]}{\exp[-\alpha^2\beta^2] + \exp[-\beta^2]} \int_0^\xi n \bar{I}(n,\zeta) dn \quad (3)$$

We have prepared some three-dimensional plots of  $p(\xi,\zeta)$  which are companions to the plots of  $\bar{I}(\xi,\zeta)$  published in the previous note; these plots are shown as Figures 1 through 12. The axes in each figure cover the ranges

$$0 \leq \xi \leq 2.5$$

$$0.5 \leq \zeta \leq 1.5$$

$$0 \leq p(\xi,\zeta) \leq 1 \quad (4)$$

In each figure, the normalized power,  $p(\xi,\zeta)$  is plotted on the vertical axis. The  $\xi$  axis appears to extend into the paper in each figure. The  $(\xi, \zeta, p(\xi,\zeta))$  coordinate axes thus form a left handed system.

Equation (3) is rather complicated, but we have found that, for  $\zeta = 1$ , the normalized power  $p(\xi,1)$  can be represented by a rather simple formula over a limited range in  $\xi$ . By a rather unsophisticated graphical analysis we have found that

$$p(\xi,1) \approx 1.25(\xi - 0.14) \quad (5)$$

Equation (5) is valid for the following conditions:

$$0.3 \leq \xi \leq 0.6 \quad (6a)$$

$$0 \leq \beta \leq 1 \quad (6b)$$

$$\alpha = 0 \quad (6c)$$

For  $\beta = 1$ , the interval on  $\xi$  may be extended to  $0.3 \leq \xi \leq 0.7$ . The accuracy of equation (5) is no worse than about 5 percent under the conditions of equation (6).

To emphasize the simplicity of equation (5) we can rewrite the expression in terms of the un-normalized focal plane power  $P(r,R)$  as follows

$$P(r,R) = 1.25 \{ [Dr/\lambda R] - 0.14 \} P_0 \quad (7)$$

where  $D$  is the outside diameter ( $D = 2b$ ) of the final transmitting aperture and  $R$  is the distance from the aperture to the focal plane.

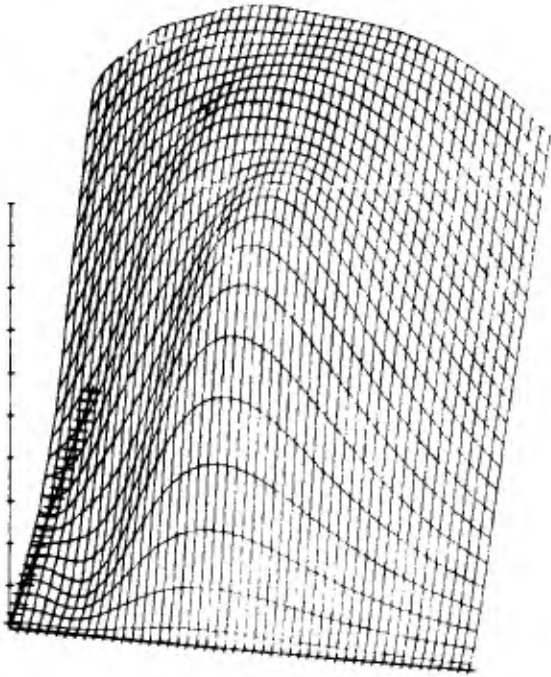


Figure 1. The  $p(\xi, \zeta)$  Surface for  $\alpha = 0, \beta = 0, \gamma = 10$

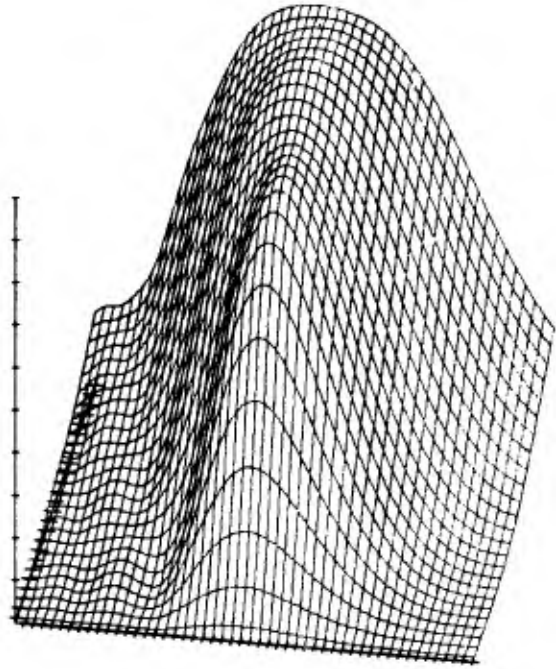


Figure 2. The  $p(\xi, \zeta)$  Surface for  $\alpha = 0, \beta = 0, \gamma = 20$

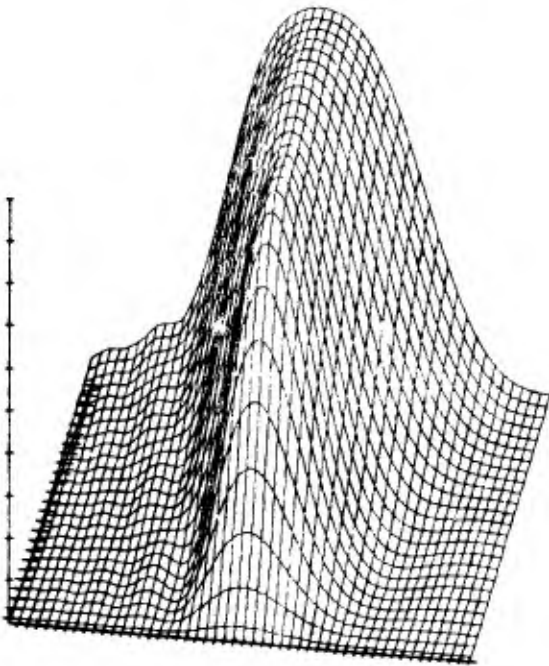


Figure 3. The  $p(\xi, \zeta)$  Surface for  $\alpha = 0, \beta = 0, \gamma = 30$

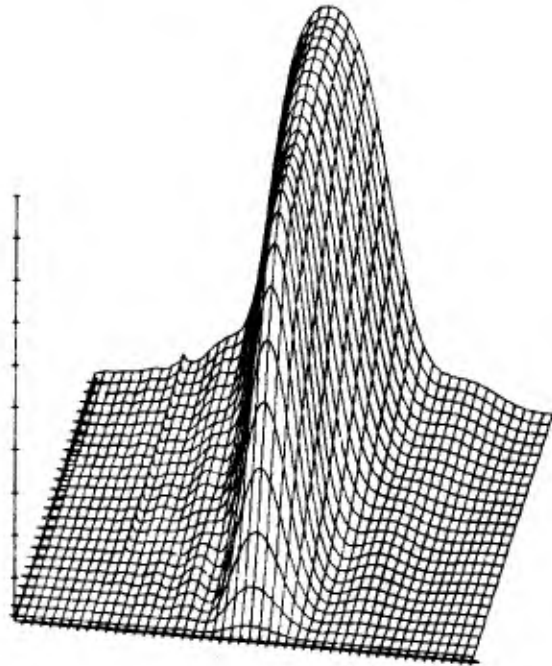


Figure 4. The  $p(\xi, \zeta)$  Surface for  $\alpha = 0, \beta = 0, \gamma = 50$

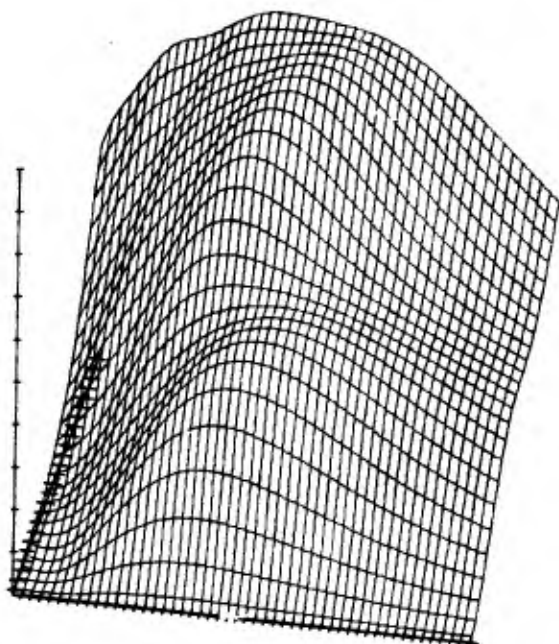


Figure 5. The  $p(\xi, \zeta)$  Surface for  $\alpha = 0.5, \beta = 0, \gamma = 10$

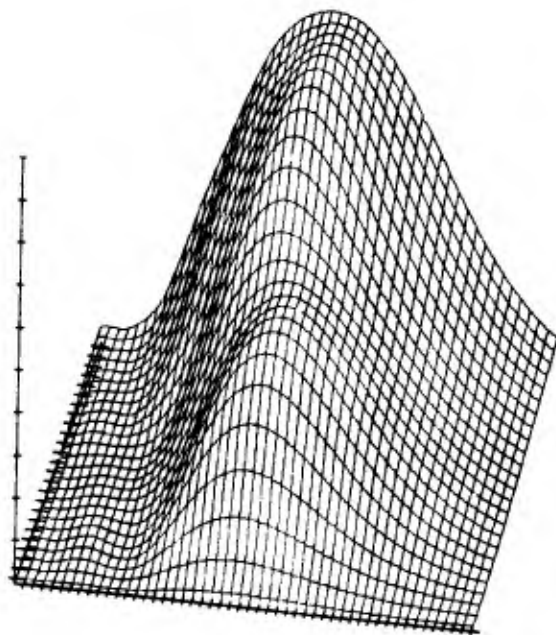


Figure 6. The  $p(\xi, \zeta)$  Surface for  $\alpha = 0.5, \beta = 0, \gamma = 20$

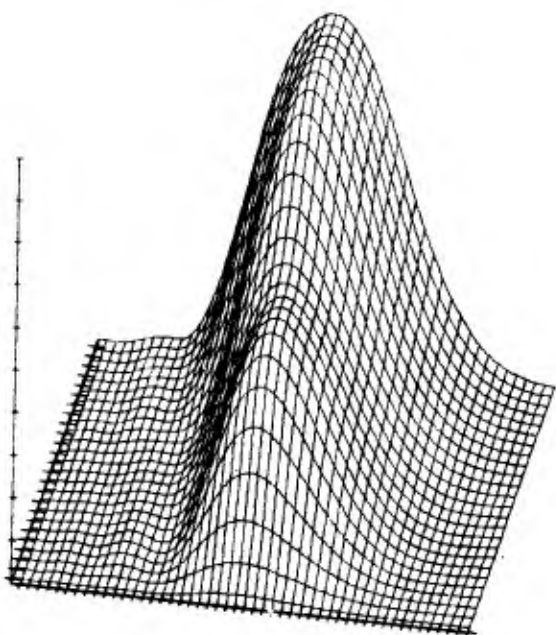


Figure 7. The  $p(\xi, \zeta)$  Surface for  $\alpha = 0.5, \beta = 0, \gamma = 30$

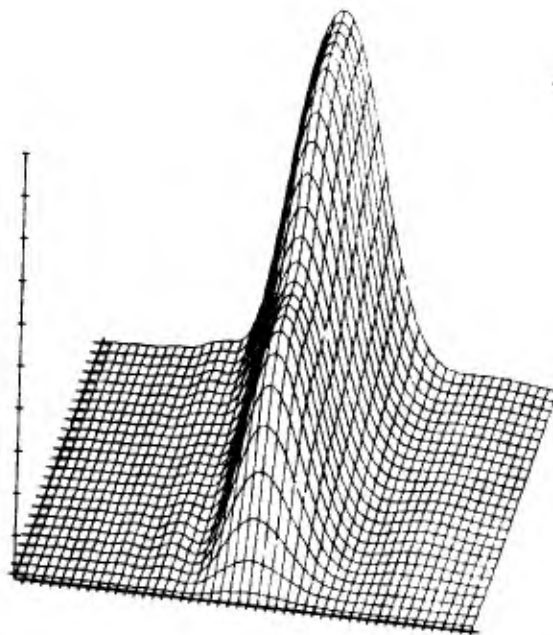


Figure 8. The  $p(\xi, \zeta)$  Surface for  $\alpha = 0.5, \beta = 0, \gamma = 50$

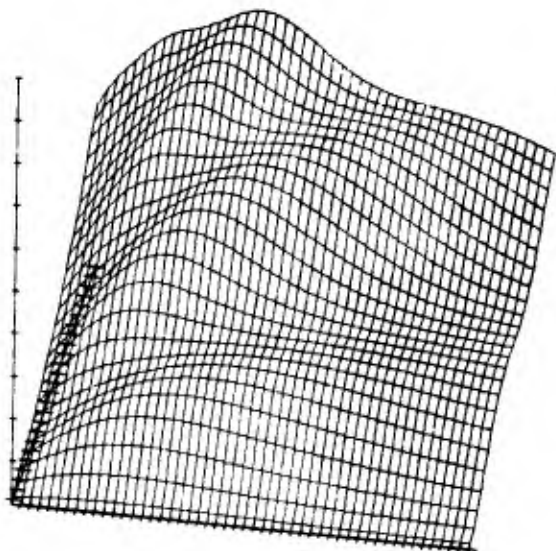


Figure 9. The  $p(\xi, \zeta)$  Surface for  $\alpha = 0.75, \beta = 1, \gamma = 10$

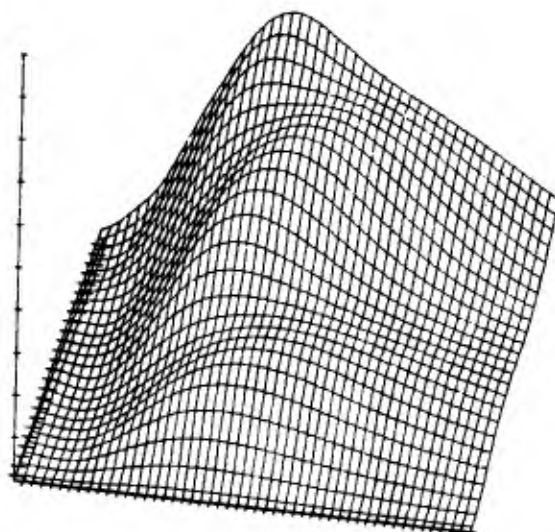


Figure 10. The  $p(\xi, \zeta)$  Surface for  $\alpha = 0.75, \beta = 1, \gamma = 20$

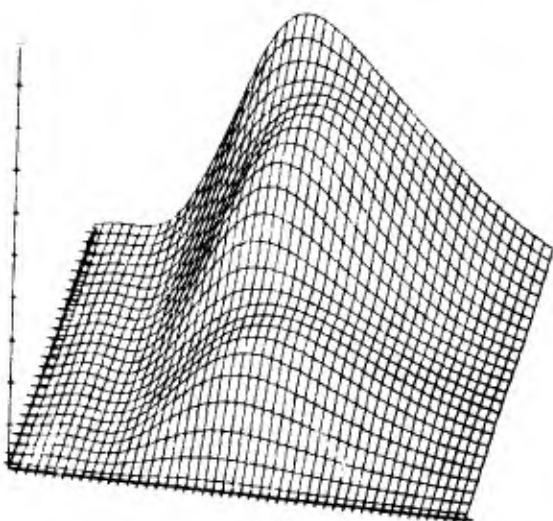


Figure 11. The  $p(\xi, \zeta)$  Surface for  $\alpha = 0.75, \beta = 1, \gamma = 30$

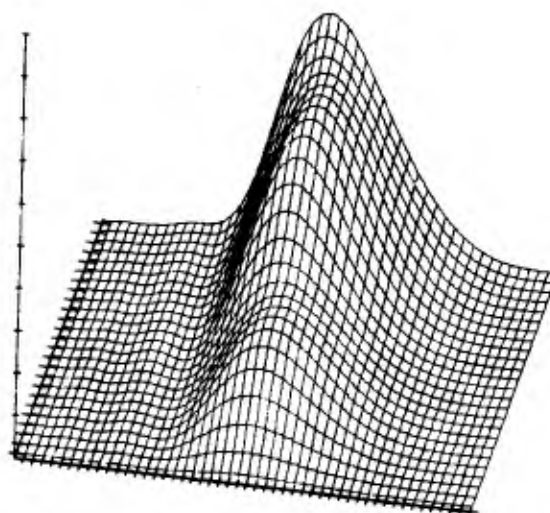


Figure 12. The  $p(\xi, \zeta)$  Surface for  $\alpha = 0.75, \beta = 1, \gamma = 50$

# COMPARISON OF FAR-FIELD IRRADIANCES FOR AXICON AND CASSEGRAIN TRANSMITTERS

D. A. Holmes, M. L. Bernabe, and R. R. Selleck

In this note, we compare the far-field irradiances projected by two different beam expanding transmitting systems. The first system is the axicon, shown in Figure 1, consisting of two conical mirrors. The second system, shown in Figure 2, is the on-axis Cassegrain telescope, consisting of two spherical mirrors.

The input beam for both systems shall consist of a truncated Gaussian whose wave amplitude is given by

$$v_i(r) = V \exp(-r^2/w^2) \text{ for } 0 \leq r \leq a \quad (1a)$$

$$v_i(r) = 0 \quad \text{for } a < r \quad (1b)$$

In equation (1),  $V$  is a constant,  $w$  is the familiar Kogelnik and Li spot size,  $r$  is the radial coordinate and  $a$  is the radius of the truncating aperture.

If the input beam, as described by equation (1), is projected to the far field without the benefit of beam expanding optics, then the diffracted wave field, evaluated on the optical axis, is given by

$$u_i = \frac{2\pi V \exp(2\pi iz/\lambda)}{i\lambda z} \int_0^a \exp(-(\rho/w)^2) \rho \, d\rho \quad (2)$$

In equation (2),  $\lambda$  is the wavelength and  $z$  is distance measured from the final aperture of radius  $a$ . The far-field on-axis irradiance is given by  $I_i = |u_i|^2$ , as follows

$$I_i = [\pi w^2 V / \lambda z]^2 [1 - \exp(-a^2/w^2)]^2 \quad (3)$$

In equation (3),  $V$  is assumed to be a real constant, without loss of generality.

We now consider the case of the axicon. The wave field in the final aperture plane (see Figure 1) is given by

$$v_a(r) = \left[ (r-b+a)/r \right]^{1/2} V \exp\left[ -(r-b+a)^2/w^2 \right] \quad (4a)$$

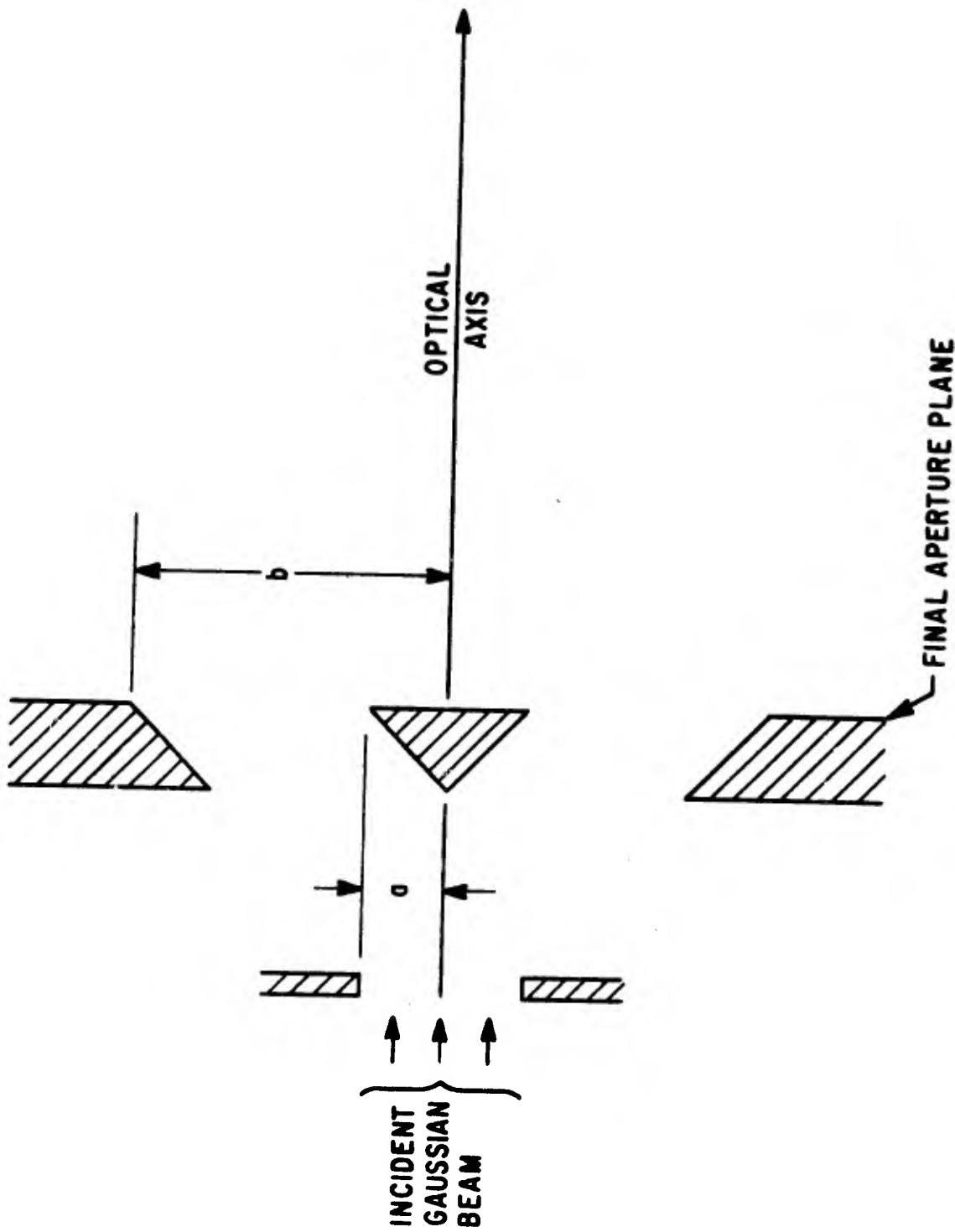


Figure 1. Axicon beam-expanding projection system. The incident Gaussian beam is clipped at the radius  $a$ . The transmitted beam, evaluated in the final aperture plane, is annular in shape with inside radius  $b-a$  and outside radius  $b$ .

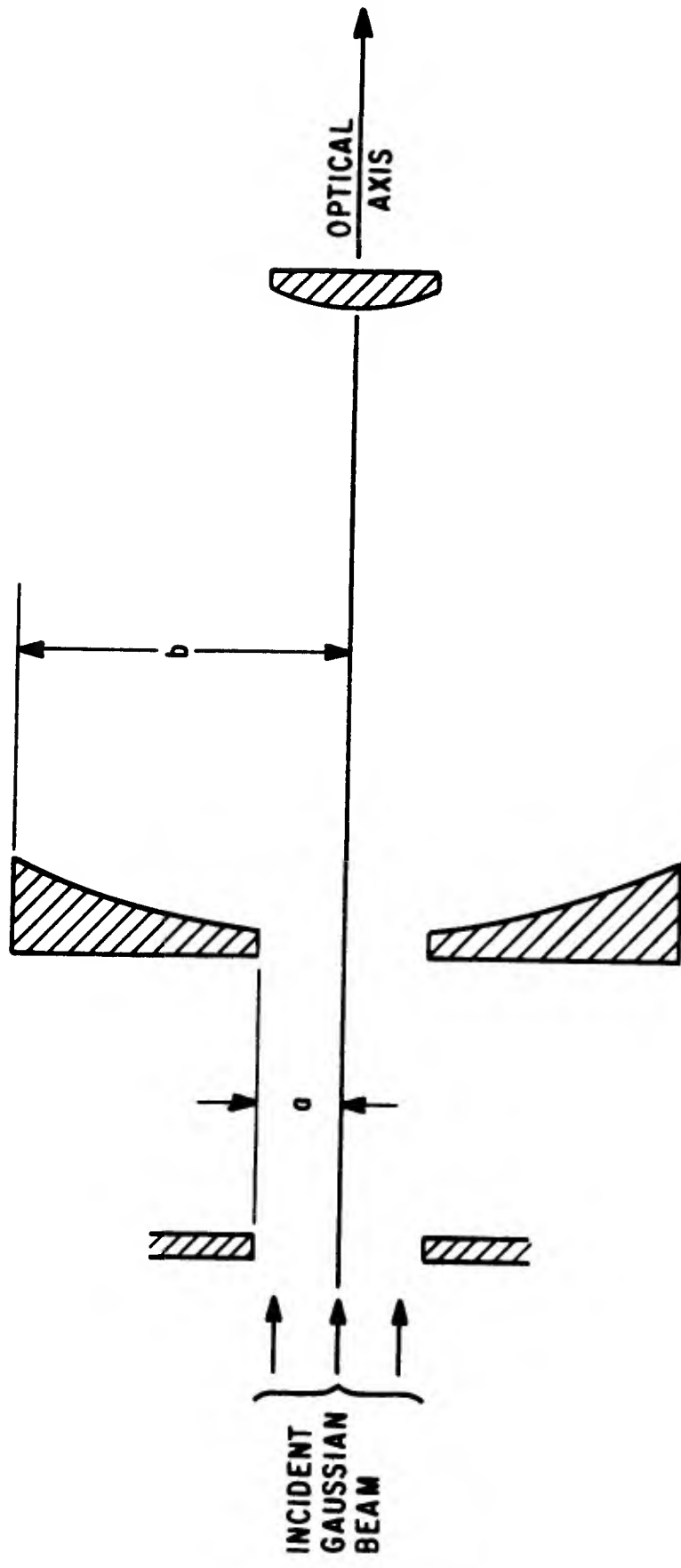


Figure 2. Cassegrain beam-expanding projection system. The incident Gaussian beam is truncated at the radius  $a$ . The smaller, convex mirror is of radius  $a$ .



for  $b-a \leq r \leq b$ , and

$$v_a(r) = 0 \text{ for } b-a > r \text{ and } b < r \quad (4b)$$

Near-field diffraction effects between mirrors are neglected in calculating equation (4).

The far-field wave amplitude, evaluated on the z-axis, is given by

$$u_a = \left( 2\pi \exp(2\pi iz/\lambda) / i\lambda z \right) \int_{b-a}^b d\rho \rho v_a(\rho) \quad (5)$$

The far-field on-axis irradiance is  $I_a = |u_a|^2$ . We shall now define a normalized far-field irradiance as  $\bar{I}_a = I_a / I_1$  where  $I_1$  is given by equation (3). Thus it is seen that  $\bar{I}_a$  measures the increase in far-field irradiance obtained by passing the truncated Gaussian wave through a beam-expanding axicon optical system.

It is convenient to define the following dimensionless parameters:

$$m = b/a \quad (6a)$$

$$\beta = a/w \quad (6b)$$

The quantity  $m$  may be called the expansion ratio or magnification, while  $\beta$  simply is the ratio of the input beam truncation to the input beam spot size.

Using equations (6) and (3), we obtain

$$\bar{I}_a = \frac{4\beta^4 \left\{ \int_0^1 dy [y(y+m-1)]^{1/2} \exp(-\beta^2 y^2) \right\}^2}{\{1 - \exp(-\beta^2)\}^2} \quad (7)$$

In equation (7), we note that the dependence on  $z$ ,  $\lambda$  and  $V$  has conveniently dropped out. In numerical computations, we shall permit  $m$  to become as small as unity for mathematical convenience.

In the case of the Cassegrain telescope, the wave amplitude over the final concave mirror (primary mirror), neglecting near field diffraction effects, is a scaled version of equation (1). The primary mirror field is thus given by

$$v_c(r) = (aV/b)\exp(-a^2r^2/b^2w^2) \quad \text{for } a \leq r \leq b \quad (8a)$$

$$v_c(r) = 0 \quad \text{for } a > r \quad \text{and} \quad b < r \quad (8b)$$

Note that we consider that the telescope is in afocal adjustment

The far-field wave amplitude, evaluated on the optical axis, is  $u_c$ , given by

$$u_c = \left(2\pi\exp(2\pi iz/\lambda)/i\lambda z\right) \int_a^b d\rho \rho v_c(\rho) \quad (9)$$

where  $z$  measures distance from the plane of the primary mirror. The far-field on-axis irradiance is given by

$$I_c = (\pi bw^2V/a\lambda z)^2 \left[ \exp\left(-a^2/bw^2\right) - \exp\left(-a^2/w^2\right) \right]^2 \quad (10)$$

We now define the normalized irradiance  $\bar{I}_c = I_c/I_i$ . The quantity  $\bar{I}_c$  thus measures the change in far-field irradiance obtained by passing the truncated Gaussian wave through the beam expanding Cassegrain telescope. Using the dimensionless coordinates (equations (6a) and (6b))

$$m = b/a$$

$$\beta = a/w$$

we obtain

$$\bar{I}_c = \frac{m^2 \left[ \exp(-\beta^2/m^2) - \exp(-\beta^2) \right]^2}{\left[ 1 - \exp(-\beta^2) \right]^2} \quad (11)$$

In Figures 3 to 7, we show some numerical calculations of  $\bar{I}_a$  and  $\bar{I}_c$  from equations (7) and (11), respectively. In the curves of  $\bar{I}_c$  versus  $m$ , notice that, when  $m$  is small,  $\bar{I}_c$  is less than unity; this is because the central obscuration (secondary mirror) prevents all the power in the input beam from being transmitted to the far-field.

The figures clearly demonstrate the limiting behavior of equation (7) for large values of  $m$ . For "large" values of  $m$  we have, from equation (7),

$$\bar{I}_a \approx \frac{4\beta^4 m \left\{ \int_0^1 dy (y)^{1/2} \exp(-\beta^2 y^2) \right\}^2}{1 - \exp(-\beta^2)^2} \quad (12)$$

which shows that  $\bar{I}_a$  is linearly dependent on  $m$  when  $m$  becomes significantly larger than one. The graphs actually show  $\bar{I}_a$  to vary nearly linearly with  $m$  for  $m \geq 1$ .

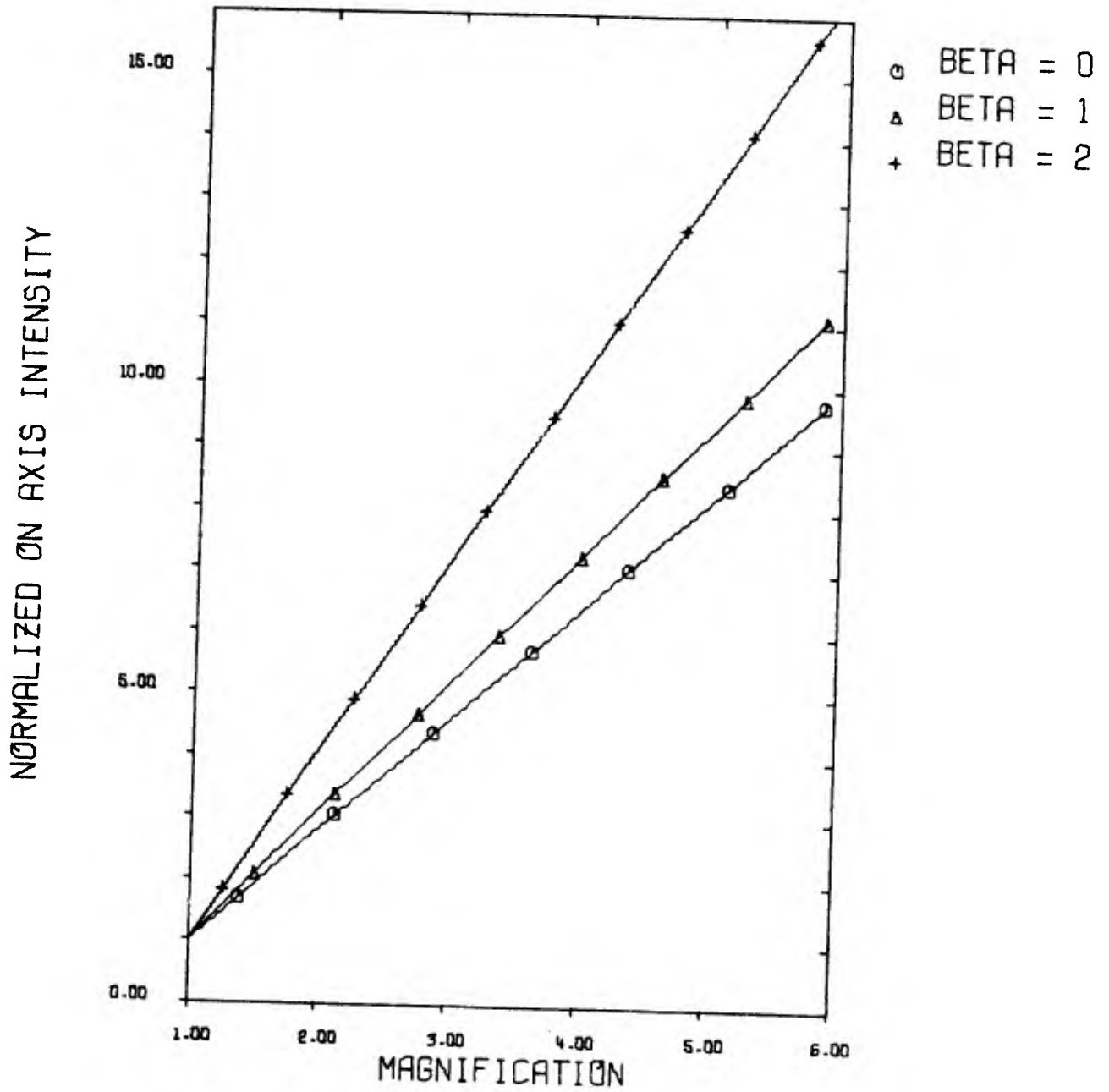


Figure 3. Irradiance calculations for the axicon system.  $I_a$  versus  $m$  for various values of  $\beta$ .

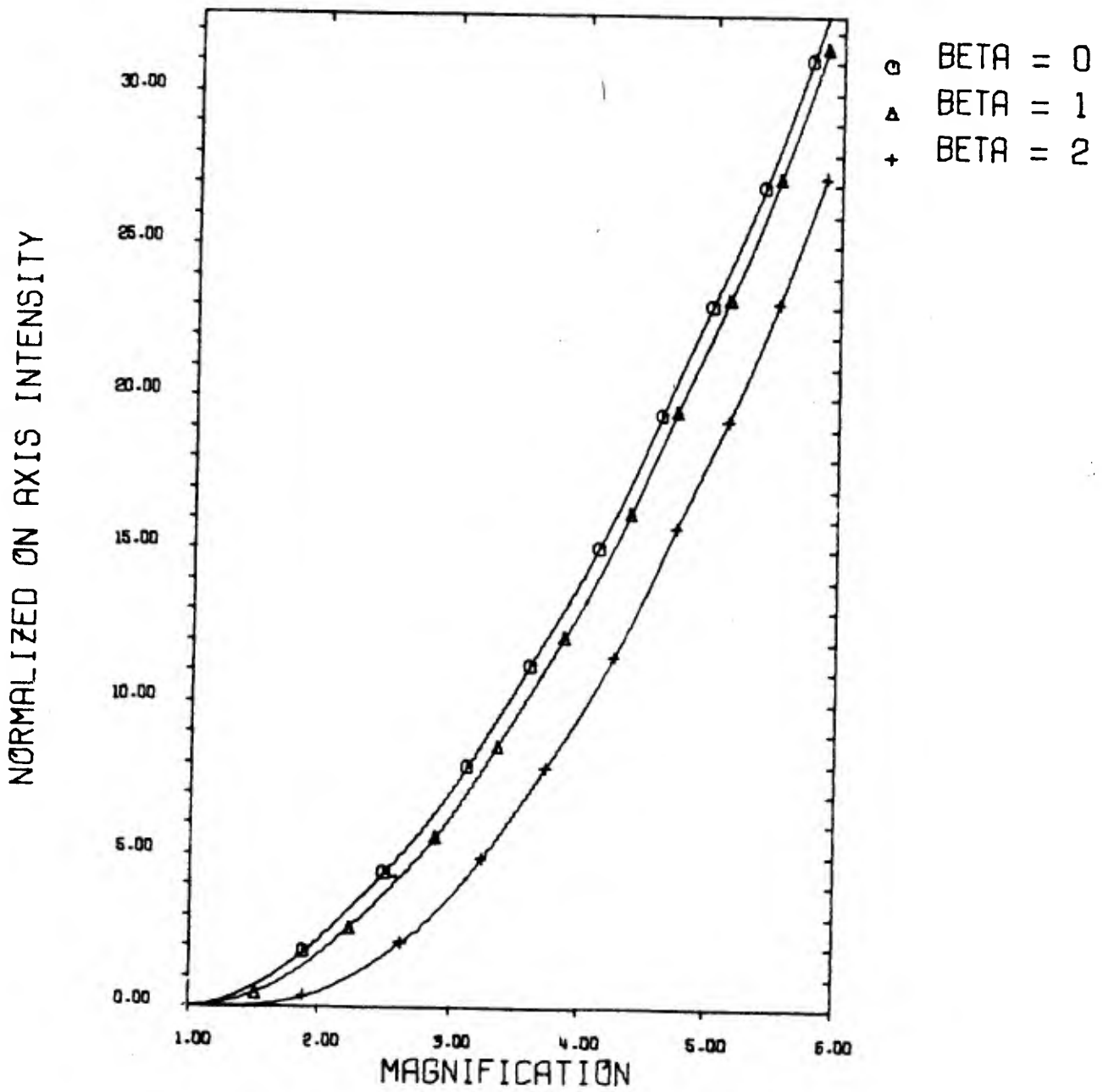


Figure 4. Irradiance calculations for the Cassegrain system.  $I_c$  versus  $m$  for various values of  $\beta$ .

BETA = 0

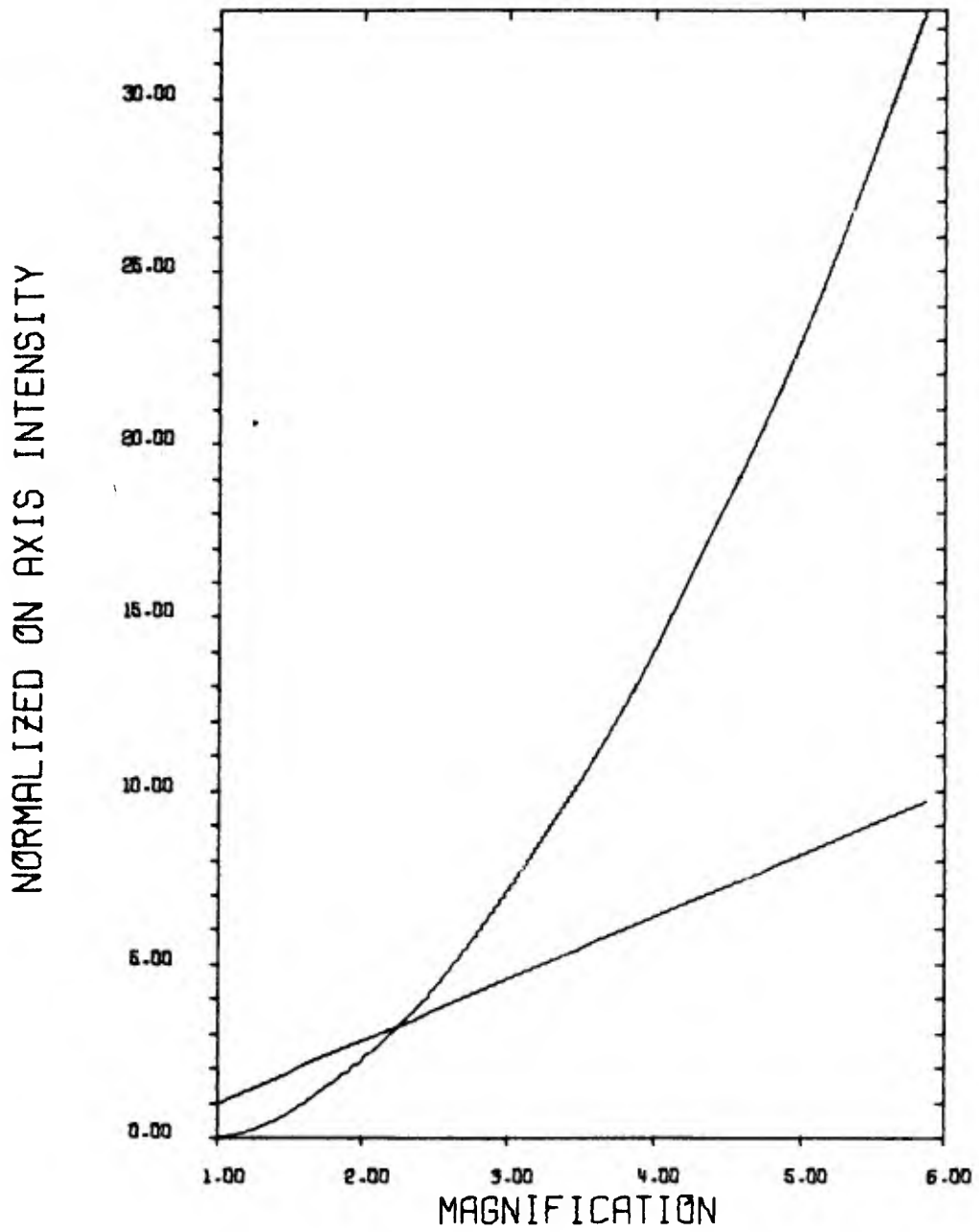


Figure 5. Comparison of  $\bar{I}_a$  and  $\bar{I}_c$  for  $\beta = 0$ .  
The nearly straight line is  $\bar{I}_a$  versus  $m$ .

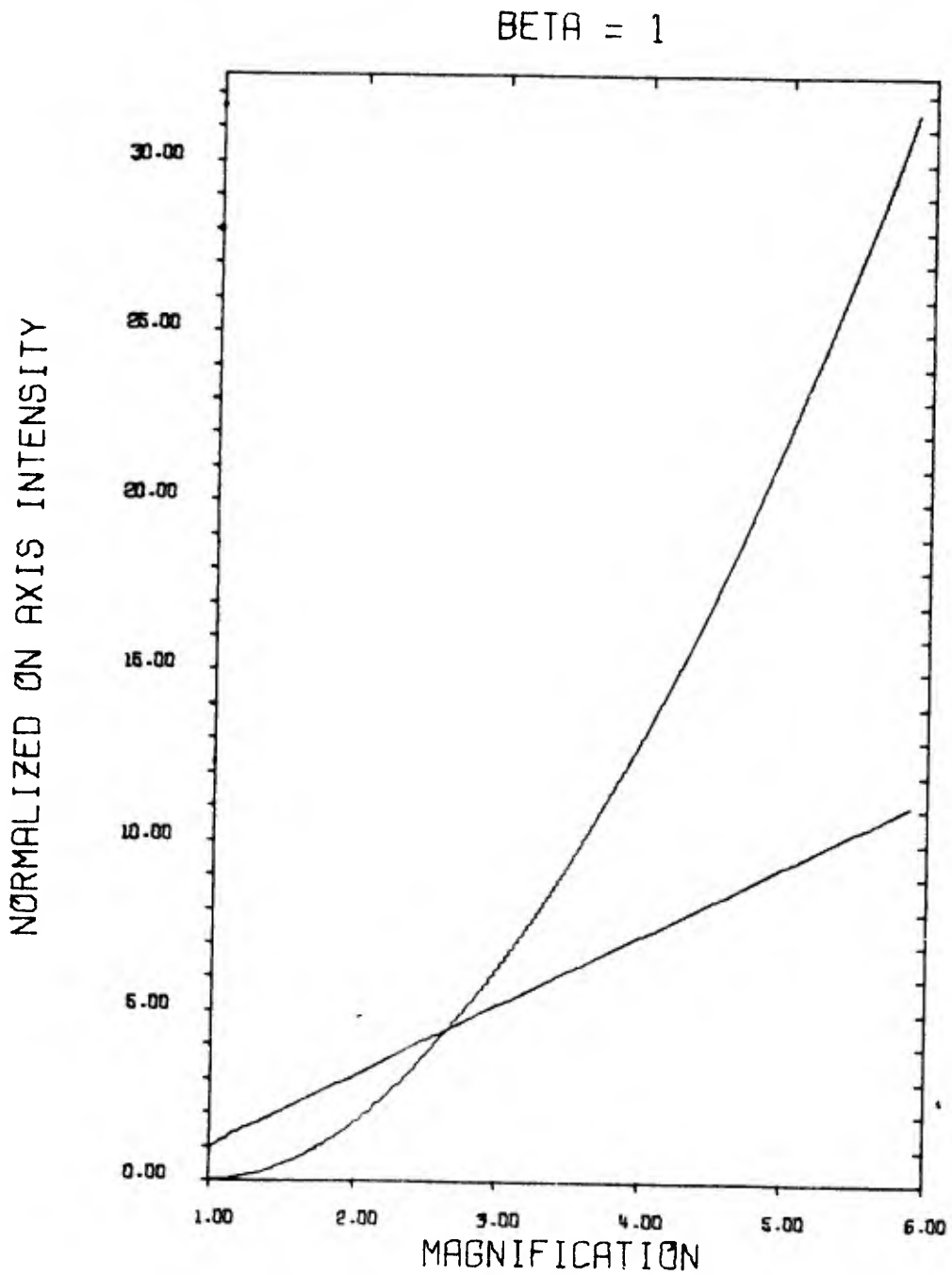


Figure 6. Comparison of  $\bar{I}_a$  and  $\bar{I}_c$  for  $\beta = 1$ .  
The nearly straight line is  $\bar{I}_a$  versus m.

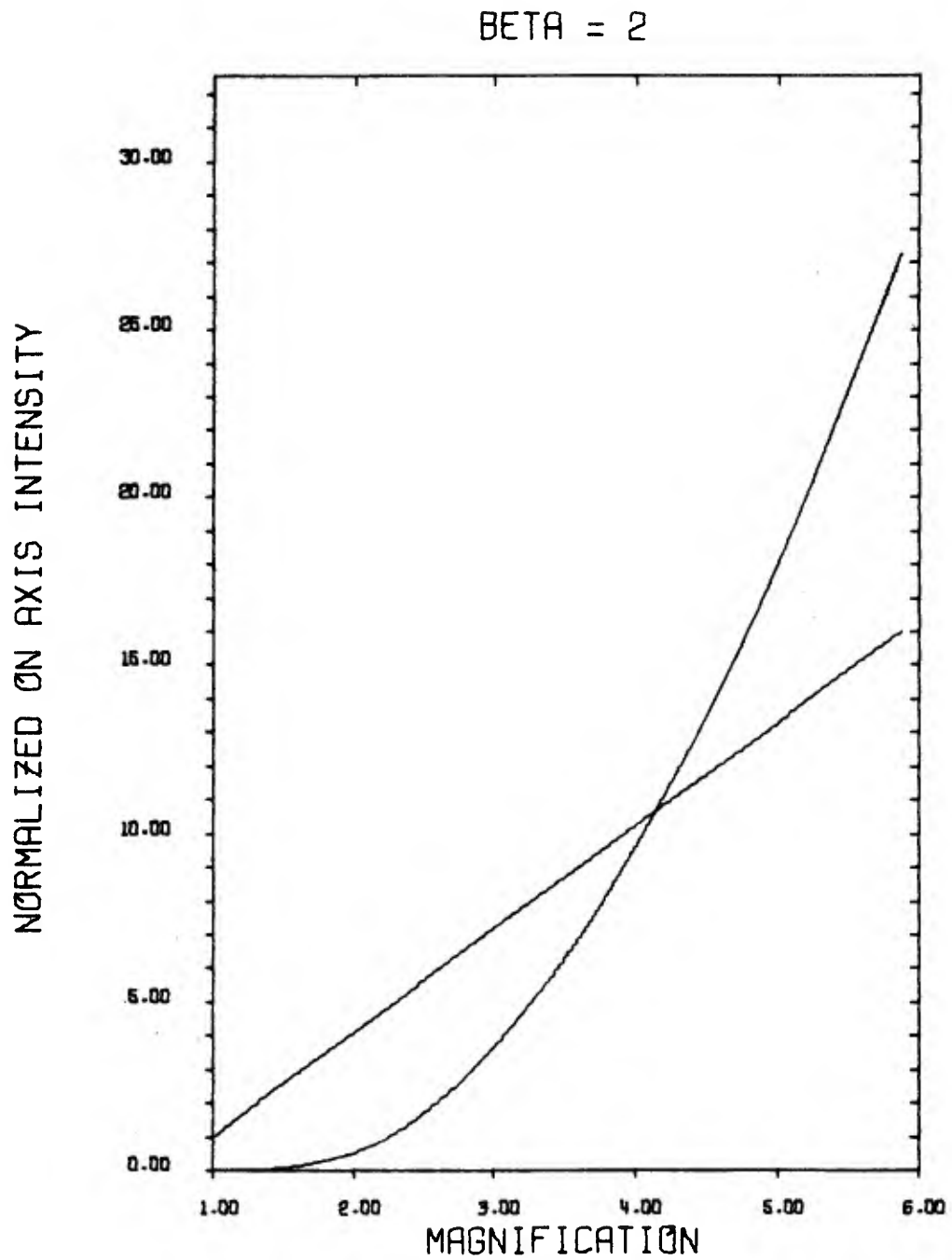


Figure 7. Comparison of  $\bar{I}_a$  and  $\bar{I}_c$  for  $\beta = 2$ .  
The nearly straight line is  $\bar{I}_a$  versus m.



ON-AXIS FOCAL PLANE INTENSITY VARIATIONS  
DUE TO TELESCOPE MIRROR MOTION

C. DeHainaut, J. E. Korka, and L. Sher

Summary

Calculations have been performed to evaluate the average loss in intensity at the focal plane when the telescope mirrors translate longitudinally in an oscillatory fashion from their nominal separation. The results indicate that in order to keep the loss in intensity less than 10 percent, the relative vibratory motion must be less than  $65 \mu$ , vector, or  $46 \mu$ , RMS.

Analysis

Assuming a uniform plane wave incident on the secondary and no aberrations in the system we obtain a beam with radius of convergence  $R$  from the telescope. This radius of convergence is a function of the radii of the secondary ( $r_1$ ) and the primary ( $r_2$ ) and of their separation ( $d$ ), and is given by

$$R = \frac{r_2(r_1 + 2d)}{2(2d + r_1 - r_2)} \quad (1)$$

The intensity on-axis normalized in the focal plane is given as a function of  $R$  and  $Z$  as

$$I = \text{sinc}^2 \left( \pi(b^2 - a^2)(Z - R) / (2\lambda Z R) \right) I_0 \quad (2)$$

where  $b$  is the outer radius of the primary,  $a$  is the radius of the obstruction,  $\lambda$  is the wavelength of the radiation, and  $z$  is the distance along the optical axis. For a given set of telescope parameters,  $a$ ,  $b$ ,  $r_1$ ,  $r_2$ , the distance to the focal plane  $z_0$  is determined by a given  $d_0$ . The variation in the normalized intensity, i.e.,  $I/I_0$  from a nominal  $d_0$ , is shown in Figure 1, where the variation is calculated in millimeters.

For oscillatory motions of the separation  $d$  of the type:

$$d = d_0 + A \sin \omega t \quad (3)$$

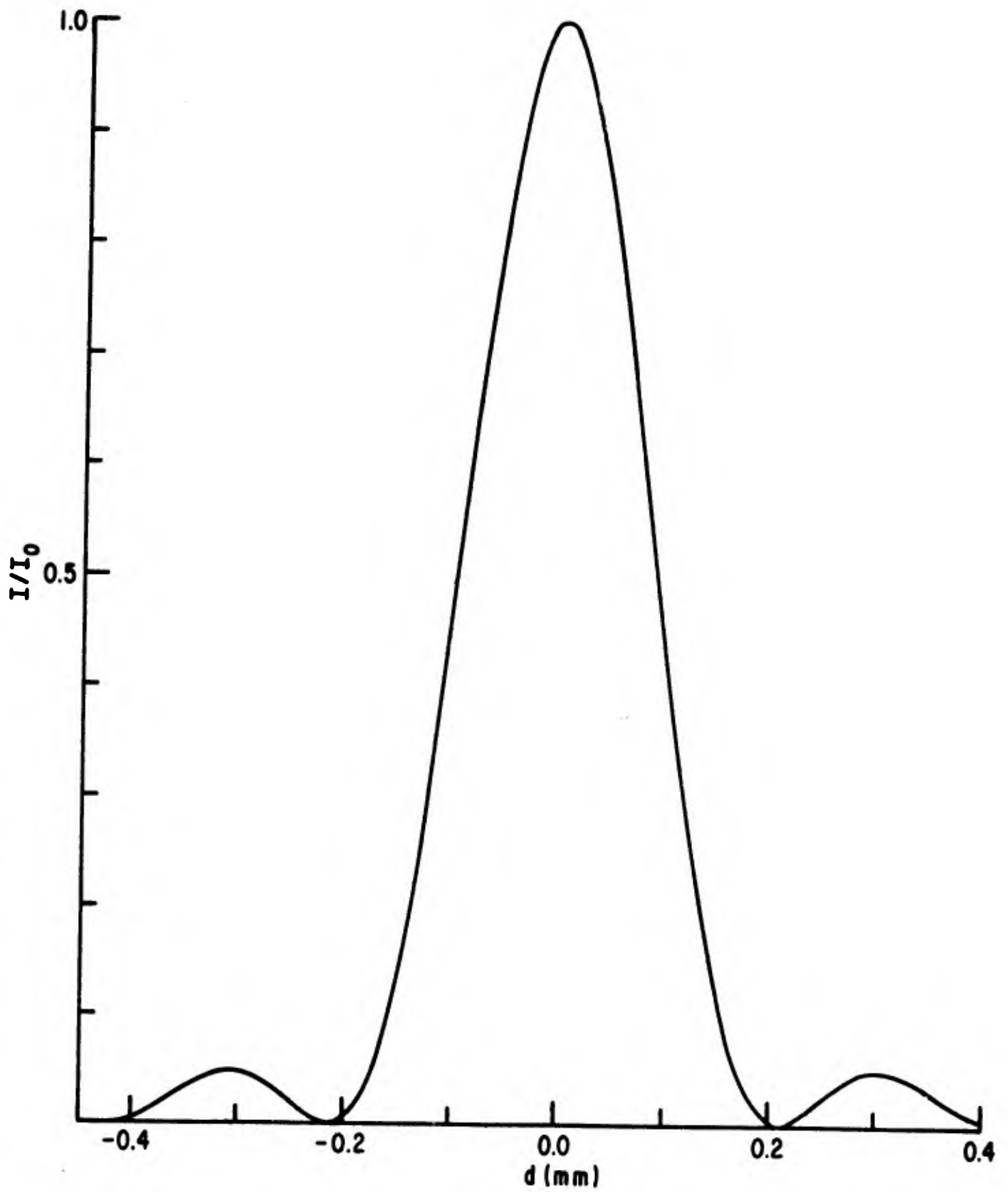


Figure 1. Normalized on-axis focal plane intensity versus primary-secondary movement from the nominal.

we wish to determine the time average of the quantity  $I/I_0$ , i.e.,

$$\overline{I/I_0} \equiv \frac{1}{T} \int_0^T (I/I_0) dt = \frac{1}{T} \int_0^T \text{sinc}^2[a, b, z, R, \lambda, d] dt \quad (4)$$

Since we have assumed a periodic input for  $d$ , we can assume that  $I/I_0$  is periodic; thus

$$\overline{I/I_0} = \frac{1}{2\pi} \int_0^{2\pi} \frac{1}{2\pi} \text{sinc}^2[a, b, \lambda, R, z, d_0, A \sin \theta] d\theta \quad (5)$$

Since there is no closed-form solution to the above integral, it must be evaluated numerically. We approximate the integral as:

$$\overline{I/I_0} = \frac{1}{2\pi} \sum_{k=1}^N \text{sinc}^2 [\dots A \sin \theta_k] \Delta\theta \quad (6)$$

where  $\Delta\theta = 2\pi/N$ ,  $\theta_k = k \frac{2\pi}{N}$ . Thus

$$\overline{I/I_0} = \frac{1}{N} \sum_{k=1}^N \text{sinc}^2 \left[ \dots A \sin \left( k \frac{2\pi}{N} \right) \right] \quad (7)$$

To note the loss in the intensity as a function of  $A$ , the quantity determined was:

$$F = \left( 1 - \overline{I/I_0} \right)$$

The quantity  $F$  was determined for several pairs of  $d_0$  and  $z$ , as a function of  $A$ , with similar results. Figure 2 shows  $F$  versus  $A$ . These results indicate that the relative motions are indeed critical, especially for equipment that may be subjected to a vibration environment. For example, the permissible relative oscillatory acceleration between the mirrors is:

$$\ddot{x}_{\max} = \omega^2 x \quad (8)$$

For  $x = 53$ , and converting to g-units:

$$\ddot{x}_{\max} = 2.1 \times 10^{-4} f^2 g_{\text{rms}} \quad (9)$$

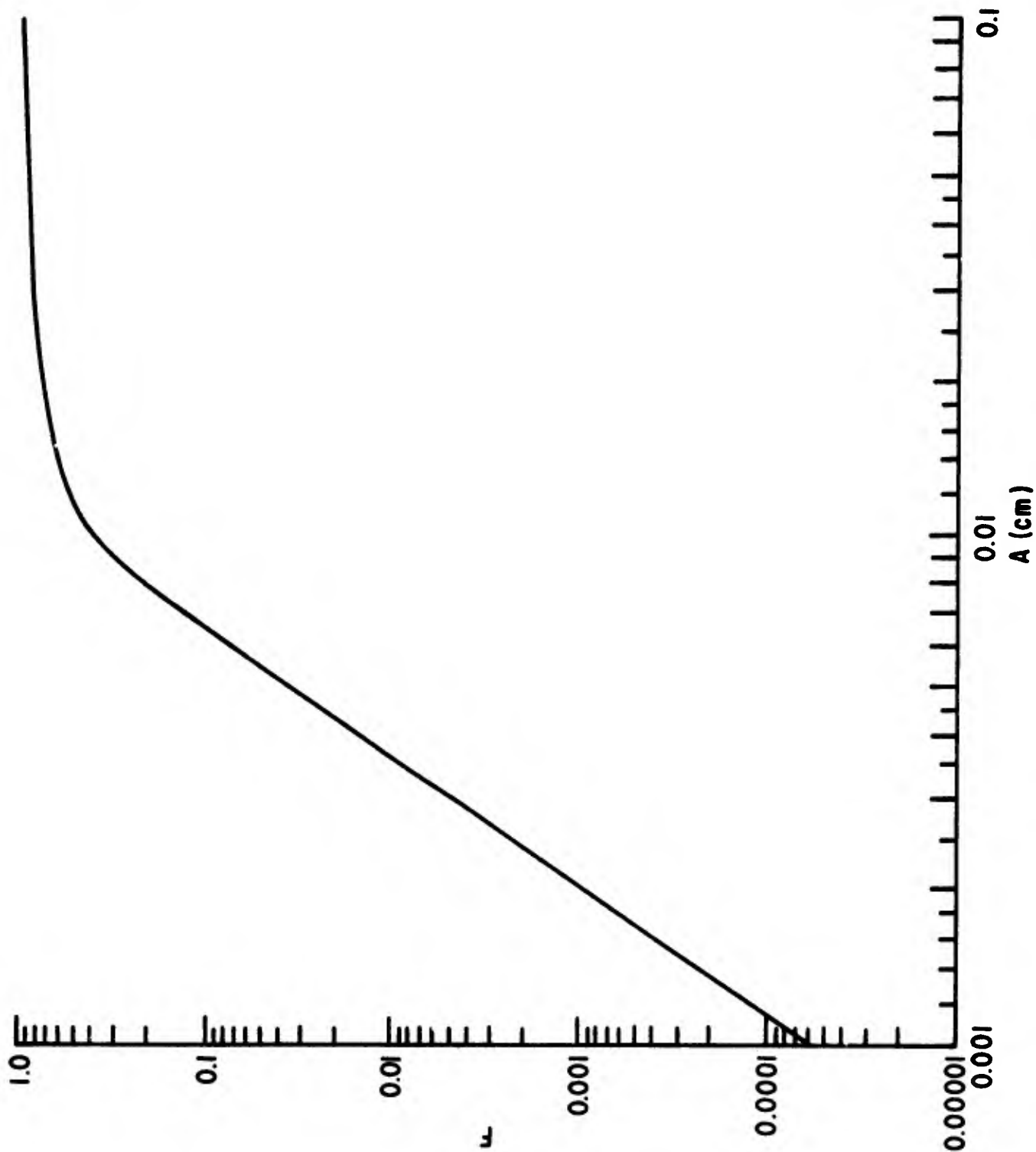


Figure 2. Relative loss in intensity versus magnitude of relative mirror motion.

where  $f$  is the oscillation frequency in Hz. Thus at

$$f = 10 \text{ Hz}, \quad \ddot{x}_{\text{max}} < 0.02 g_{\text{rms}}$$

$$f = 30 \text{ Hz}, \quad \ddot{x}_{\text{max}} < 0.19 g_{\text{rms}}$$

$$f = 100 \text{ Hz}, \quad \ddot{x}_{\text{max}} < 2 g_{\text{rms}}$$

AN IMAGING TECHNIQUE FOR  
BEAM FORMING AND POWER REMOVAL

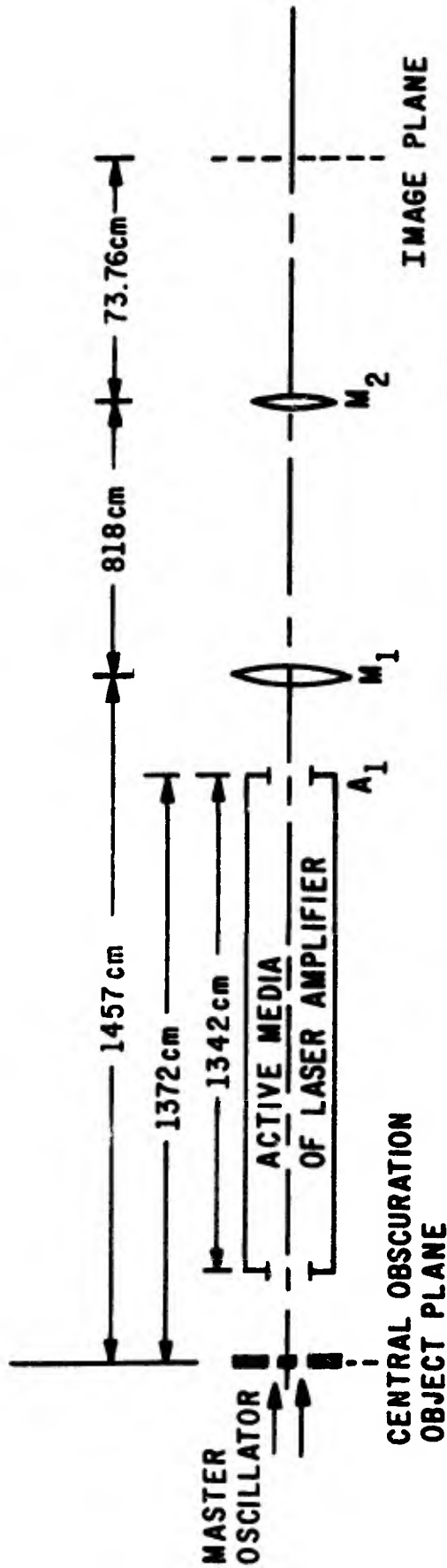
D. A. Maier, J. E. Korka, and R. R. Selleck

A method of obtaining a desired field distribution at a specific plane with a master oscillator-power amplifier laser system was investigated theoretically and experimentally. We consider a beam generated by a CO<sub>2</sub> laser oscillator and amplified by passing through a CO<sub>2</sub> laser amplifier. The objective is to control the intensity and power distribution in this beam at a particular plane beyond the amplifier section. The method is simple, yet novel in this application. A system of mirrors or lenses is used to image a plane prior to the amplifier into its conjugate plane after the amplifier. If diffraction and nonlinearity of laser gain are ignored, the optical field in the object plane will be reproduced, magnified or reduced, by the optical system in the image plane. If diffraction and nonlinearity of the amplifier are small effects it is possible to control the intensity and power distribution at a plane after the amplifier by placing an aperture with the desired transmittance in the master oscillator beam prior to the amplifier.

The feasibility of removing power from the central portion of an amplified CO<sub>2</sub> beam using a central obscuration in the master oscillator beam was investigated. Removing power from a laser beam has application if this beam is projected through an on-axis Cassegrain telescope. The central part of the beam in such a telescope will be reflected back toward the laser device. Figure 1 illustrates the experimental apparatus which was also used as a model to perform diffraction calculations.

The Fresnel diffraction integral was used to calculate the field distributions at successive planes in the system. The optical field,  $U_{n+1}$ , at the (n+1)th plane was found by using the field,  $U_n$ , in the nth plane as follows:

$$U_{n+1}(\rho_{n+1}) = \left\{ \frac{2\pi A_n}{i\lambda z_n} e^{ikz_n} e^{\frac{ik\rho_{n+1}^2}{2z_n}} \right\} \int_{a_n}^{b_n} U_n(\rho_n) e^{\frac{ik\rho_n^2}{2z_n} (1-z_n\phi_n)} J_0\left(\frac{k\rho_n\rho_{n+1}}{z_n}\right) \rho_n d\rho_n$$



$A_1 = 4.44$  cm diameter,  $\phi = 0$   
 $M_1 = 10.16$  cm diameter,  $\phi = .0019379$   
 $M_2 = 7.62$  cm diameter,  $\phi = .066357$

Figure 1. Schematic diagram of experimental apparatus and model for theoretical calculations.

where

$U$  = complex amplitude of field

$A$  = constant related to the magnitude of the field

$\lambda$  = vacuum wavelength of light

$z_n$  = axial distance from plane  $n$  to plane  $n+1$

$k$  = propagation constant =  $2\pi/\lambda$

$\rho_n$  = radial coordinate in the  $n$ th plane

$a$  = the inner radius of any annular aperture

$b$  = the outer radius of any aperture

$\phi_n$  = the optical power of the  $n$ th surface

$J_0$  = zeroth order Bessel function of the first kind

The object plane field was assumed to be:

$$U_0(\rho_0) = U \exp\left[-(\rho_0/w)^2 - i\pi\rho_0^2/\lambda R\right]$$

where  $U$  was normalized for unit power between  $a_0$  and  $b_0$

$w$  = Gaussian spot size

$R$  = the radius of curvature of the input phase front

Figure 2 is a plot of the calculated intensity distribution in the image plane for  $a_0 = 0.3175$  cm,  $b_0 = 2.5$  cm,  $w = 1.77$  cm, and  $R = \infty$ .

Experimentally the image-plane intensity and power distributions were observed on quenched phosphorescent screens and by variable aperture power scans. With an annular object an annular image was formed with and without the amplifier active. With the amplifier off the central spot of intensity, predicted by calculations, was not noted. With the amplifier on and operating in the saturated gain region, an annular image with an intense central spot was observed. The power was measured with a variable radius aperture with and without the central obscuration in the master oscillator beam. Figure 3 is a plot of the percentage of power removed from the image plane as a function of radius. Forty-one percent of the power which had been present in the center of the amplified beam was removed by placing a central obscuration in the object plane. The total power in the beam remained nearly constant.



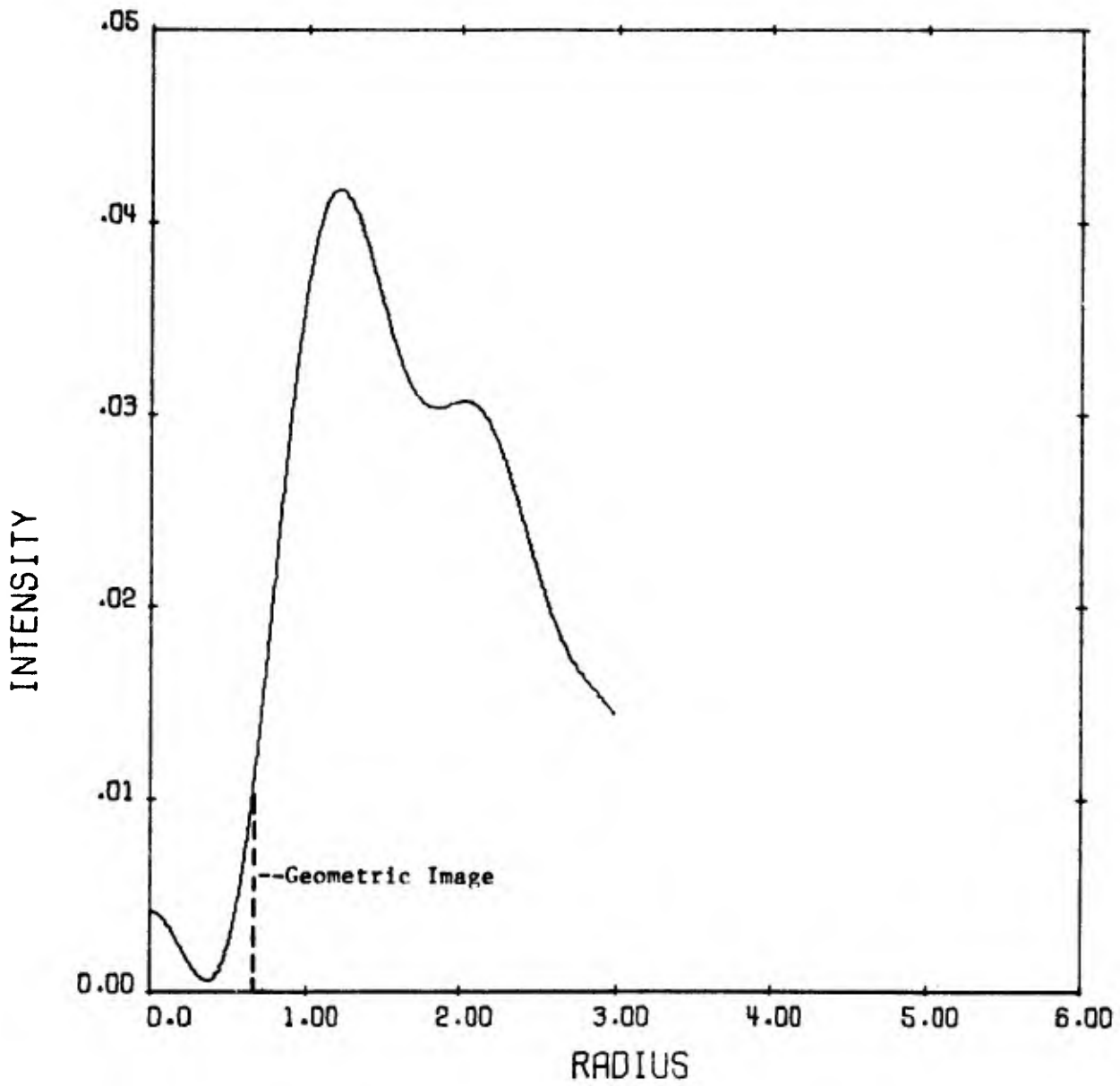


Figure 2. Calculated intensity distribution 73.76 cm from  $M_2$  (image plane).

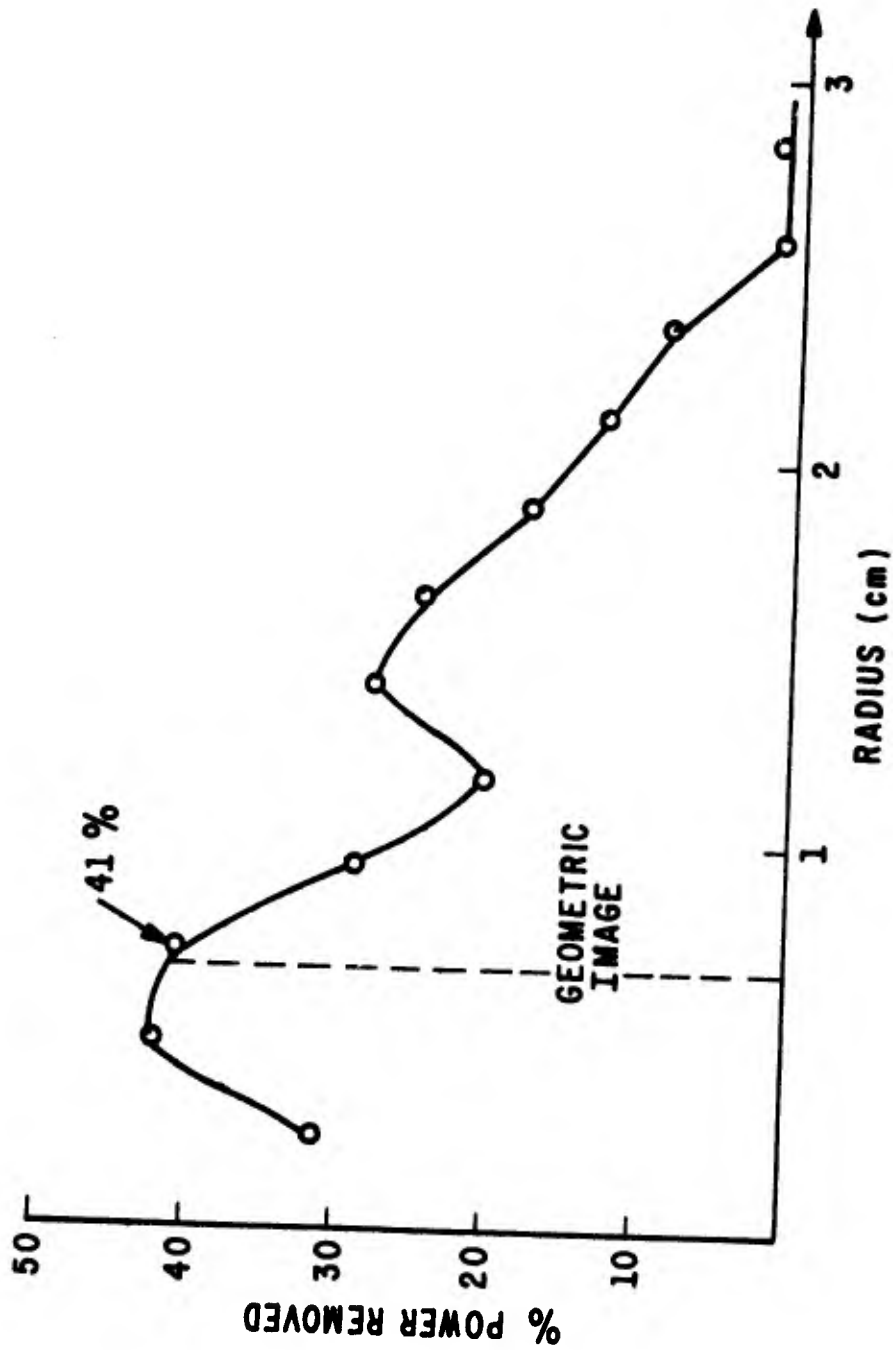


Figure 3. Percent power removed from image as a function of radius (power amplifier on).

These calculations and experiments demonstrated that power could be removed from the center of an amplified laser beam using a central obscuration in the input beam and an imaging technique. If the obscuration can be resolved by the optical system, some advantage will be gained with this technique even when the amplifier is saturated. The less saturated the gain media, the better this technique is expected to work.

Further experiments are planned to show the applicability of the imaging technique for beam power removal in a specific system. A better understanding of the capabilities and limitations of this method will be obtained.

# A REGENERATIVE RING AMPLIFIER FOR A CHEMICAL LASER

John A. Love III

With the advent of high-power chemical lasers, the challenge of efficiently extracting a high-energy chemical laser beam must be met. To date, an unstable confocal resonator has been coupled to a one-kilowatt arc discharge HF laser at Aerospace Corporation in El Segundo, California. High-energy, 1.5 times diffraction limited, beams have been successfully extracted. For this laser, the small signal gain-length product ( $\alpha_0 L$ ) is approximately unity. The saturation intensity ( $I_s$ ) is estimated to be about 200 watts/cm<sup>2</sup>. For lasing media with such high saturation parameters, the regenerative ring amplifier is a promising candidate for extracting high-energy beams by using relatively low input intensities ( $I_0 \ll I_s$ ) from a master oscillator. Admittedly, there might be some engineering constraints which would prohibit the use of a regenerative ring amplifier with a particular laser. However, this subject will not be addressed in this paper.

Regenerative ring amplifiers (Figure 1) operate in two ways: Unconditionally stable and conditionally stable<sup>1</sup>. The unconditionally stable ring ( $G_0 R < 1$ ) cannot oscillate by itself and will amplify only when there is an injected signal. The conditionally stable ring ( $G_0 R \geq 1$ ,  $GR < 1$ ) can oscillate by itself. However, if a sufficiently large signal is injected, the gain will saturate to the point where oscillation is inhibited and only amplification can occur.

I chose to calculate the steady state output by watching the temporal build-up of the electric field input to the amplifier just inside of the ring. The expressions to be derived must consider the electric field amplitude and not the power. This is due to the phase change upon reflection from a dielectrically coated mirror as shown by the Fresnel reflection coefficients<sup>2</sup>. The steady-state electric field input amplitude to the amplifying region is the sum of the following infinite series:

$$E_{IN} = \left[ \dots \left\{ [(tg_1 r + t)g_2 r + t]g_3 r + t \right\} g_4 r \dots + t \right] E_0 \quad (1)$$

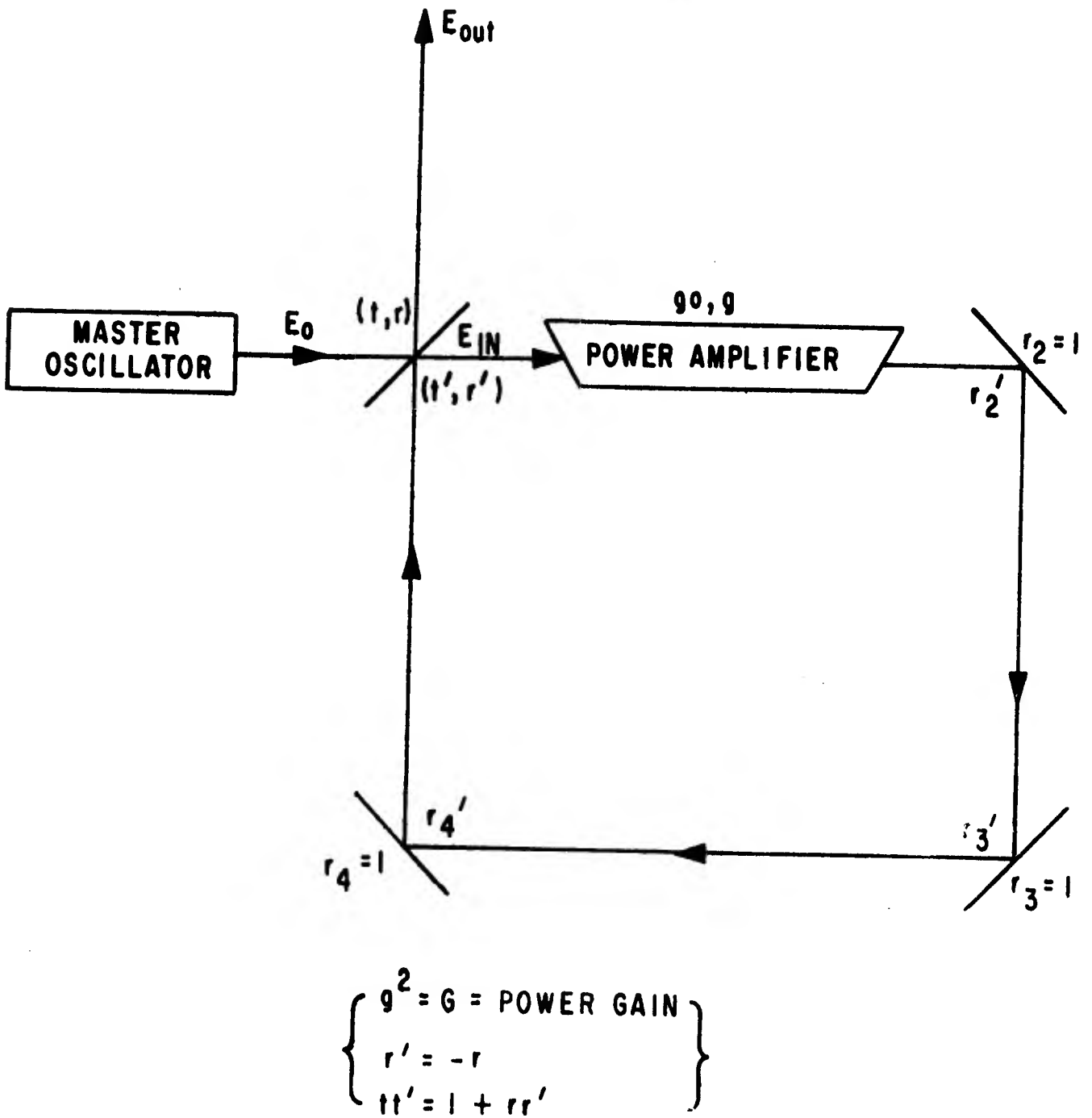


Figure 1. Reflective regenerative ring amplifier.

where the terms inside each successive pair of brackets are the input to the amplifier upon each successive pass. For example,  $(tg_1r+t)E_0$  is the input to the amplifier on the second pass and  $(tg_1r+t)g_2r+t E_0$  is the input on the third pass. For equation (1):

$E_0$  = electric field amplitude from the master oscillator.

$t$  = electric field transmission coefficient into the ring amplifier.

$r$  = external electric field reflection coefficient for the input mirror.\*

$g_i = \exp(1/2\alpha_i L)$  = the electric field gain for the  $i^{\text{th}}$  pass.

$\alpha_i$  = saturated power gain coefficient for the  $i^{\text{th}}$  pass.

Equation (1) can be rewritten:

$$E_{IN} = t + \dots g_4 r t + g_4 g_3 r^2 t + g_4 g_3 g_2 r^3 t + g_4 g_3 g_2 g_1 r^4 t \quad (2)$$

The steady-state electric field output amplitude is:

$$E_{out} = rE_0 - E_{IN} g_{ss} t' \quad (3)$$

where

$g_{ss}$  = steady-state saturated gain for the electric field.

$t'$  = electric field transmission coefficient out of the ring amplifier with  $tt' = 1+rr'$ .

The above treatment differs from that of Buczek<sup>1</sup>. He derived coupled analytical expressions for the output power.

Figure 2 presents data for an amplifier having a homogeneously broadened gain medium. Figure 3 presents data when the gain is inhomogeneously broadened. For the former,

$$\alpha = \frac{\alpha_0}{1 + I/I_s} \quad (4)$$

---

\*In reality, this reflection coefficient is  $r'_1 r'_2 r'_3 r'_4$  where  $r'_i$  is the internal electric field reflection coefficient for the  $i^{\text{th}}$  mirror. For  $r_1 = r'_1$  and assuming that mirrors 2, 3, and 4 are perfect reflectors ( $r_2=r_3=r_4=1$ ), the final product is  $r$ .

**A REGENERATIVE RING AMPLIFIER**

**{ — : UNCONDITIONALLY STABLE }**  
**{ - - - : CONDITIONALLY STABLE }**

**GAIN IS HOMOGENEOUSLY BROADENED**

**$\alpha_0 = 0.008 \text{ CM}^{-1}$   $L = 150 \text{ CM.}$ ,  $P_S = 80 \text{ WATTS}$**

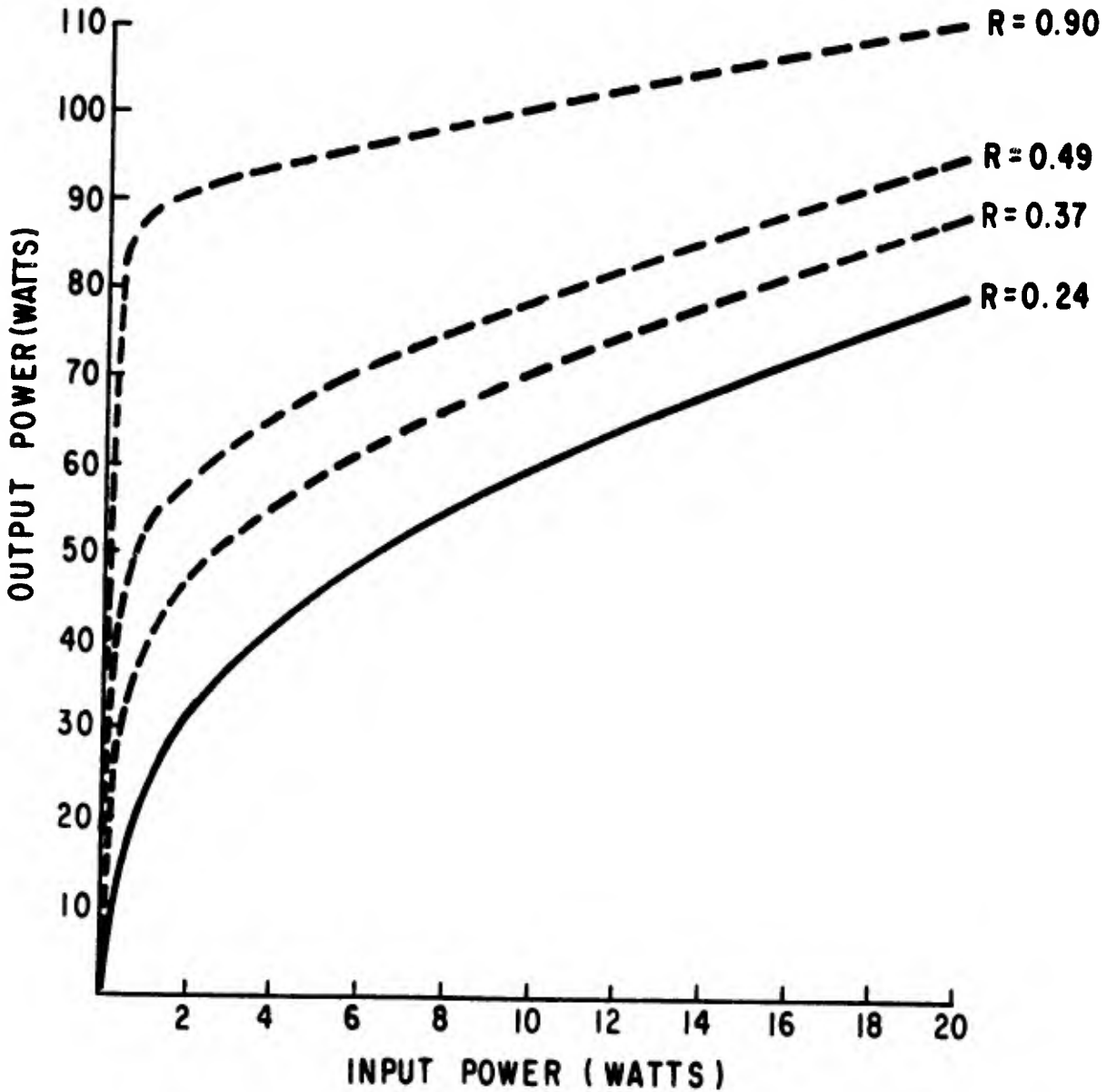


Figure 2. Regenerative ring amplifier for medium with homogeneously broadened gain.

### A REGENERATIVE RING AMPLIFIER

{ — : UNCONDITIONALLY STABLE }  
{ - - : CONDITIONALLY STABLE }

GAIN IS INHOMOGENEOUSLY BROADENED

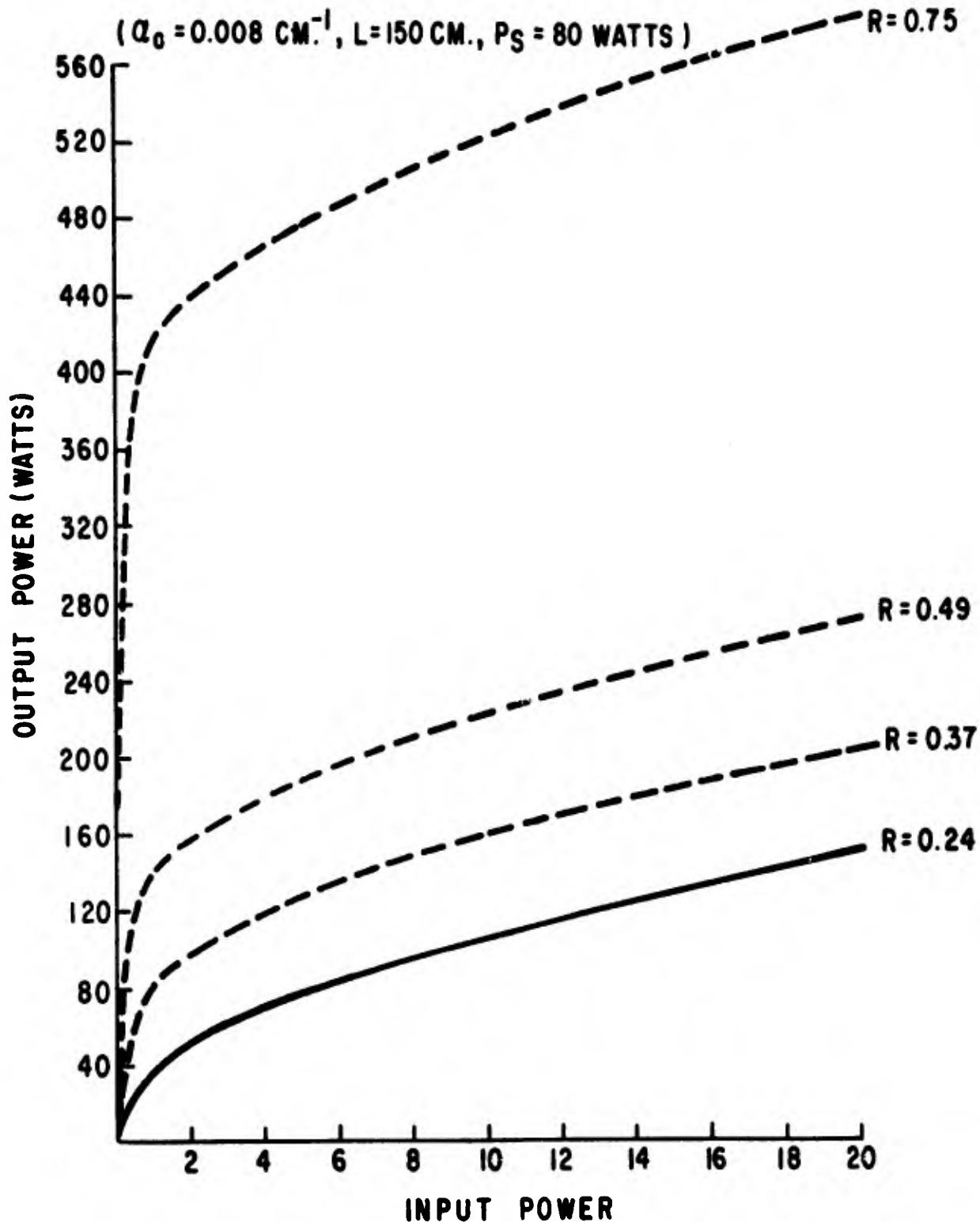


Figure 3. Regenerative ring amplifier for medium with inhomogeneously broadened gain.



For the latter,

$$\alpha = \frac{\alpha_0}{\sqrt{1 + I/I_s}} \quad (5)$$

Equation (5) deserves some special attention. First, the small signal gain is assumed to be the same as in the homogeneous case; that is, the number density of atoms at the center frequency is the same. Second, the saturated gain is larger for the inhomogeneous case than for the homogeneous case since the number density of atoms in the inhomogeneous line width is larger. Therefore, the gain relationship in equation (5) implies a non-constant atomic number density case. The gain in an HF-DF lasing zone is inhomogeneously broadened. However, the constancy of the atomic number density is not validated. Nevertheless, equation (5) will be assumed to be more representative of a chemical laser than equation (4).

Figures 2 and 3 present data for a low gain system, such as that treated by Buczek. Common to both data sets is the conclusion that if the reflectivity of the input beam splitter is high (conditionally stable), a low input field is sufficient to "tickle" the ring amplifier. For high reflectivity, the number of passes that the field stored within the ring ( $=E_{IN}$ ) takes to achieve a steady state becomes very large. As a result, the power stored within the ring is very high and the net output power is very high. Notice that the low "tickle" power is about one percent of the saturation parameter.

Comparison of Figure 3 with Figure 2 shows that the ring amplifier has a large steady state saturated gain for the inhomogeneously broadened case (non-constant atomic number density case).

Figure 4 compares a low, inhomogeneously broadened, gain system with a high gain system. The obviously anticipated results are produced. For a high gain system, the numerical data show that the reflectivity (R) has an upper bound where  $GR = 1$ . The higher the small signal gain, the lower this upper bound.

Figure 5 presents data typical of high gain chemical lasers.

In conclusion, a reflective ring amplifier is an effective optical means whereby a low input power from a master oscillator can produce a very high output power from high gain media. This "tickle" power is of the order of one percent of the saturation parameter ( $P_s$ ).

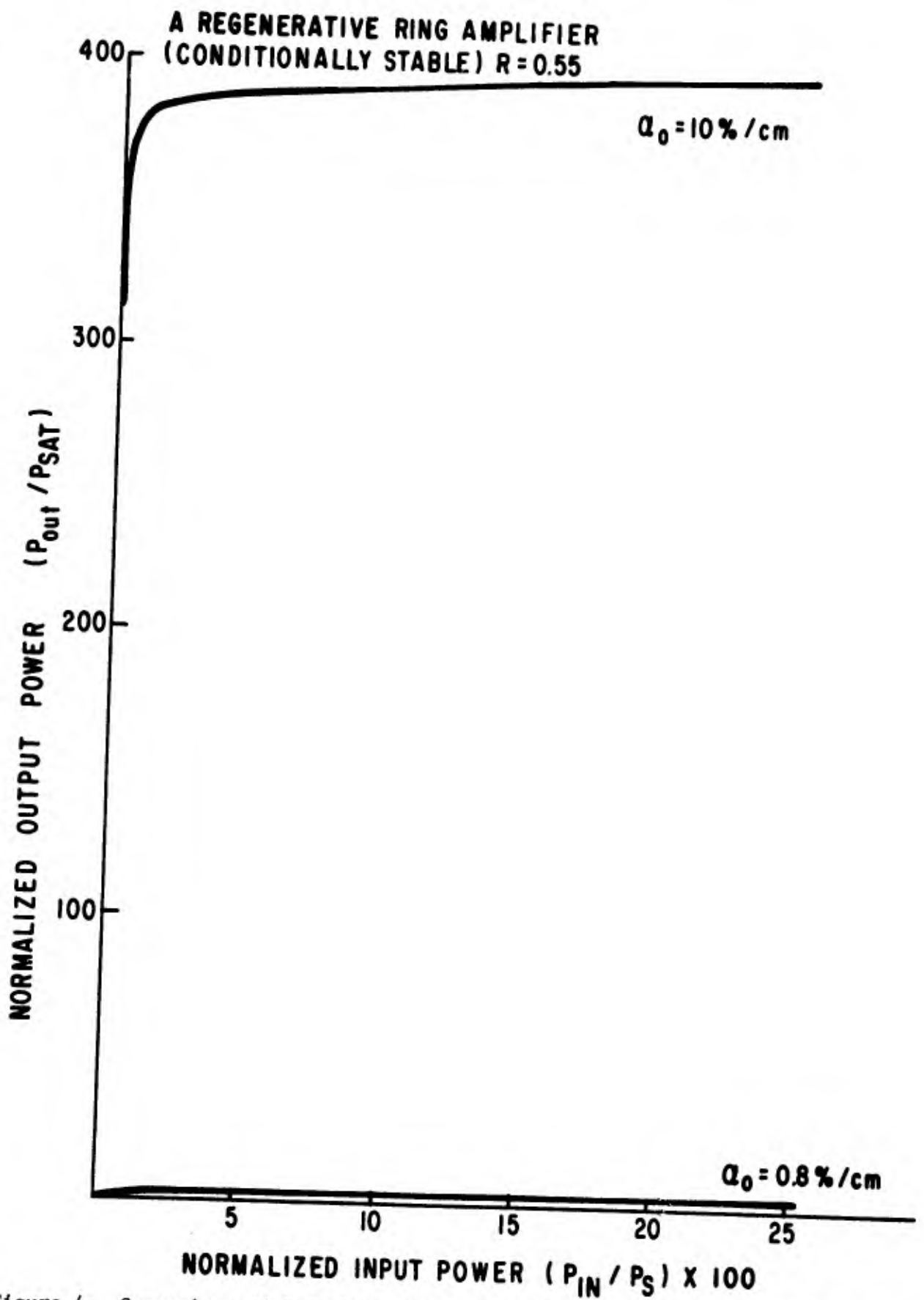


Figure 4. Comparison of low gain system ( $\alpha_0 = 0.8$  percent/cm) with high gain system ( $\alpha_0 = 10$  percent/cm). Gain is inhomogeneously broadened.

TYPICAL CHEMICAL LASER  
SATURATED RING AMPLIFIER

$Q_0 = 10\% / \text{cm}$ ;  $L = 7$  inches

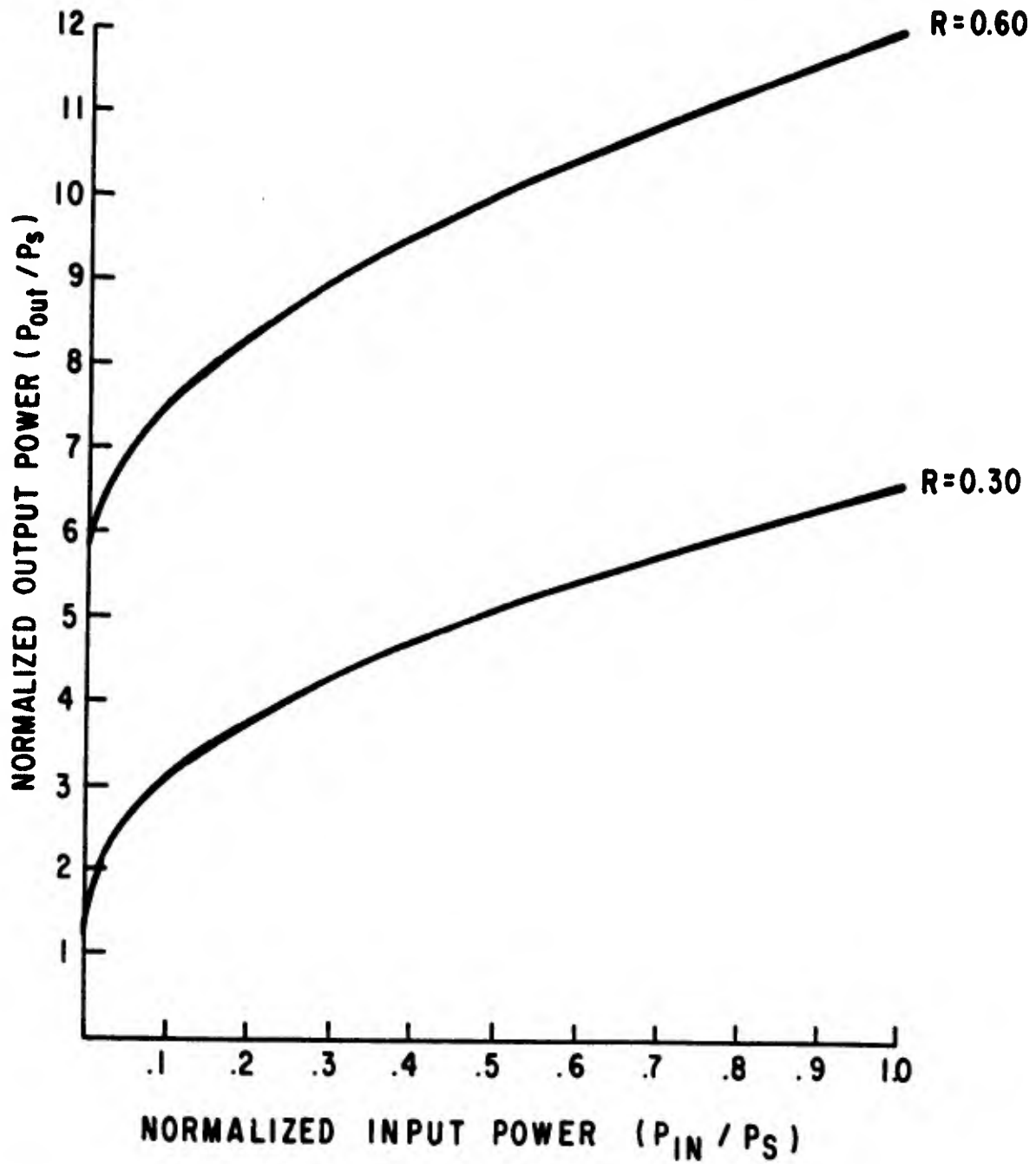


Figure 5. Behavior of high gain chemical laser.

The author is indebted to Major E. Gieselmann and Lt R. Selleck for their many elucidating comments.

#### REFERENCES

1. Buczek, C., et al., "CO<sub>2</sub> Regenerative Ring Power Amplifiers," United Aircraft Research Laboratories Internal Memorandum, undated.
2. Klein, M. V., Optics, John Wiley & Sons, New York, 1970.

## TELESCOPIC AMPLIFIER

D. A. Holmes, P. V. Avizonis, J. A. Love, and J. E. Korka

We consider the amplification of a laser beam by a gain medium that is uniformly distributed between the lenses of a beam-expanding Galilean telescope. Such a telescope, in afocal adjustment, is shown in Figure 1. The common focal point is identified by the point F on the optical axis.

The laser beam is considered to be propagating from left to right in Figure 1. Between lenses the beam occupies a conical region that is presumed to be filled with a uniformly distributed small signal gain  $\alpha_0$ .

To treat this amplifier problem, we set up the approximate geometrical model depicted in Figure 2. We consider a conical beam, of half-angle  $\theta_0$ , that appears to be coming from point F. A spherical coordinate system is set up with F as the origin and the z-axis as shown in Figure 2.

The spherical surface that occupies the region  $r = f$  and  $\theta \leq \theta_0$  is taken as the input boundary; i.e., over this surface the conical beam flux is taken to be the same as the irradiance distribution of the laser beam as it enters the negative lens of the telescope. The output boundary surface is taken as the spherical surface  $r = mf$  and  $\theta \leq \theta_0$ ; it is essentially at this surface that the amplified conical beam is recollimated by the positive lens.

In Figure 2, let us refer to the volume element  $Sdr$  and write a power balance for this volume element. The power entering the element is  $IS$ , where we assume now that the irradiance  $I$  is uniform over the area  $S$ . Similarly, the power leaving the volume element is  $(I+dI)(S+dS)$ . The power generated and added to the conical beam in the volume element  $Sdr$  is simply  $\alpha ISdr$ , where the gain  $\alpha$  is assumed to be essentially constant throughout the volume element and of the form

$$\alpha = \alpha_0 / [1 + I/I_S] \quad (1)$$

$I_S$  is the saturation flux and  $\alpha_0$  is the small signal gain.

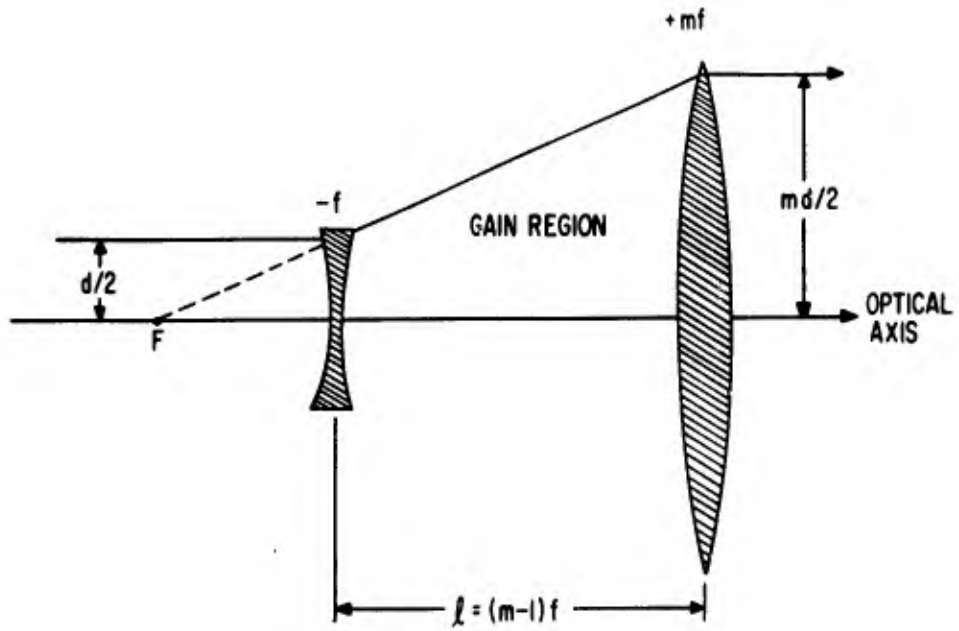


Figure 1. Geometrical configuration under consideration. In the gain region, the uniformly distributed small signal gain is  $\alpha_0$ .

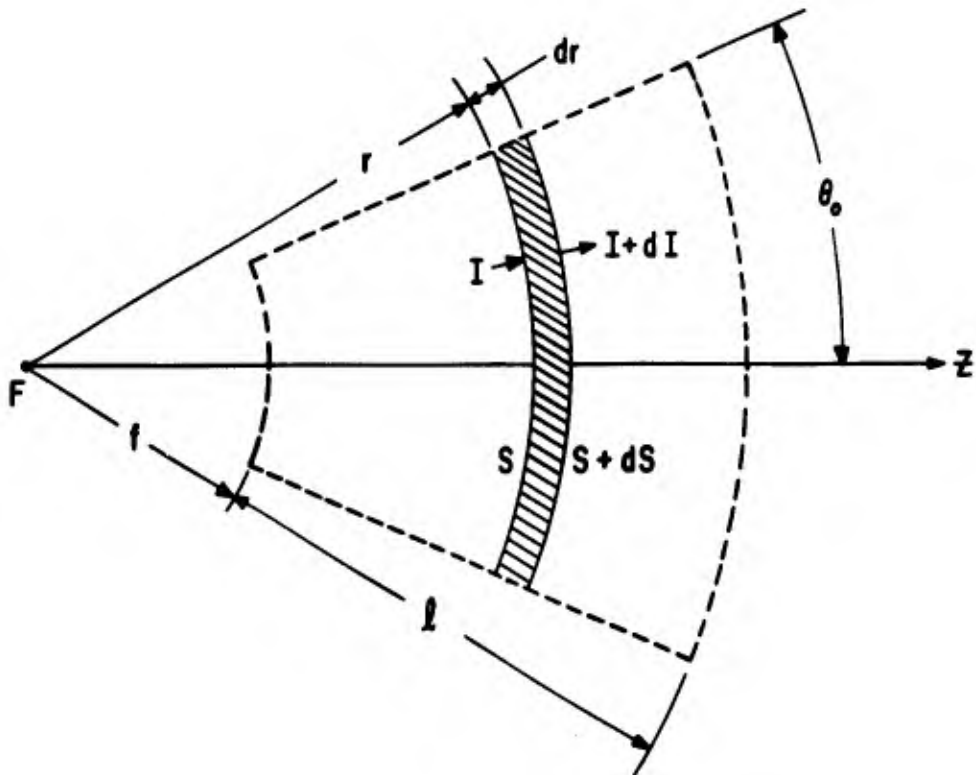


Figure 2. Approximate analytical model, valid for lenses with large f-numbers. The dotted lines delineate the boundaries of the conical beam. The center of the spherical surfaces is the point F.

The power balance on the volume element  $Sdr$  gives

$$(I+dI)(S+dS)-IS = \alpha ISdr$$

$$IdS+SdI = \alpha ISdr \quad (2)$$

The area  $S$  is given by

$$S = 4\pi r^2 \sin^2(\theta_0/2) \quad (3)$$

Using equations (1) and (3) in equation (2), we obtain

$$dI/dr + 2I/r = \alpha_0 I / [1 + I/I_S] \quad (4)$$

The initial condition on  $I$  is simply that  $I = I_1$  at  $r = f$ ; the final condition is that  $I = I_2$  when  $r = mf$ . The power gain of the amplifier is

$$G_p = m^2 I_2 / I_1 \quad (5)$$

There are two instances where equation (4) reduces to an easily solved linear equation: the highly saturated amplifier and the small signal amplifier.

In the highly saturated amplifier, we have

$$I/I_S \gg 1 \quad (6)$$

for all values of  $r$ . In this case, the solution for  $I$  is approximately

$$I = \alpha_0 I_S r / 3 + [I_1 - \alpha_0 I_S f / 3] (f/r)^2 \quad (7)$$

and the power gain is

$$G_p = 1 + \alpha_0 \ell (m^2 + m + 1) (I_S / 3 I_1) \quad (8)$$

In the small signal amplifier, we have

$$I/I_S \ll 1 \quad (9)$$

for all values of  $r$ . The solution for  $I$  is approximately

$$I = I_1 [f/r]^2 \exp[\alpha_0 (r-f)] \quad (10)$$

and the power gain is

$$G_p = \exp(\alpha_0 \ell) \quad (11)$$

Some numerical solutions of equation (4) have been obtained by computer integration. To prepare numerical illustrations, equation (4) was transformed with the following substitutions.

$$i = I/I_S; \text{ (dimensionless irradiance)} \quad (12a)$$

$$y = r/f = (m-1)r/\ell; \text{ (dimensionless coordinate)} \quad (12b)$$

Using equation (12), we thus obtain

$$di/dy + 2i/y = \alpha_0 \ell i / [(m-1)(1+i)] \quad (13)$$

An alternative differential equation can be derived by defining  $p = iy^2$ ; then equation (13) becomes

$$(m-1)(y^2+p)dp = \alpha_0 \ell py^2 dy \quad (14)$$

In Figures 3 to 14 we show numerical integrations of equation (13). The plots show  $i$  versus  $y$  for a variety of values of  $m$ ,  $\alpha_0 \ell$ , and  $i_1$ . In Figures 15 and 16 we show the power gain  $G_p$  versus  $\alpha_0 \ell$  with  $m$  and  $i_1$  as parameters.



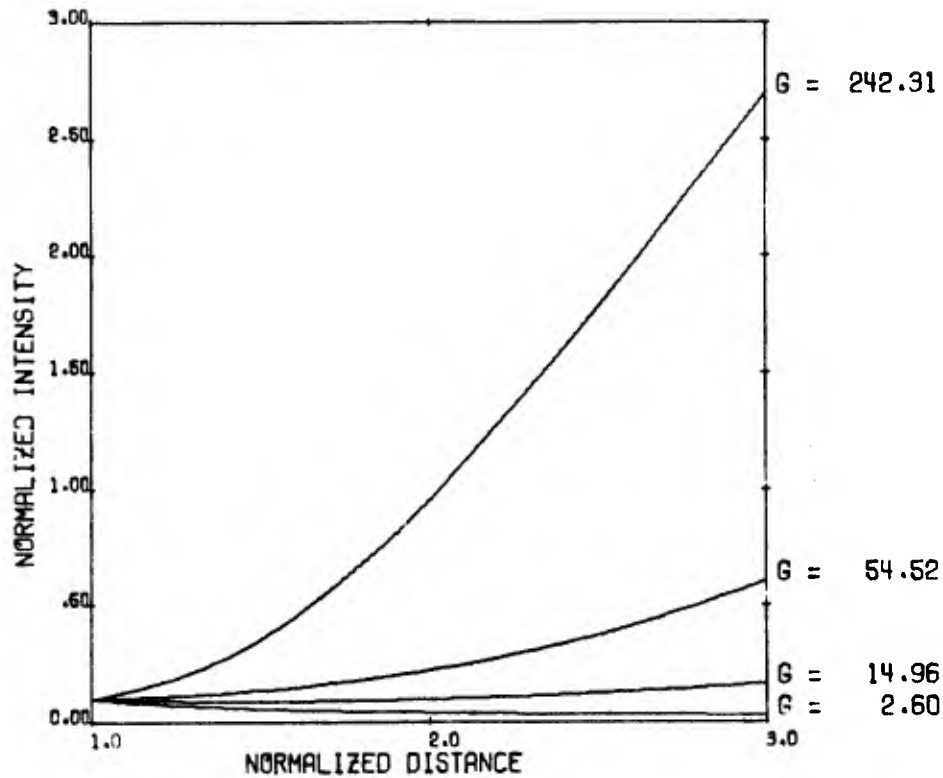


Figure 3.  $I/I_S$  versus  $r/f$  with an initial condition of  $I_1 = I_S/10$ . The telescope expansion ratio is  $m=3$ . From bottom to top, the curves are identified by the parameter values  $\alpha_0 l = 1, 3, 5,$  and  $10$ . The power gain for each curve is indicated by the  $G$  value at the right border.

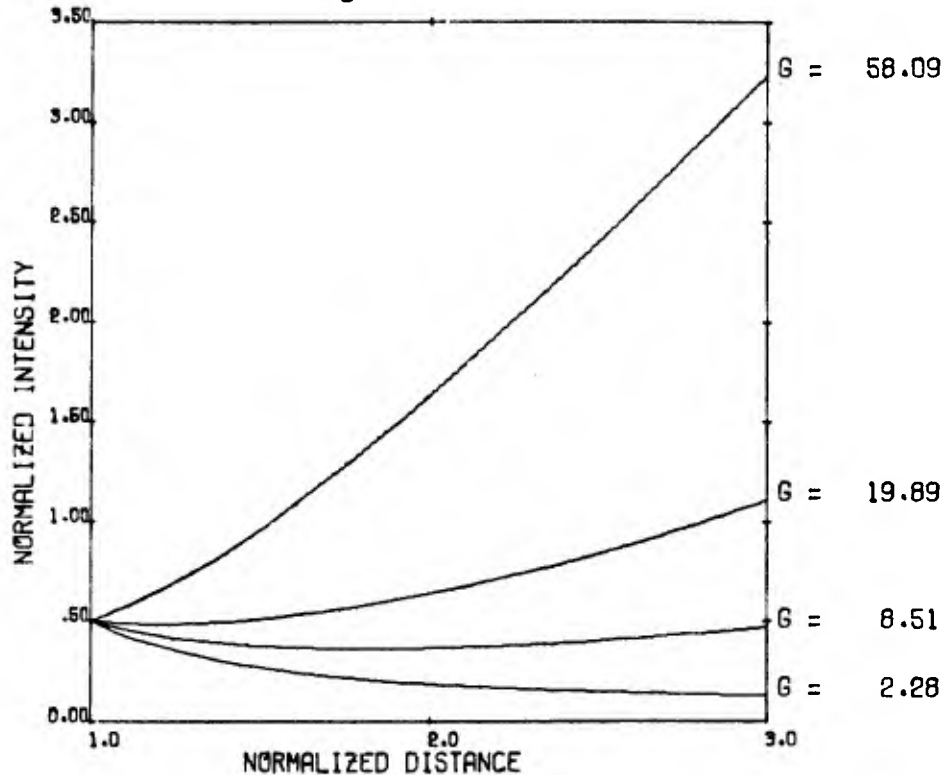


Figure 4.  $I/I_S$  versus  $r/f$  with an initial condition of  $I_1 = I_S/2$ . The telescope expansion ratio is  $m=3$ . From bottom to top, the curves are identified by the parameter values  $\alpha_0 l = 1, 3, 5,$  and  $10$ . The power gain for each curve is indicated by the  $G$  value at the right border.

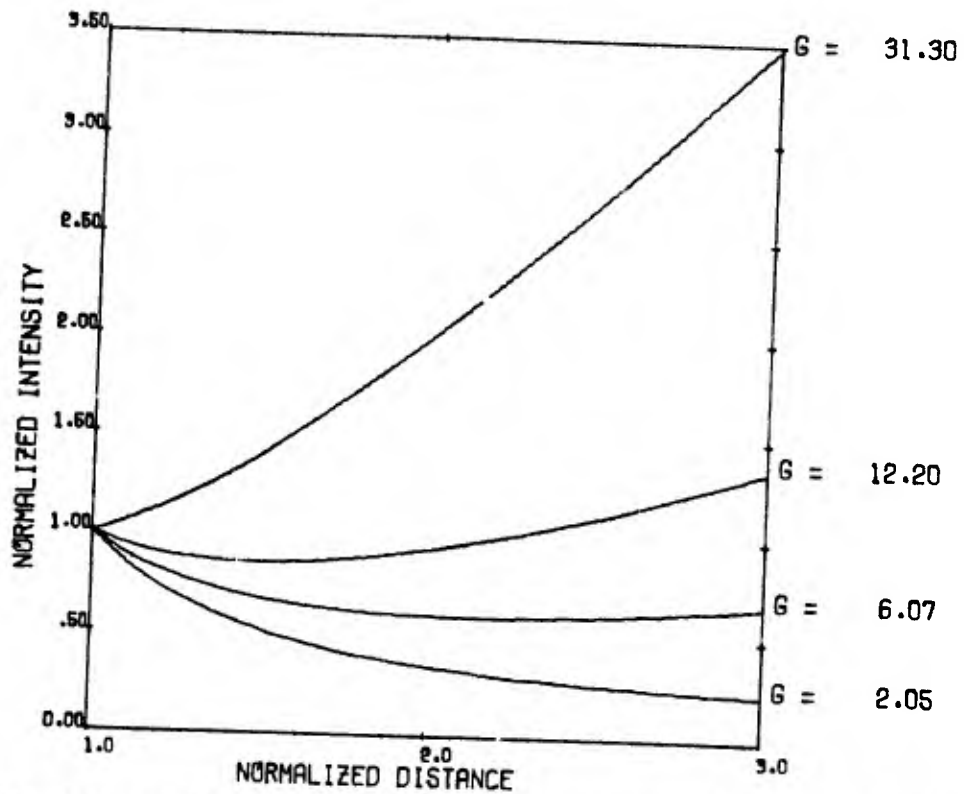


Figure 5.  $I/I_S$  versus  $r/f$  with an initial condition of  $I_1=I_S$ . The telescope expansion ratio is  $m=3$ . From bottom to top, the curves are identified by the parameter values  $\alpha_0 \ell = 1, 3, 5,$  and  $10$ . The power gain for each curve is indicated by the  $G$  value at the right border.

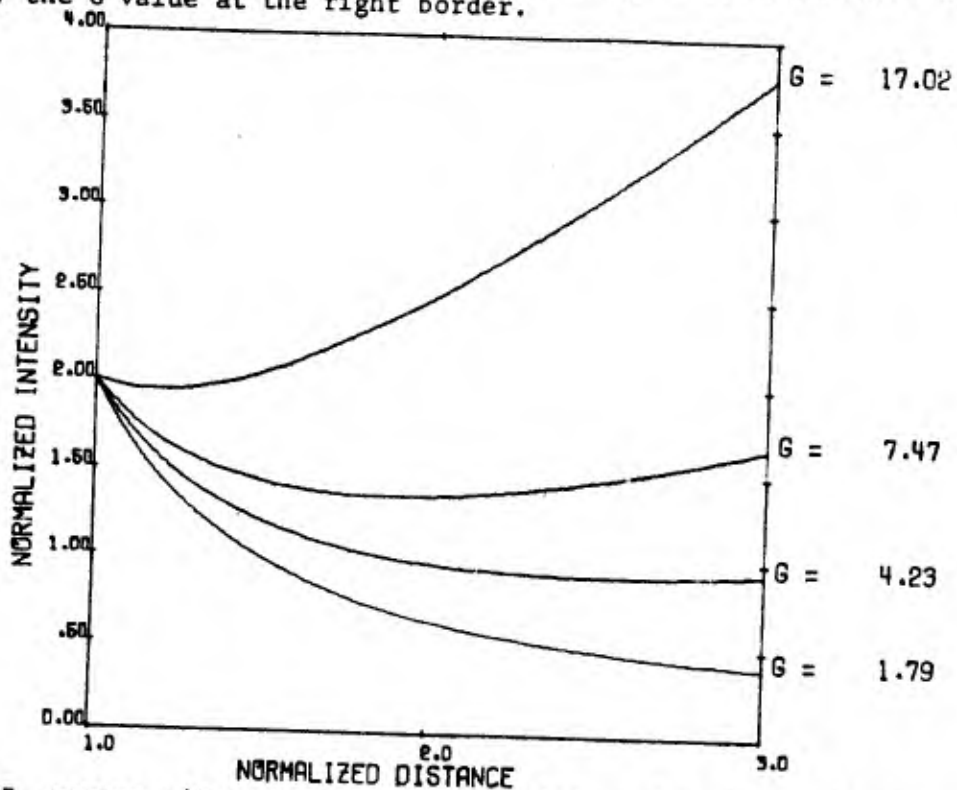


Figure 6.  $I/I_S$  versus  $r/f$  with an initial condition of  $I_1=2I_S$ . The telescope expansion ratio is  $m=3$ . From bottom to top, the curves are identified by the parameter values  $\alpha_0 \ell = 1, 3, 5,$  and  $10$ . The power gain for each curve is indicated by the  $G$  value at the right border.

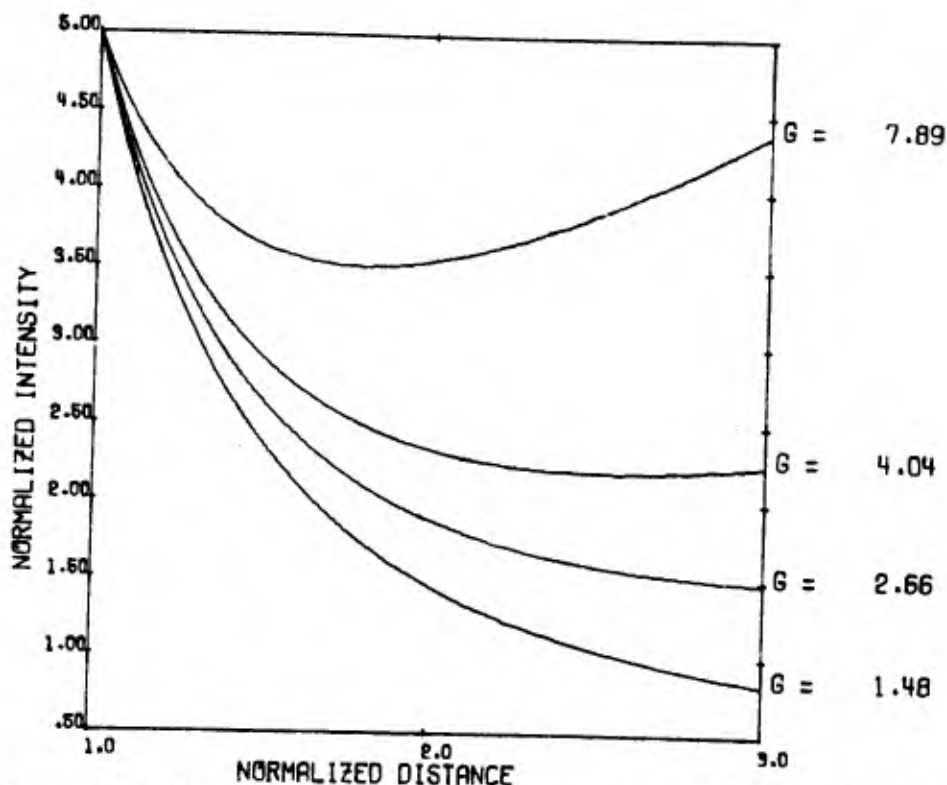


Figure 7.  $I/I_0$  versus  $r/f$  with an initial condition of  $I_1=5I_0$ . The telescope expansion ratio is  $m=3$ . From bottom to top, the curves are identified by the parameter values  $\alpha_0 l = 1, 3, 5,$  and  $10$ . The power gain for each curve is indicated by the  $G$  value at the right border.

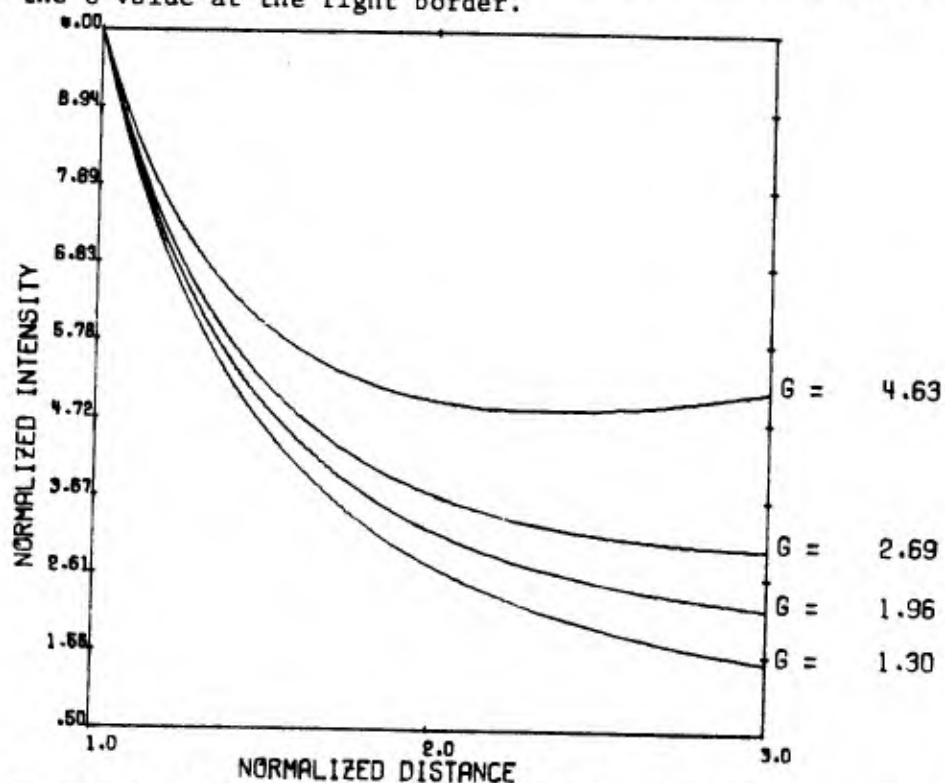


Figure 8.  $I/I_0$  versus  $r/f$  with an initial condition of  $I_1=10I_0$ . The telescope expansion ratio is  $m=3$ . From bottom to top, the curves are identified by the parameter values  $\alpha_0 l = 1, 3, 5,$  and  $10$ . The power gain for each curve is indicated by the  $G$  value at the right border.

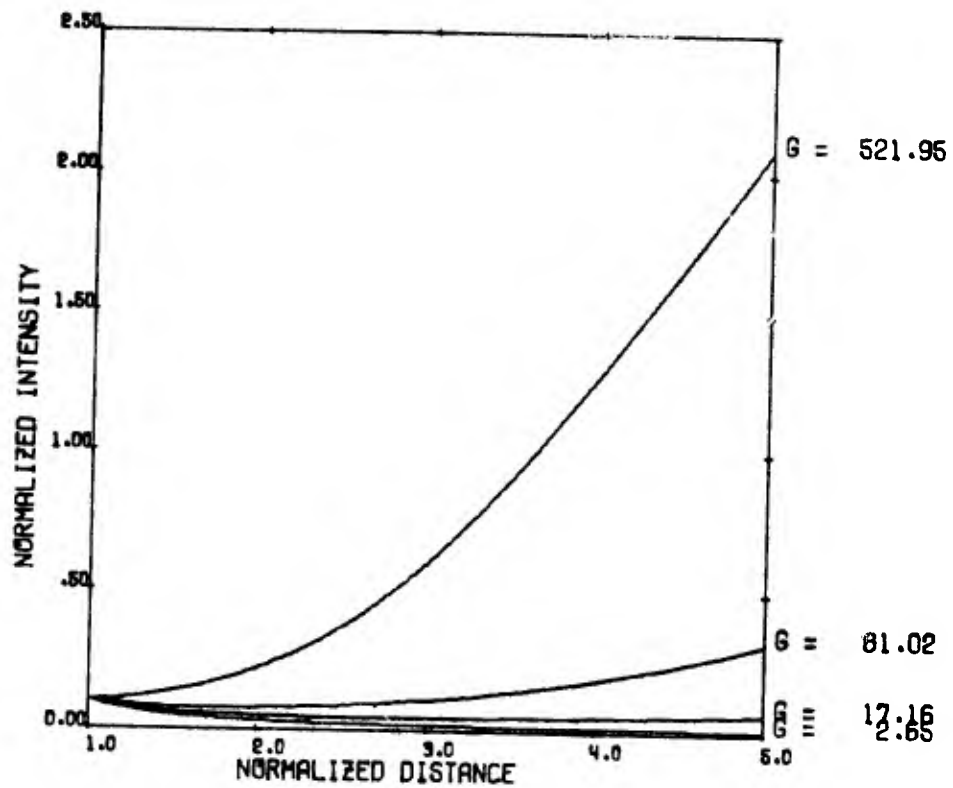


Figure 9.  $I/I_S$  versus  $r/f$  with an initial condition of  $I_1 = I_S/10$ . The telescope expansion ratio is  $m=5$ . From bottom to top, the curves are identified by the parameter values  $\alpha_0 l = 1, 3, 5,$  and  $10$ . The power gain for each curve is indicated by the  $G$  value at the right border.

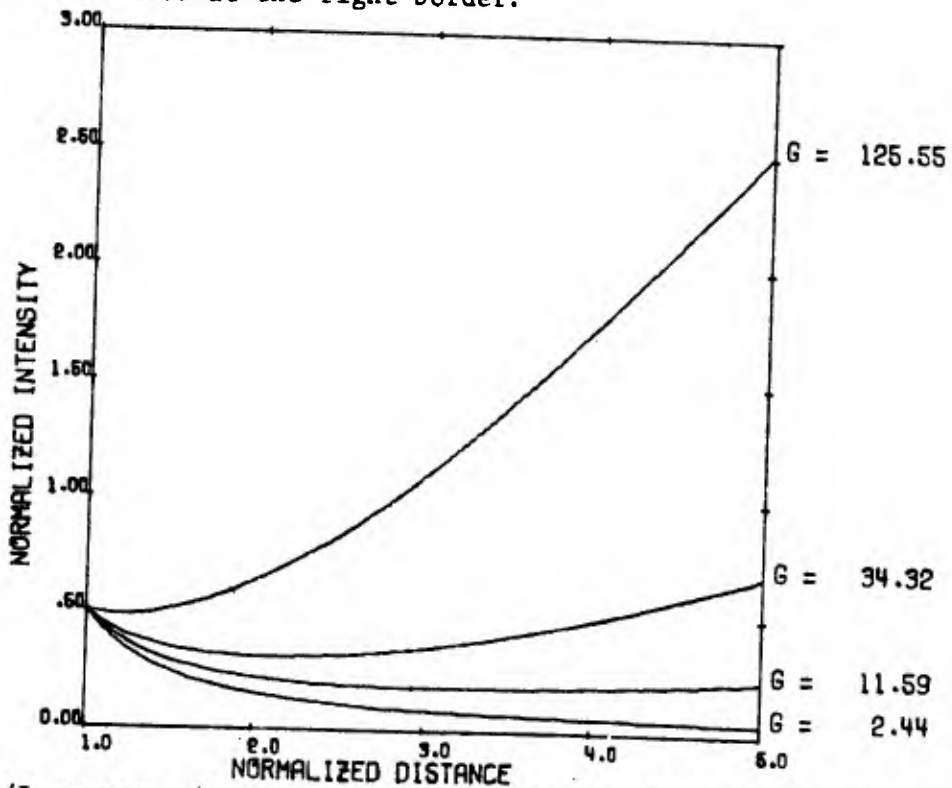


Figure 10.  $I/I_S$  versus  $r/f$  with an initial condition of  $I_1 = I_S/2$ . The telescope expansion ratio is  $m=5$ . From bottom to top, the curves are identified by the parameter values  $\alpha_0 l = 1, 3, 5,$  and  $10$ . The power gain for each curve is indicated by the  $G$  value at the right border.

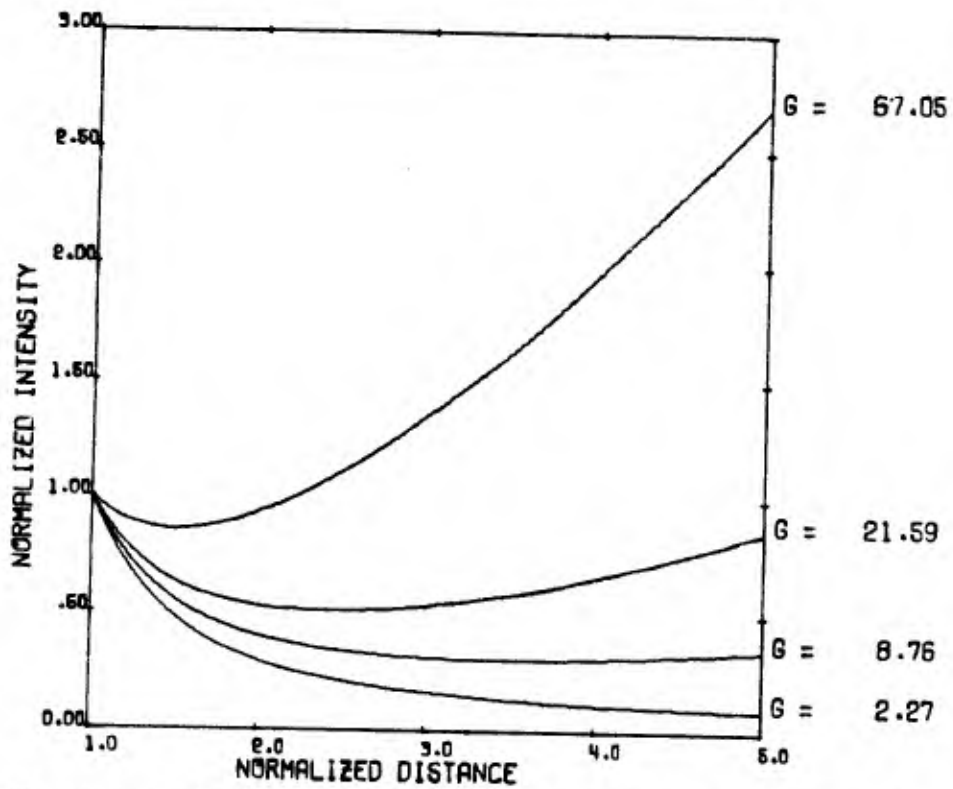


Figure 11.  $I/I_0$  versus  $r/f$  with an initial condition of  $I_1=I_0$ . The telescope expansion ratio is  $m=5$ . From bottom to top, the curves are identified by the parameter values  $\alpha_0 l = 1, 3, 5,$  and  $10$ . The power gain for each curve is indicated by the  $G$  value at the right border.

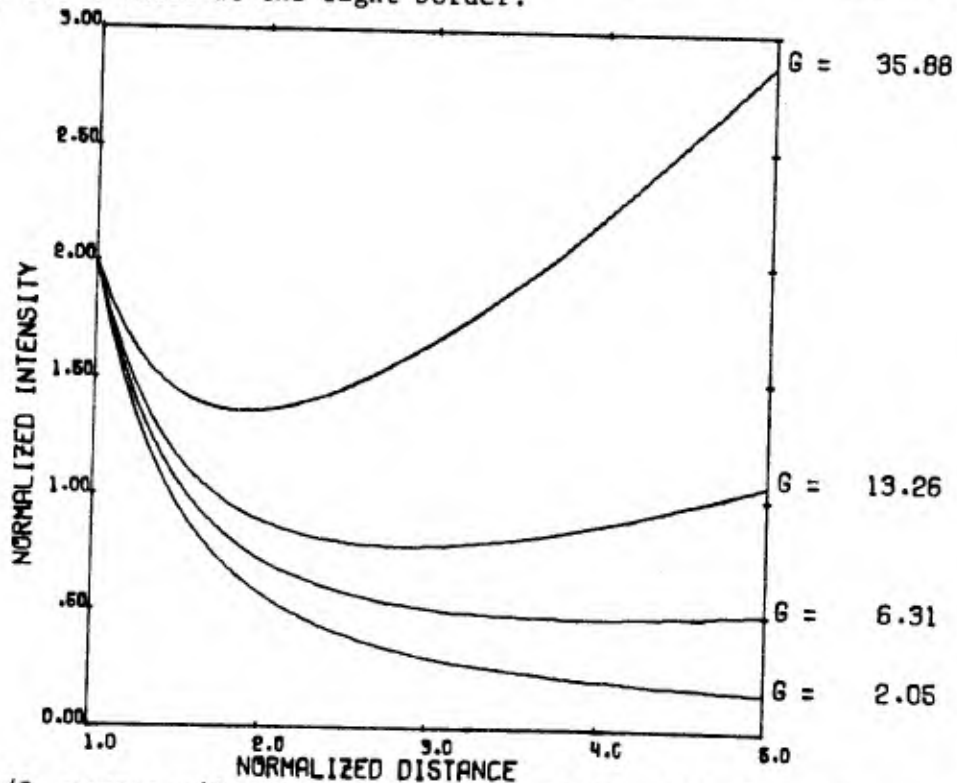


Figure 12.  $I/I_0$  versus  $r/f$  with an initial condition of  $I_1=2I_0$ . The telescope expansion ratio is  $m=5$ . From bottom to top, the curves are identified by the parameter values  $\alpha_0 l = 1, 3, 5,$  and  $10$ . The power gain for each curve is indicated by the  $G$  value at the right border.

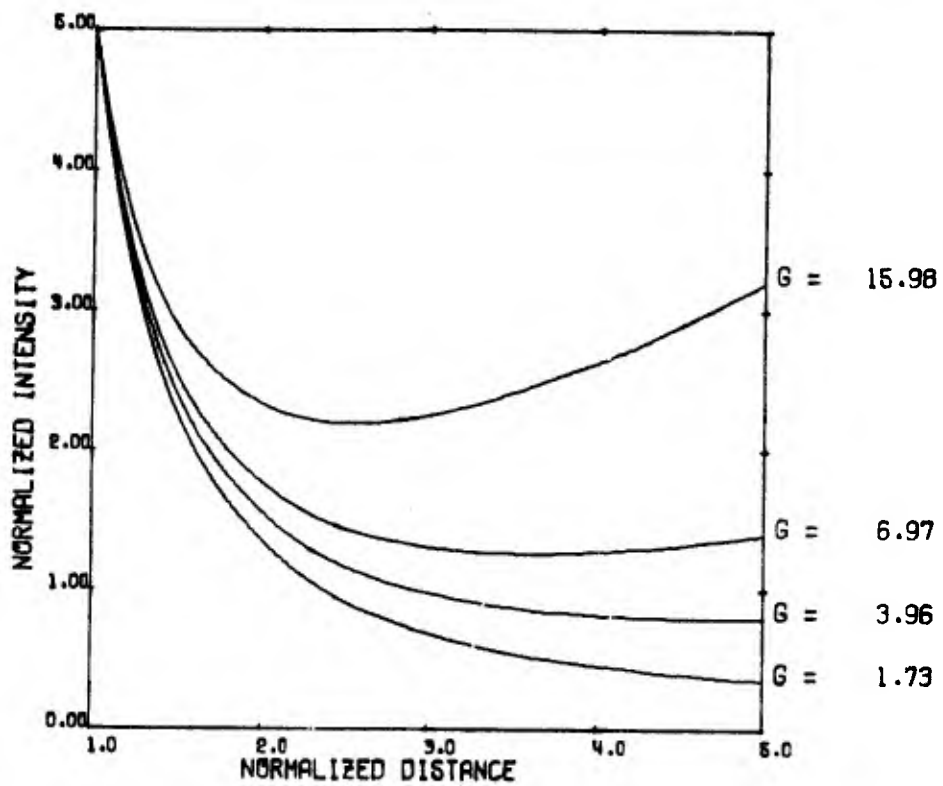


Figure 13.  $I/I_0$  versus  $r/f$  with an initial condition of  $I_1=5I_0$ . The telescope expansion ratio is  $m=5$ . From bottom to top, the curves are identified by the parameter values  $\alpha_0 l = 1, 3, 5,$  and  $10$ . The power gain for each curve is indicated by the  $G$  value at the right border.

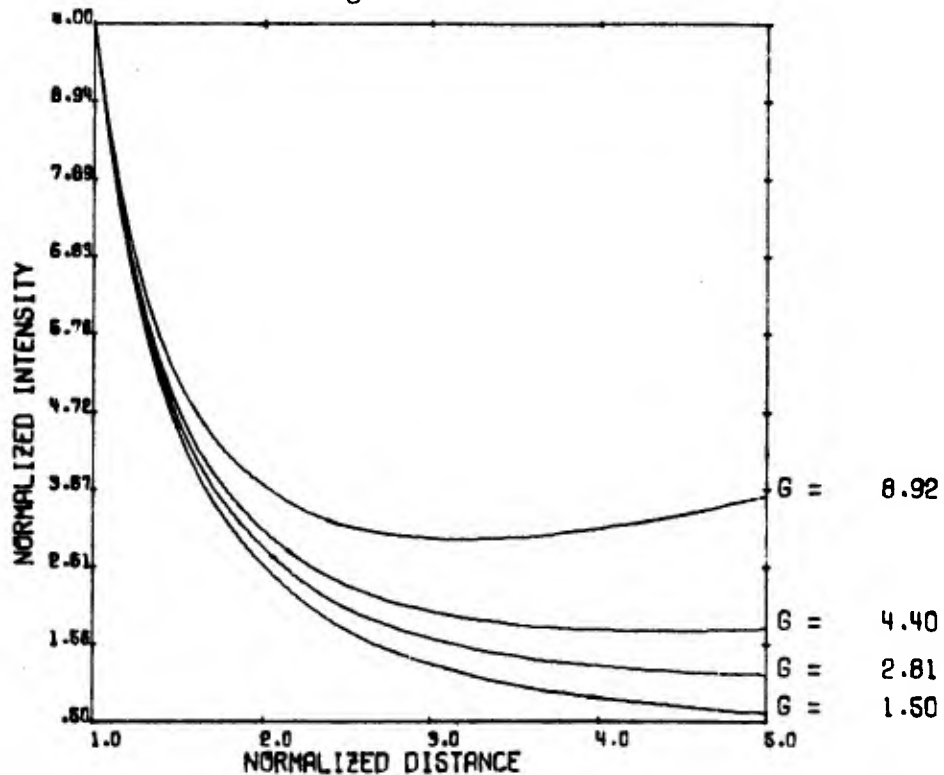


Figure 14.  $I/I_0$  versus  $r/f$  with an initial condition of  $I_1=10I_0$ . The telescope expansion ratio is  $m=5$ . From bottom to top, the curves are identified by the parameter values  $\alpha_0 l = 1, 3, 5,$  and  $10$ . The power gain for each curve is indicated by the  $G$  value at the right border.

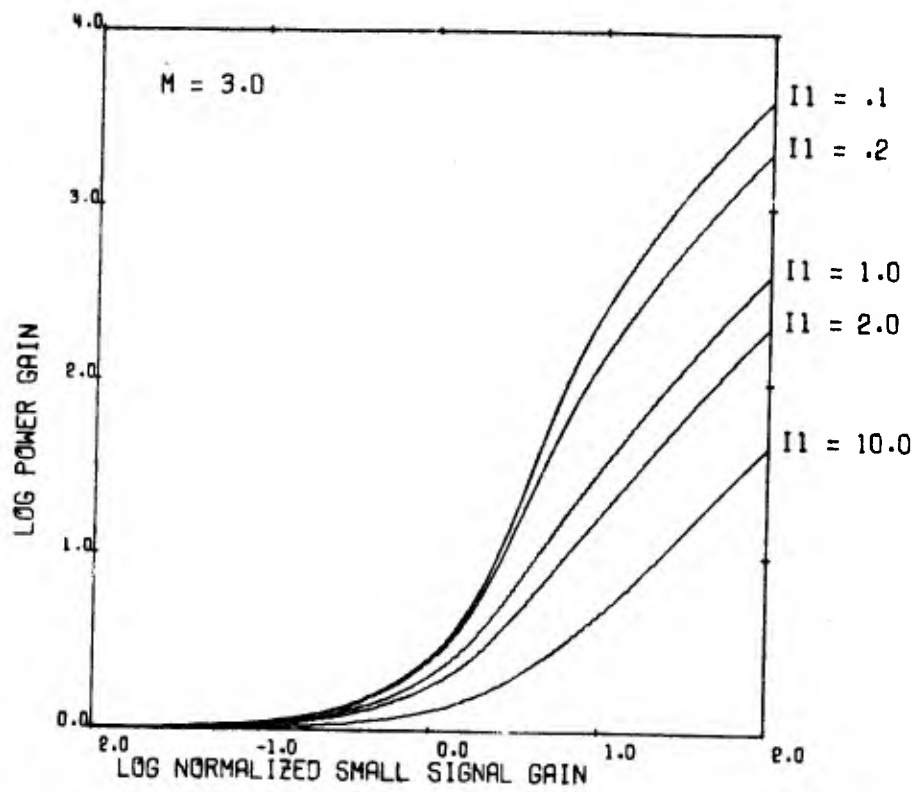


Figure 15.  $\log_{10} G_p$  versus  $\log_{10} \alpha_0 l$  for a telescope magnification of  $m=3$ . Each curve is identified by a different initial condition  $i_1$ , as indicated by the values at the right border.

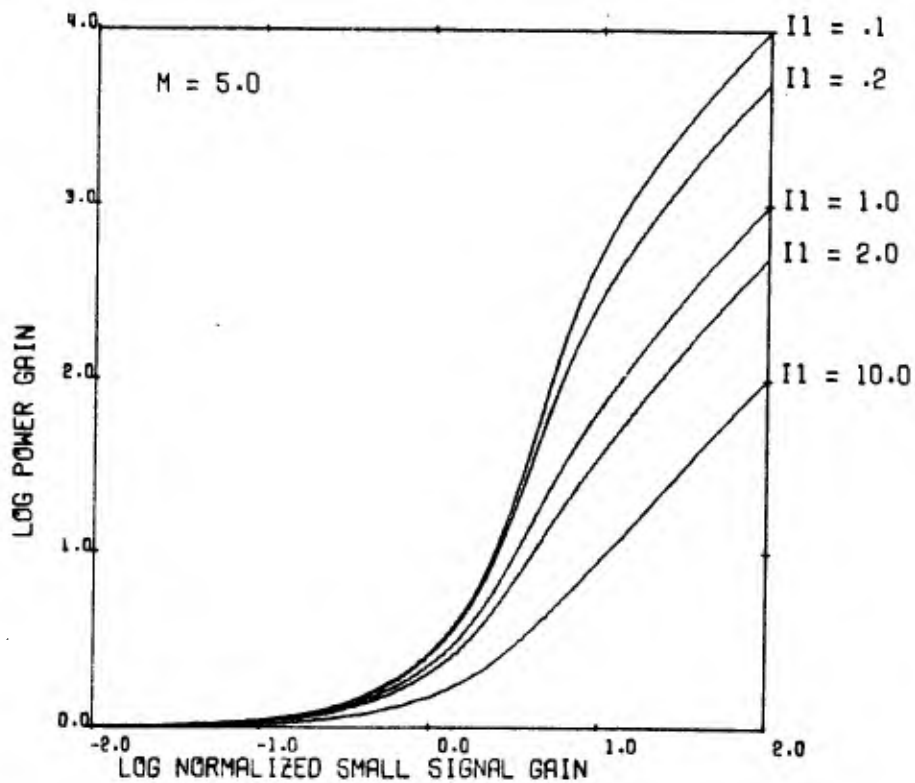


Figure 16.  $\log_{10} G_p$  versus  $\log_{10} \alpha_0 l$  for a telescope magnification of  $m=5$ . The initial condition  $i_1$  of the normalized irradiance is indicated for each curve by the column of numbers at the right border.

# GAUSSIAN BEAM PROPAGATION THROUGH A DIELECTRIC PLATE

D. A. Holmes

Using a geometrical approach, Pierre Laures<sup>1</sup> has investigated the propagation of a Gaussian beam through a refractive index discontinuity. In the present work, we consider a similar problem from the electromagnetic wave standpoint. The wave approach allows an analytical estimate of the complex amplitude factors of the reflected and transmitted beams, in addition to giving the location of the beam waists. More significantly, a wave approach can include the effects of internal reflections within a dielectric plate. Within the approximations used to obtain Gaussian beam solutions to the wave equation,<sup>2</sup> the transmittance of a Gaussian beam through a dielectric plate is identical to the plane-wave transmittance.

We now discuss the transmission of a coherent light beam, with a Gaussian intensity profile, through a dielectric plate, limiting ourselves to the case of normal incidence. Consider the beam to be travelling in medium 1 in the positive  $z$  direction with a transverse electric field:

$$u_1^+ = \left(w_{01}^+\right)^2 E_1^+ f_1^+(z) \exp \left[ -jk_1 z - f_1^+(z) r^2 \right] \quad (1a)$$

where

$$f_1^+(z) = +j(k_1/2) / \left[ z - z_1^+ + j(k_1/2) \left(w_{01}^+\right)^2 \right] \quad (1b)$$

$$k_1 = 2\pi n_1 / \lambda \quad (1c)$$

In the above equations\*,  $\lambda$  is the vacuum wavelength,  $n_1$  is the refractive index in medium 1,  $w_{01}^+$  is the "beam radius" when the phase front is plane and  $E_1^+$  is simply a constant amplitude parameter. The beam waist is located in the plane  $z = z_1^+$ . The transverse electric field  $u_1^+$  is perpendicular to the  $z$  axis.

---

\*Much of the notation in this paper is the same as that used in reference 2.



The dielectric plate, medium 2, is defined by the plane boundaries  $z=z_p$  and  $z=z_p+d$ , where  $d$  is the thickness of the plate. The refractive index of the plate is  $n_2$ . Medium 3 occupies the region  $z>z_p+d$  and is characterized by refractive index  $n_3$ . In this work, we obtain an analytical expression for the Gaussian beam propagating in medium 3 due to the beam incident in medium 1. We shall also find an expression describing the reflected beam in medium 1.

By changing the subscript 1 in equation (1) to a subscript 3, e.g.,  $u_1^+ \rightarrow u_3^+$ , then we have an expression for the transmitted electric field in medium 3. The electric field of the reflected beam in medium 1 is written as

$$u_1^- = \left(w_{01}^-\right)^2 E_1^- f_1^-(z) \exp \left[ +jk_1 z - f_1^-(z)r^2 \right] \quad (2a)$$

$$f_1^-(z) = -j(k_1/2) / \left[ z-z_1^- - j(k_1/2) \left(w_{01}^-\right)^2 \right] \quad (2b)$$

We describe the wave field within the plate as a superposition of a positively travelling beam and a negatively travelling beam. The electric field,  $u_2^+$ , of the positively travelling beam is written similarly to equation (1) while the electric field,  $u_2^-$ , of the negatively travelling beam is written similarly to equation (2).

The parameters of the reflected and transmitted beams are found by requiring the total tangential electric and magnetic fields to be continuous across the plane interfaces. Continuity of the electric field leads to

$$f_1^+(z_p) = f_1^-(z_p) = f_2^+(z_p) = f_2^-(z_p) \quad (3a)$$

$$f_2^+(z_p+d) = f_2^-(z_p+d) = f_3^+(z_p+d) \quad (3b)$$

From equation (3) we obtain

$$w_{01}^+ = w_{01}^- = w_{02}^+ = w_{02}^- = w_{03}^+ \quad (4)$$

$$z_1^- = 2z_p - z_1^+ \quad (5a)$$

$$z_2^+ = \left( 1 - \frac{n_2}{n_1} \right) z_p + \frac{n_2}{n_1} z_1^+ \quad (5b)$$

$$z_2^- = \left(1 + \frac{n_2}{n_1}\right) z_p - \frac{n_2}{n_1} z_1^+ \quad (5c)$$

$$z_3^+ = \left(1 - \frac{n_3}{n_2}\right) d + \left(1 - \frac{n_3}{n_1}\right) z_p + \frac{n_3}{n_1} z_1^+ \quad (5d)$$

Continuity of the electric fields also requires that

$$E_1^+ e^{-jk_1 z_p} + E_1^- e^{+jk_1 z_p} = E_2^+ e^{-jk_2 z_p} + E_2^- e^{+jk_2 z_p} \quad (6a)$$

$$E_2^+ e^{-jk_2(z_p+d)} + E_2^- e^{-jk_2(z_p+d)} = E_3^+ e^{-jk_3(z_p+d)} \quad (6b)$$

In order to obtain equation (6) we have used equations (3) and (4).

In the Gaussian beam approximation, we assume that the transverse magnetic fields are proportional to the electric fields, so that continuity of the total tangential magnetic fields across the dielectric interfaces leads to

$$-jk_1 E_1^+ e^{-jk_1 z_p} + jk_1 E_1^- e^{+jk_1 z_p} = -jk_2 E_2^+ e^{-jk_2 z_p} + jk_2 E_2^- e^{+jk_2 z_p} \quad (7a)$$

$$-jk_2 E_2^+ e^{-jk_2(z_p+d)} + jk_2 E_2^- e^{+jk_2(z_p+d)} = -jk_3 E_3^+ e^{-jk_3(z_p+d)} \quad (7b)$$

Equations (6) and (7) are analogous to equations which describe plane wave propagation. The solutions for  $E_3^+$  and  $E_1^-$  can be written as

$$\frac{E_3^+}{E_1^+} = \frac{\exp[j(k_3 - k_1)z_p + jk_3 d]}{\left[\frac{n_1 + n_3}{2n_1}\right] \cos(k_2 d) + j \left[\frac{n_1 n_3 + n_2^2}{2n_1 n_2}\right] \sin(k_2 d)} \quad (8)$$

$$\frac{E_1^-}{E_1^+} = e^{-j2k_1 z_p} \left\{ \frac{n_2(n_1 - n_3) + j(n_1 n_3 - n_2^2) \tan(k_2 d)}{n_2(n_1 + n_3) + j(n_1 n_3 + n_2^2) \tan(k_2 d)} \right\} \quad (9)$$

The electric fields of the transmitted and reflected beams are now completely determined in terms of the incident beam parameters for the geometry under consideration. We have used the approximation that the transverse electric and magnetic fields are perpendicular to the z-axis. In finding the transverse magnetic fields from the Maxwell equations, we invoked approximations of the following type,

$$\left. \begin{aligned} \frac{\partial u_i^+}{\partial z} &\approx -jk_i u_i^+ \\ \frac{\partial u_i^-}{\partial z} &\approx +jk_i u_i^- \end{aligned} \right\} i = 1, 2, 3 \quad (10)$$

which are valid within the Gaussian beam approximation<sup>2</sup>. These approximations led to the relationships (6), (7), (8), and (9), which are identical to the complex-amplitude relationships describing plane-wave propagation.

#### REFERENCES

1. Laures, P., "Geometrical Approach to Gaussian Beam Propagation," Appl. Opt., 6, p. 747, 1967.
2. Kogelnik, H., and Li, T., "Laser Beams and Resonators," Appl. Opt., 5, p. 1550, 1966.

REFLECTANCE CALCULATIONS FOR LOSSLESS  
MULTILAYER DIELECTRIC STACKS

J. E. Korka, M. L. Bernabe, and D. A. Holmes

The theory of using alternating high- and low-index quarter-wave thin-film layers to obtain high-efficiency reflection coatings has been considered by Heavens<sup>1</sup>. It is the purpose of this paper to present a quick method to determine how many layers of low absorption film materials will be needed on a given substrate to obtain a highly reflective surface. We shall define  $R$  as the intensity reflectivity,  $n_s$  as the real substrate index of refraction,  $n_0$  as the real refractive index of the incident media,  $n_1$  as the next layer and so forth to  $n_\ell$ , the real index of the medium next to the substrate, and  $\ell$  the total number of layers in the system.

A formula for the maximum reflectance of a non-absorbing quarter wave stack has been derived<sup>2</sup> and is given by

$$R = [(1-P)/(1+P)]^2 \quad (1)$$

where  $P$  for a system with an even number of layers is

$$P_{\text{even}} = \left[ \frac{n_\ell}{n_{\ell-1}} \frac{n_{\ell-2}}{n_{\ell-3}} \dots \frac{n_2}{n_1} \right]^2 \frac{n_0}{n_s} \quad (2)$$

and  $P$  for a system with an odd number of layers is

$$P_{\text{odd}} = \left[ \frac{n_\ell}{n_{\ell-1}} \frac{n_{\ell-2}}{n_{\ell-3}} \dots \frac{n_3}{n_2} n_1 \right]^2 \frac{1}{n_0 n_s} \quad (3)$$

The systems we are concerned with are alternating hi-lo layers of the same materials with the incident medium being air. We can then define the index ratio  $\alpha = n_\ell/n_{\ell-1}$  and  $n_0 = 1.0$ . Substituting for these expressions we can reduce the expressions for  $P$  to

$$P_{\text{even}} = \alpha^\ell / n_s \quad (4)$$

$$P_{\text{odd}} = \alpha^{\ell-1} / (n_s / n_1^2) \quad (5)$$

The expression for R can then be reduced to two forms

$$R_{\text{even}} = \left[ \frac{(n_s - \alpha^\ell)}{(n_s + \alpha^\ell)} \right]^2 \quad (6)$$

$$R_{\text{odd}} = \left[ \frac{\left( \left( n_s / n_1^2 \right) - \alpha^{\ell-1} \right)}{\left( \left( n_s / n_1^2 \right) + \alpha^{\ell-1} \right)} \right]^2 \quad (7)$$

These expressions can also be used for the absorbing substrates. All one needs to do is use the complex refractive index for the substrate and the absolute square instead of the simple square in equations (6) and (7). We can further reduce equation (7) if we define a reduced substrate index

$$n'_s = n_s / n_1^2$$

and the even quantity  $\ell' = \ell - 1$  and obtain

$$R_{\text{odd}} = \left[ \frac{(n'_s - \alpha^{\ell'})}{(n'_s + \alpha^{\ell'})} \right]^2 \quad (8)$$

By comparing equations (6) and (8) we see that we need data for even-layer systems only since all odd-layer systems can be reduced to equivalent even-layer systems.

Figures 1 through 10 are for such even-layer systems and may be used as an aid to determine how many layers one must coat to obtain a given reflectance greater than 95 percent. However, one must remember that this treatment neglects absorption in the layers and thus can be used only in cases where the films are only slightly absorbing.

#### REFERENCES

1. Heavens, O. S., "Optical Properties of Thin Solid Films," Butterworth Scientific Publications, London, PP. 215-221, 1955.
2. Military Standard, Optical Design (MIL-HDBK-141), 5 October 1962.

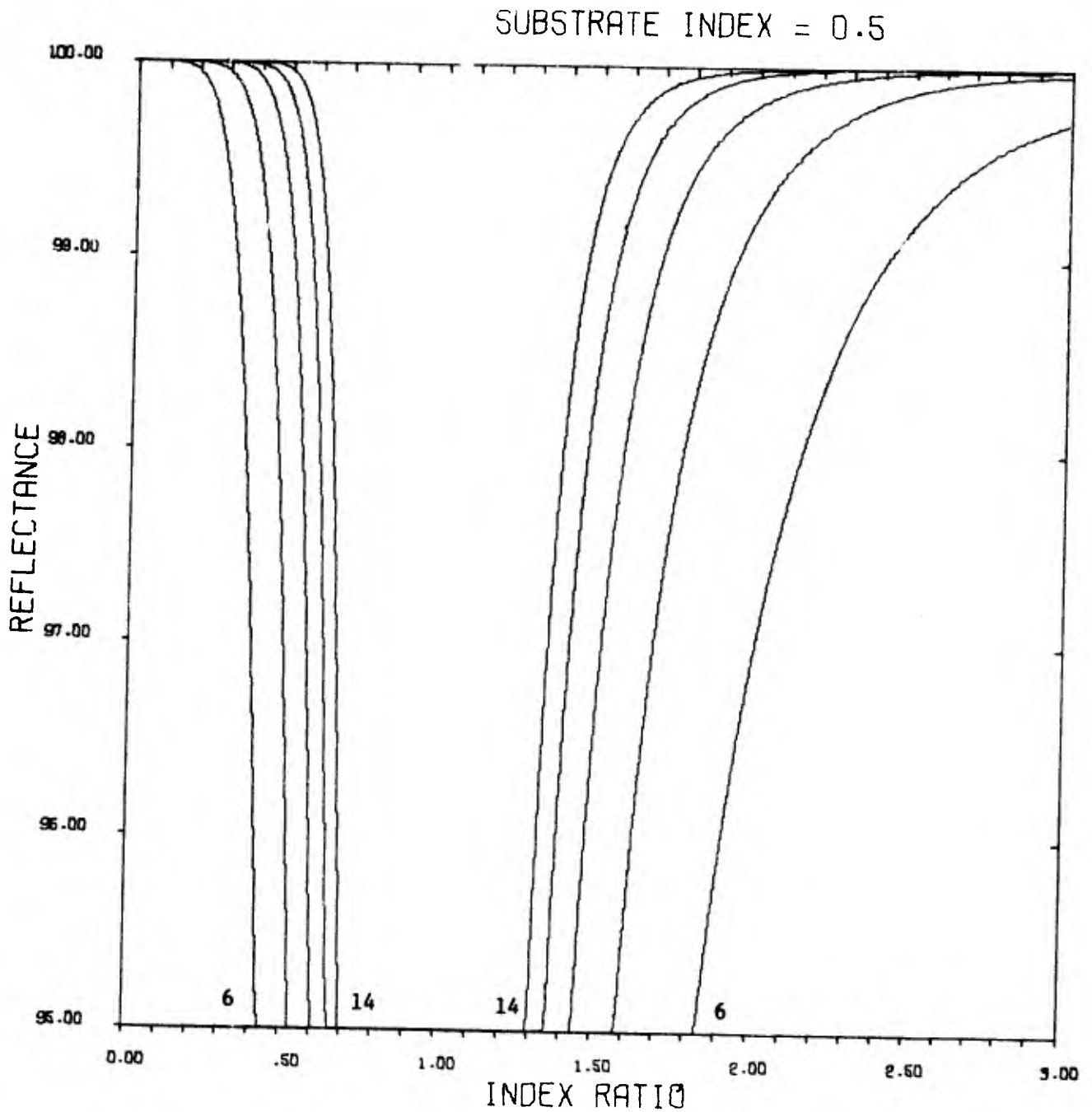


Figure 1.  $R$  versus  $\alpha$  for a substrate with a real index of refraction of 0.5. The curves shown are for multilayer stacks of 6, 8, 10, 12, and 14 layers. The curves for the 14-layer stack are centermost while the outermost curves are for 6 layers.

SUBSTRATE INDEX = 1.5

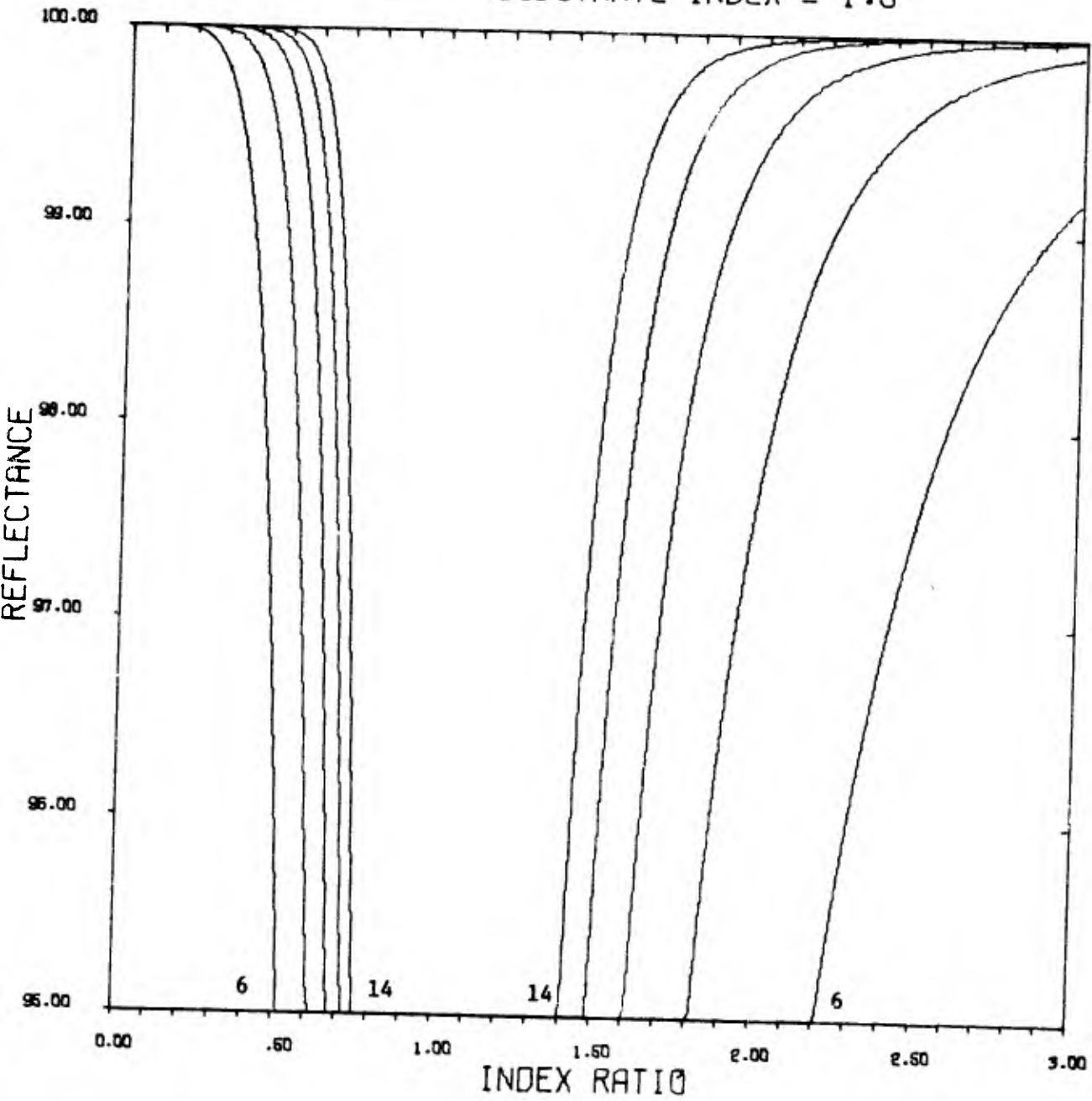


Figure 2. R versus  $\alpha$  for a substrate with a real index of refraction of 1.5. The curves shown are for multilayer stacks of 6, 8, 10, 12, and 14 layers. The curves for the 14-layer stack are centermost while the outermost curves are for 6 layers.

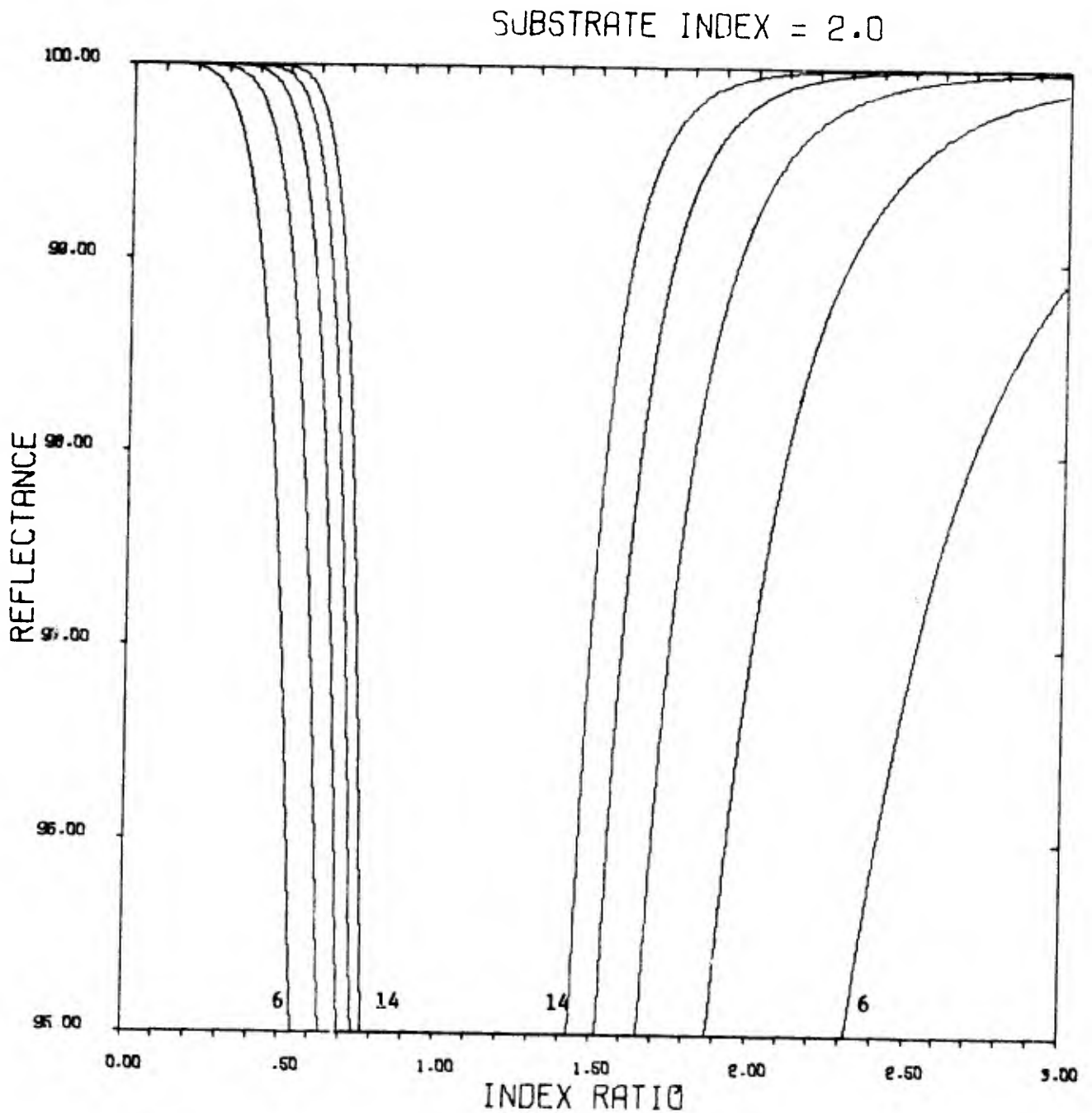


Figure 3.  $R$  versus  $\alpha$  for a substrate with a real index of refraction of 2.0. The curves shown are for multilayer stacks of 6, 8, 10, 12, and 14 layers. The curves for the 14-layer stack are centermost while the outermost curves are 6 layers.



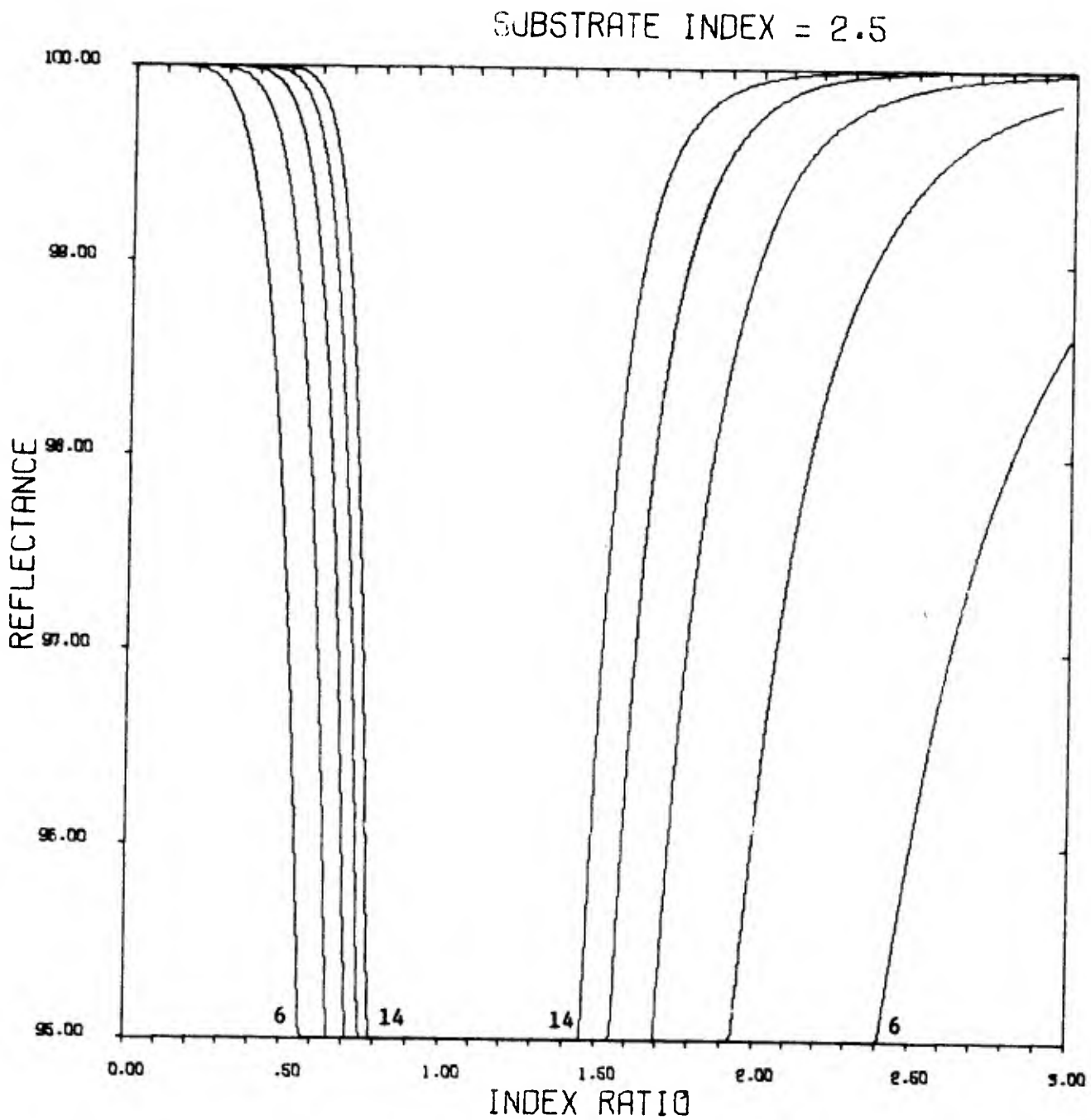


Figure 4.  $R$  versus  $\alpha$  for a substrate with a real index of refraction of 2.5. The curves shown are for multilayer stacks of 6, 8, 10, 12, and 14 layers. The curves for the 14-layer stack are centermost while the outermost curves are for 6 layers.

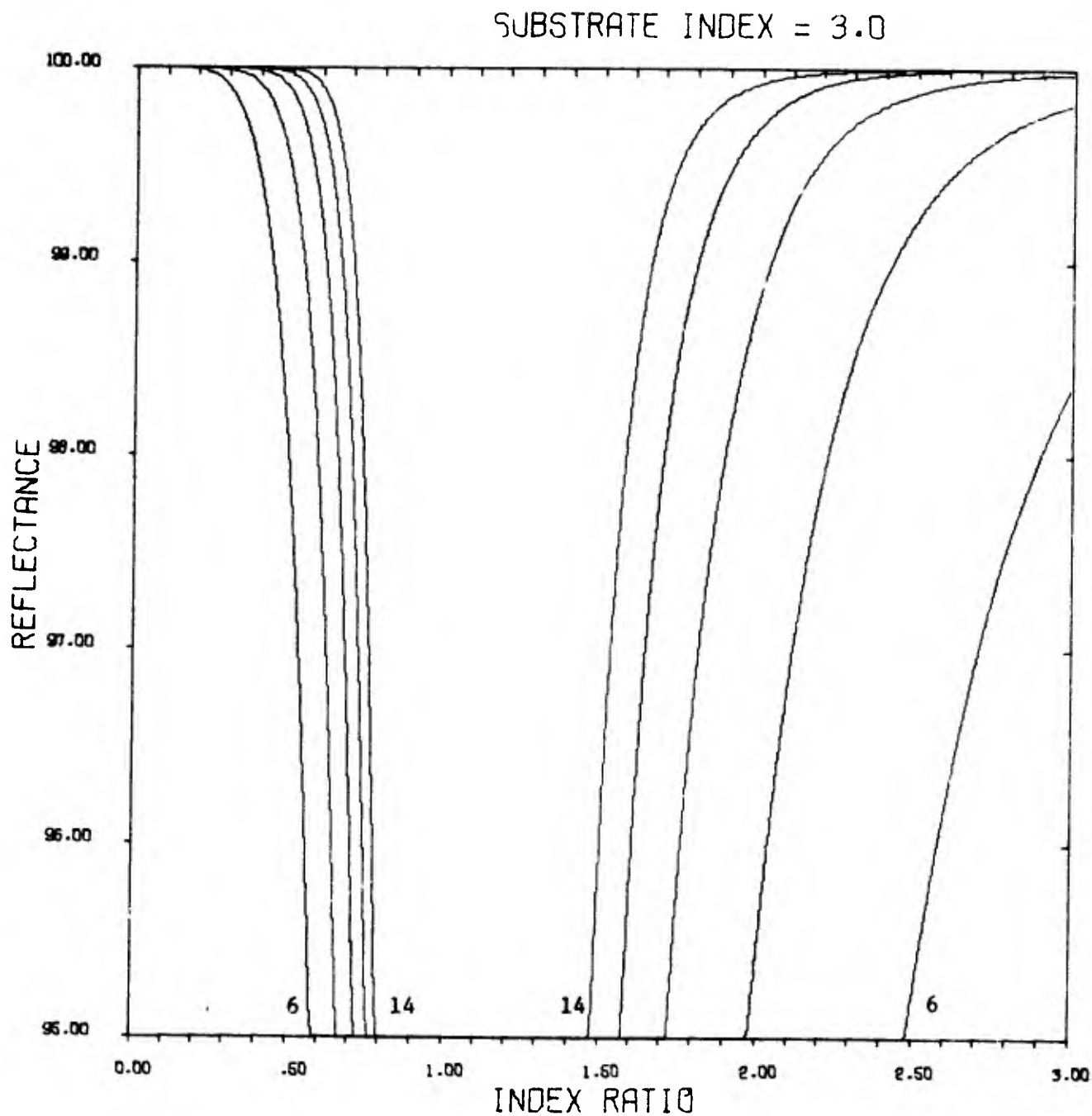


Figure 5.  $R$  versus  $\alpha$  for a substrate with a real index of refraction of 3.0. The curves shown are for multilayer stacks of 6, 8, 10, 12, and 14 layers. The curves for the 14-layer stack are centermost while the outermost curves are for 6 layers.

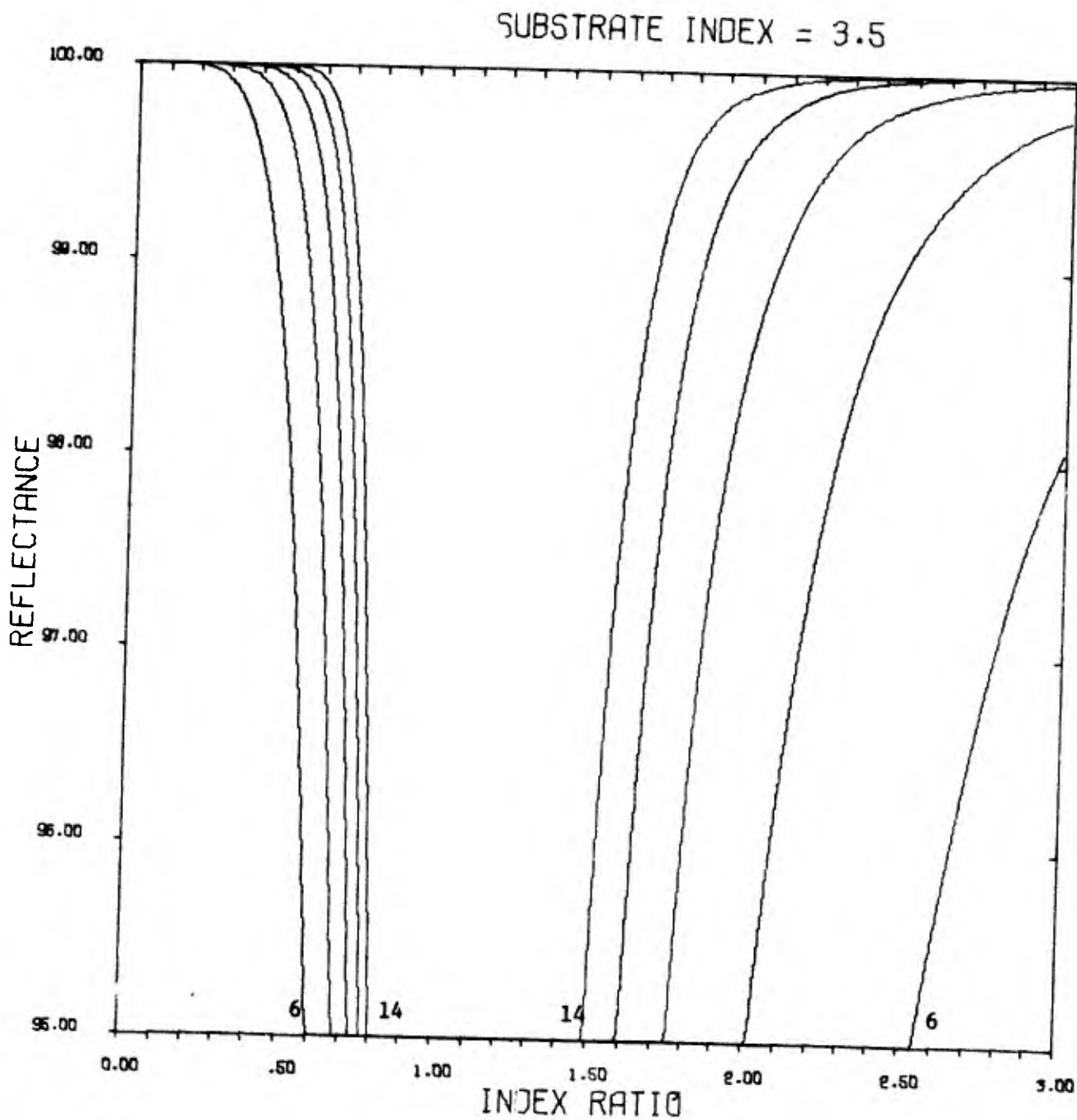


Figure 6. R versus  $\alpha$  for a substrate with a real index of refraction of 3.5. The curves shown are for multilayer stacks of 6, 8, 10, 14, and 14 layers. The curves for the 14-layer stack are centermost while the outermost curves are for 6 layers.

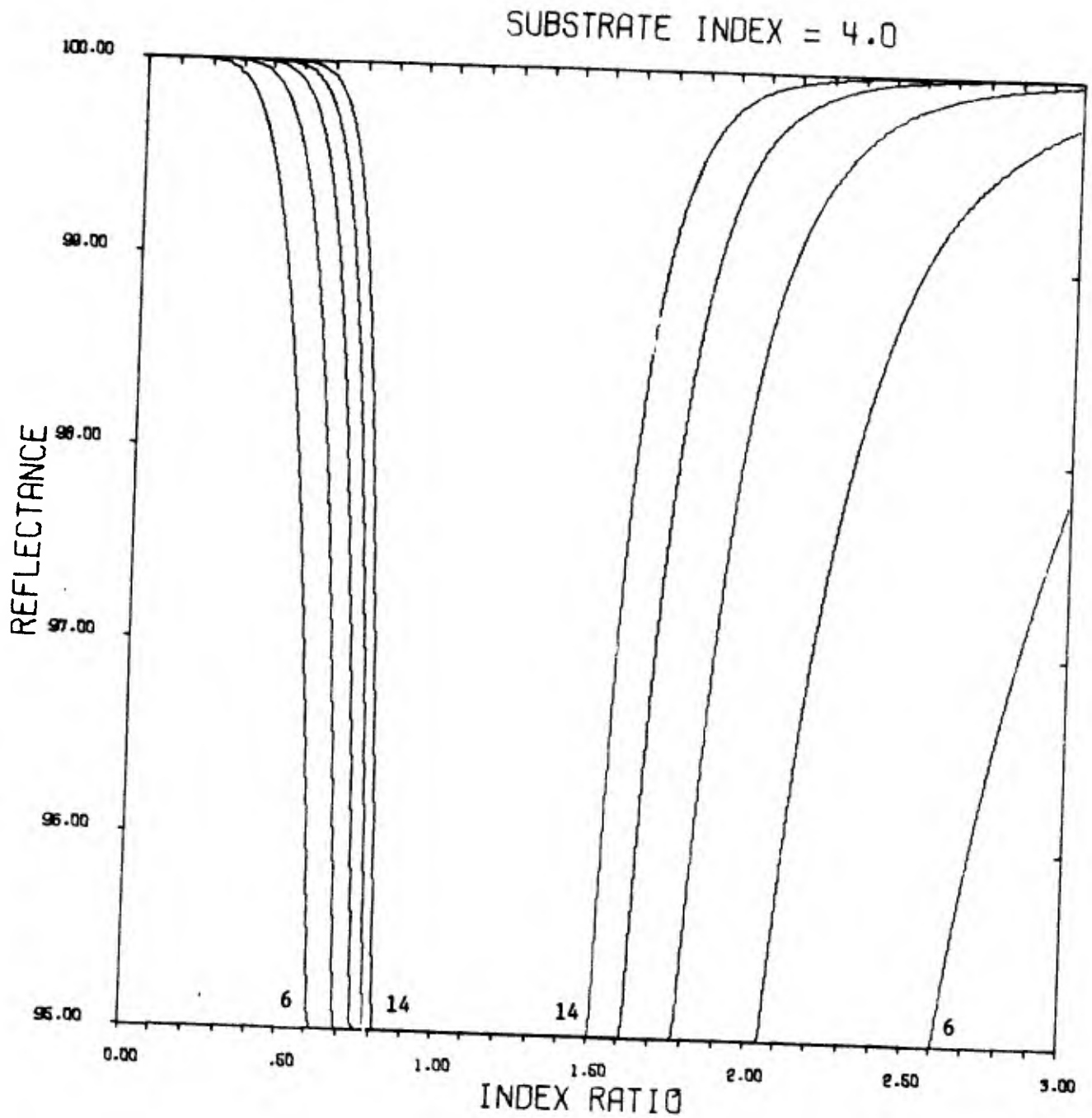


Figure 7.  $R$  versus  $\alpha$  for a substrate with a real index of refraction of 4.0. The curves shown are for multilayer stacks of 6, 8, 10, 12, and 14 layers. The curves for the 14-layer stack are centermost while the outermost curves are 6 layers.

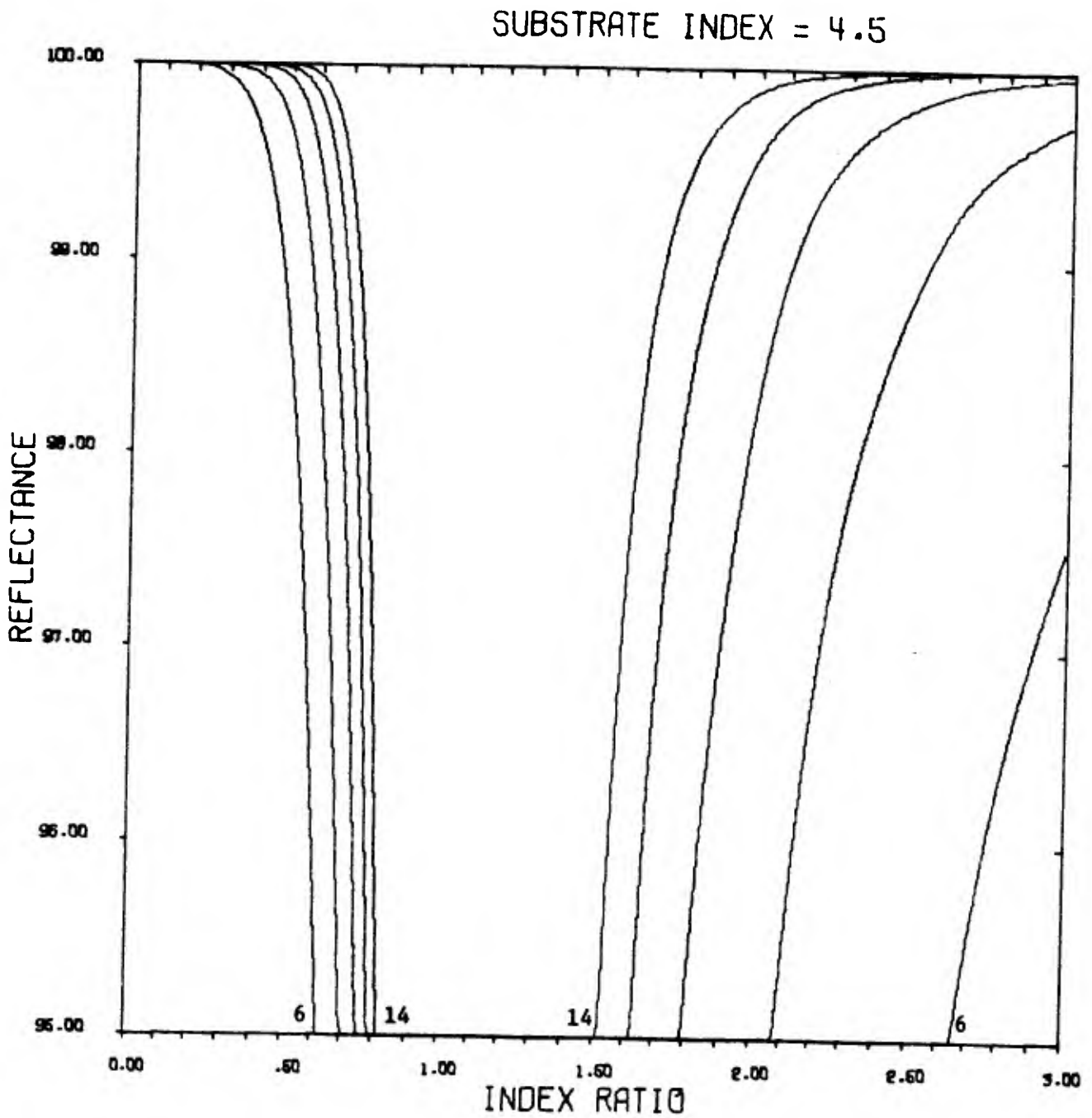


Figure 8.  $R$  versus  $\alpha$  for a substrate with a real index of refraction of 4.5. The curves shown are for multilayer stacks of 6, 8, 10, 12, and 14 layers. The curves for the 14-layer stack are centermost while the outermost curves are for 6 layers.

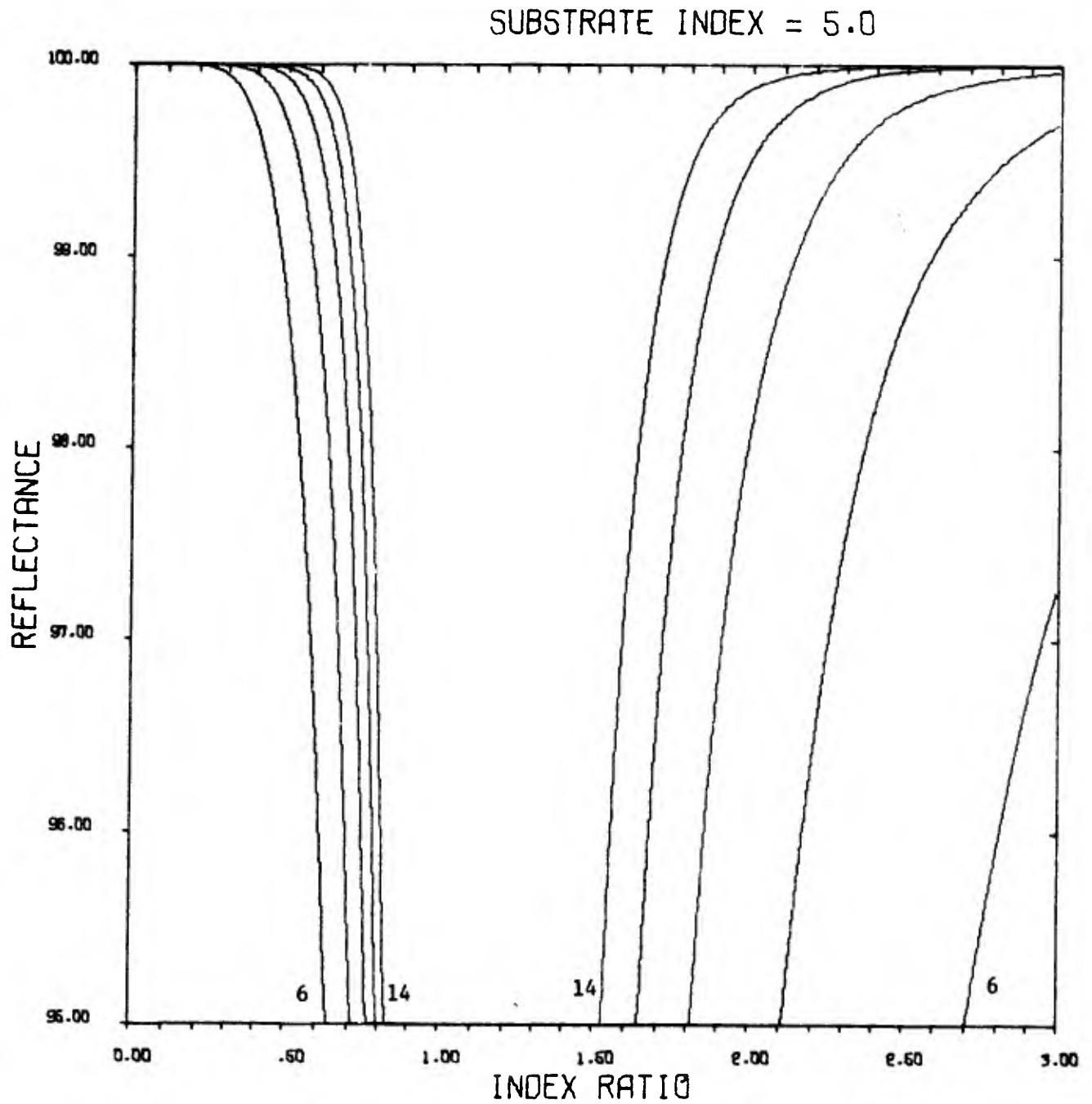


Figure 9.  $R$  versus  $\alpha$  for a substrate with a real index of refraction of 5.0. The curves shown are for multilayer stacks of 6, 8, 10, 12, and 14 layers. The curves for the 14-layer stack are centermost while the outermost curves are for 6 layers.

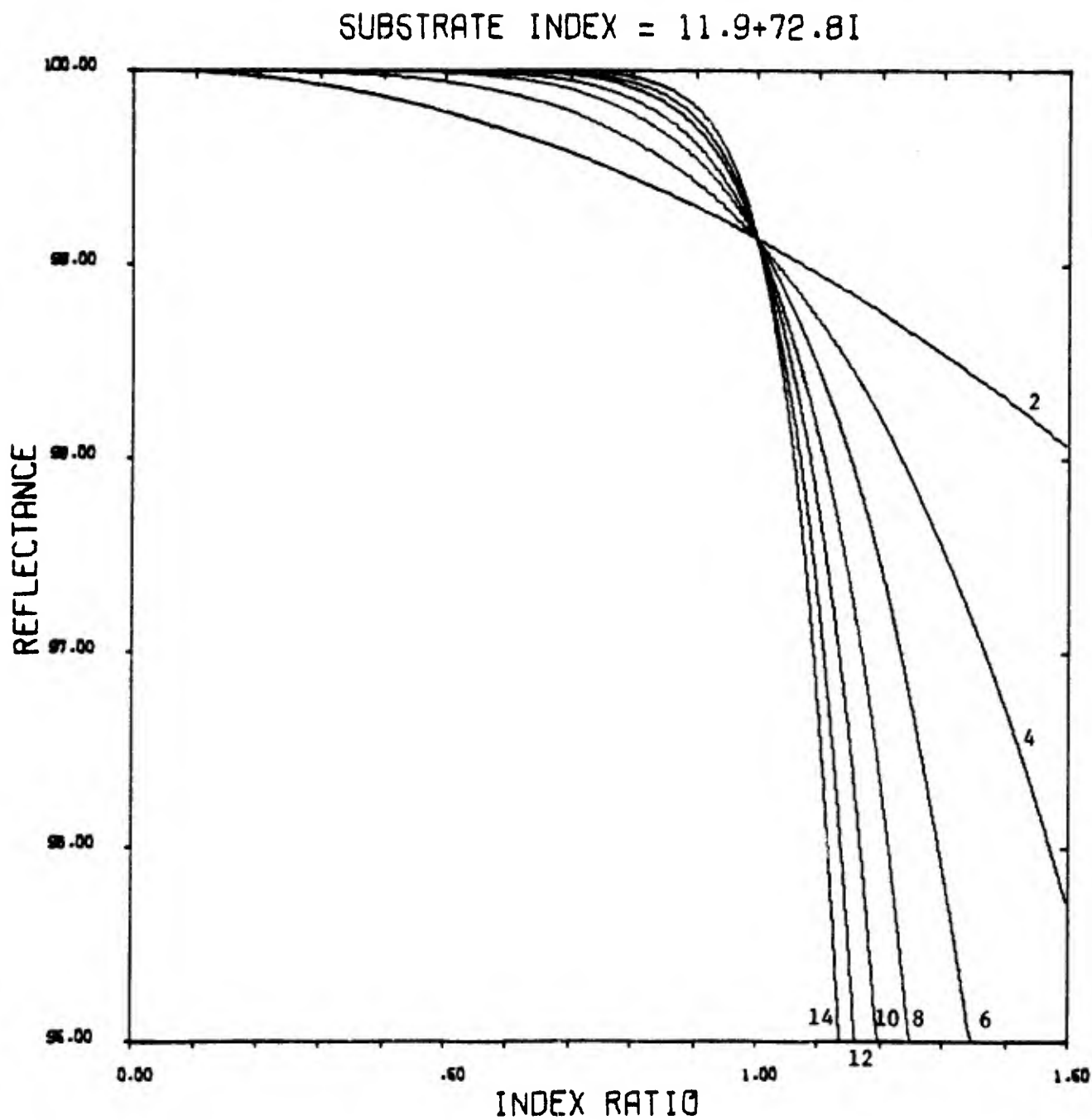


Figure 10.  $R$  versus  $\alpha$  for a silver substrate with complex index of refraction  $11.9 + 72.8i$ . The curves shown are for 2, 4, 6, 8, 10, 12, and 14 layers.

# TRANSMISSION THROUGH LASER WINDOWS FOR COHERENT AND INCOHERENT RADIATION

John Loomis

## Introduction

The linear attenuation of radiation passing through a material window follows Beer's law:

$$P_x = P_o e^{-\beta x} \quad (1)$$

where  $P_x$  is the radiation power at distance  $x$  into the window,  $P_o$  is the power at  $x = 0$  and  $\beta$  is the absorption coefficient of the material. In addition to attenuation, radiation impinging on a window will undergo multiple reflections off the front and back surfaces of the window. For off-normal angles of incidence, small beam diameters and thick windows, these multiple reflections may be spatially distinct. For incoherent radiation the degree of spatial coincidence of multiple reflections does not affect the proportionality between reflected, transmitted, and absorbed radiation. However, when coherent radiation undergoes multiple reflections which are spatially coincident, interference effects modify these relationships.

Although the exhibition of interference effects in a plane, parallel transparent plate is a standard subject in most optics texts,<sup>1</sup> it is important to develop a consistent notation and set of equations appropriate for the study of windows as components in a laser system. The relevant experimental quantities are the amounts of reflected, transmitted and absorbed power as a function of the incident power and material properties. The remainder of this paper will be devoted to calculating these quantities for coherent and incoherent radiation normally incident on a plane, parallel plate of window material. The analysis is based on that given by R. Weil<sup>2</sup> in calculating absorption coefficients when interference effects are present.



Calculations

Consider the situation depicted in Figure 1. A laser beam of constant intensity  $P_0$  is directed normally onto a plane, parallel window of thickness  $l$ , absorption coefficient  $\beta$ , and index of refraction  $n$ . Of this incident power, an amount,  $P_F$ , is reflected backwards, a portion  $P_T$  is transmitted, and the remainder  $P_A$  is absorbed. Multiple reflections occur at faces A and B of the window because the absorption is assumed to be small and the window to be thin. In the steady state situation, a standing wave will develop in the window with components traveling in both directions.

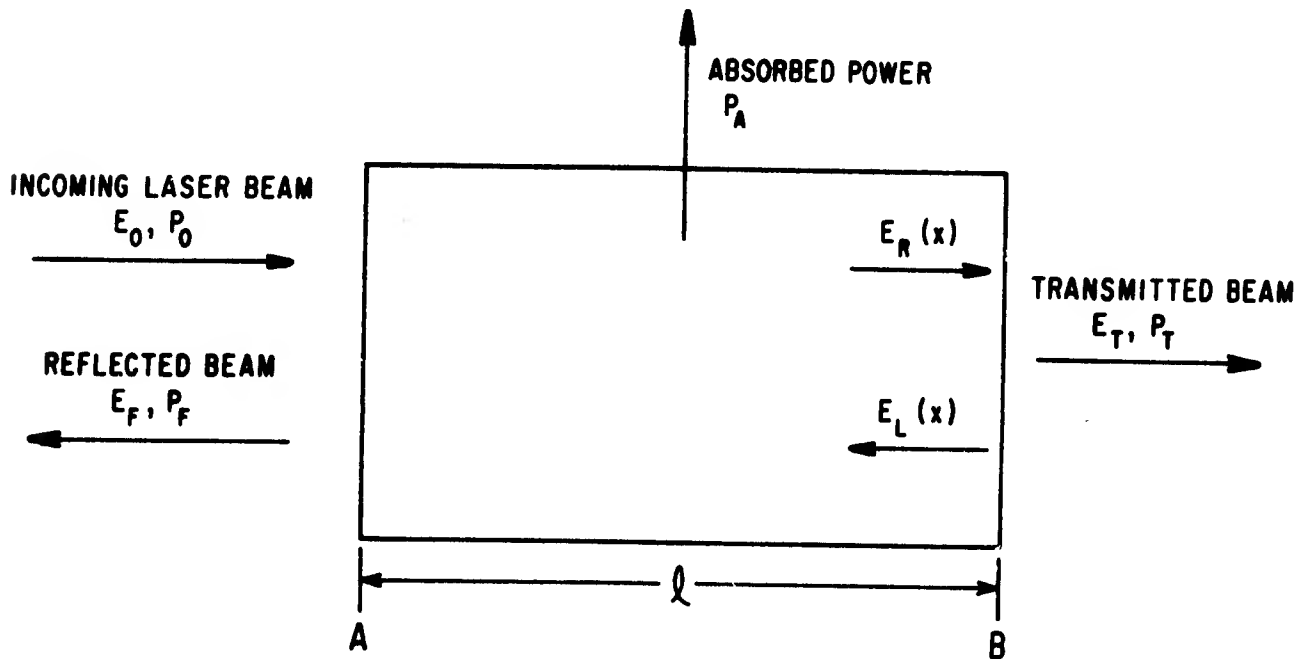


Figure 1. Distribution of wave trains for laser beam propagating through a material window.

The amplitude reflection and transmission coefficients  $r_{qv}$  and  $t_{qv}$  will depend on the boundary ( $q = A$  or  $B$ ) and on the direction of incident light ( $v = \text{Left or Right}$ ) at that boundary. Let  $\gamma = \beta/2 + \kappa$  where

$$\kappa = \frac{2\pi n}{\lambda_0}$$

inside the material,

$$\kappa = \frac{2\pi}{\lambda_0}$$

in air, and  $\lambda_0$  is the radiation wavelength in air. Let  $E_x$  denote the amplitude of the electric field at  $x$ . The power in a given direction at a given location (boundary B for example) may be obtained for coherent radiation by summing the amplitudes of the component multiple reflections and then squaring. For incoherent radiation, the power is given by summing the squares of the amplitude of the component multiple reflections. Table I shows the component amplitudes at boundary B. The amplitude from the  $(2m + 1)$ th pass through the window goes as

$$a_m = r_{BR}^m r_{AL}^m \exp[-2m\gamma\ell] \quad (2)$$

The net power is then proportional to

$$S_{\text{coh}} = \left( \sum_{m=0}^{\infty} a_m \right)^2$$

for coherent radiation and

$$S_{\text{incoh}} = \sum_{m=0}^{\infty} a_m^2 \quad (3)$$

for incoherent radiation. The sum is a geometric series which equals

$$S_{\text{coh}} = \frac{1}{1-a_1}^2 \quad (4)$$

and

$$S_{\text{incoh}} = \frac{1}{1-a_1^2} \quad (5)$$

respectively. The powers at boundary B are

$$P_R = nE_R^2 = nE_0^2 t_{AR}^2 \exp(-\beta\ell)S \quad (6)$$

Table I  
ANALYSIS OF MULTIPLE REFLECTIONS OF LASER BEAM WITH INITIAL AMPLITUDE E  
(Taken from Reference 2)

No. Passes Through Sample	Component of $E_R$ at Boundary B	Component of $E_L$ at Boundary B	Component Transmitted by $E_T$
1	$E_0^t r_{AR}^m \exp(-\gamma\ell)$	$E_0^t r_{BR}^m \exp(-\gamma\ell)$	$E_0^t r_{BR}^m \exp(-\gamma\ell)$
3	$E_0^t r_{BR}^m r_{AR}^m \exp(-3\gamma\ell)$	$E_0^t r_{BR}^m r_{AL}^m \exp(-3\gamma\ell)$	$E_0^t r_{BR}^m r_{AL}^m \exp(-3\gamma\ell)$
5	$E_0^t r_{BR}^m r_{AL}^m \exp(-5\gamma\ell)$	$e_0^t r_{BR}^m r_{AL}^m \exp(-5\gamma\ell)$	$E_0^t r_{BR}^m r_{AL}^m \exp(-5\gamma\ell)$
$2m+1$	$E_0^t r_{BR}^m r_{AL}^m \exp(-(2m+1)\gamma\ell)$	$E_0^t r_{BR}^{m+1} r_{AL}^m \exp(-(2m+1)\gamma\ell)$	$E_0^t r_{BR}^m r_{AL}^m \exp(-(2m+1)\gamma\ell)$

$$P_L = nE_L^2 = nE_O^2 t_{AR}^2 r_{BR}^2 \exp(-\beta l) S \quad (7)$$

$$P_T = E_T^2 = E_O^2 t_{AR}^2 t_{BR}^2 \exp(-\beta l) S \quad (8)$$

where S is

$$S_{\text{coh}} = \frac{1}{1 - 2r_{BR}r_{AL} \exp(-\beta l) \cos(2\kappa l) + r_{BR}^2 r_{AL}^2 \exp(-2\beta l)} \quad (9)$$

or

$$S_{\text{incoh}} = \frac{1}{1 - r_{BR}^2 r_{AL}^2 \exp(-2\beta l)} \quad (10)$$

as appropriate. The power absorbed in the sample from the right travelling wave is

$$P_{AR} = P_R \exp(\beta l) - P_R \quad (11)$$

and from the left travelling wave,

$$P_{AL} = P_L - P_L \exp(-\beta l) \quad (12)$$

for a total absorbed power of

$$P_A = nE_O^2 S t_{AR}^2 [1 - \exp(-\beta l)] [1 + r_{BR}^2 \exp(-\beta l)] \quad (13)$$

For incoherent radiation, the power reflected from the window is

$$P_F = r_{AR}^2 P_O + t_{AL}^2 P_L \exp(-\beta l) \quad (14)$$

For coherent radiation, the power reflected is obtained from

$$P_F = E_F^2 \quad (15)$$

where

$$E_F = r_{AR} E_O + t_{AL} E_L \exp(-\gamma l) \quad (16)$$

The amplitude coefficients  $t$  and  $r$  may be replaced by reflectivity and transmittivity coefficients  $T$  and  $R$  where, as shown on pages 41 and 42 of reference 1,

$$T + R = 1 \quad (17)$$

$$nt_{AR}^2 = nt_{BL}^2 = \frac{1}{n} t_{BR}^2 = \frac{1}{n} t_{AL}^2 = T \quad (18)$$

$$r^2 = R \quad (19)$$

$$r_{AR} = r_{BL} = -r_{BR} = -r_{AL} = \frac{n-1}{n+1} \quad (20)$$

Transmitted, absorbed, and reflected power may now be expressed as

$$P_T = T^2 P_O S \exp(-\beta l) \quad (21)$$

$$P_A = (1-R) P_O S [1 - \exp(-\beta l)] [1 + R \exp(-\beta l)] \quad (22)$$

and, for the coherent case:

$$P_F = R P_O + T P_O S_{coh} \exp(-\beta l) [R(R+1) \exp(-\beta l) - 2R \cos(2\kappa l)] \quad (23)$$

or, for the incoherent case:

$$P_F = R P_O + T^2 R P_O S_{incoh} \exp(-2\beta l) \quad (24)$$

where

$$S_{coh} = \frac{1}{1 - 2R \exp(-\beta l) \cos(2\kappa l) + R^2 \exp(-2\beta l)} \quad (25)$$

and

$$S_{incoh} = \frac{1}{1 - R^2 \exp(-2\beta l)} \quad (26)$$

### Discussion

The absorption of incoherent radiation can be expressed as

$$P_A = P_O [1 - \exp(-\beta l)] \frac{1-R}{1-R \exp(-\beta l)} \quad (27)$$

from equations (22) and (26). In the limit of low absorption coefficients, equation (27) can be rewritten as

$$\beta = \frac{P_A}{\ell P_O} \quad (28)$$

The absorption of both coherent and incoherent radiation can be obtained from combining equations (21) and (22) to eliminate S,

$$P_A = P_T [1 - \exp(-\beta \ell)] \frac{1+R}{T} \frac{\exp(-\beta \ell)}{\exp(-\beta \ell)} \quad (29)$$

Again in the limit of small absorption coefficients, equation (29) can be expressed as

$$\beta = \frac{P_A}{\ell P_T} \frac{1-R}{1+R} \quad (30)$$

As pointed out by Weil, equation (30) might also be written

$$\beta = \frac{P_A}{\ell P_T} \frac{t_{BR}^2}{n(1 + r_{BR}^2)} \quad (31)$$

In this form it is apparent that applying an anti-reflection coating to the back face, so that  $r_{BR} \rightarrow 0$  and

$$\frac{t_{BR}^2}{n} \rightarrow 1$$

reduces equation (31) to

$$\beta = \frac{P_A}{\ell P_T} \quad (32)$$

for both incoherent and coherent radiation.

The appropriate expression to use in calculating the absorption coefficient of an uncoated material for either coherent or incoherent radiation is

$$\beta = \frac{P_A}{\ell P_T} \frac{2n}{n^2+1} \quad (33)$$

where equations (19) and (20) have been used to replace R in equation (30) by the index of refraction.

Interference effects may be monitored by measuring either  $P_T$ ,  $P_A$ , or  $P_F$  since each depends on  $S_{coh}$ . In the limit of low absorption,

$$P_T = P_o \frac{(1-R)^2}{1-2R\cos(2\kappa\ell)+R^2} \quad (34)$$

$$P_F = P_o \frac{2R[1-\cos(2\kappa\ell)]}{1-2R\cos(2\kappa\ell)+R^2} \quad (35)$$

$$P_A = \beta\ell P_o \frac{(1-R)(1+R)}{1-2R\cos(2\kappa\ell)+R^2} \quad (36)$$

The important term is  $\cos(2\kappa\ell)$  where  $\kappa = \frac{2\pi n}{\lambda}$ . Variations in its argument can swing equation (34), for example, from

$$\text{max. } P_T = P_o$$

to

$$\text{min. } P_T = \left(\frac{1-R}{1+R}\right)^2 P_o$$

For CdTe,

$$R = \left(\frac{n-1}{n+1}\right)^2 = 0.21$$

and the transmitted power could be reduced by as much as 56 percent for a change of  $\pi$  in the argument of  $\cos(2\kappa\ell)$ . Assume that  $\lambda = 10$  microns and  $\ell = 5$ mm. The thickness and index of refraction will vary with temperature. For CdTe,

$$\eta = \frac{1}{n} \frac{dn}{dT} = 4 \times 10^{-5} \text{ } ^\circ\text{C}^{-1}$$

$$\alpha = \frac{1}{\ell} \frac{d\ell}{dT} = 6 \times 10^{-6} \text{ } ^\circ\text{C}^{-1}$$

$$n = 2.67$$

and the temperature change required to change the transmitted power from its maximum to its minimum value is

$$\Delta T = \frac{1}{4} \frac{\lambda}{n\ell} \frac{1}{\alpha + \eta} \quad (37)$$

$$\Delta T = 4.1^\circ\text{C}$$

Assume now that both faces of a CdTe window are coated with anti-reflection coating such that  $R = 0.01$  at  $\lambda = 10$  microns. Roughly speaking, for incoherent radiation 1 percent of the power will be reflected off each face of the window while 98 percent of the incident power is transmitted, assuming negligible absorption. Under the same conditions for coherent radiation, as the temperature of the window changes, the transmitted power will fluctuate between 96 percent and 100 percent  $P_0$  while the reflected power varies correspondingly from 4 percent to zero. If the output of a given laser system is sufficiently coherent, then, interference effects will be important in evaluating the performance of windows. Reflected power, in particular, may increase to as much as twice the reflected power of incoherent radiation.

### Conclusions

The transmission of laser radiation through windows depends on the degree of coherence of the laser beam. With coherent radiation, multiple reflections off the front and back faces of the window may interfere. These interference effects, when present, may be observed by measuring variations in transmitted power as a function of the temperature of the window. Since they are highly temperature dependent, interference effects may affect the performance of windows in high power laser systems.

The correct expression for the absorption coefficient  $\beta$  is

$$\beta = \frac{P_A}{\ell P_T} \frac{n}{n^2+1}$$

where  $P_A$  is the power absorbed by the window,  $P_T$  is the power transmitted by the window,  $\ell$  is the thickness of the window and  $n$  is the index of refraction. The dependence on  $n$  arises because of reflections off the back face of the sample. The expression is independent of the coherence of the radiation since interference changes in  $P_A$  are directly proportional to interference changes in  $P_T$ .

### REFERENCES

1. Born, M., and Wolf, E., Principles of Optics, 4th Ed., Pergamon Press, Oxford, 1970.
2. Weil, R., "Calculation of Small Optical Absorption Coefficients from Calorimetric Experimental Data," J. Appl. Phys., 41, pp. 3012-3014, 1970.



## POINTING AND TRACKING SIMULATION AND DESIGN

Robert J. Johnson

### Introduction

The pointing and tracking systems presented by Hughes Aircraft Company in the Field Test Telescope (FTT) and the General Electric Company in the Laser Beam Control System (LBCS) have created a need for evaluations which will determine whether or not these systems will meet the required Air Force Weapons Laboratory (AFWL) specifications. In meeting this need the AFWL has taken two courses of action. The first is an experimental testing of the FTT (the LBCS is not in hardware form) and the second is an analytical study of both the FTT and the LBCS. It is the latter course of action with which this report is concerned.

By taking an analytical approach, it is possible not only to duplicate control system response through simulation but also to predict the response in realistic tracking situations. In either case, if the systems are not performing adequately, an analytical approach provides some logic to determine the source of the inadequacy and an intelligent means by which to overcome it.

### Approach

Several steps are being followed in the analysis of the FTT and the LBCS. The first is to define the dynamical model. This model allows the systems to be simulated in the time domain by using the digital computer. These simulations in turn make it possible to interject realistic tracking problems into the control loops and thus afford a means of evaluating the system performance capabilities. Finally, if the performance is not acceptable, there are two digital computer programs available for optimizing system parameters toward improved performance.

Dynamical Model and Simulation. The control systems of both trackers have been depicted by block diagrams as shown in Figures 1 and 2 for the FTT and in Figure 3 for the LBCS. The diagrams of the FTT represent an accumulation and detailed expansion of several simplified block diagrams submitted by Hughes. The block diagram of the LBCS is rather simplified, but this is commensurate with the state of development of the system.

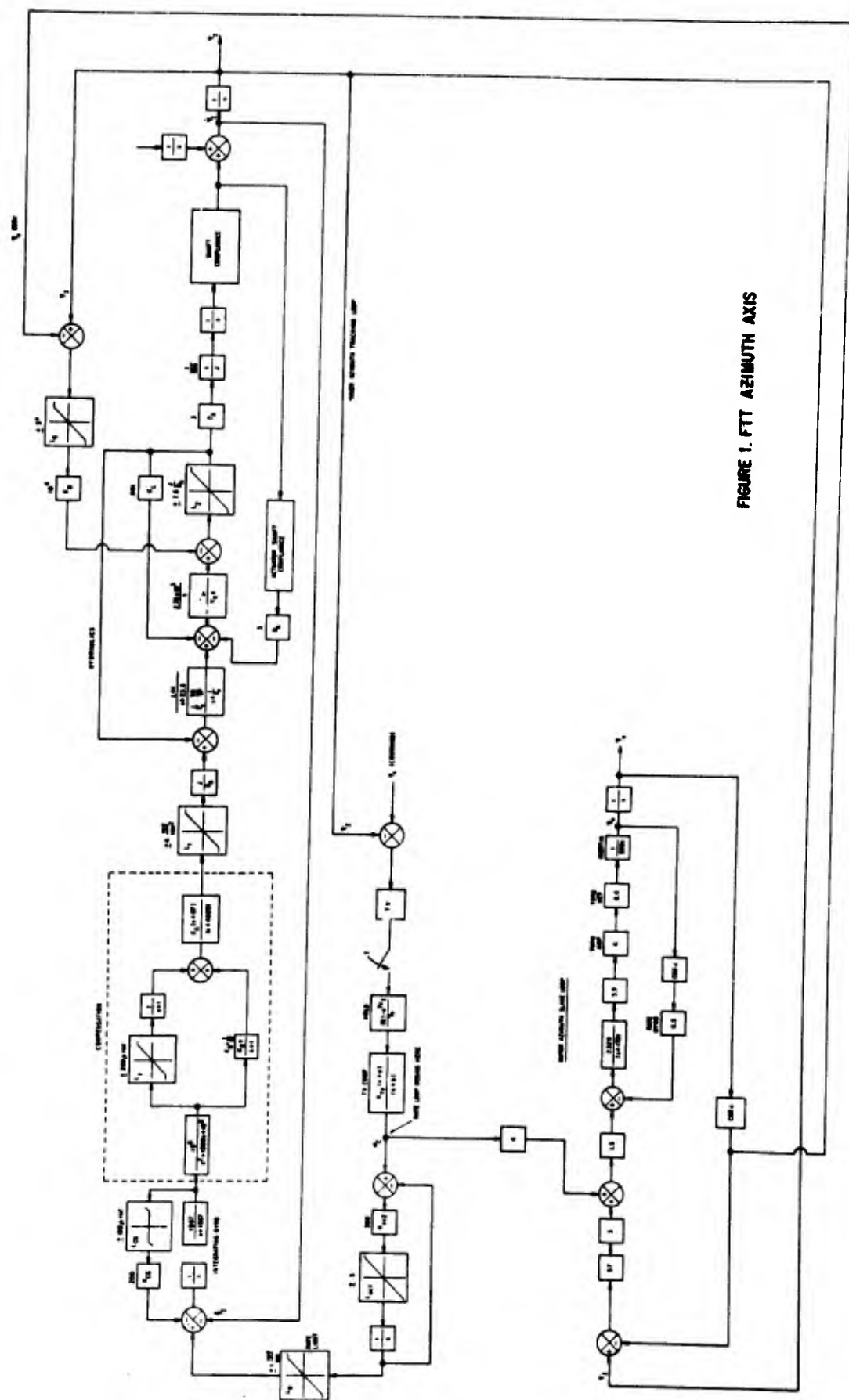


FIGURE 1. FTTH AZIMUTH AXIS



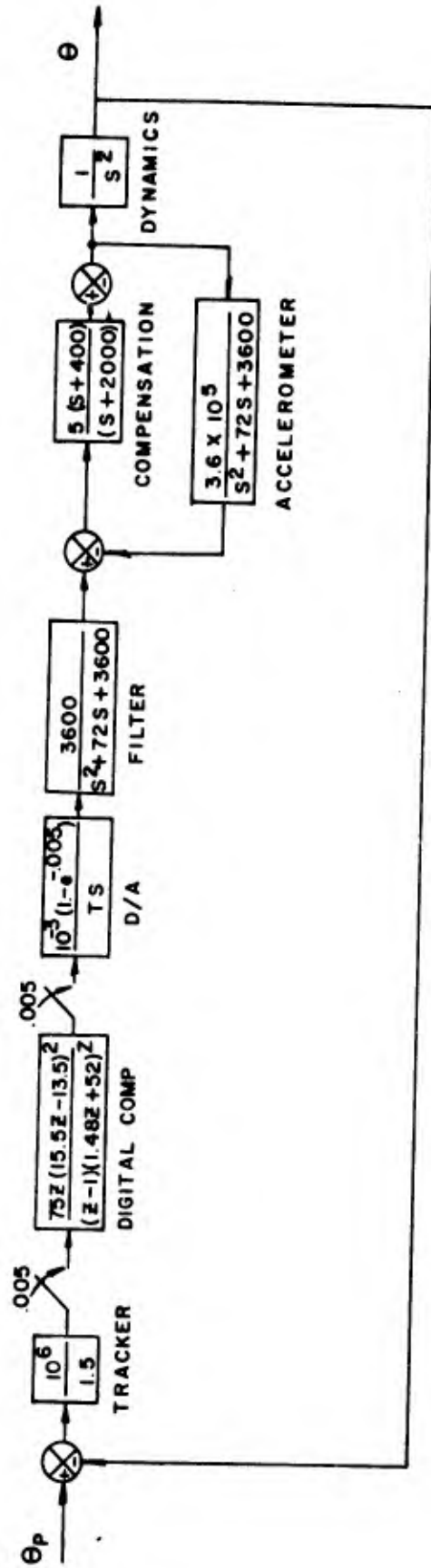


FIGURE 3 - LBCS TRACKING LOOP

To model these systems it is necessary to convert the Laplace domain representations of Figures 1, 2, and 3 into the time domain. The time domain will permit a comparison of the simulation results with actual transient test results.

The time domain description is effected by a dynamical (state) model of the form

$$\dot{\underline{x}}(t) = \underline{f}(\underline{x}(t), \underline{u}(t), t); \quad \underline{x}(t_0) = \underline{x}_0 \quad (1)$$

where

$\underline{x}(t)$  = n-dimensional vector describing the system state

n = order of the system

$\underline{u}(t)$  = m-dimensional vector describing the input to the system

m = number of external inputs to the system

This model represents a set of first order differential equations which can be solved on a digital computer by any number of integration schemes.

Optimization. In the event that the responses obtained from either of the trackers are not acceptable, it is desirable to have a method that will manipulate the system until acceptability is obtained. Several methods are available for adjusting system parameters, given the dynamical model, such that an optimal or suboptimal performance is obtained.

To optimize the performance of the tracker, it is necessary to specify a criterion by which to judge the performance. A commonly used criterion is defined by

$$PI = \int_{t_0}^{t_f} [w_1(x_1 - x_{d1})^2 + w_2(x_2 - x_{d2})^2 + \dots + w_n(x_n - x_{dn})^2] dt \quad (2)$$

where

$x_1, x_2, \dots, x_n$  are the system states

$x_{d1}, x_{d2}, \dots, x_{dn}$  are the desired system states

$w_1, w_2, \dots, w_n$  are weighting coefficients, whose sum must be unity

From equation (1) one can redefine the state model as

$$\dot{\underline{x}}(t) = \underline{f}(\underline{x}(t), \underline{P}, t); \quad \underline{x}(t_0) = \underline{x}_0 \quad (3)$$

where  $\underline{P}$  is a parameter vector of dimension  $p$ .  $\underline{P}$  represents a set of free parameters (i.e., free to be adjusted) in the system described by equation (3).

The method by which optimization is effected is as follows:

1. Select an initial set of parameters.
2. Solve the dynamical system described by equation (3) over the time interval of interest.
3. Measure the performance criterion of equation (2) over the same time interval.
4. Adjust the parameters and repeat steps 1, 2, and 3.
5. Continue until the best value is obtained for the performance criterion.

Obviously there must be some method for logically adjusting the parameters to minimize equation (2); otherwise the adjustment would require excessive computing time.

The method now being used for optimization is a combined grid and star search which has been implemented on the digital computer.<sup>1,2</sup> It was chosen for its simplicity and availability. The search proceeds by establishing an initial grid based upon the magnitude of pre-established parameter bounds and then reducing the size of this grid in a direction that leads to a minimum value of the performance criterion. In addition to this method, another technique is being considered which functions by a pattern search.<sup>3</sup> This latter method promises simpler operation.

### Results

The major emphasis in obtaining results has been placed upon modeling and simulation. These results have been needed to allow comparison with experimental data and thus to establish model integrity. As the integrity has been gained, the model has been subjected to realistic tracking problems that typify what will be expected of the working system. When the model does not seem to perform adequately, it has been subjected to parameter optimization in an attempt to obtain a more satisfactory system.

Dynamical Model and Simulation. The FTT has been the major concern in modeling and simulation. This emphasis is due to the fact that the FTT exists as hardware, whereas the LBCS does not.

#### FTT

The first step taken in simulating the FTT was to model the rate loops included within the tracking loops of Figures 1 and 2. Using the form dictated by equation (1), the total system is modeled by a set of 38 dynamical equations (i.e.,  $n = 38$ ). Once simulation was initiated upon the digital computer, it became necessary to simplify the model by neglecting the structural dynamics. As indicated earlier, these structural terms are of a very high frequency and created stability problems in the integration methods used for digital simulation. These problems occurred because of the need to integrate at a rate about ten times faster than the fastest time constant in the system. In practice it was necessary to utilize a small step size ( $\Delta t = .00001$ ) to simulate without the structural dynamics.

A step size as small as that indicated above is not generally desirable from the standpoint of computer computation time. Thus a root-finding program was implemented upon the digital computer to determine which elements in the FTT control system responded at a fast enough rate to justify the need for the small step size. These roots directly indicate how fast the system responds. By isolating the elements involved, it was felt it might be possible to either neglect the problem causers or at least determine a more exact integration step size (hopefully smaller). Unfortunately, finding the roots of the characteristic equation polynomials for the inner azimuth and elevation control systems became a problem in itself. The roots involved were found to range from very small to very large and thus created difficulties for the root-solving program. It became necessary to try several different methods of root extraction before one was finally found (courtesy of Hughes Aircraft Company) which gave the proper roots. These roots are given in Tables 1 and 2 for the inner azimuth and elevation axes respectively. Although these roots include the structural dynamics, it is possible to isolate them and locate the roots that require the small step size when integration is done with the structural dynamics excluded. These roots are

$$\lambda_{13} = -3.94 \times 10^3$$

$$\lambda_{12} = -1.636 \times 10^3$$

for inner azimuth, and

$$\lambda_{15} = -3.94 \times 10^3$$

$$\lambda_{14} = -1.64 \times 10^3$$

for elevation. In both cases the first root listed is in the system compensation, and the second is in the gyro.

TABLE 1

Inner Azimuth Closed Loop Roots

$$\lambda_{1,2} = -1.99238 \times 10^3 + j4.60663 \times 10^4$$

$$\lambda_{3,4} = -8.76971 \times 10 + j1.96192 \times 10^3$$

$$\lambda_{5,6} = -6.59004 \times 10^2 + j6.31359 \times 10^2$$

$$\lambda_{7,8} = -1.02220 \times 10^2 + j4.02792 \times 10^2$$

$$\lambda_{9,10} = -1.21687 \times 10^2 + j9.53510 \times 10$$

$$\lambda_{11} = -1.18367 \times 10$$

$$\lambda_{12} = -1.63688 \times 10^3$$

$$\lambda_{13} = -3.94029 \times 10^3$$

TABLE 2

Elevation Closed Loop Poles

$$\lambda_{1,2} = -1.95540 \times 10^3 + j3.88878 \times 10^4$$

$$\lambda_{3,4} = -2.10594 \times 10^2 + j4.22491 \times 10^3$$

$$\lambda_{5,6} = -9.27303 \times 10 + j1.95493 \times 10^3$$

$$\lambda_{7,8} = -6.60066 \times 10^2 + j.36102 \times 10^2$$

$$\lambda_{9,10} = -9.50174 \times 10 + j3.99305 \times 10^2$$

$$\lambda_{11,12} = -1.23302 \times 10^2 + j9.47690 \times 10$$

$$\lambda_{13} = -1.18363 \times 10$$

$$\lambda_{14} = -1.64077 \times 10^3$$

$$\lambda_{15} = -3.94016 \times 10^3$$



An effort was made to simulate the elevation axis rate loop of the FTT with the two roots listed above removed; however, the results were not successful. It is possible that some further assumptions could be made which would allow these roots to be neglected yet insure a working simulation. In addition, there has been a frequency domain study on the FTT done in parallel with this time domain investigation. The results of this study indicate that the FTT control systems are operating in a region which has very little margin for stability. This stability problem combined with the wide spread of very fast and very slow responding transients in the system is apparently precipitating another difficulty in finding the time solution to the FTT model. With such a combination it seems that the added "dynamics" of a multi-ordered integration scheme are influential on the stability of the time solution. To overcome this problem, the natural recourse was to decrease the step size for the integration scheme. However, for the system at hand the step size was already small and computing time would become an even greater problem. To overcome the effects of the high-order integration scheme and reduce computing time, a very simple Euler method of integration was employed.<sup>4</sup> While such a scheme tends to have less accuracy than a higher order one, the net effect was to reduce the computing time required by a factor of four and increase the amount of allowable leeway in the integration step size.

Rate Loop: The simulation of the rate loop for both the inner azimuth and elevation axes, with only structural dynamics excluded, produced results which indicated that the Coulomb friction inherent in the FTT should be accounted for in the model. This friction is described as shown in Figure 4. Figures 5 and 6 are plots of the inner azimuth and elevation axes, respectively, for two arbitrary levels of friction. The variables plotted are measured at the output of the quadratic filter immediately following the gyro in Figures 1 and 2.

Position Loop: Only one comparison between simulation and actual data has been made on the FTT for the position loop. There are other simulations, as will be shown, but they are devoted to the interjection of test inputs and scenarios into the position inputs of only the model. A comparison of results is shown in Figure 7. The plot illustrates the FTT and model responses for a step command interjected directly following the TV compensator in the elevation tracking loop.

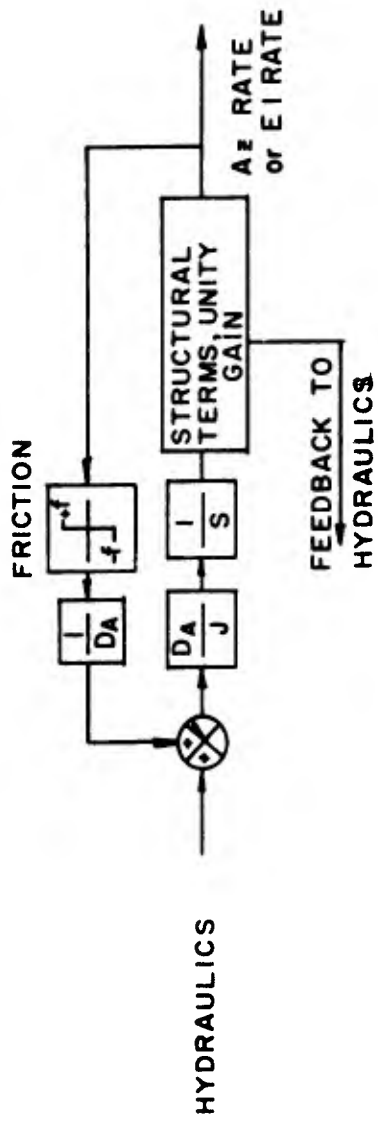
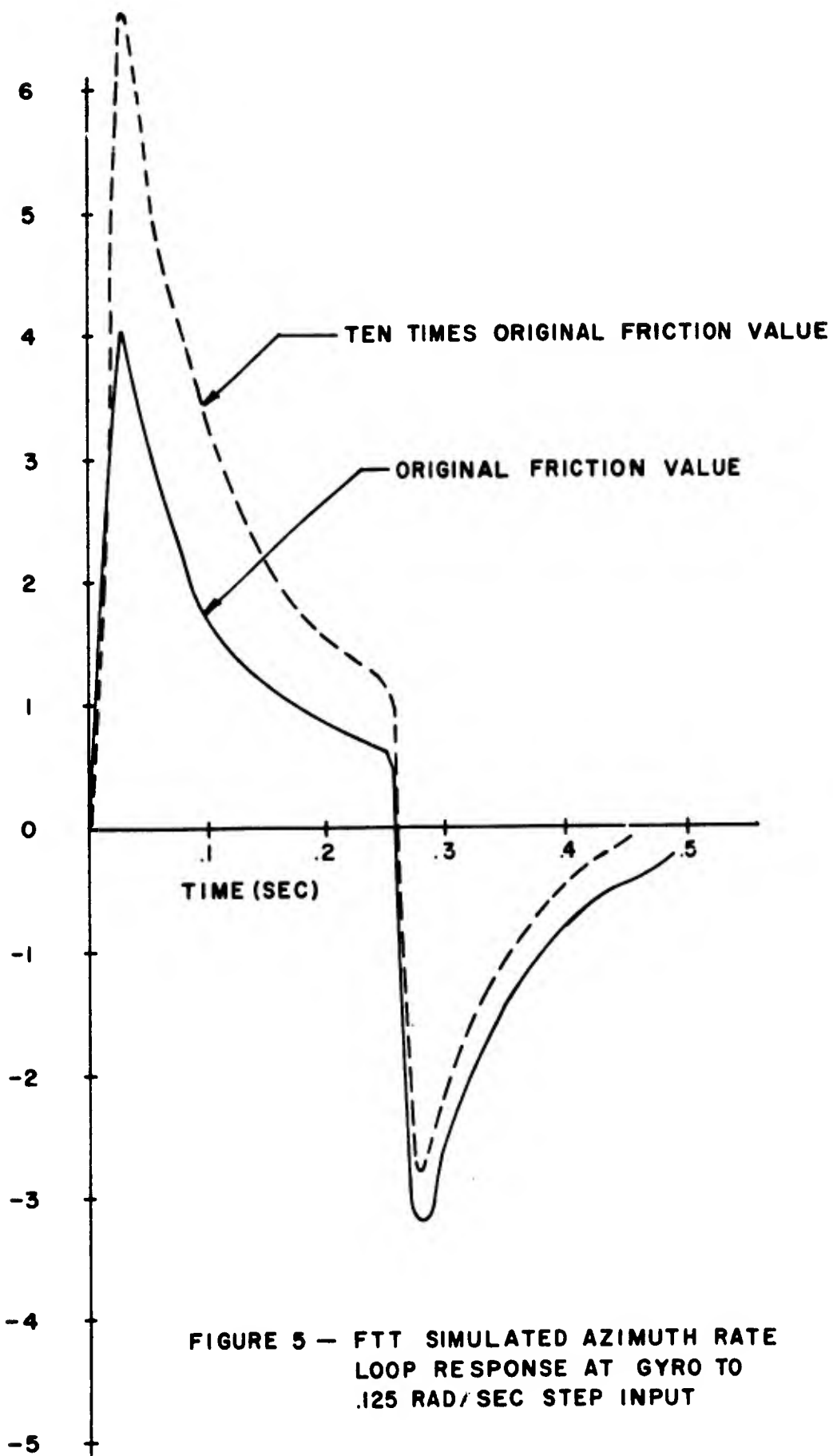


FIGURE 4 -- COULOMB FRICTION MODEL



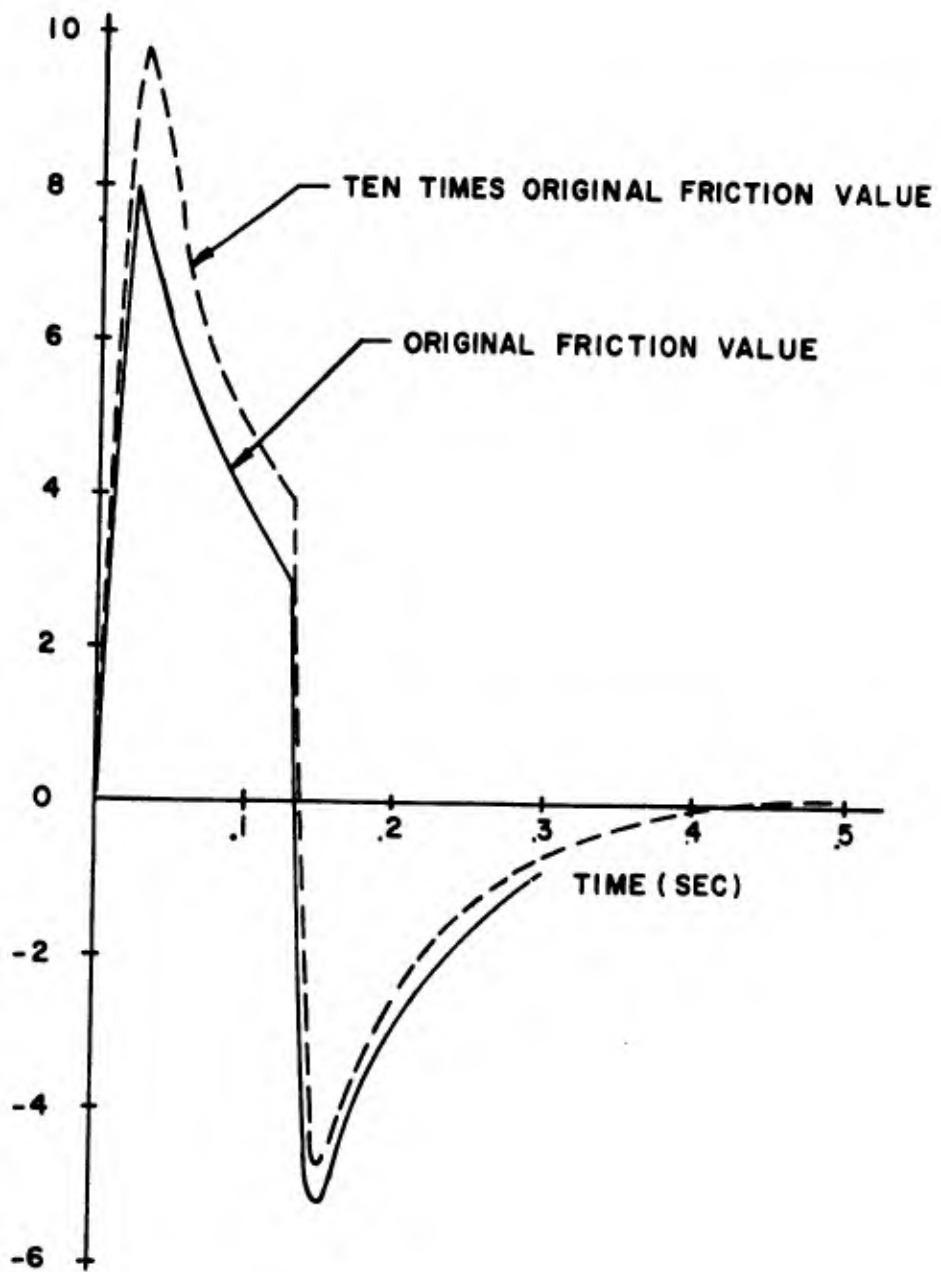


FIGURE 6 - FTT SIMULATED ELEVATION RATE LOOP RESPONSE AT GYRO TO 125 RAD/SEC STEP INPUT

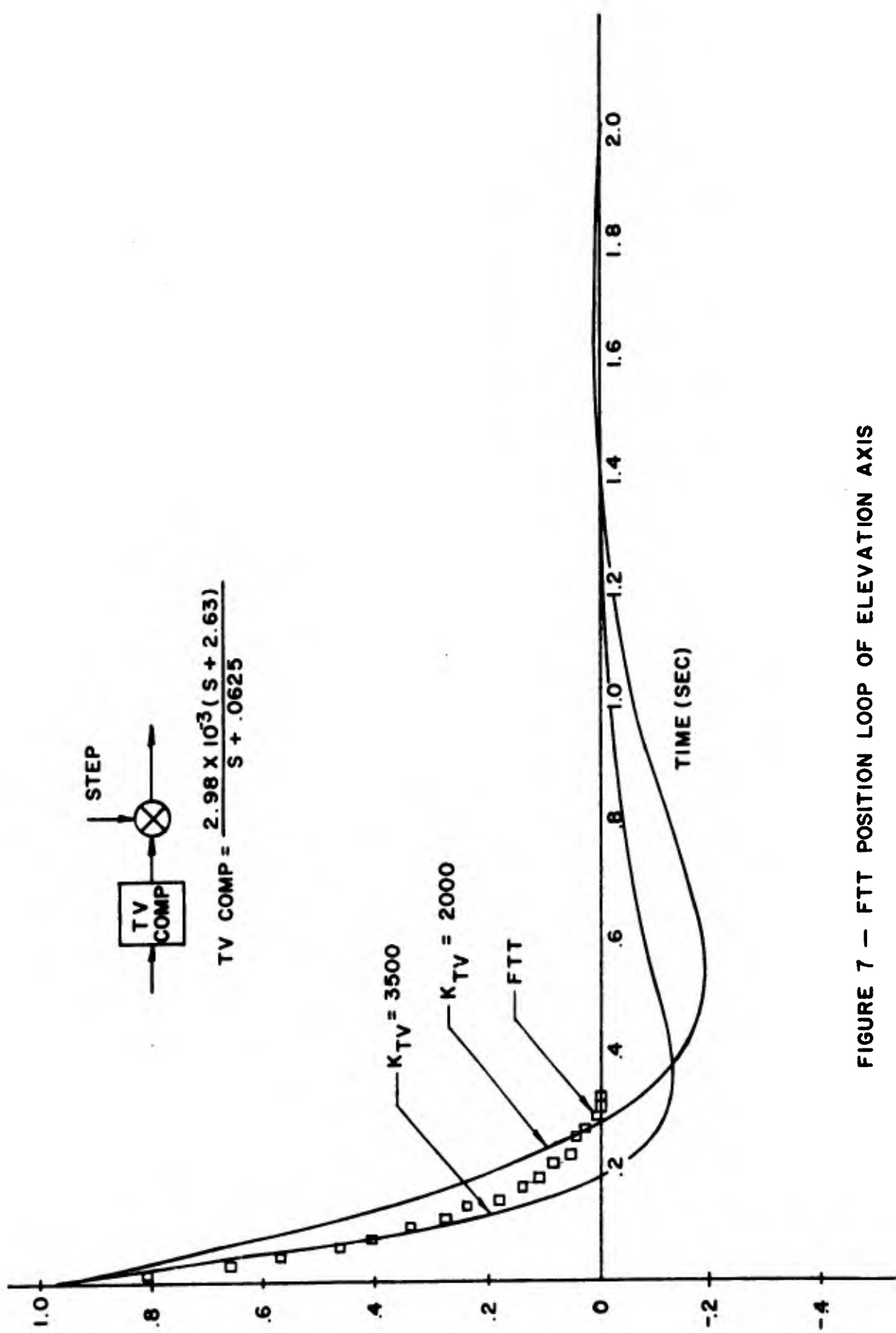


FIGURE 7 — FT T POSITION LOOP OF ELEVATION AXIS

There are a number of inputs being injected as direct position commands into the simulated azimuth and elevation tracking loops combined. The first to be considered is a constant acceleration command and is shown in Figure 8 as it is applied to the azimuth and elevation axes. The system error response is shown in Figures 9 and 10 for azimuth and elevation, respectively. The TV compensator used to generate these plots is given by

$$\text{TV COMP} = K_{\text{TV}} \frac{\left(\frac{S}{28} + 1\right)}{S} \quad (4)$$

The sample rate is 120/second, and  $K_{\text{TV}} = 1600$ .

The second input to be considered is a scenario and is shown in Figures 11 and 12 for azimuth and elevation commands, respectively. These commands are in aircraft coordinates and must be transformed into tracker coordinates to be meaningful. The transformation for the elevation axis is one to one and thus can be used as is. For the azimuth axis the transformation is effected by the relationship

$$\eta_c = \int_{t_0}^t \dot{\eta}_s \cos \epsilon_c dt \quad (5)$$

where  $\dot{\eta}_s$  is the time derivative of the tracker coordinate variable plotted in Figure 11,  $\epsilon_c$  is the variable plotted in Figure 12, and  $\eta_c$  is the transformed position input to azimuth axis. The system error response is shown in Figures 13 and 14 for the azimuth and elevation axes, respectively.

#### LBCS

The simulation of the LBCS has met with stability problems, and thus a solution has yet to be obtained. These problems appear during simulation on the digital computer and cause the system dynamical response to diverge to the point of computer overflow. The LBCS is presently being examined for possible redesign of the digital compensator.

Optimization. The FFT systems are presently in the initial stages of being optimized with the program of reference 2. Although there are no conclusive results available yet, the preliminary indications are that computing time will be long. Additionally, the FFT appears to be operating in a narrow range of

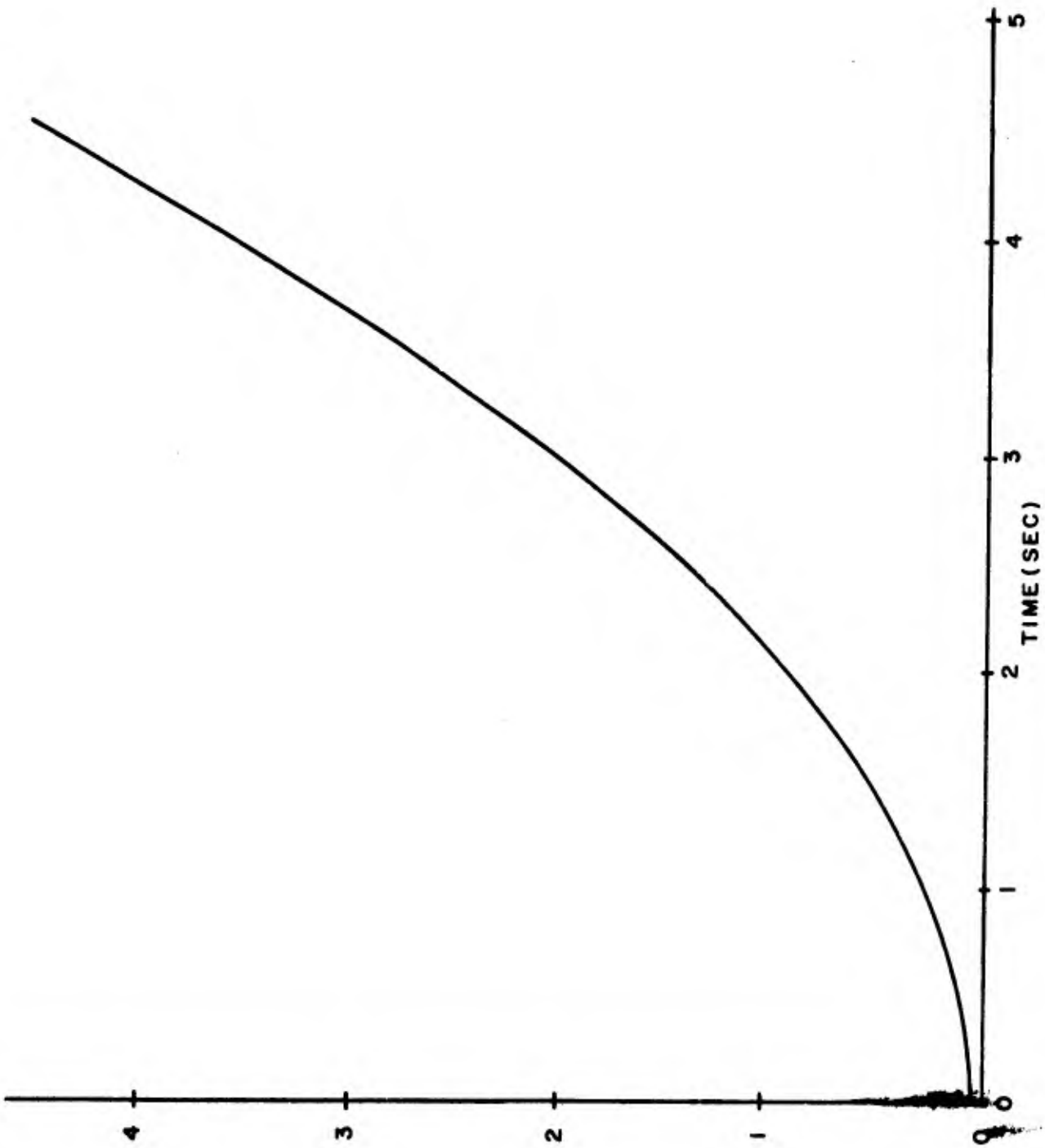


FIGURE 8 -- CONSTANT ACCELERATION COMMAND

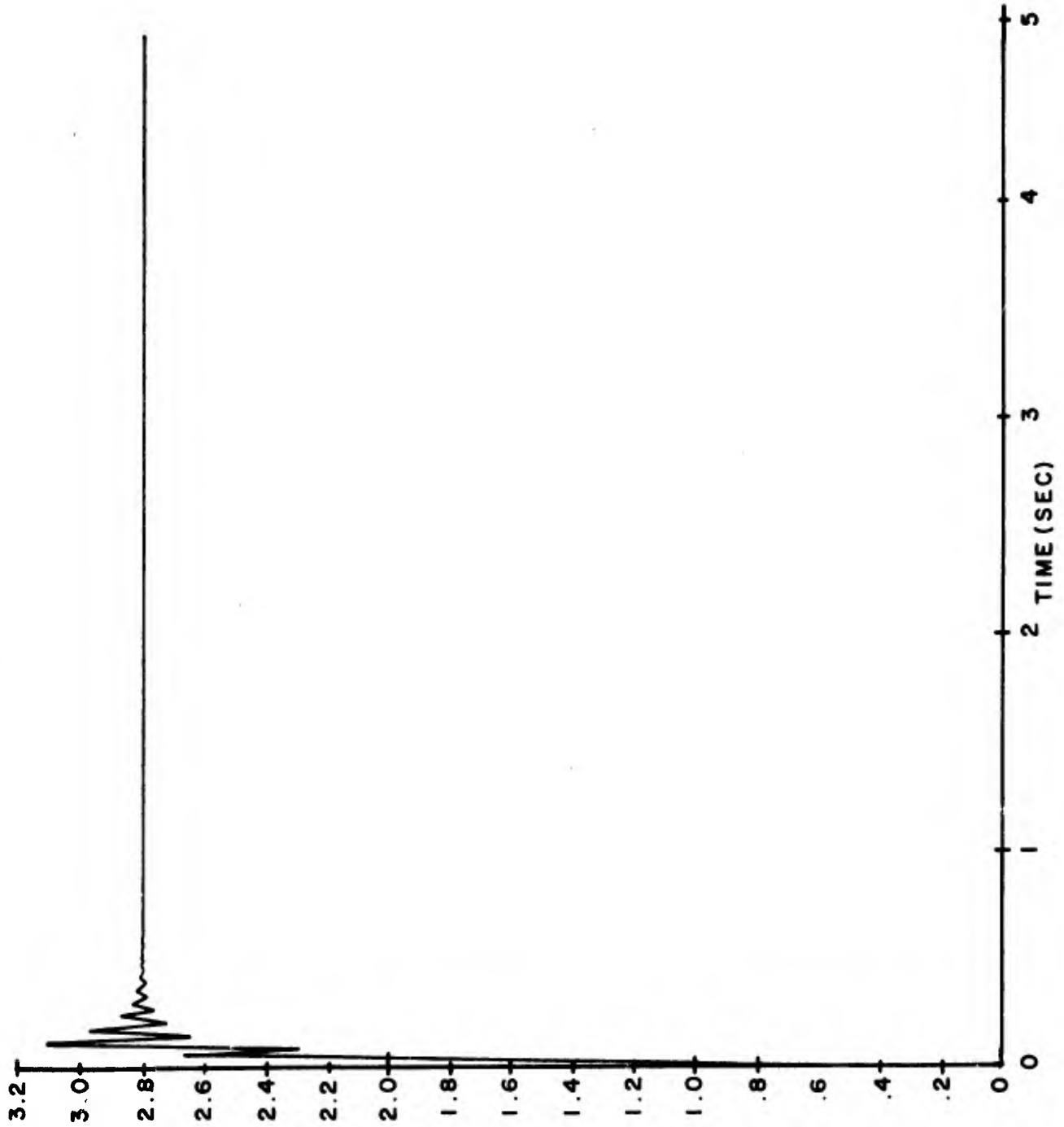


FIGURE 9 -- AZIMUTH AXIS ERROR FOR CONSTANT ACCELERATION  
COMMAND



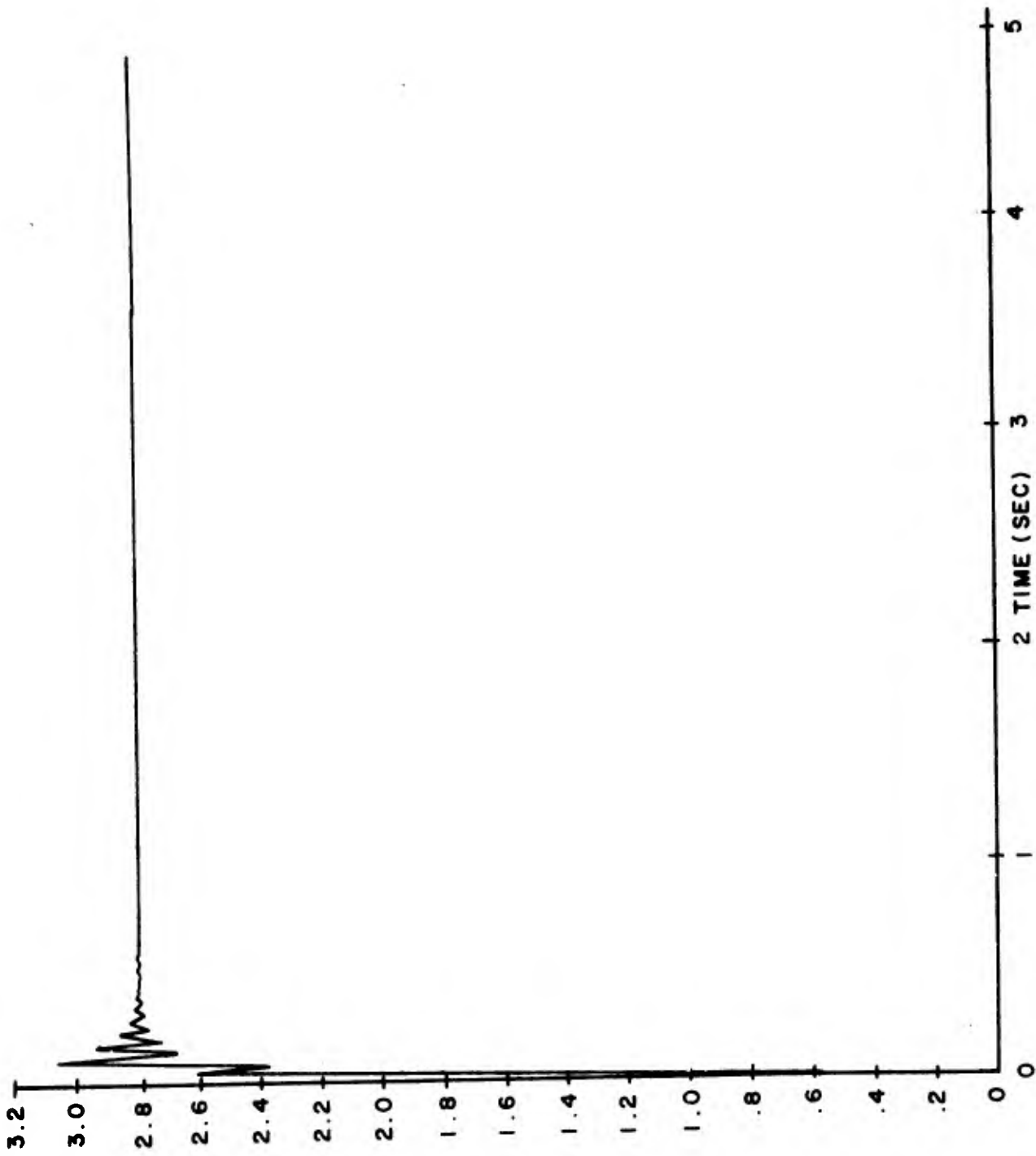


FIGURE 10 - ELEVATION AXIS ERROR FOR CONSTANT ACCELERATION COMMAND

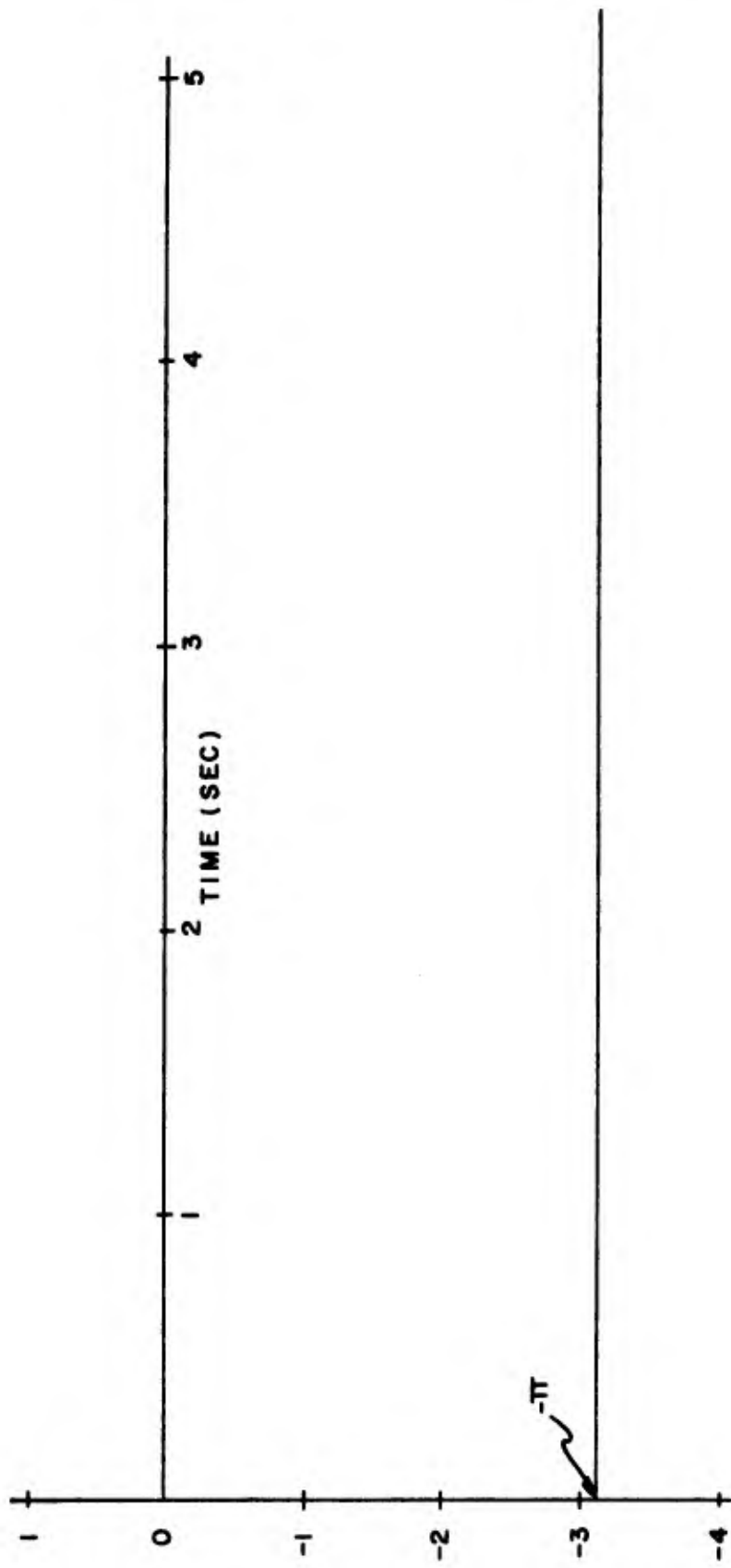


FIGURE 11 - AZIMUTH AXIS SCENARIO COMMAND

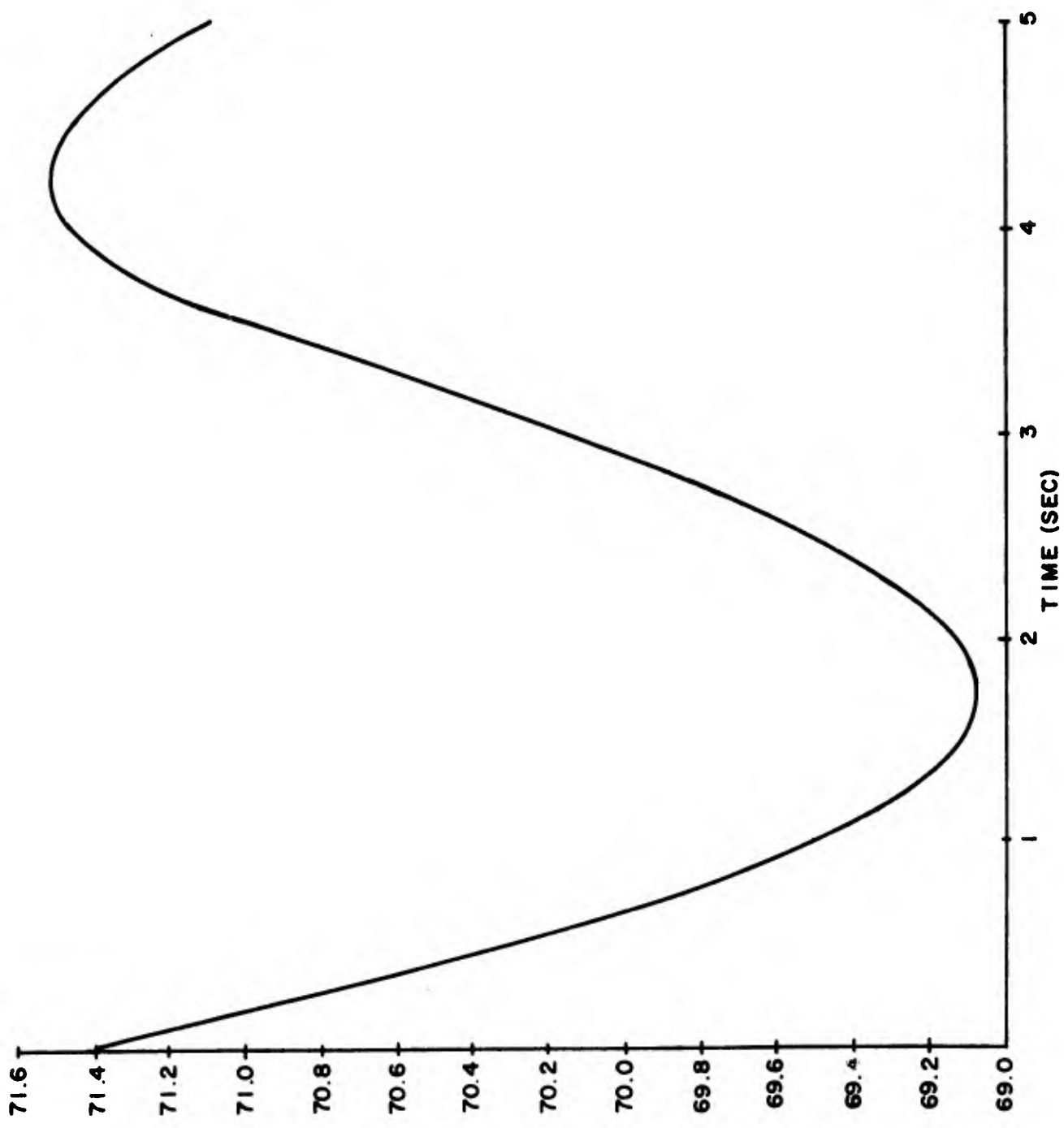


FIGURE 12 - ELEVATION AXIS SCENARIO COMMAND

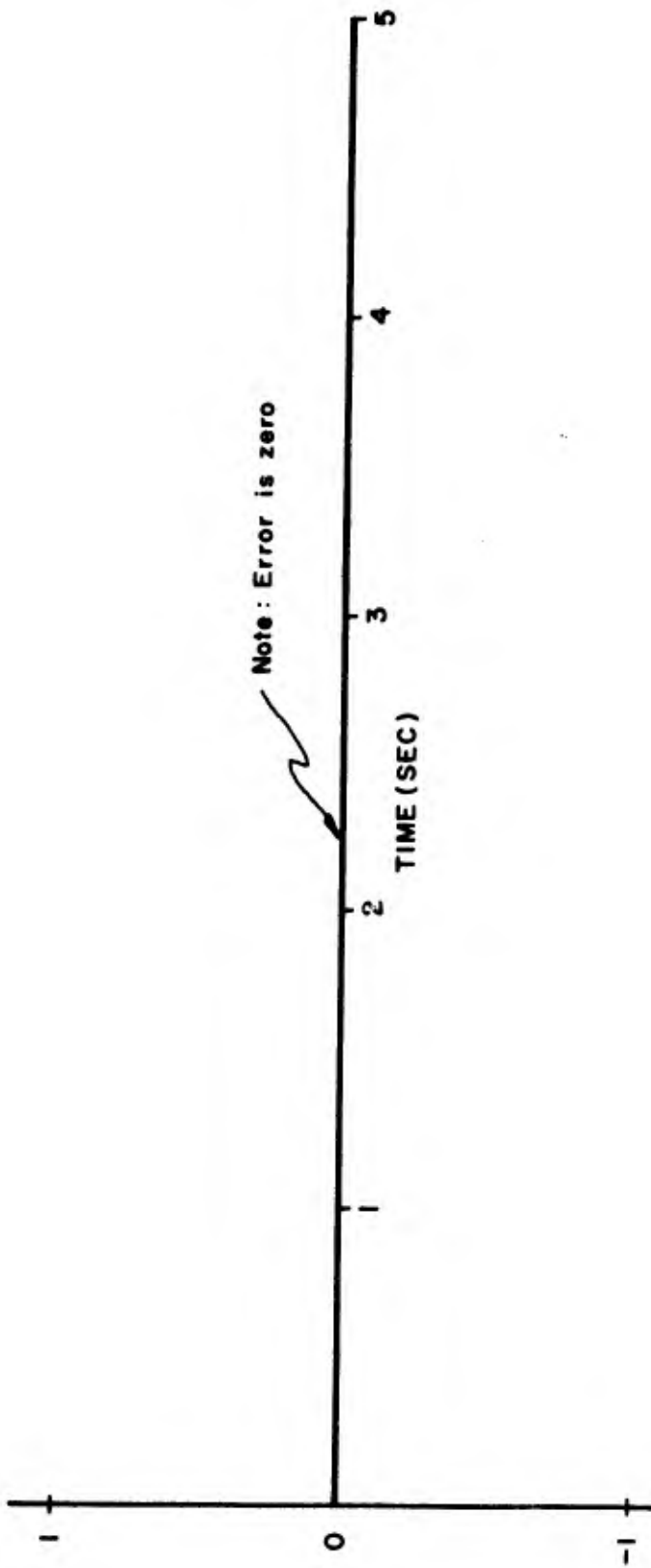


FIGURE 13 -- AZIMUTH AXIS ERROR FOR SCENARIO COMMAND

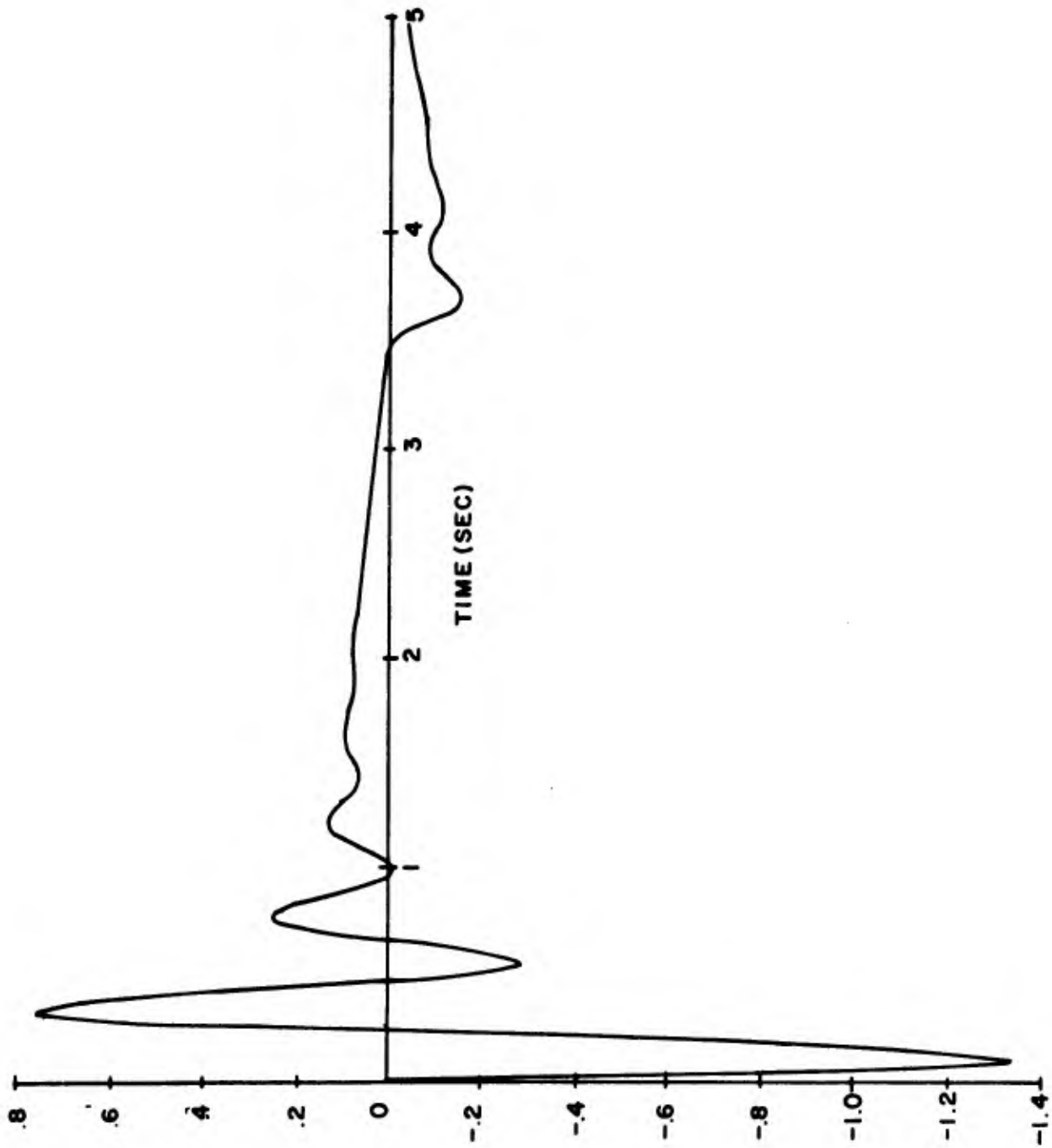


FIGURE 14 - ELEVATION AXIS ERROR FOR SCENARIO COMMAND

stability margin and is thus extremely sensitive to parameter variations. With this type of sensitivity, it has been difficult to obtain any reasonable convergence upon an optimum parameter.

The nature of parameter optimization schemes seems to be such that they are better suited to optimizing one system than another depending upon the search technique involved. With this suitability in mind, the optimization scheme of reference 3 will be implemented in addition to the one now being used with the hope of obtaining more meaningful results.

#### REFERENCES

1. Mischke, R. C., An Introduction to Computer Aided Design, Englewood Cliff, NJ: Prentice-Hall, Inc., 1968.
2. Zeiger, G., An Algorithm for Parameter Optimization in Dynamic System Design, M.S. Report, Dept of Mech and Aerospace Eng, Oklahoma State University.
3. Moore, C. F., et al., Multidimensional Optimization Using Pattern Search, LSU-T-TR-23, AFOSR Contract No. F-44620-68-C-0021.
4. Hildebrand, F. B., Introduction to Numerical Analysis, New York: McGraw-Hill, 1956.

## GEOMETRIC OPTICS OF THERMAL BLOOMING IN GASES: I

P. V. Avizonis, C. B. Hogge, R. R. Butts, and J. R. Kenemuth

### Introduction

The thermo-optical effects on the laser beam due to absorption by the media that the beam is propagating through have been treated by a number of authors, primarily in liquid media.<sup>1-8</sup> An interesting treatment was that of Akhimanov<sup>9</sup> which presented a very nice approach to the thermal blooming problem in a liquid by using Maxwell's equation. The analytical solutions were obtained in the geometric limit at steady state; consequently, the results were no different than that of the Eikonal approaches.

Gebhardt and Smith<sup>10</sup> were the first to publish such thermo-optical effects in gases in the presence of transverse mass flow to the propagation direction. Their approach was a steady state, paraxial ray deflection angle Eikonal approximation, in one dimension. Smith<sup>11</sup> further reported a steady state paraxial ray intensity formulation in terms of the divergence of the ray vector field.<sup>12</sup> We have reported our initial investigations of such propagation effects in gases<sup>13</sup> in the transient and late times (times long compared to the acoustical transient time across the laser beam), using paraxial Eikonal formalisms. It was found that several disagreements with previous work existed. First, the experiments indicated that in all cases (except with very small  $\alpha z$ , where  $\alpha$  is the absorption coefficient and  $z$  is the absorption path length and  $\alpha z < 0.1$ ) a Gaussian beam became an expanding doughnut for all subsequent times before convective mass flow became significant. This is in opposition to the data and calculations reported by Smith.<sup>11</sup> We believe that this may be due to the way that data was taken, namely integrating the laser beam profile over the aperture of a variable diameter iris. Furthermore, the formulation of the ray intensity equation, as represented by Equations 8 and 9 of Reference 11, is not quite correct, in the sense that the independent radial parameter " $r$ " is not the same as the initial radial parameter in  $I(r,0)$  of the Eikonal formalism as developed by Born and Wolf.<sup>12</sup> As a result, Smith did not obtain the caustics on the periphery of the beam, which is characteristic of a doughnut.<sup>13</sup>

As indicated by Born and Wolf,<sup>12</sup> the ray intensity equation can only be used for the ratio of intensities along any one given particular ray, and not as a

a general functional relationship within the ray field of different rays. If properly used, the doughnut shape is indeed obtained theoretically<sup>13</sup> in reasonable agreement with experiment. This leads to the second dilemma, in that the paraxial treatment of the Eikonal represents a first order expansion of the ray vector, and thus should be good only in the limit of the thin lens approximation. On the other hand, the experiments reported<sup>13</sup> were, in some cases, substantially beyond the thin lens situation, yet the agreement with calculations was still satisfactory.

Because of the above mentioned discrepancies, a detailed development of both the energy absorption and Eikonal formalisms is examined in this report. Since we are dealing with two coupled equations (an energy balance equation which describes absorption, heating, and heat dissipation, and beam intensity or ray optics equation, which describes the resultant behavior of the beam), each equation is examined for its significance, and then their coupling is determined. The energy balance starts with equations of continuity, momentum, and of state; the consequent behavior of media density to the laser beam intensity is thus determined. The conditions for the reduction of the above equations to simple thermodynamic functions (including kinetic effects of vibrational energy relaxation into translation) are established. The Eikonal equation is then analyzed in terms of limitations of higher order terms in the determination of the ray trajectories. In addition, we show that the approximations inherent to the paraxial solution (and to higher order solution for that matter) can be relegated solely to the aspect of the determination of the ray trajectories. That is, once a particular set of trajectories is specified (and it does not really matter how one gets this description), one need not introduce additional approximation errors into the determination of the intensity profiles as is usually done with the ubiquitous "paraxial approximations."

Using the thermodynamics developed here, we will show the time development of collimated Gaussian beams subjected to a number of cross-wind speeds. The stationary intensity profiles obtained in the asymptotic limits of long time periods are indicated for some of the more interesting wind velocities.

Throughout the calculations made, we constantly try to judge the validity of the perturbation expansion on the description of the intensity profile. In addition, several cases are presented where second order terms are retained in the expression obtained for the ray trajectory. Here too, we try to determine the parametric range of validity of the results.



## Theory

This problem may be approached by first examining the physics of energy deposition into the gaseous media, then the behavior of ray optics, and finally the self-consistent influence of the above upon each other.

### A. Energy Deposition

The energetics are examined first by considering the equations of continuity and momentum.

$$\partial\rho/\partial t + \rho\nabla\cdot v + v\cdot\nabla\rho = 0$$

$$\partial v/\partial t + (v\cdot\nabla)v = -(1/\rho)\nabla P \quad (1)$$

The usual thermodynamic notation is used, where density is  $\rho$ ,  $v$  is the particle velocity, and  $P$  is the pressure. A first order perturbation expansion is used on the density and pressure, since the physical effect here is very small ( $\alpha I$  is maximally on the order of  $0.1 \text{ watts/cm}^3$ , and more like  $0.01$ , where  $I$  is the laser intensity). Therefore with  $\rho = \rho_0 + \rho_1$  and  $P = P_0 + P_1$ , the equations of continuity and momentum become

$$\partial\rho_1/\partial t + \rho_0\nabla\cdot v = 0$$

$$\partial v/\partial t = -(1/\rho_0)\nabla P_1 \quad (2)$$

By differentiating in time the continuity equation and combining it with the momentum equation, the wave equation of interest is obtained.

$$\partial^2\rho_1/\partial t^2 = \nabla^2 P_1 \quad (3)$$

The pressure definition may be obtained from the energy equation,

$$\rho T \partial S/\partial t = \phi - \nabla\cdot q \quad (4)$$

where  $T$  is the temperature,  $S$  is the entropy,  $\phi$  is the viscous dissipation (it will be assumed that  $\phi = 0$  for gaseous systems) and  $q$  is the sum of heat sources and losses.

$$-\nabla \cdot \mathbf{q} = \nabla \cdot (K\nabla T) + (\partial E / \partial t)_o \quad (5)$$

If heat conduction and absorption of optical power are the only important heat flow parameters, then  $q$  is defined by equation (5), where  $K$  is thermal conductivity and  $(\partial E / \partial t)_o$  is the absorbed and thermalized laser power per unit volume. It will be defined more explicitly later. If the ideal gas equation of state is now evoked,  $PV = RT$ , where  $V$  is the specific volume ( $V = 1/\rho$ ) and  $R$  is the gas constant, and defining the entropy as  $T\partial S = C_v \partial T + P\partial V$  (where  $C_v$  is the heat capacity at constant volume), the time dependent pressure relationship may be obtained with some manipulation.

$$\rho \partial P / \partial t = (\gamma - 1) \rho^2 T \partial S / \partial t + \gamma \rho \partial \rho / \partial t \quad (6)$$

Here  $\gamma = C_p / C_v$ , where  $C_p$  is the heat capacity at constant pressure. Combining equation (6) with (5), the pressure definition is obtained.

$$\rho \partial P / \partial t = (\gamma - 1) \rho [\nabla \cdot (K\nabla T) + (\partial E / \partial t)_o] + \gamma P \partial \rho / \partial t \quad (7)$$

If the expansions in pressure and density are applied to equation (7), as in equation (1), the first order perturbation form of equation (7) is obtained.

$$\rho_o \partial P_1 / \partial t = (\gamma - 1) \rho_o [\nabla \cdot (K\nabla T_1) + (\partial E / \partial t)_o] + \gamma P_o \partial \rho_1 / \partial t \quad (8)$$

Substituting the above relationship into equation (3) by differentiating it once in time and recognizing that the sound speed  $c$  may be defined as  $c = (\gamma RT)^{1/2}$ , the driven sound equation is obtained.

$$(\partial / \partial t) [\partial^2 \rho_1 / \partial t^2 - c^2 \nabla^2 \rho_1] = (\gamma - 1) [\nabla^2 (K\nabla^2 T) + (\partial E / \partial t)_o] \quad (9)$$

The heat input rate (energy thermalization rate) is established by kinetics of the system. For simplified kinetics of a two level system, where the only important parameters are the energy absorption rate from the lower level and relaxation of the upper (assuming no depletion of lower level), the kinetics may be obtained from energy balance.

$$(dE/dt)_{abs} = (dE/dt)_{vib} + (dE/dt)_o \quad (10)$$

Here  $dE_{\text{abs}}/dt$  is the absorbed power from the laser beam and is equal to  $\alpha I_{\ell}$  (energy required to take the molecules from the lower vibrational state to the upper one).  $E_{\text{vib}}$  is the energy in the vibrational state, and  $E_0$  is the energy that has relaxed from the vibrational state into heat.

This kind of system is quite a good representation of how the absorption of  $10.6\mu$  radiation would work if the beam was passed through a cell containing  $\text{CO}_2$  gas.<sup>13</sup> In this case, the absorbed laser energy drives the molecules from the lower vibrational level (100 - the symmetric stretching mode) to the upper vibrational level (001 - the asymmetric stretching mode). Consequently, energy in the upper vibrational state for  $\text{CO}_2$ ,  $E_{\text{vib}}$  is represented by the number density "N" of molecules that are in the (001) state. The vibrational energy relaxes from this state by means of thermalizing collisions with other  $\text{CO}_2$  molecules. The life time of molecules in the 001 state is thus defined as  $\tau$ . All other kinetic rates for  $\text{CO}_2$  are much faster, therefore, they are neglected for this discussion.

$$(dE/dt)_{\text{vib}} = h\nu(dN/dt) = \alpha I_{\ell} - h\nu N/\tau$$

$$h\nu N = \alpha I_{\ell} [1 - \exp(-t/\tau)]$$

The absorption coefficient is assumed to be independent of time, thus no absorption bleaching is possible. The heat input rate may be then determined.

$$(dE/dt)_0 = \alpha I_{\ell} [1 - \exp(-t/\tau)] \quad (11)$$

The importance of the heat conduction term of equation (9) (where it was assumed that over the temperature range of interest, the thermal conductivity was constant) may be assessed by taking the terms in the right-hand brackets as a change in the volumetric heating rate of the system,  $\partial q/\partial t$ ,

$$\partial q/\partial t = K\nabla^2 T + \alpha I_{\ell} [1 - \exp(-t/\tau)]$$

and solving the above equation by transforming it into a temperature form ( $\rho_0 C \partial T/\partial t = \partial q/\partial t$ ). The laser intensity is assumed to have a Gaussian profile,  $I_{\ell} = I_0 \exp(-2R^2/w^2)$ , where  $R$  is the radial position,  $w$  is the radius at  $\exp(-2)$ , and  $I_0$  is the peak intensity. It will be assumed that  $I_{\ell}$  does not significantly deplete due to absorption along  $z$ , thus  $\partial^2 T/\partial z^2 \approx 0$ . Under such conditions,

$\nabla^2 T = \partial^2 T / \partial R^2 + (1/R) \partial T / \partial R$  (radial symmetry), the temperature equation may be solved using Hankel transformation<sup>14</sup> in R. The on-axis solution ( $R = 0$ ) is quite simple, and may be approximated by equation (12).

$$T(0, t) \simeq (\alpha w_0^2 I_0 / 4c\rho_0 K) \ln(1 + 8Kt/w_0^2) \quad (12)$$

It is quite evident that the temperature will grow linearly with time until the value of  $8Kt/w_0^2 > 1$ , then the rate of temperature growth will decrease due to conduction from the beam axis. For atmospheric gases the thermal diffusivity  $\beta = K/\rho_0 C \simeq 0.25 \text{ cm}^2$ ; for a typical beam radius of 2 cm, it would take 2 seconds before conduction became significant. Consequently, for experimental times of less than 2 seconds, conductivity may be neglected, and equation (9) may be integrated once in time after equation (11) is substituted into it.

$$\partial^2 \rho_1 / \partial t^2 - c^2 \nabla^2 \rho_1 = (\gamma - 1) \{ t - \tau [1 - \exp(-t/\tau)] \} \alpha \nabla^2 I_\ell \quad (13)$$

The next part in the examination of the linearized hydrodynamic equation (equation (13)) is to determine how important is the role of the transient part; namely  $\partial^2 \rho_1 / \partial t^2$  term. To accomplish this, we make the assumption that the laser intensity  $I_\ell$  is Gaussian and in the region of interest it is not substantially depleted. Consequently, we study equation (13) without z dependence. This may not be necessarily the "realistic" condition from the experimental sense, but nevertheless it is pertinent to the determination of the importance of the time transient. This is so because if we assume no significant laser intensity depletion, this represents the "most severe" condition to driving the density waves as the intensity is maximum. Also, as before, it is assumed that  $\alpha$  is constant.

The solution may be obtained by assuming a form of  $\rho$  such that

$$\rho_1(R, t) = -(\alpha/c^2)(\gamma - 1) \{ \{ t - \tau [1 - \exp(-t/\tau)] \} I_\ell(R) - (1/\tau) \phi(R, t) \exp(-t/\tau) \} \quad (14)$$

where  $\phi(R, t)$  is an arbitrary function to be determined. Performing the appropriate differentiation, with  $\nabla^2 = \partial^2 / \partial R^2 + (1/R) \partial / \partial R$  and defining  $I_\ell(R) = I_0 \exp(-2R^2/w_0^2)$ , the equation for  $\phi(R, t)$  is obtained.  $\partial^2 / \partial z^2$  is approximated to be zero under the rationale of the preceding paragraph.

$$\frac{\partial^2 \phi}{\partial \tau^2} - \frac{2}{\tau} \frac{\partial \phi}{\partial \tau} + \frac{\phi}{\tau^2} - c^2 \nabla^2 \phi = I_\ell(R) \quad (15)$$

This equation may be solved by performing the Laplace transformation in time ( $t \rightarrow s$ ) and the Hankel transformation in  $R$  ( $R \rightarrow \sigma$ ). The boundary conditions are

$$\left[ \frac{\partial \rho_1}{\partial \tau} \right]_{t=0} = 0$$

(since  $\rho_1$  is a small perturbation), and the boundaries on  $\phi$  become  $\phi(0, R) = 0$  and

$$\left[ \frac{\partial \phi}{\partial t} \right]_{t=0} = 0$$

$$\phi(s, \sigma) = I(\sigma) / s [(s - 1/\tau)^2 + v^2 \sigma^2]$$

$$\frac{d\phi(t, \sigma)}{dt} = \frac{w^2 I_0}{4c\sigma} \exp[-(w^2 \sigma^2 / 8 - t/\tau)] \sin(c\sigma t)$$

Here, the Hankel transformation of the Gaussian ( $R \rightarrow \sigma$ ) was accomplished as defined below.

$$\int_0^\infty R I_\ell(R) J_\ell(\sigma R) dR - (w^2 I_0 / 4) \exp[-w^2 \sigma^2 / 8] = 1(\sigma)$$

The inversion of  $\sigma \rightarrow R$  is performed in a similar manner as the Hankel transform is self-reciprocal.

$$d\phi(R, t) / dt = (w^2 I_0 / 4c) \exp(t/\tau) \int_0^\infty \exp(-w^2 \sigma^2 / 8) \sin(vt\sigma) J_\ell(\sigma R) d\sigma \quad (16)$$

The on-axis case ( $R=0$ ) of equation (14), and consequently, that of equation (16) may be examined from the point of trying to ascertain the importance of the second term in the large brackets,  $(1/\tau) \phi(0, t) \exp(-t/\tau)$  as a function of time, as opposed to the first term in the large brackets  $\{t - \tau[1 - \exp(-t/\tau)]\} I_0$  in terms of their importance to  $\rho(0, t)$ .

Equation (16) may, in the case of  $R=0$ , be integrated to yield

$$d\phi(o,t)/dt = -i(\sqrt{2\pi}/4c)wI_o \exp(t/\tau - 2c^2 t^2/w^2) \text{Erf}(i\sqrt{2} ct/w) \quad (17)$$

where Erf is the error function, in this case of imaginary argument, and is defined below.

$$\text{Erf}(i\sqrt{2} ct/w) = 2\sqrt{2/\pi}(c/w) \int_0^t \exp(2c^2 \xi^2/w^2) d\xi$$

The on-axis ( $R=0$ ) solution of equation (14) becomes now

$$\begin{aligned} \rho(o,t) = & -(\alpha/c^2)(\gamma-1)(2P_T/\pi) \left\{ (1/w^2) \{t-\tau[1-\exp(-t/\tau)]\} \right. \\ & \left. + i\sqrt{2\pi} (1/4\tau cw) \exp(-t/\tau) \int_0^t \exp[\xi/\tau - 2c^2 \xi^2/w^2] \text{Erf}(i\sqrt{2} c\xi/w) d\xi \right\} \end{aligned} \quad (18)$$

where  $I_o$  was defined as  $2P_T/\pi w^2$  for a Gaussian beam with  $P_T$  being the total power.

The absolute magnitude of the first term in the large brackets on the right-hand side of equation (18) is plotted in Figure 1a as a function of  $t$  in terms of  $\tau$ , for various radii  $w$  of the beam. A  $\tau \approx 4 \times 10^{-5}$  sec was selected, and approximates the relaxation rate of the 001 level of  $\text{CO}_2$  at a 0.1 of an atmosphere. Likewise, the second term,

$$\Psi = i\sqrt{2\pi} (1/4\tau cw) \exp(-t/\tau) \cdot \int_0^t \exp(\xi/\tau - 2c^2 \xi^2/w^2) \text{Erf}(i\sqrt{2} c\xi/w) d\xi$$

is plotted in Figure 1b for the same  $w$ , for comparison purposes. It is quite evident that the first term is greater and grows much faster, while the second term dies out rapidly and represents the transient solution to the on-axis form of equation (14). Quite evidently, after a  $t > 10\tau$ , the first term dominates the solution in all cases by more than an order of magnitude, and the time transient terms of equation (18) may be neglected. Consequently, the steady

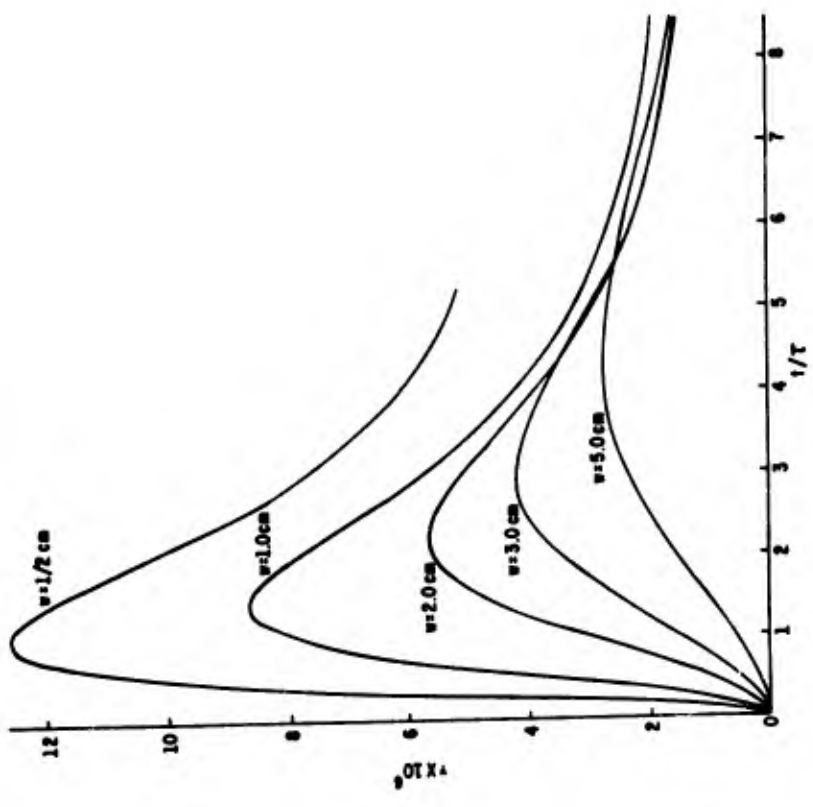
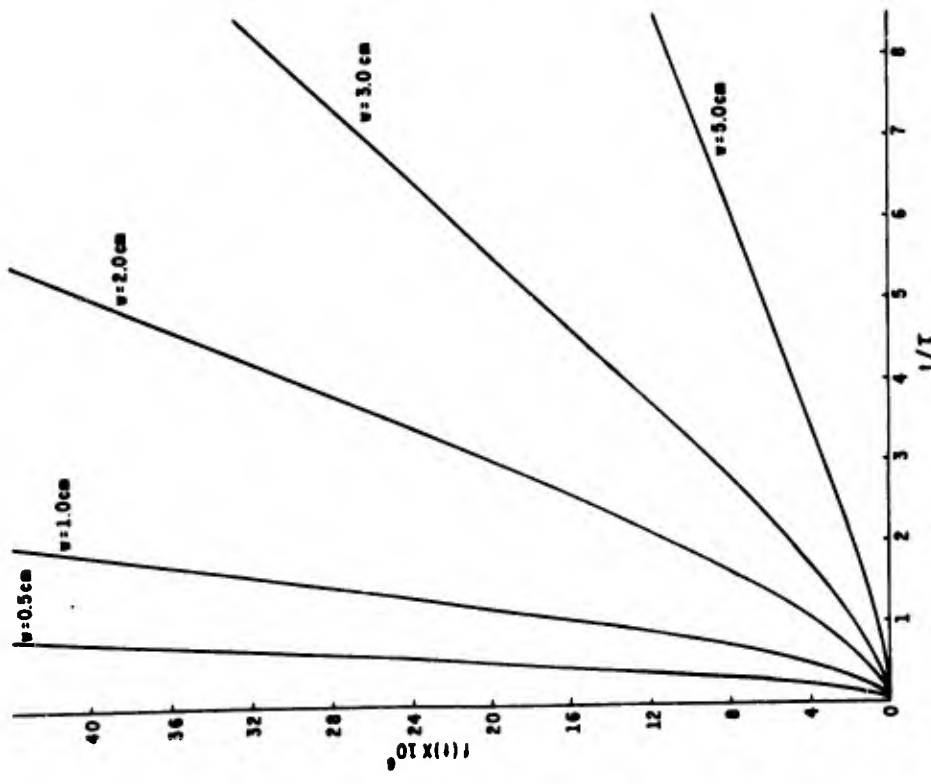


Figure 1

a. Contribution to  $\rho_1$  by thermodynamic-kinetic term  $f(t)$ .

b. Contribution to  $\rho_1$  by fluid dynamic term  $\psi(t)$  as a function of dimensionless time for various beam radii.

state solution of equation (14) becomes

$$\rho_1(R,t) = -(\alpha/c^2)(\gamma-1)(t-\tau)I(R) \quad (19)$$

and this may also be directly obtained from the First Law of Thermodynamics. The conclusion here is that steady state solutions to the sound equation are quite adequate in most situations associated with thermal blooming and may be obtained through either the First Law of Thermodynamics<sup>13</sup> or by setting the time derivatives of equation (13) to zero. On the other hand, for very small beam radii, the transient term may initially dominate for some value of  $t/\tau$  and lead to higher order beam instabilities.

The next case of interest is that of thermal blooming in the presence of wind. It will be assumed that the wind is uniform both in direction and intensity along the propagation axis, and is at right angles to the  $z$  axis. The problem may be formulated again by considering the equations of continuity and momentum, and linearizing them as before.

If the wind velocity is in the  $x$  direction, and the beam is propagating in the  $z$  direction, then the Euler's Equation becomes

$$\left(\frac{\partial}{\partial t} + v \frac{\partial}{\partial x}\right) \left[ \left(\frac{\partial}{\partial t} + v \frac{\partial}{\partial x}\right)^2 - c^2 \nabla^2 \right] \rho_1 = (\gamma-1) [1 - \exp(-t/\tau)] \alpha \nabla^2 I \quad (20)$$

where  $v$  is the wind velocity and  $\nabla^2 = \partial^2/\partial x^2 + \partial^2/\partial y^2 + \partial^2/\partial z^2$ . The development of the above equation follows exactly the development of the no wind case except that  $v = v_1 + v$ , namely the velocity is composed of particle velocity and wind velocity  $v$  having only an  $x$  component. Again, based upon similar arguments as under no-wind case, a steady state solution may be obtained if third order and second order time derivatives are dropped (under the same justification as before). Under the assumption that wind is subsonic, i.e.,  $c > v$  and consequently  $c^2 \gg v^2$ , equation (19) reduces to

$$\left(\frac{\partial}{\partial t} + v \frac{\partial}{\partial x}\right) \rho_1 = (\alpha/c^2)(\gamma-1)I(x,y,z) \quad (21)$$

where the value of  $1 - \exp(-t/\tau) \approx 1$ , since the steady state solutions assume that  $t/\tau \gg 1$ . The above equation may be written in explicit integral form of the retarded solution.



$$\rho_1 = -(\alpha/c^2 v)(\gamma-1) \int_{x-vt}^x I(x', y, z) dx' \quad (22)$$

First order explicit relationships have been thus developed between gas density perturbation and laser intensity after the transients have died out, both with wind (equation (22)) and without wind (equation (19)). Having defined the relationship between laser intensity and gas density, one may now proceed to the solution of the Eikonal equations where the above relationships are coupled through the refractive index as defined below.

$$(n-1)/(n_0-1) = \rho/\rho_0 = 1 + \rho_1/\rho_0 \quad (23)$$

## B. Geometrical Optics Treatment of Thermal Blooming

### 1. Geometrical Optics

In the presence of weak index of refraction changes, it is customary to solve the equations of geometrical optics by a perturbation expansion of the type by Keller.<sup>15</sup> There one assumes that any departure from a straight line ray trajectory is driven by

$$n(\bar{r}, t, \epsilon) = n_0 + n_1(\bar{r}, t) \quad (24)$$

where  $n(\bar{r}, t, \epsilon)$  is the local index of refraction at time  $t$  located at vector position  $\bar{r}$ , and where  $n_1(\bar{r}, t)$  is the perturbation to the constant index  $n_0$ . The parameter  $\epsilon$  measures the departure of  $n$  from  $n_0$  and will eventually be set equal to unity. One then proceeds by expanding the parametric representation for the ray trajectories in a Taylor series expansion around  $\epsilon = 0$ ,

$$\bar{r}(s, t, \bar{R}_0, \epsilon) = \bar{r}_0(s, t, \bar{R}_0) + \epsilon \bar{r}_1(s, t, \bar{R}_0) + (\epsilon^2/2!) \bar{r}_2(s, t, \bar{R}_0) + \dots \quad (25)$$

where it is assumed that

$$n(\bar{r}, t, \epsilon) = n[\bar{r}_0 + \bar{r}_1 + (\epsilon^2/2!) \bar{r}_2 + \dots, t] \quad (26)$$

In equation (25),  $\bar{R}_0$  is the initial location of a particular ray, usually taken at  $s = 0$ , where  $s$  is the ray arc length. One can show that the quantities appearing in equations (24), (25), and (26) must satisfy the "ray equation" of geometrical optics

$$(d/ds)(n\bar{r}/ds) = \nabla n \quad (27)$$

with two boundary conditions:

$$\bar{r}(0, t, \bar{R}_0) = \bar{R}_0$$

and

$$d\bar{r}(0, t, \bar{R}_0)/ds = \bar{u} \quad (28)$$

where  $\bar{u}$  specifies the initial direction of the ray at  $\bar{r} = \bar{R}_0$ . For our work here, we will always take  $\bar{u} = \hat{e}_z$ , where  $\hat{e}_z$  is a unit vector along the z axis, the assumed direction of propagation. Inserting equations (25) and (26) into (27) it is possible to evaluate succeeding terms in the Taylor series representation for  $\bar{r}$ . The first three such terms are

$$\bar{r}_0(s, \bar{R}_0) = \hat{e}_z s + \hat{e}_r R_0 ; \bar{R}_0 = \hat{e}_r \bar{R}_0 \quad (29)$$

$$\bar{r}_1(s, t, \bar{R}_0) = \int_0^s (s-\sigma) \nabla_T n_1(\bar{r}, \sigma) \Big|_{\bar{r}=\bar{r}_0(\sigma)} d\sigma \quad (30)$$

$$\begin{aligned} \bar{r}_2(s, t, \bar{R}_0) = 2 \int_0^s (s-\sigma) \left\{ (\bar{r}_1 \cdot \nabla_T) \nabla_T n_1 - (1/2) \nabla_T n_1^2 - \hat{e}_z \cdot \nabla_T n_1 \cdot \int_0^\sigma \nabla_T n_1 \Big|_{\bar{r}=\bar{r}_0(\tau)} d\tau \right. \\ \left. - \hat{e}_z \cdot \nabla n_1 \int_0^\sigma \nabla_T n_1(\bar{r}, t) \Big|_{\bar{r}=\bar{r}_0(\tau)} d\tau \right\} \Big|_{\bar{r}=\bar{r}_0(\sigma)} d\sigma \quad (31) \end{aligned}$$

where  $\nabla_T$  = transverse gradient, and where boundary conditions of equation (28) have already been applied. The degree of complexity of succeeding equations increases rapidly with result that most often only the sum of equations (29) and (30) is used to trace ray trajectories. Clearly, such a representation for  $r$  should only be valid when  $\bar{r}_1 \gg \bar{r}_2$  and  $(d\bar{r}/ds) \approx \hat{e}_z$ . This is the familiar "paraxial" approximation. Simply stated, this approximation assumes that the

true ray trajectories  $\bar{r}$  do not deviate "much" from the unperturbed ray trajectories  $\bar{r}_0$ .

It has been our contention and concern that in many of the experiments which are or were pursued, the conditions for validity of the paraxial optics were being violated (because one had the formation of "strong thermo-optical lenses") to the extent that higher order terms in the expansion for  $\bar{r}$  (equation (25)) should be kept. Therefore, in the next section, after the three physical problems considered in this report are described, a comparison is made of the traces for  $\bar{r}_0$ ,  $\bar{r}_0 + \bar{r}_1$ , and  $\bar{r}_0 + \bar{r}_1 + \bar{r}_2$  for the analytically simplest case.

## 2. Test Cases and Intensity Distributions

For the purposes here, one can conveniently describe three different problems. The first problem considers short-time regimes, with no wind. These conditions produce the purest form of the well known thermal blooming, the physical result being a beam which rapidly diverges with time. The case is also the simplest analytically because of the cylindrical symmetry of the problem.

The second and third problems are actually the same, the only difference being the time regimes of interest. For these cases, a constant cross wind is assumed. Case 2 treats the time development of the beam intensity profile for short-time regimes after the beam power has been turned on. Case 3 is then the steady state wind problem, or in other words, Case 2 for long-time regimes. The refractive index equations to be used for these three problems were developed earlier. It is stressed again that the solutions obtained here for all the intensity patterns are not self-consistent, in that the index changes described by equations (19), (22), and (23) use the initial intensity distribution and do not allow for subsequent changes. However, it is apparently true that two important effects happen near the transmitter: (1) the intensity pattern remains very close to its unperturbed shape; and (2) most of the ray bending is imparted in this region. As a result, we have seen remarkable agreement between experiment and theory.<sup>13</sup>

Computation of intensity patterns can be accurately accomplished within the approximations of ray optics if one simply specifies the complete family of ray trajectories  $\bar{r}(s,t,\bar{R}_0)$ . (For a fixed time  $t$ , the family is specified here by all possible initial points  $\bar{R}_0$ .) That is to say, when performed properly, the tasks of determining the trajectories  $\bar{r}(s,t,\bar{R}_0)$ , and then computing the

resulting intensity patterns can be completely separated with the desirable result that one needs only to introduce errors into the approximation for the analytic form of  $\bar{r}(s,t,\bar{R}_0)$ . Thus, because there was some question of the accuracy of the paraxial approximations, we will compare the ray traces of  $\bar{r}_0 + \bar{r}_1$  and  $\bar{r}_0 + \bar{r}_1 + (\bar{r}_2/2)$  for the experimental Case 1 as described above.

In Figure 2, a plot of first and second order perturbation to the ray trajectory versus  $\bar{R}_0$  is presented for the most severe ray bending case of high pressure (400 torr) and long times ( $\sim 300$  msec). Clearly, even when the deviation of the rays from their unperturbed position ( $\bar{R}_0$ ) is large, the first order paraxial approximation still agrees fairly well with the more accurate second order solution. Because the second order solution is significantly more complex than the first, it was felt that the deviation of these quantities as shown in Figure 2 was not sufficient to require the use of the second order solution in the computation of the intensity profiles.

One can show that the intensity along any particular ray of a family of rays is given by<sup>12</sup>

$$I(\bar{r}(s),t,\bar{R}_0) = I(\bar{r}(0),t,\bar{R}_0) \exp\left\{-\int_0^s (\nabla \cdot \frac{d\bar{r}}{ds'}) ds'\right\} \quad (32)$$

where  $\bar{r}(0) = \bar{R}_0$  and where  $I(\bar{r}(s),t,\bar{R}_0)$  and  $I(\bar{r}(0),t,\bar{R}_0)$  are the intensities at  $\bar{r}(s)$  and  $\bar{r}(0)$ , respectively. The integration of equation (32) is taken along the particular ray of interest. It is important to realize here that when one computes the intensity in this fashion, it is only proper to plot  $I(\bar{r}(s),t,\bar{R}_0)$  versus  $\bar{r}(s,t,\bar{R}_0)$ . It is a common mistake to plot  $I(\bar{r}(s),t,\bar{R}_0)$  versus  $\bar{R}_0$ .

The line integrations are most easily performed when trajectories are parametrically represented as they are in this case. However, to perform the divergence operation and subsequent line integration indicated in equation (32), one would seemingly have to first solve for  $s = s(\bar{r}(\bar{R}_0,t))$  unless some other simplifications are made (i.e., identifying  $\partial/\partial x \rightarrow \partial/\partial x_0$ , etc., where  $x_0$  is the x-coordinate of  $\bar{R}_0$ ). This problem can be circumvented by appropriate identification of parametric coordinates and by use of a Jacobian in the following way:

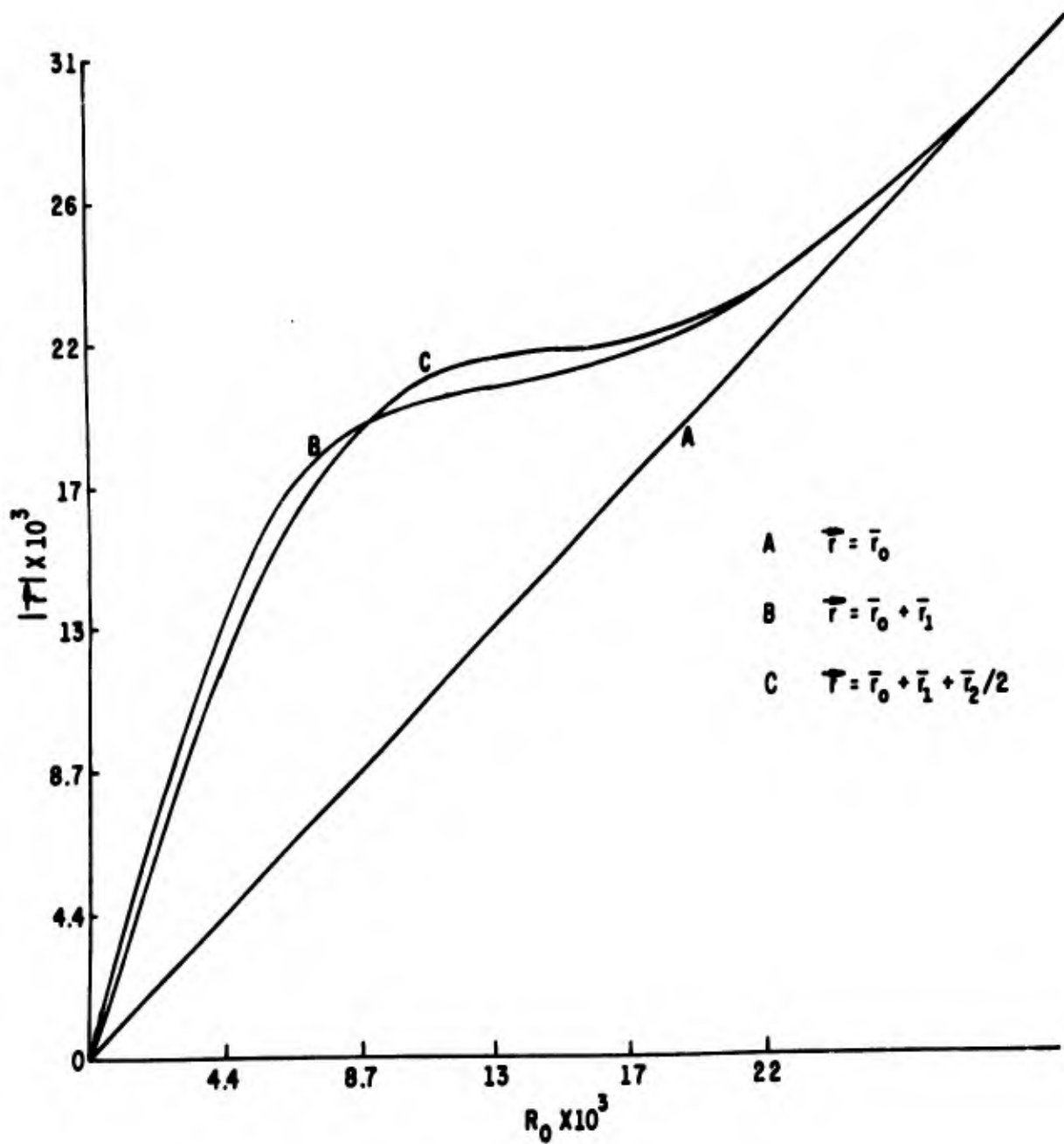


Figure 2. Evaluation of the importance of second order term in the Taylor Series Expansion of the Eikonal ray trajectories.

$$\bar{d}\bar{r}/ds = \bar{f}(s, t, \bar{R}_0) = \bar{f}(s, t, x_0, y_0)$$

$$\nabla \equiv (\partial/\partial x, \partial/\partial y, \partial/\partial z)$$

$$\bar{r}(s, t, \bar{R}_0) = [x(s, t, \bar{R}_0), y(s, t, \bar{R}_0), z(s, t, \bar{R}_0)]$$

then

$$\nabla \cdot \bar{d}\bar{r}/ds = (J\nabla_0) \cdot \bar{d}\bar{r}/ds \quad (33)$$

where

$$J = \begin{bmatrix} \partial x_0/\partial x & \partial y_0/\partial x & \partial s/\partial x \\ \partial x_0/\partial y & \partial y_0/\partial y & \partial s/\partial y \\ \partial x_0/\partial z & \partial y_0/\partial z & \partial s/\partial z \end{bmatrix} = \begin{bmatrix} \partial x/\partial x_0 & \partial y/\partial x_0 & \partial z/\partial x_0 \\ \partial x/\partial y_0 & \partial y/\partial y_0 & \partial z/\partial y_0 \\ \partial x/\partial s & \partial y/\partial s & \partial z/\partial s \end{bmatrix}^{-1} \quad (34)$$

and

$$\nabla_0 \equiv \begin{bmatrix} \partial/\partial x_0 \\ \partial/\partial y_0 \\ \partial/\partial s \end{bmatrix} \quad (35)$$

The quantity on the right side of equation (33) will thus remain a function of the parametric coordinates, so that the proper line integration specified in equation (32) can be performed. This procedure introduces no error into the computation of the intensity profile on a nonplanar surface of constant phase. The intensity profile in a plane perpendicular to the propagation direction ( $I_{\perp}(r, t, R_0)$ ) is thus more properly given by

$$I_{\perp}[\bar{r}(s), t, \bar{R}_0] = I[\bar{r}(s), t, \bar{R}_0][\hat{e}_z \cdot \bar{d}\bar{r}(s)/ds] \quad (36)$$

Thus, by using the procedures described above, it is possible to achieve a rigorously normalized and correct intensity distribution, no matter how bad or good the approximations may have been for  $\bar{r}(s, t, \bar{R}_0)$ . In particular, for the

case of an initially collimated beam and the paraxial approximations for  $\bar{r}(s,t,\bar{R}_0)$  (which is what is being treated here) equations (34) and (36) become respectively as below.

$$J = \begin{bmatrix} \partial x_0/\partial x & \partial y_0/\partial x & 0 \\ \partial x_0/\partial y & \partial y_0/\partial y & 0 \\ \partial x_0/\partial z & \partial y_0/\partial z & 1 \end{bmatrix} = \begin{bmatrix} \partial x/\partial x_0 & \partial y/\partial x_0 & 0 \\ \partial x/\partial y_0 & \partial y/\partial y_0 & 0 \\ \partial x/\partial s & \partial y/\partial s & 1 \end{bmatrix}^{-1} \quad (37a)$$

$$I[\bar{r}(s),t,\bar{R}_0] = I[\bar{r}(s),t,\bar{R}_0] \quad (38a)$$

For the cylindrically symmetric problem, equation (37a) reduces further to

$$J = \begin{bmatrix} \partial R_0/\partial R & 0 & 0 \\ 0 & 1 & 0 \\ \partial R_0/\partial z & 0 & 1 \end{bmatrix} = \begin{bmatrix} \partial R/\partial R_0 & 0 & 0 \\ 0 & 1 & 0 \\ \partial R/\partial s & 0 & 1 \end{bmatrix}^{-1} \quad (37b)$$

where  $\nabla_0 = (1/R_0)(\partial/\partial R_0)(R_0)$ , which is useful where no asymmetry exists such as winds perpendicular to z axis.

The two-dimensional solution for the intensity specified by equation (32), using equations (22) and (23) to describe the refractive index, is plotted in Figures 3 and 4. The former is at a fixed observation distance ( $z = 560$  cm) showing the intensity profiles as a function of time; the latter is at a steady state distribution ( $t \rightarrow \infty$ ) at observation distances between  $z = 0$  and  $z = 560$  cm.

Under the appropriate conditions, it is possible to obtain an analytical expression for the laser intensity distribution along either the x or y axis. If it is assumed that the wind is out of the minus x-axis, equations (22) and (23) may be combined to specify the refractive index under small perturbation limits.

$$n(x,y,z) = 1 + (n_0 - 1) \left\{ 1 - \alpha[(\gamma - 1)/c^2 \rho_0 v] \int_{x-vt}^x I_\ell(x,y,z) dx \right\} \quad (40)$$

Using the paraxial approximation for ray trajectories, equation (32) for the intensity, and computing along  $y_0 = 0$  axis, it is possible to derive an analytical, non-self-consistent (as described earlier) intensity distribution

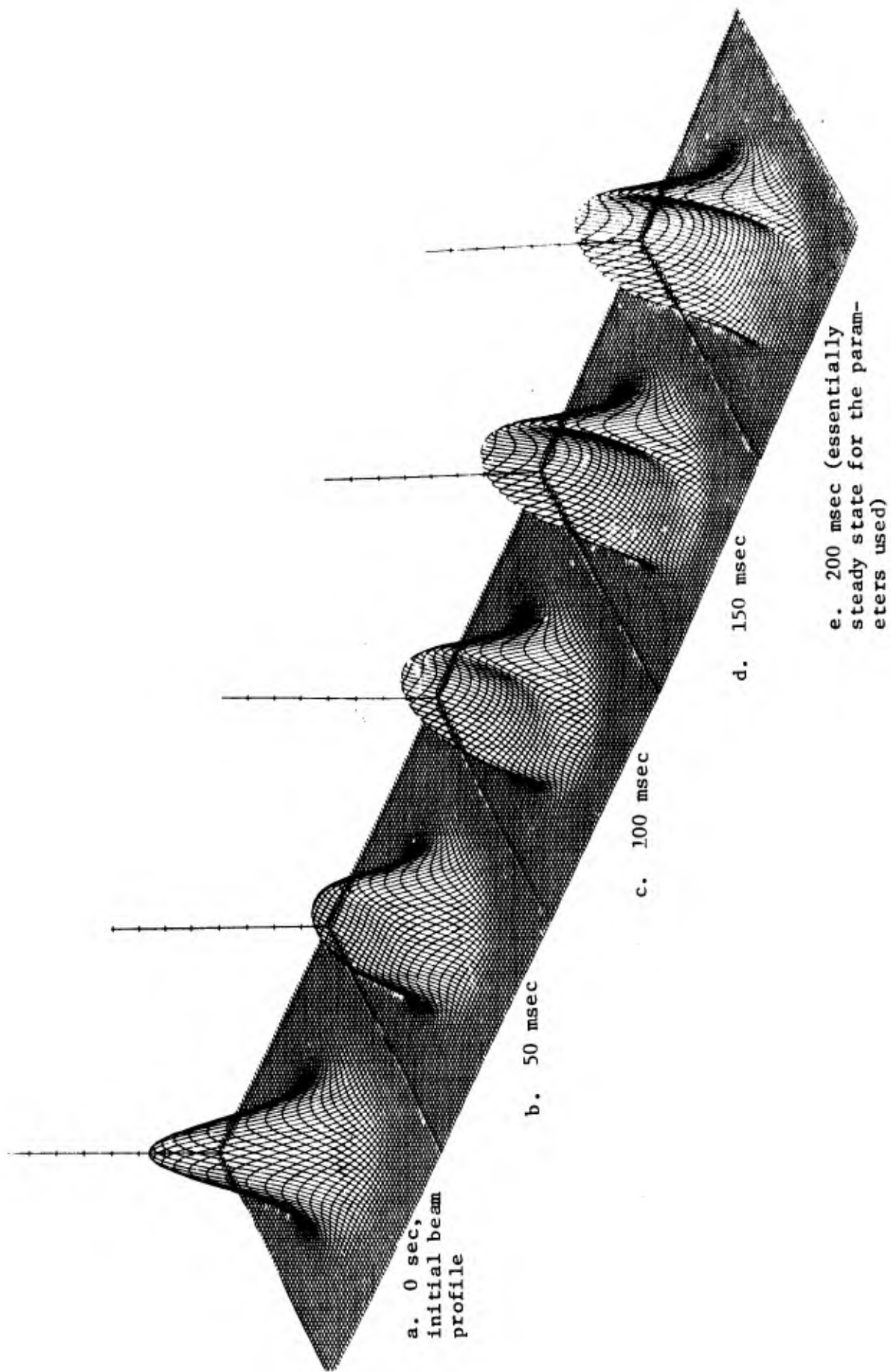


Figure 3. Development of a thermally bloomed beam with a 50-cm/sec wind as a function of time.  $P_T=63$  watts,  $z = 560$  cm,  $w = 1.5$  cm,  $\alpha = 2 \times 10^{-3}$  cm<sup>-1</sup>, and  $\gamma = 1.4$ . The time development occurs as listed above.



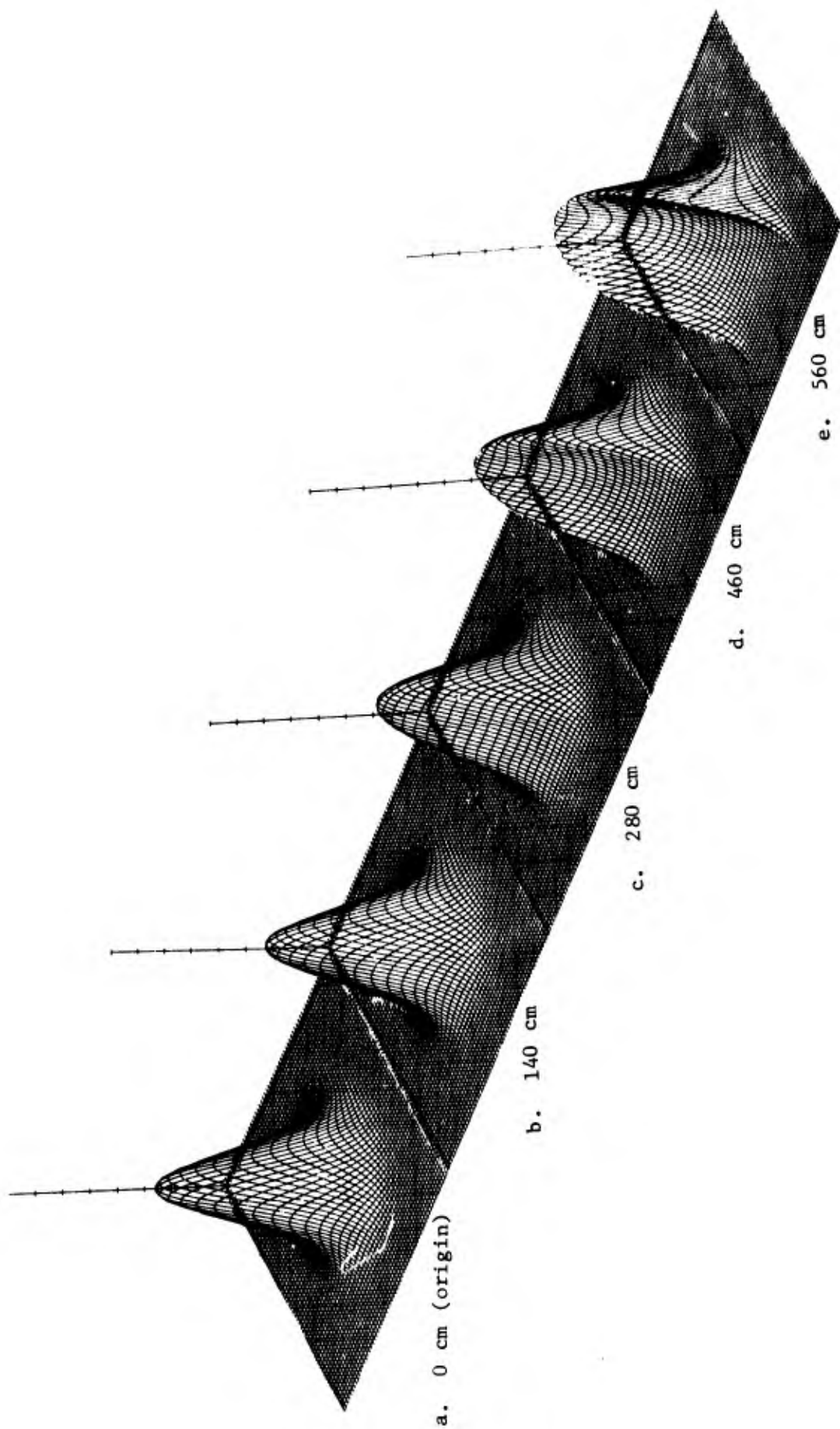


Figure 4. Development of thermally bloomed beam with a 50-cm wind at steady state for various distances from the transmitter. The beam parameters are the same as in Figure 3. Notice that the beam does not change substantially its profile in the first half of the distance that it is propagating. This supports our contention that non-self-consistent calculations are reasonably good representations of the effect.

(see appendix).

$$\ln(I/I_0) = (-2M/\alpha) \left\{ \phi \int_0^z \frac{[1-\exp(-\alpha s)] ds}{1 + (2M\phi/\alpha^2)[\alpha s - 1 + \exp(-\alpha s)]} \right. \\ \left. + \theta \int_0^z \frac{[1-\exp(-\alpha s)] ds}{1 + (2M\theta/\alpha^2)[\alpha s - 1 + \exp(-\alpha s)]} \right\} \quad (41)$$

where

$$M = 2(\gamma-1)(n_0-1)\alpha I_0/c^2\rho_0 w^2 v$$

$$\phi = x_0 \exp(-2x_0^2/w^2) - (x_0 - vt) \exp[-2(x_0 - vt)^2/w^2]$$

$$\theta = \int_{x_0 - vt}^{x_0} \exp(-2x^2/w^2) dx$$

For this derivation, as before, a collimated Gaussian beam is used

$$I_0 = I_{00} \exp(-2x_0^2/w^2)$$

As mentioned before, the solution is along  $y_0 = 0$ , and  $x_0$  and  $y_0$  are ray positions in the  $z = 0$  plane,  $w$  is the  $e^{-2}$  radius of the laser beam, and it is assumed to be the same along both the  $x$  and  $y$  axes.

Equation (41) may be integrated to yield the analytical expression for the intensity ratio.

$$\frac{I(x, 0, z)}{I_{00}} = \frac{\exp(-2x^2/w^2)}{\{1 + (2M\phi/\alpha^2)[\alpha z - 1 + \exp(-\alpha z)]\} \{1 + (2M\theta/\alpha^2)[\alpha z - 1 + \exp(-\alpha z)]\}} \quad (42)$$

Under steady state conditions, i.e.,  $vt \gg x_0$ ,  $\phi$  and  $\theta$  become

$$\phi_{ss} = x_0 \exp(-2x_0^2/w^2) \\ \theta_{ss} = \int_{-\infty}^{x_0} \exp(-2x^2/w^2) dx \quad (43)$$

Since the right-hand side of equation (42) is written in terms of  $x_0$ , and the desired intensity definition is in terms of  $x$ , a transformation from  $x_0$  to  $x$  is required as defined below and derived in the appendix.

$$x = x_0 - (M/\alpha^2)[\alpha z - 1 + \exp(-\alpha z)] \exp(2x_0^2/w^2)$$

Equation (42) under steady state conditions is plotted in Figure 5, with wind  $v$  as a parameter,  $z = 560$  cm and  $\alpha = 2 \times 10^{-3}$  cm<sup>-1</sup>. It is interesting to note that one sees the beam bending effect asymptoting (established by the location of the intensity peak) to a value of  $z/w \approx 1$  or one beam radius. Also, there is an intensification effect at certain slow wind velocities which has been experimentally seen in certain instances.<sup>16</sup>

### Validity Limits

In considering the use of the above discussed techniques, it is necessary to investigate the limits of validity of such techniques. It is especially important to examine the density-refractive index relationship defined by equations (19) and (23). These relationships are based upon weak interactions where the solution for the sound wave equation may be specified by  $\rho = \rho_0 + \epsilon \rho_1$ , where  $\epsilon$  is the order of smallness. If we specify a stronger interaction one has to look at the next order term, namely  $\rho = \rho_0 + \epsilon \rho_1 + \epsilon^2/2 \rho_2$ . This is derived and discussed in more detail in a subsequent report,<sup>17</sup> and extended to the sum of all orders of smallness, resulting in a refractive index equation covering all values of density perturbations. For the case of plane thermal blooming

$$n = 1 + (n_0 - 1) \exp \left\{ - \frac{(\gamma - 1) \alpha (t - \tau) I_0 \exp[-2R^2/w^2 - \alpha z]}{c^2 \rho_0} \right\} \quad (44)$$

the refractive index relation becomes as above.

This examination is carried in the form of the symmetrical-no wind problem, but it could have been just as well done for the wind case.

Series solutions for the ray trajectories and the intensity distribution may be obtained for the Eikonal equations using the equation for the index of refraction (equation (44)) derived elsewhere.<sup>17</sup> We consider only the transverse gradient of the index of refraction and thus the differential equation of interest becomes indicated

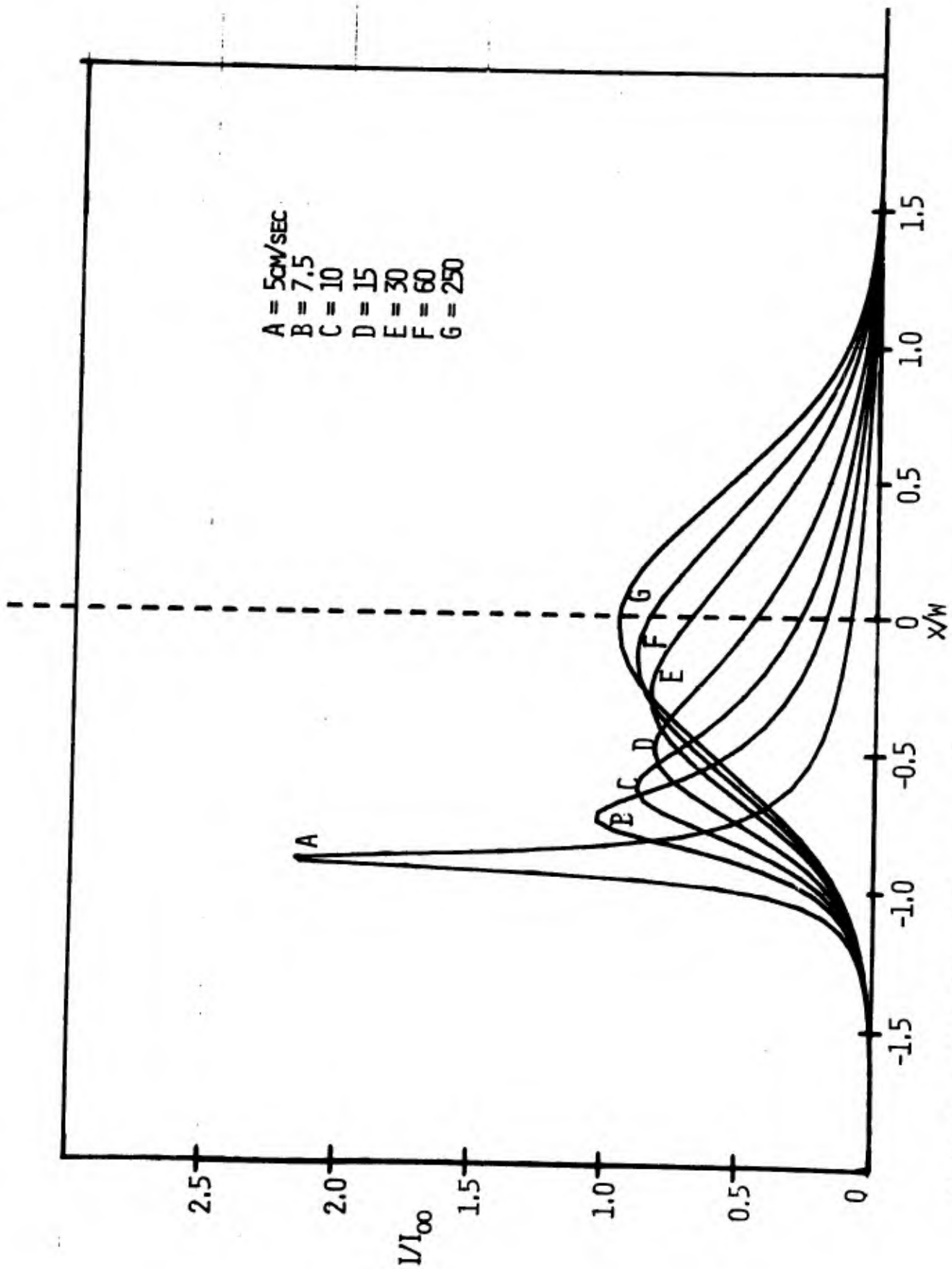


Figure 5. Intensity profiles at  $z = 560$  cm for various wind velocities at steady state along  $y = 0$  plane. Notice the intensification and bending effects for slow wind speeds. Also notice that at sufficiently high winds, no thermo-optical effects occur. Beam parameters are the same as in Figure 3.

$$\frac{d}{ds} \left( n \frac{dr}{ds} \right) = \nabla_{\perp} n$$

The solutions of this equation require integrations along the ray trajectories. If we assume an initially collimated beam for which  $r(t=0) = r_0$ , then the effect of the ray deviations on the values of  $n$  and  $\nabla_{\perp} n$  along the actual ray trajectories may be included by expanding these expressions in a Taylor series about  $r = r_0$ .

If as a first approximation, paraxial ray trajectories are assumed, it is possible to calculate the first order terms in time for the ray trajectories. The second order approximations to the ray trajectories are then used to obtain second order terms in time for the ray trajectories. Using the ray trajectories obtained in this manner, the intensity distribution may be obtained from equation (32).

The solutions for the trajectories and intensity distribution rapidly increase in complexity as higher order terms in the series solution are obtained. Solutions to fourth order in time have been obtained but are so unwieldy as to be of little practical use. Some general observations can, however, be made based on these solutions.

The dominant terms in the coefficients of the powers of time in the series solution are independent of pressure. Thus, the pressure dependence should be expected to be weak. This is in agreement with the experimental observations.

The dominant terms in the coefficients of the powers of time are those for which  $n_0 - 1$  appears to the same power as the time. A large multiplicative constant always accompanies  $n_0 - 1$  to the same order in which  $n_0 - 1$  appears. Thus a series expansion in  $n_0 - 1$  should not be expected to converge rapidly. This should be expected on the physical grounds as a result of the nature of the refractive index driving function.

The lowest order of  $z$  appearing in the dominant coefficients for the different orders of time increases for high orders of time. Thus while  $z^2$  is the lowest order in  $z$  for the term of first order in time,  $z^4$  is the lowest order in  $z$  for the term of second order in time,  $z^6$  is the lowest order in  $z$  for the term of third order in time, and  $z^8$  is the lowest order in  $z$  for the term of fourth order in time. Thus an expansion in  $z$  would have to be carried to many orders to correctly represent time dependence of relatively low order.

A characteristic time is determined by the nature of the absorbing gas and the power and diameter of the laser beam. Normalizing the time to this characteristic time scale permits one to estimate the rapidity of convergence of the series solution. In general, convergence is rapid when the normalized time is much less than unity. For the conditions of the experiment the fourth order series solution converges with less than 5 percent error for 100 msec at 25 torr and 140 msec at 200 torr. Thus an even higher order solution is required in order to achieve good convergence to the 200-msec experimental observation.<sup>13</sup>

The above considerations lead us to conclude that the approximation of the exponential refractive index equation (42) by series expansion in time does not lead to solutions which converge sufficiently rapidly to be accurate for experimental conditions normally encountered. On the other hand, if the absorption coefficient is low, as in air, then the first order approximation to exponential form of the refractive index is adequate. Because of the above rationales the evaluation of thermal blooming with and without wind has to be also accomplished with the exponential form, and this is covered in a subsequent report.<sup>17</sup>

#### APPENDIX

Equation (41) which describes the ray intensity may be derived by following the steps outlined by equations (29), (30), (32), and (33), if  $y_0$  (the  $y$  coordinate in the  $z = 0$  plane) is set to zero. It is easily shown that if  $y_0 = 0$ , also the wind is in the  $x$  plane. Equation (32), whose solution is the case in point, becomes

$$I(x,0,z) = I(x_0,0,0) \exp\left\{-\int_0^z [\nabla \cdot (d\bar{r}/ds)] ds\right\} \quad (I-1)$$

For this derivation,  $\bar{r}$  is taken as the paraxial ray trajectory vector, and based upon the rationales presented earlier and in Figure 3, it is limited to  $\bar{r} = \bar{r}_0 + \bar{r}_1$ . From equations (29) and (30), one therefore has

$$\bar{r} = \hat{\epsilon}_x \left[ x_0 + \int_0^s (s-\sigma) \frac{\partial n}{\partial x} \Big|_{\bar{r}_0} d\sigma \right] + \hat{\epsilon}_y \left[ y_0 + \int_0^s (s-\sigma) \frac{\partial n}{\partial y} \Big|_{\bar{r}_0} d\sigma \right] + \hat{\epsilon}_z s \quad (I-2)$$

$$\frac{d\bar{r}}{ds} = \hat{\epsilon}_x \int_0^s \frac{\partial n}{\partial x} \Big|_{\bar{r}_0} d\sigma + \hat{\epsilon}_y \int_0^s \frac{\partial n}{\partial y} \Big|_{\bar{r}_0} d\sigma + \hat{\epsilon}_z \quad (I-3)$$

where  $\epsilon_x, \epsilon_y, \epsilon_z$  are Cartesian unit vectors. Using equations (33) and (37a), it is possible to define  $\nabla \cdot d\bar{r}/ds$ .

$$\begin{aligned} \nabla \cdot \frac{d\bar{r}}{ds} \Big|_{\bar{r}} &= \left[ \int_0^s \frac{\partial^2 n}{\partial x^2} \Big|_{\bar{r}_0} d\sigma \right] \left( \frac{\partial x_0}{\partial x} \right) + \left[ \int_0^s \frac{\partial^2 n}{\partial x \partial y} \Big|_{\bar{r}_0} d\sigma \right] \left( \frac{\partial y_0}{\partial x} + \frac{\partial x_0}{\partial y} \right) \\ &+ \left[ \int_0^s \frac{\partial^2 n}{\partial y^2} \Big|_{\bar{r}_0} d\sigma \right] \left( \frac{\partial y_0}{\partial y} \right) \end{aligned} \quad (I-4)$$

Note that the integration indicated by equation (I-1) is along the ray trajectories  $\bar{r}$ . By the transformation used to obtain equation (I-4), one can now integrate along the  $\bar{r}_0$  trajectory, or more specifically, along the parametric variable which characterizes the ray trajectories "s."

Using equation (40) for the index of refraction, it is readily shown that along  $y = y_0 = 0$  the following relationships exist:

$$\begin{aligned} \int_0^s \frac{\partial^2 n}{\partial x^2} d\sigma &= (2M/\alpha) [(1-\exp(-\alpha s)) \{x_0 \exp(-2x_0^2/w^2) \\ &- (x_0 - vt) \exp(-2(x_0 - vt)^2/w^2)\}] = (2M/\alpha) [1-\exp(-\alpha s)] \phi \\ \int_0^s \frac{\partial^2 n}{\partial y^2} d\sigma &= (2M/\alpha) [1-\exp(-\alpha s)] \int_{x_0 - vt}^{x_0} \exp(-2x/w^2) dx \\ &= (2M/\alpha) [1-\exp(-\alpha s)] \theta \end{aligned} \quad (I-5)$$

$$\int_0^s \frac{\partial^2 n}{\partial x_0 \partial y_0} d\sigma = 0$$

$$\left. \frac{\partial n(x,y,z)}{\partial x} \right|_{\mathbf{r}_0} = \frac{\partial n(x_0, y_0, z)}{\partial x_0}$$

$$\left. \frac{\partial n(x,y,z)}{\partial y} \right|_{\mathbf{r}_0} = \frac{\partial n(x_0, y_0, z)}{\partial y_0}$$

The evaluation of  $\partial x_0/\partial x$ ,  $\partial y_0/\partial x$ ,  $\partial x_0/\partial y$ , and  $\partial y_0/\partial y$  as required by equation (I-4) is accomplished by first noting (from equation (I-2)) that

$$x = x_0 + \int_0^s (s-\sigma) \frac{\partial n}{\partial x_0} d\sigma$$

$$y = y_0 + \int_0^s (s-\sigma) \frac{\partial n}{\partial y_0} d\sigma \quad (I-6)$$

after which the evaluation of the Jacobian of equation (37a) (or rather its inverse) yields the necessary derivatives (at  $y_0 = y = 0$ ). Equation (I-4) becomes as written below.

$$\nabla \cdot (d\mathbf{r}/ds) \Big|_{y_0=0} = \left[ \int_0^s \frac{\partial^2 n}{\partial x_0^2} d\sigma \right] \left( \frac{\partial x}{\partial x_0} \right)^{-1} + \left[ \int_0^s \frac{\partial^2 n}{\partial y_0^2} d\sigma \right] \left( \frac{\partial y}{\partial y_0} \right)^{-1} \quad (I-7)$$

as it is readily determined (from equation (I-6)) that  $\partial x/\partial y_0 = \partial y/\partial x_0 = 0$ .

Substituting the appropriate derivatives of equation (I-6) into (I-7) and combining with (I-5), it is possible to perform the integration along "s" as required by (I-1), thus resulting in the intensity equation (41) for the case of  $y = 0$  and wind in the x plane.



## REFERENCES

1. Gordon, J. P., Leite, R. C. C., Moore, R. S., Porto, S. P. S., Whinnery, J. R., "Long-Transient Effects in Lasers with Inserted Liquid Samples," J. Appl. Phys. 36, 3, 1965.
2. Callen, W. R., Huth, B. G., Pantell, R. H., "Optical Patterns of Thermally Self-Defocused Light," Appl. Phys. Letters 11, 103, 1967.
3. Whinnery, J. R., Miller, D. T., Dabby, F., "Thermal Convection and Spherical Aberration Distortion of Laser Beams in Low-Loss Liquids," IEEE J. Quantum Electronics QE-3, 382, 1967.
4. Carman, R. L., Kelley, P. L., "Time Dependence in the Thermal Blooming of Laser Beams," Appl. Phys. Letters 12, 241, 1968.
5. Leite, R. C. C., Moore, R. S., Whinnery, J. R., "Low Absorption Measurements by Means of the Thermal Lens Effect Using an He-Ne Laser," Appl. Phys. Letters 5, 141, 1964.
6. Rieckhoff, K. E., "Self-Induced Divergence of CW Laser Beams in Liquids-- A New Nonlinear Effect in the Propagation of Light," Appl. Phys. Letters 9, 87, 1966.
7. Leite, R. C. C., Porto, S. P. S., Damen, T. C., "The Thermal Lens Effect as a Power-Limiting Device," Appl. Phys. Letters 10, 100, 1967.
8. Inaba, H., Ito, H., "Observation of Power-Dependent Distortion of an Infrared Beam at 10.6  $\mu\text{m}$  from a CO<sub>2</sub> Laser During Propagation in Liquids," IEEE J. Quantum Electronics QE-4, 45, 1968.
9. Akhmanov, S. A., Krindach, D. P., Migulin, A. V., Sukorukov, A. P., Khokhlov, R. V., "E-12-Thermal Self-Actions of Laser Beams," IEEE J. Quantum Electronics QE-4, 568, 1968.
10. Gebhardt, F. G., Smith, D. C., "Effects of Wind on Thermal Defocusing of CO<sub>2</sub> Laser Radiation," Appl. Phys. Letters 14, 52, 1969.
11. Smith, D. C., "Thermal Defocusing of CO<sub>2</sub> Laser Radiation in Gases," IEEE J. Quantum Electronics QE-5, 600, 1969.
12. Born, M., Wolf, E., Principles of Optics, Pergamon, New York, p. 116, 1959.
13. Kenemuth, J. R., Hogge, C. B., Avizonis, P. V., "Thermal Blooming of a 10.6- $\mu$  Laser Beam in CO<sub>2</sub>," Appl. Phys. Letters 17, 220, 1970.
14. Carslaw, H. S., Jaeger, J. C., Conduction of Heat in Solids, University Press, Oxford, p. 460, 1959.
15. Keller, J. B., "Wave Propagation in Random Media," Proceedings of Symposia in Applied Mathematics, 13, p. 227, Amer. Math. Soc., New York, 1960.
16. Hull, R. J., "Proceedings of the Laser Propagation Meeting," LTP-3, III, 3-87, Lincoln Laboratories, 1969.

17. Kenemuth, J. R., Hogge, C. B., Butts, R. R., Avizonis, P. V., "Geometric Optics of Thermal Blooming in Gases II," to be published.

## A GEOMETRICAL OPTICS TREATMENT OF THERMAL BLOOMING

C. B. Hogge and R. R. Butts

In a geometric, or ray, optics treatment of the problem of thermal blooming of a laser beam propagating in an absorbing medium, it is customary to make what is called the "paraxial" approximation. This approximation consists of representing the ray trajectories by the first order terms in a perturbation expansion solution of the ray equation. In the terminology used below, the paraxial approximation corresponds to setting  $r = r_0 + r_1$ . In what follows, we examine the validity of this approximation for a severe case of a beam propagating through a highly absorbing medium by comparing the relative sizes of the first and second order terms in the perturbation expansion. We also investigate the convergence of another series solution of the ray equation.

By the ray equation, we mean

$$\frac{d}{ds} \left( n \frac{dr}{ds} \right) = \nabla n$$

where  $n$  denotes the index of refraction,  $r$  is the vector  $(R, z)$  to a point on a light ray, and  $s$  denotes arc length measured along a ray. We derive  $n$  by assuming the relation

$$\frac{n - 1}{\rho} = \frac{n_0 - 1}{\rho_0}$$

where  $\rho$  denotes density, and  $\rho_0$  and  $n_0$  denote the initial density and refractive index, respectively. The density can be found from the first law of thermodynamics and the equation of state of an ideal gas. Assumption of no wind and of a collimated beam with a Gaussian initial intensity profile results in the following form for  $n$ :

$$n = 1 + (n_0 - 1) \exp \left\{ -k_1 t e^{-k_2 R^2} e^{-\alpha z} \right\}$$

where  $\alpha$  is the absorption coefficient of the gas,  $k_2$  is a constant depending on the beam size, and  $k_1$  is a constant which depends on both the gas and the

peak initial intensity. Time and the spatial coordinates are denoted by  $t$ ,  $R$ , and  $z$ , respectively, the  $z$ -axis being the axis of the beam. If one assumes a wind of speed  $v$  in the  $x$  direction, then the index of refraction takes the form

$$n = 1 + (n_0 - 1) \exp \left\{ \frac{-k_1}{v} e^{-\alpha z} \int_{x-vt}^x e^{-k_2 u^2} du \right\}$$

We emphasize that these calculations are not self-consistent in the sense that the initial intensity profile is used to calculate the refractive index; the fact that the intensity changes with time is not taken into account. The methods illustrated below are the same, in principle, for the problem of thermal blooming with or without wind. To simplify the arithmetic, we will treat here only the case with cylindrical symmetry (i.e., no wind). The problem of thermal blooming in the presence of a wind is treated more extensively by Dr. Avizonis elsewhere in this digest.

We investigated two methods for obtaining an approximate solution to the ray equation--a perturbation expansion due to J. B. Keller\* and a power series expansion. A third method, a different power series expansion, was investigated by Dr. John Kenemuth.\*\*

In the perturbation expansion, one writes the index of refraction as

$$n = 1 + \epsilon \mu$$

and assumes that the components of the corresponding ray trajectories are holomorphic in  $\epsilon$ . It is understood that we are interested in the value of  $r$  when  $\epsilon = 1$ . The equation to be solved is

$$\frac{dn}{ds} \frac{dr}{ds} + \frac{d^2 r}{ds^2} n = \nabla n$$

with conditions

$$r|_{s=0} = (R_0, 0) \quad \text{and} \quad \left. \frac{dr}{ds} \right|_{s=0} = \hat{e}_z$$

---

\*Keller, J. B., "Wave Propagation in Random Media," Proceedings of Symposia in Applied Mathematics, 13, p. 227, Amer. Math. Soc., New York, 1960.

\*\*Private communication.

where  $\hat{e}_R$  and  $\hat{e}_z$  denote unit vectors in the radial and z directions, respectively. We write

$$\mathbf{r} = \mathbf{r}_0 + \epsilon \mathbf{r}_1 + \epsilon^2 \mathbf{r}_2 + \dots$$

Then

$$\epsilon \frac{d\mu}{ds} \sum_{i=0}^{\infty} \epsilon^i \frac{d\mathbf{r}_i}{ds} + (1 + \epsilon\mu) \sum_{i=0}^{\infty} \epsilon^i \frac{d^2\mathbf{r}_i}{ds^2} = \epsilon \nabla\mu$$

Setting  $\epsilon = 0$  in the above equation, we obtain

$$\frac{d^2\mathbf{r}_0}{ds^2} = 0$$

Integrating, we get

$$\mathbf{r}_0 = R_0 \hat{e}_r + s \hat{e}_z$$

Differentiating the ray equation with respect to  $\epsilon$  and setting  $\epsilon = 0$  yields

$$\frac{d^2\mathbf{r}_1}{ds^2} = \nabla\mu \Big|_{\mathbf{r}=\mathbf{r}_0} - \left( \frac{d\mathbf{r}_0}{ds} \cdot \nabla\mu \Big|_{\mathbf{r}=\mathbf{r}_0} \right) \frac{d\mathbf{r}_0}{ds}$$

with

$$\mathbf{r}_1 \Big|_{s=0} = \frac{d\mathbf{r}_1}{ds} \Big|_{s=0} = 0$$

The solution is

$$\mathbf{r}_1(s) = \int_0^s (s-t) \nabla_{T\mu}(\mathbf{r}_0(t)) dt$$

where  $\nabla_T$  denotes the transverse gradient operator. Successive differentiations yield further coefficients in the expansion. Solving for  $\mathbf{r}_2$ ,

$$\begin{aligned}
r_2(s) = & \int_0^s (s-t) \left\{ (r_1 \cdot \nabla_T) \nabla_T^\mu(r_0(t)) - \frac{1}{2} \nabla_T^{\mu^2}(r_0(t)) \right. \\
& - \hat{e}_z \nabla_T^\mu(r_0(t)) \cdot \int_0^t \nabla_T^\mu(r_0(\tau)) d\tau \\
& \left. - \frac{\partial \mu}{\partial z} \int_0^t \nabla_T^\mu(r_0(\tau)) d\tau \right\} dt
\end{aligned}$$

An alternate method of obtaining an approximate solution is to regard the transverse component of  $r$  as a function of  $R_0$  and  $z$ , say  $f(R_0, z)$ . Expanding in  $z$ , we get

$$f(R_0, z) = f_0(R_0) + f_1(R_0)z + f_2(R_0) \frac{z^2}{2!} + \dots$$

Our initial conditions tell us that  $f_0(R_0) = R_0$  and  $f_1(R_0) = 0$ . It remains to solve for  $f_n$  when  $n \geq 2$ . This can be done by taking successive derivatives with respect to  $s$ , setting  $s = 0$  at each step. The result to order  $z^4$ , is

$$\begin{aligned}
f(R_0, z) = & R_0 + \frac{1}{n} \frac{\partial n}{\partial R} \frac{z^2}{2!} + \frac{1}{n} \left[ \frac{\partial^2 n}{\partial R \partial z} - \frac{2}{n} \frac{\partial n}{\partial R} \frac{\partial n}{\partial z} \right] \frac{z^3}{3!} \\
& + \frac{1}{n} \left[ \frac{\partial^3 n}{\partial R \partial z^2} + \frac{1}{n} \frac{\partial n}{\partial R} \frac{\partial^2 n}{\partial R^2} + \frac{1}{n^2} \left( \frac{\partial n}{\partial R} \right)^3 \right. \\
& \left. - \frac{3}{n} \frac{\partial n}{\partial z} \frac{\partial^2 n}{\partial R \partial z} + \frac{6}{n^2} \frac{\partial n}{\partial R} \left( \frac{\partial n}{\partial z} \right)^2 - \frac{3}{n} \frac{\partial^2 n}{\partial z^2} \frac{\partial n}{\partial R} \right] \frac{z^4}{4!}
\end{aligned}$$

where  $n$  and all its derivatives appearing in the coefficients are evaluated at  $R = R_0$  and  $z = 0$ .

Given the ray trajectories, there are several ways in which one can calculate the intensity. For the perturbation expansion we used

$$I(R, z) = I(R_0, 0) \exp \left\{ - \int_0^z \left( \nabla \cdot \frac{dr}{ds'} \right) ds' \right\}$$

For the ray trajectories given by the power series expansion,

$$I(R, z) = I(R_0, 0) \frac{R_0}{R} \left( \frac{\partial f}{\partial R_0} \right)^{-1} \left[ 1 + \left( \frac{\partial f}{\partial z} \right)^2 \right]^{1/2}$$

An advantage of the power series approximation is that one can derive an analytic form for the intensity, whereas use of the perturbation expansion requires machine computation of integrals to evaluate the intensity.

A question of practical importance is the celerity of convergence of the various expansions. With each expansion, as one keeps more terms to approximate the ray trajectories, the intensity calculations rapidly become unwieldy.

Computations of the ray trajectories were done using parameters pertinent to an experiment done by Dr. Kenemuth using a CO<sub>2</sub> laser propagating in a CO<sub>2</sub> absorption cell. The values of the various parameters are as follows:

$$\alpha = 0.3 \text{ (meters)}^{-1}$$

$$\text{Power} = 63 \text{ watts}$$

$$\text{Beam waist} = 1.7 \text{ cm}$$

$$\text{Pressure} = 100, 200, \text{ and } 400 \text{ torr}$$

$$z = 5.59 \text{ meters}$$

Because of the large value of  $\alpha z$ , which is a characteristic length for the system, the power series exhibited slow convergence rendering accurate intensity calculations impractical. Fortunately, in the perturbation expansion,  $|r_2| \ll |r_1|$ , indicating rapid convergence. Therefore, intensity calculations were done using the approximation  $r = r_0 + r$ . The results of the calculations are illustrated in Figure 1 where the intensity (normalized by dividing by the initial peak intensity) is plotted as a function of  $R$  for times ranging from 0 to 260 milliseconds in 20-millisecond increments. The on-axis intensity decreases with time. The pressure was taken to be 400 torr.

In addition to the calculations described above, Dr. J. R. Kenemuth derived an approximation for the ray trajectories using an iterative technique involving

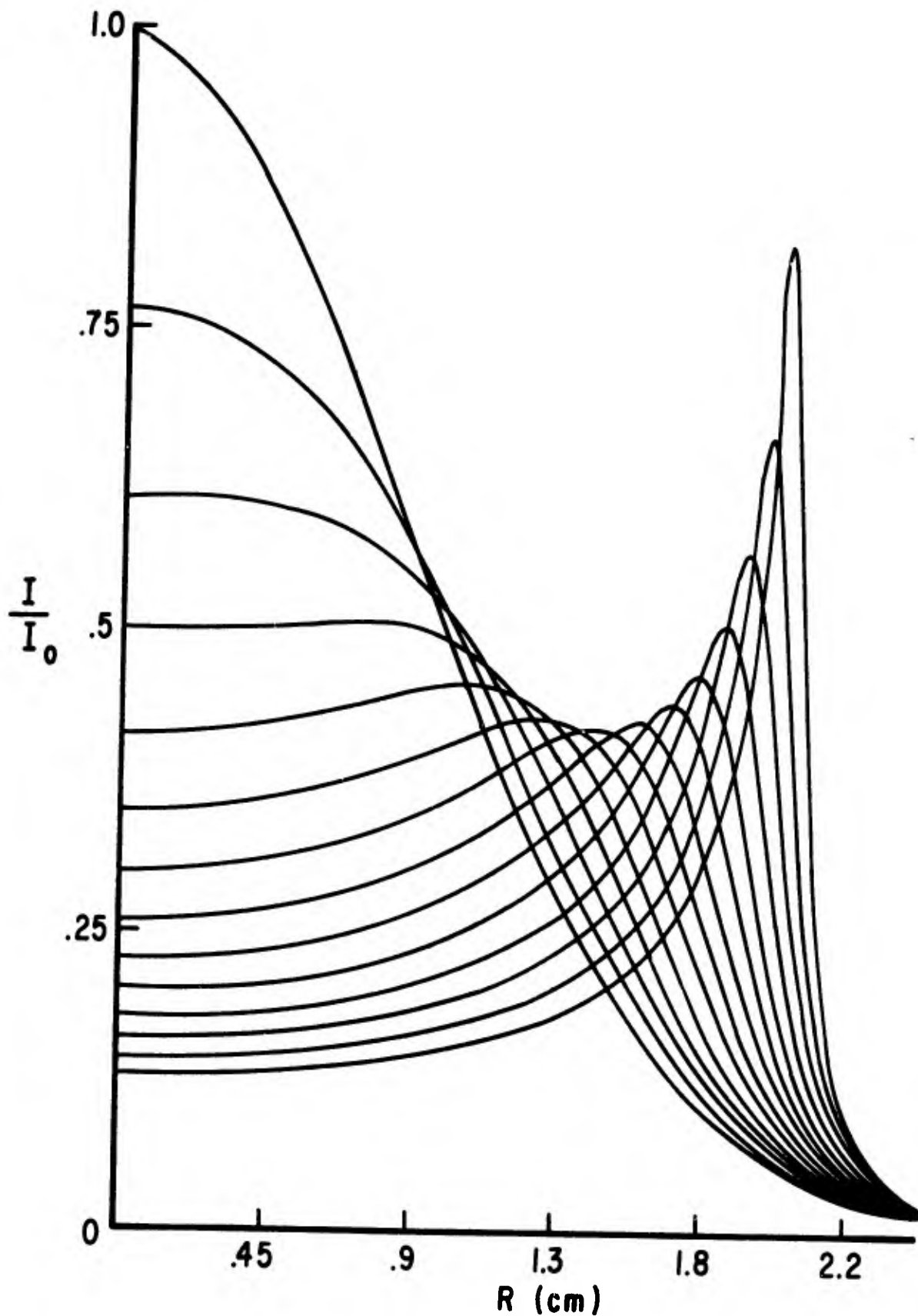


Figure 1. Normalized intensity as function of distance. The curves are parametric in time running from  $t=0$  (top curve at  $R=0$ ) to  $t=260$  msec (bottom curve at  $R=0$ ) in increments of 20 msec.



Taylor series expansions of the gradient of the index of refraction in time and in  $R - R_0$ . Intensity calculations using this approximation are in progress.

The various approximations for the ray trajectories are compared in Figures 2, 3, and 4, where  $R$  is plotted as a function of  $R_0$  for  $z = 5.59$  meters and a pressure of 400 torr. The times are 60, 120, and 260 milliseconds, respectively. Shown are the approximations obtained by letting  $r = r_0 + r_1$  and  $r = r_0 + r_1 + r_2$  in the perturbation expansion,

$$R = f_0 + f_2 \frac{z^2}{2!} + f_3 \frac{z^3}{3!} + f_4 \frac{z^4}{4!}$$

in the power series expansion, and  $R$  correct to order  $t^3$  using Dr. Kenemuth's techniques. For reference, the line  $R = R_0$  is also shown on these plots.

The authors wish to express their appreciation to Mr. William Trebilcock for the computer plots.

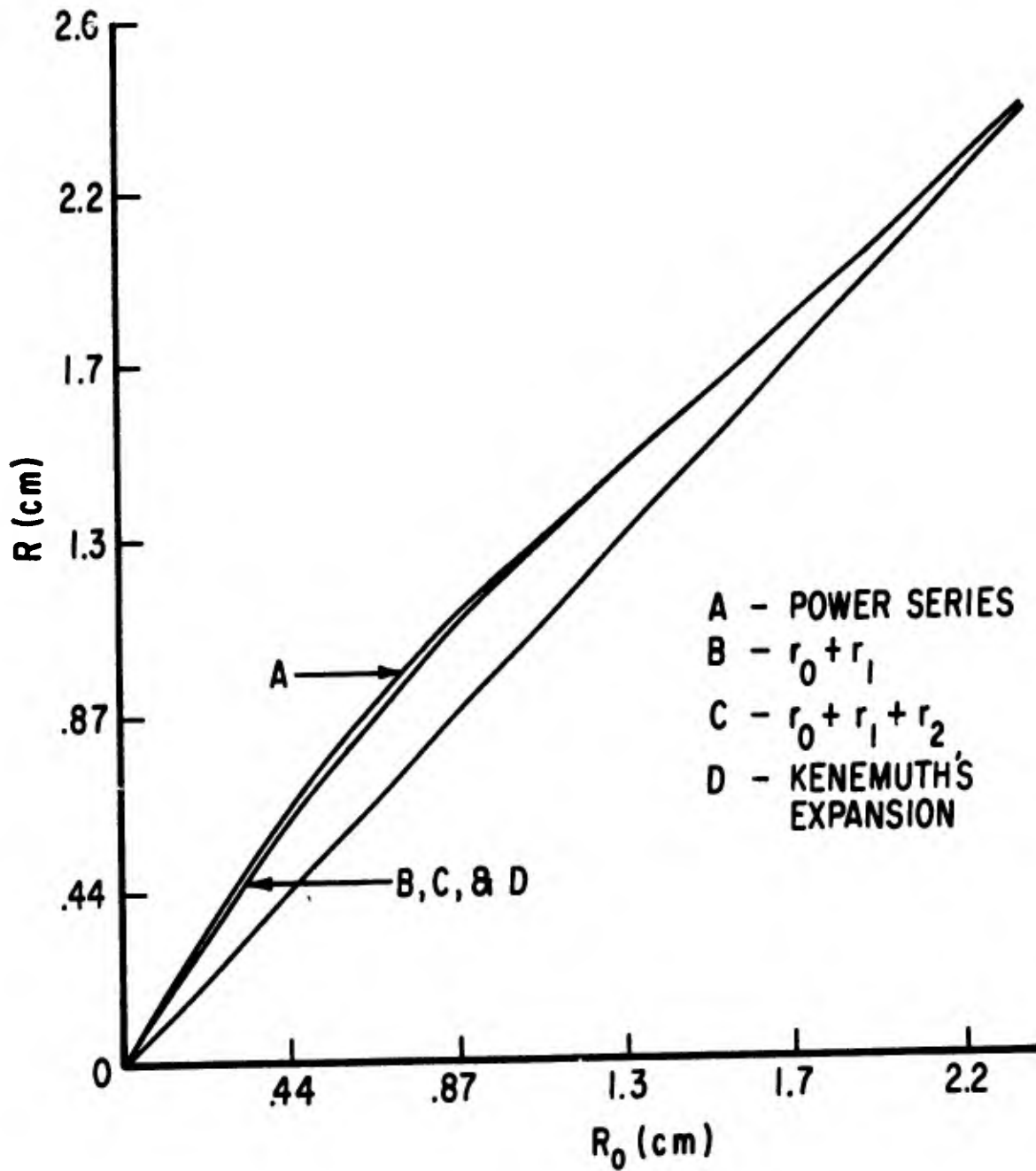


Figure 2. Comparison of ray trajectories for the case of  $z=5.59$  m and  $p=400$  torr. Time is 60 msec.

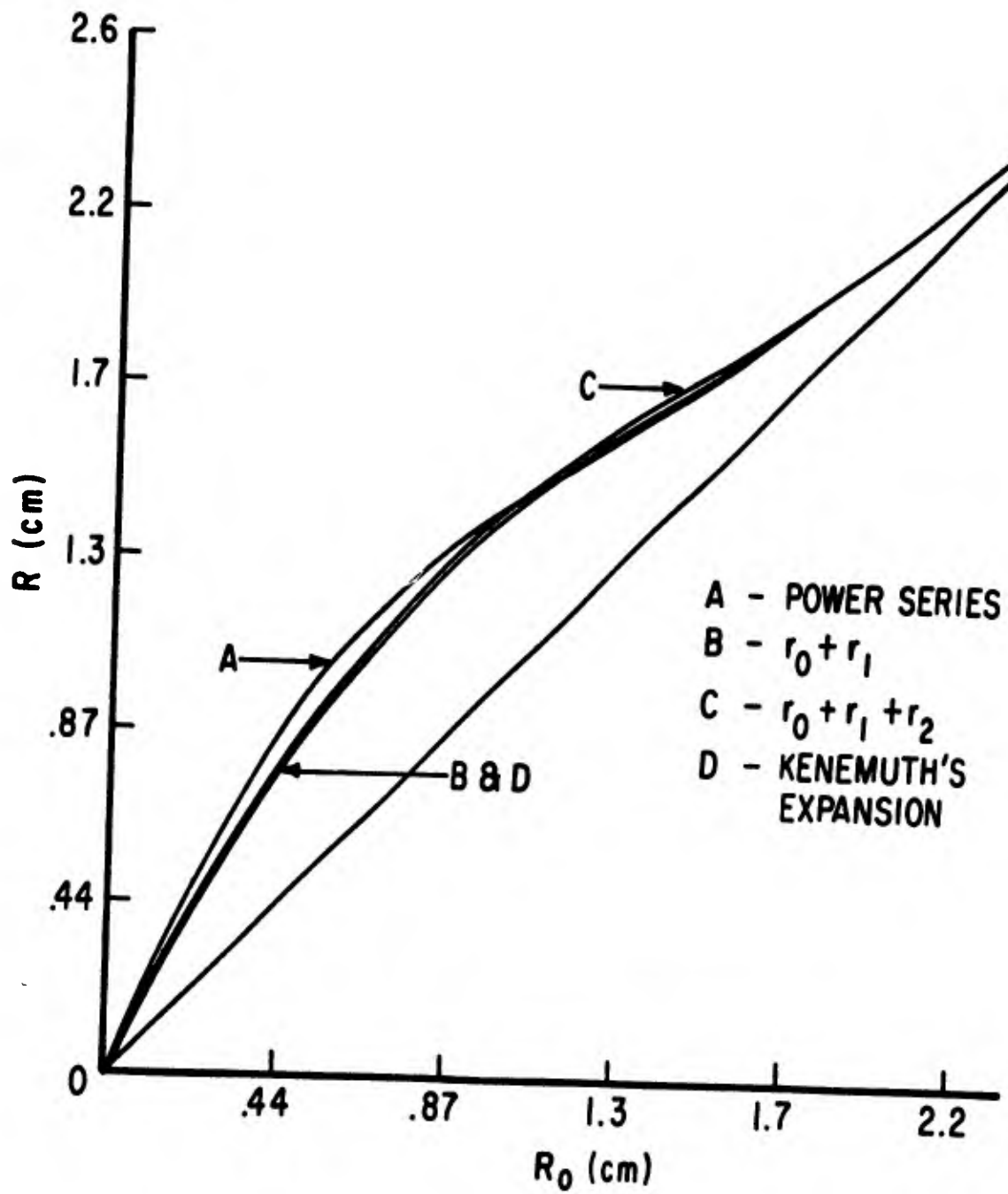


Figure 3. Comparison of ray trajectories for the case of  $z=5.59$  m and  $p=400$  torr. Time is 120 msec.

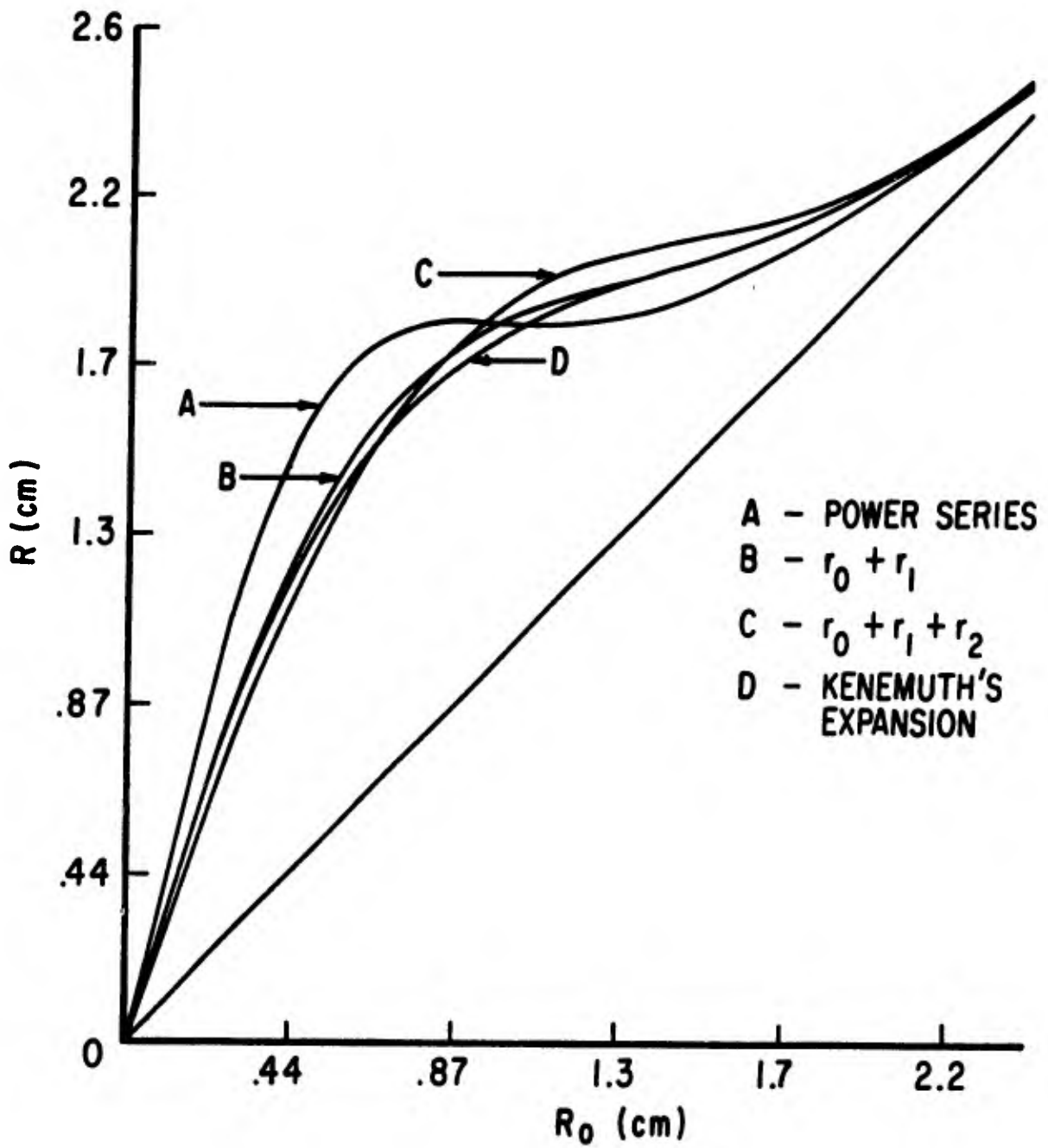


Figure 4. Comparison of ray trajectories for the case of  $z=5.59$  m and  $p=400$  torr. Time is 260 msec.

## EXPERIMENTAL INVESTIGATION OF THERMAL BENDING

W. L. Visinsky

Laser beam propagation in an absorbing medium leads to a heating of the medium with a subsequent change in the refractive index. The initial Gaussian distribution of the beam is distorted to an annular distribution which expands radially outward in a symmetrical fashion. Buoyancy forces come into play after several hundred milliseconds and the hot rising gas sets up a convective wind perpendicular to the propagation axis. This wind then leads to the crescent-shaped intensity distribution of the laser beam caused by the beam bending into the region of higher refractive index (into the wind). The time-dependent effects of the absorption of laser energy by the medium are, initially, thermal blooming and, finally, thermal bending once the convective wind is established. This paper will present the theory and experimental verification of thermal bending for those situations when the medium is not assumed to be stationary.

### Thermal Bending

A laser beam propagating in an absorbing medium which is not stationary will see changes in the refractive index of the medium. If the velocity of the medium (here assumed to be perpendicular to the propagation axis) is much greater than the convective velocity previously discussed, the major effect will be a bending of the laser beam into the wind. For very low wind speeds one would expect to see blooming. In fact, at zero velocity, the beam undergoes only thermal blooming. At very high wind speeds, the beam should propagate as if there were no absorbing medium present. These conditions define the constraints on laser beam propagation in a wind.

### Theory

The optical axis of the beam is taken as the z-axis and the wind is assumed to be in the direction of the x-axis. We further assume that the gradient of the refractive index is normal to the z-axis such that<sup>1</sup>

$$(dn/dz) = 0$$

Then the vector equation

$$d/ds(ndR/ds) = \nabla n$$

has a z component

$$d/ds(n dz/ds) = \frac{dn}{dz} = 0$$

Taking

$$dz/ds = \cos \theta$$

we have

$$d/ds(ncos \theta) = 0$$

or

$$ncos \theta = \text{constant} \quad (1)$$

where

$n$  = index of refraction

$\theta$  = angle the ray path makes with the x-axis

For the atmosphere,  $n \approx 1$  and heating leads to a decrease in the refractive index of the air which gives a new refractive index of  $1 - |\Delta n|$ . If we assume that the rays are initially parallel to the optical axis ( $\theta_0 = 0$ ) and set up equation (1) for the near and far field, we have

$$(1 - |\Delta n|) \cos \theta_0 = n \cos \theta$$

or

$$1 - |\Delta n| = \cos \theta$$

For small  $\theta$  the expansion leads to the expression

$$\theta = (2\Delta n)^{1/2} \quad (2)$$

We must now determine the change in the refractive index as a function of the intensity of the beam and the parameters which characterize the medium. Equating the increased energy content of the medium with the energy absorbed from the beam at constant pressure, and using the equation of state of an ideal gas, Kenemuth, Hogge, and Avizonis<sup>2</sup> arrive at a density solution

$$\rho = \rho_0 \exp[-\alpha(\gamma-1)I(R,Z)t/\gamma P_0] \quad (3)$$

where

$\rho$  = density

$\gamma = C_p/C_v$  = ratio of the specific heat capacities

$\alpha$  = absorption coefficient

$P_0$  = pressure

$I(R,Z)$  = laser beam intensity at radius R

$t$  = time the laser beam has been on

If the refractive index may be related to the density of the atmosphere, by  $(n-1)/\rho = (n_0-1)/\rho_0$ , we can substitute in equation (3) and solve for  $\Delta n = n - n_0$ :

$$\rho/\rho_0 = (n-1)/(n_0-1) = \exp[-\alpha(\gamma-1)I(R,Z)t/\gamma P_0] \quad (4)$$

Expanding the exponential and retaining the first order term leads to

$$\Delta n = (n_0-1)(\alpha(\gamma-1)I(R,Z)t/\gamma P_0)$$

which upon substitution into equation (2) yields

$$\theta = (2(n_0-1)(\alpha(\gamma-1)I(R,Z)t/\gamma P_0))^{1/2} \quad (5)$$

In this derivation we have not made any assumptions as to the wind. In fact this expression would just define the expansion of the laser beam in a symmetrical fashion in thermal blooming; the change in the refractive index is cylindrically symmetrical.

To introduce the wind into equation (5), we first define a characteristic time as

$$t_c = 2R_o/V_x$$

where

$R_o$  = radius of the beam

$V_x$  = velocity of the wind

This characteristic time indicates how long a particular parcel of air has been in the beam; moreover, it is a measure of the amount of beam energy which will appear in the medium as heat. Substitution of the characteristic time into equation (5) yields

$$\theta = (4(n_o - 1)((\gamma - 1)dI(R, Z)R_o/\gamma P_o V_x))^{1/2} \quad (6)$$

The introduction of the wind into the equation also changes the symmetry that is inherent in the thermal blooming situation. For times which are shorter than  $t_c$ , the symmetry should still exist. However, for times greater than  $t_c$ , the symmetry no longer exists. In these situations, the region of higher refractive index is one direction--into the wind--so that we should see the beam bend.

Tucker and Hancock<sup>1</sup> arrive at the following equation for bending into the wind:

$$\theta = (8/3(N_o - 1)\alpha I_o(R_o)/C_p T_o V_x)^{1/2} \quad (7)$$

Equations (6) and (5) agree well; in fact, the only difference is the numerical multiplication factor.

Equations (5) or (6) can be used to determine the amount of bending into the wind for times greater than the characteristic time. It may not always be advantageous to talk about bending since as the speed increases the degree of bend will decrease. Although the degree of bending may be extremely difficult to measure for higher wind speeds, the beam diameter will give the required measure of beam bending. This is true because, as we have just shown, the degree of bending is directly related to the size to which the beam would expand in the characteristic time if there were no wind present. This can perhaps be even better illustrated by referring again to Tucker and Hancock. Their expression for  $\theta_{max}$  for the case of no wind is given as



$$\theta_{\max} = \left( 2(n_o - 1) \alpha P_o t / C_p T_p \right)^{1/2} \quad (8)$$

If we use the characteristic time defined earlier and relate  $\theta_{\max}$  with and without a wind, we see that

$$\left( \theta_{\max} \right)_{\text{wind}} = \left( 0.817 \theta_{\max} \right)_{\text{still air}} \quad (9)$$

The fact that the basic equations for bending and blooming are related is logical. Referring back to the point that the increased energy content of the air is directly related to the absorption of laser energy, the time the parcel of air is in the beam is the only time in which energy may be absorbed with a wind present. The basic absorption process is the same with or without a wind, and the characteristic time determines the amount of energy deposited. One argues, therefore, that following the characteristic time, the beam will show a steady-state bending into the wind. The lateral dimensions of the crescent-shaped beam as well as the extent of the bending will be directly related to the maximum extent the laser beam would have bloomed to in that characteristic time in the absence of any wind.

#### Experimental Considerations

We have already indicated that, because of the convective wind established in thermal blooming, thermal bending is the end product of the blooming process. This bending, however, would be difficult to measure in terms of the velocity of the wind. What is needed is a system which will have the capability of varying the wind speed and the direction of the wind. This would provide the capability of investigating the full range of bending phenomena which we have discussed--from the maximum bending to the point where the medium no longer absorbs sufficient energy to produce any detrimental effects on the beam. Various methods of providing this capability will be discussed.

A wind tunnel would provide the full range of wind velocities desired. However, a well designed wind tunnel with the associated gas supply is an expensive item to build and to maintain. Turbulence, always present in a wind tunnel, may also present problems at very low wind velocities.

Perhaps the easiest way to obtain a full range of wind velocities is to slew the laser beam through the absorbing medium, thereby simulating the wind blowing across the beam. A single rotating mirror can provide this slewing capability.<sup>3</sup> The simulated wind velocities, in such a case, are not constant

across the entire beam propagation path and it would be difficult to relate a specific degree of bending to a specific wind velocity. The reduction of data obtained with a slewed beam would be tedious.

Translating the laser beam through the absorbing medium would provide a constant velocity along the entire beam path. The degree of bending into the simulated wind could be easily obtained for a wide range of wind speeds. To fully investigate thermal bending, we must have the capability of translating a laser beam at higher velocities. Since the heating of the medium due to absorption will begin to thermally bloom the beam in a few milliseconds, we should have the capability of providing simulated wind velocities whose corresponding characteristic time ( $t_c = 2R_o/V_x$ ) would approach the initial thermal blooming time. This velocity, of course, would be the velocity at which the laser beam would propagate as if there were no absorbing medium present. If, for example, we assume a time for the onset of thermal blooming of 2 msec and a beam radius of 1 cm, the corresponding maximum velocity of interest is 100 cm/sec. The system to be described in this paper provides a means of reaching these maximum velocities as well as a means of investigating those velocities which give thermal bending.

#### Translator Design

We can slew a beam through a medium by using one rotating mirror. By using two rotating mirrors, we can take the angular motion of beam slewing and convert it into translational motion. The system used in the experimental investigation of thermal bending is based on this principle and is illustrated in Figure 1. Figure 2 illustrates the location and use of the beam translator in the experiment.

The CO<sub>2</sub> laser beam, with a peak power of approximately 100 watts and a beam spot size of approximately 2 cm, enters the input side of the beam translator. This side of the translator consists of two 6-inch mirrors which rotate in phase with each other and are separated by a distance of approximately 17 inches at a 45° angle. The synchronization of phase is provided and maintained through the use of the gearing system consisting of a 5-inch drive gear and two 12-inch driven gears. A DC servomotor is used to drive the 5-inch gear. In current operation the beam first strikes the low mirror and is slewed across the face of the top mirror. The rotation of the top mirror converts the slew into translation through the absorption cell which contains pure CO<sub>2</sub>. Motor rotation is reversible and, thus, provides the capability of changing the

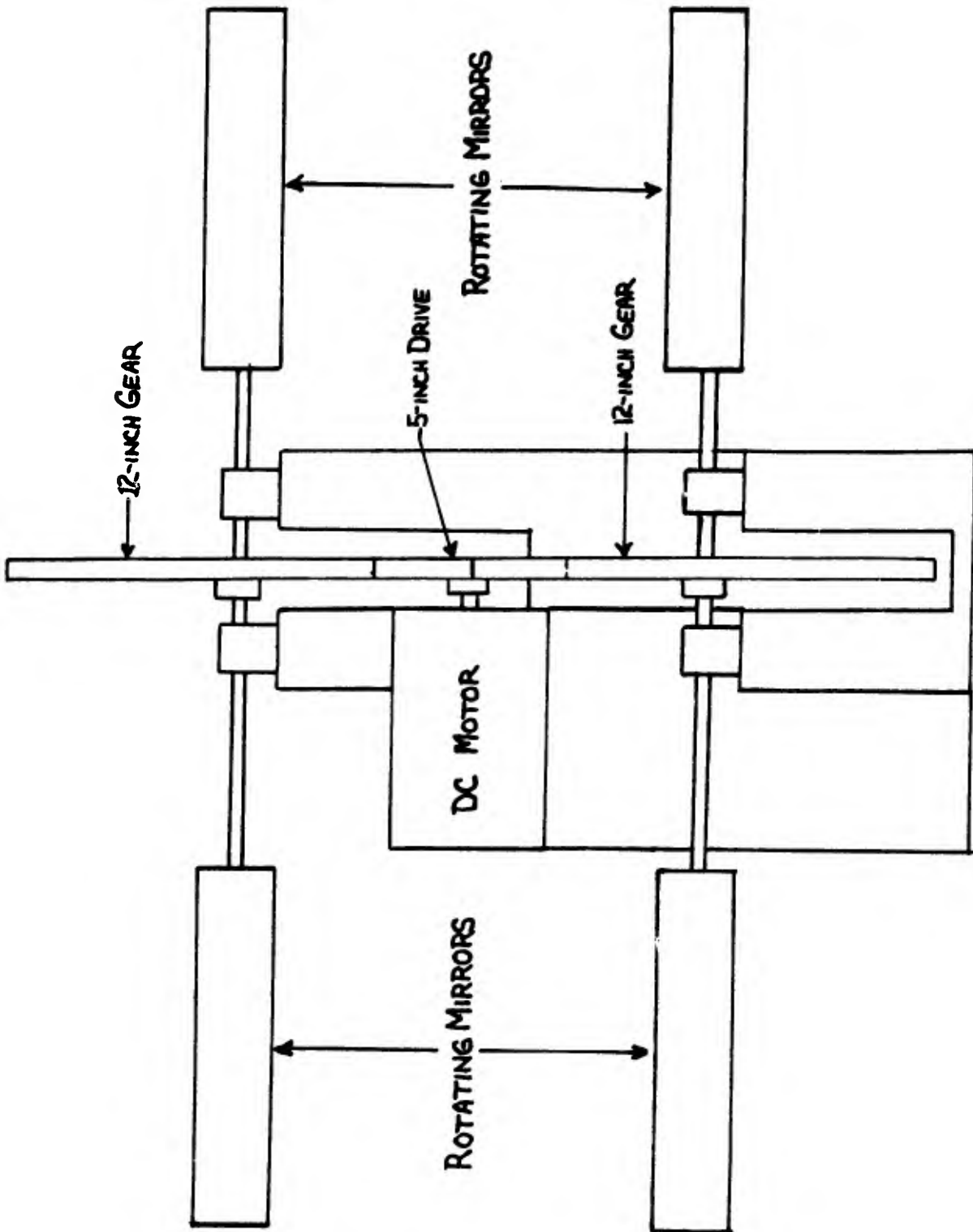


Figure 1. Beam Translator

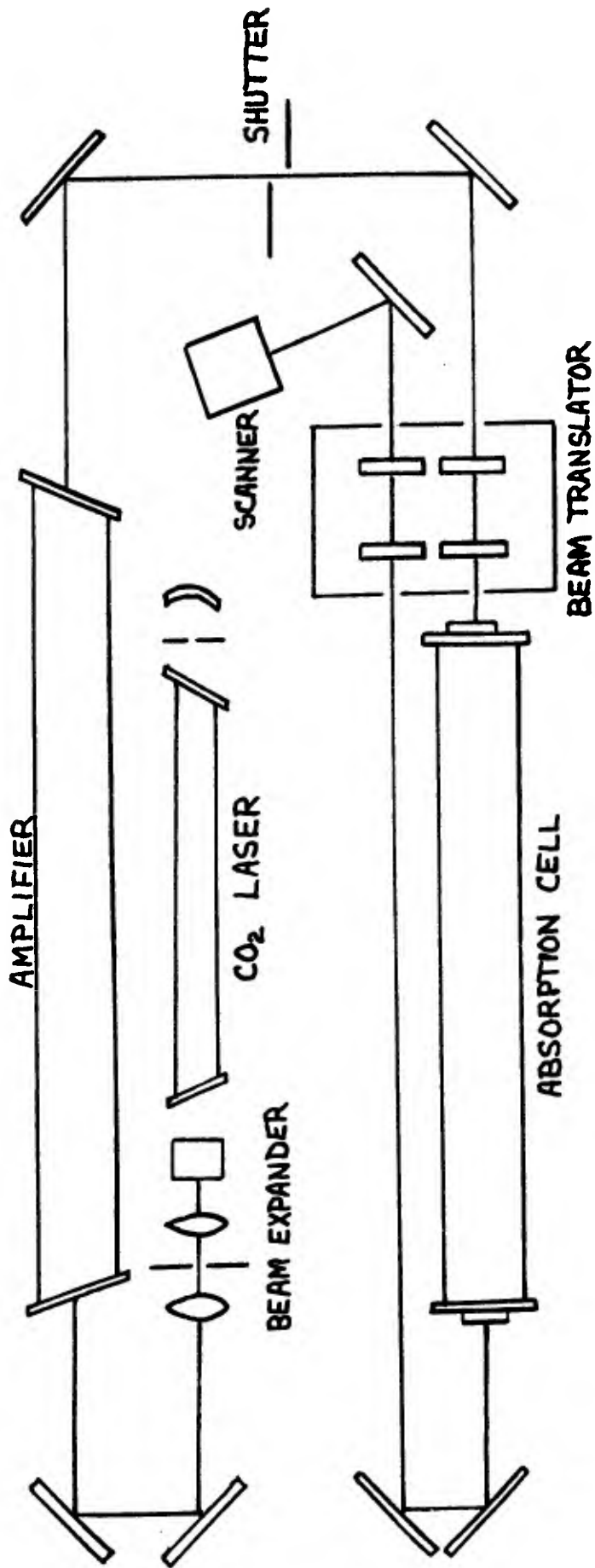


Figure 2. Experimental Arrangement

simulated wind direction.

Two turning mirrors are used at the end of the absorption cell to bring the beam back into the beam translator on the output side. The function of this side of the beam translator, which is a mirror image of the input side, is to take the translation out of the laser beam and provide a stationary beam in position. This greatly facilitates the investigation of the beam profile with a scanning system. The scanning system used in this experiment provides both real-time viewing of CO<sub>2</sub> beams and recording capability. Framing rate is 400 frames/sec.

The system we have just described provides the capability of translating a laser beam through an absorbing medium. The simulated wind in such a system may be varied from 0 to approximately 3000 cm/sec, providing the capability of investigating the full range of thermal bending. It has the advantages of repeatability, fine control, and low cost. We will now discuss the experimental results using this system to investigate thermal bending.

#### Experimental Results

This section describes the translation at various velocities of a CO<sub>2</sub> laser beam through a CO<sub>2</sub> medium. The absorption coefficient was measured at a CO<sub>2</sub> pressure of 25 torr and was found to be approximately  $2 \times 10^{-3} \text{ cm}^{-1}$ . This absorption coefficient was assumed to be constant for the range of CO<sub>2</sub> pressures used in this experiment. Total length of the absorption cell is 559 cm and total translation distance in the cell is 7.62 cm. Wind velocities have been investigated from a low of about 15 cm/sec to a high of 250 cm/sec for CO<sub>2</sub> pressures of 100 torr and 200 torr in the absorption cell.

At the lower velocities the crescent shape and the bending into the wind are readily apparent. As the wind velocity increases, the crescent shape closes up into what appears to be a flattened Gaussian distribution. At still higher velocities the flattening of the beam shape is not evident, but the size of the beam is still characteristic of the size that the beam would have bloomed to in the characteristic time. Figure 3 illustrates the above effects. These pictures were taken from the scanner viewing screen and they show quite vividly how the laser beam bending decreases with increasing wind speed. The maximum extent of thermal blooming for the same condition of 200 torr CO<sub>2</sub> in the absorption cell as well as the original beam size are also shown for comparison. In Figure 4 we compare the extent to which a stationary beam blooms as a

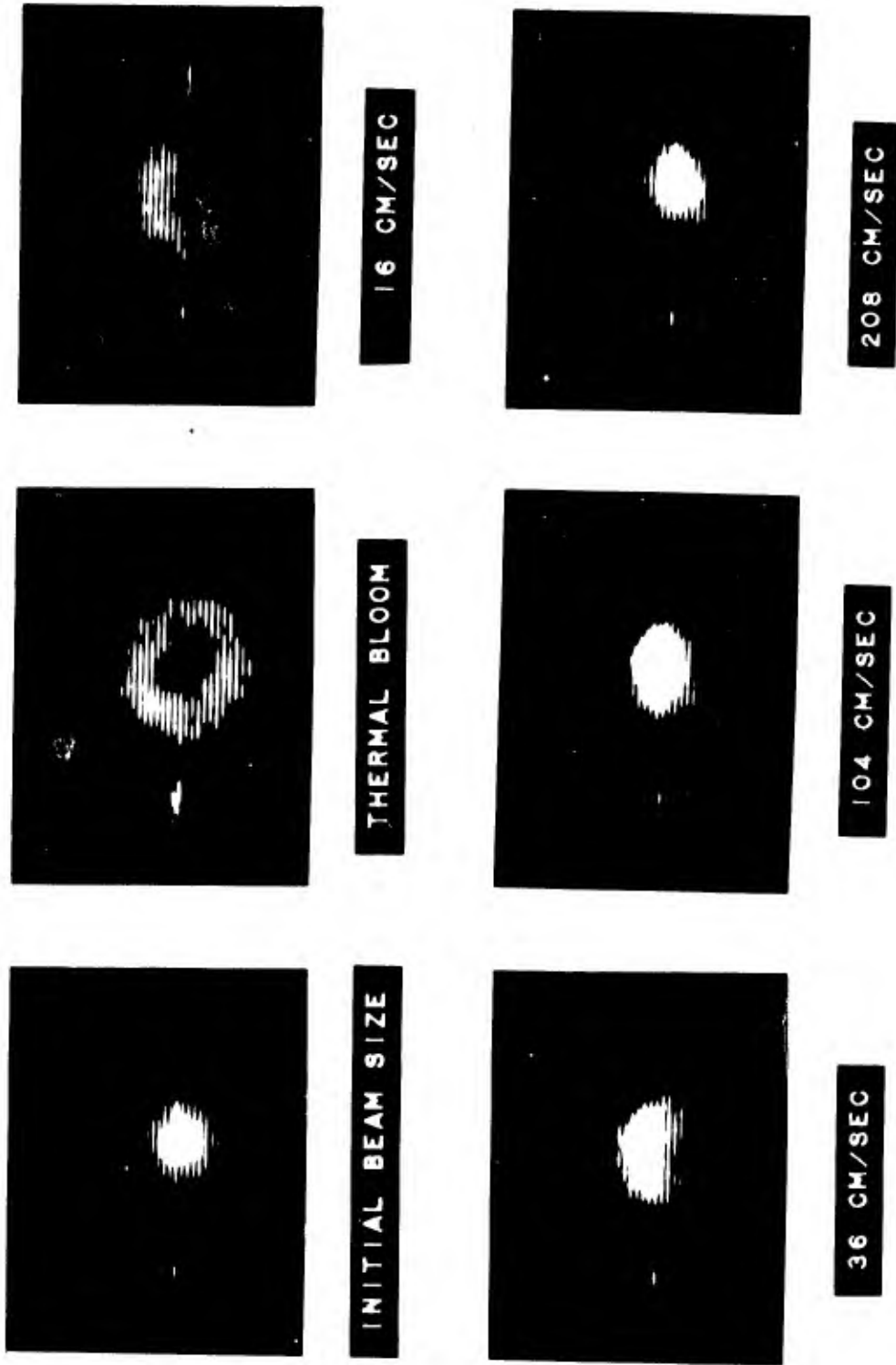


Figure 3. Beam Bending as a Function of Beam Velocity. Wind Direction is Down.

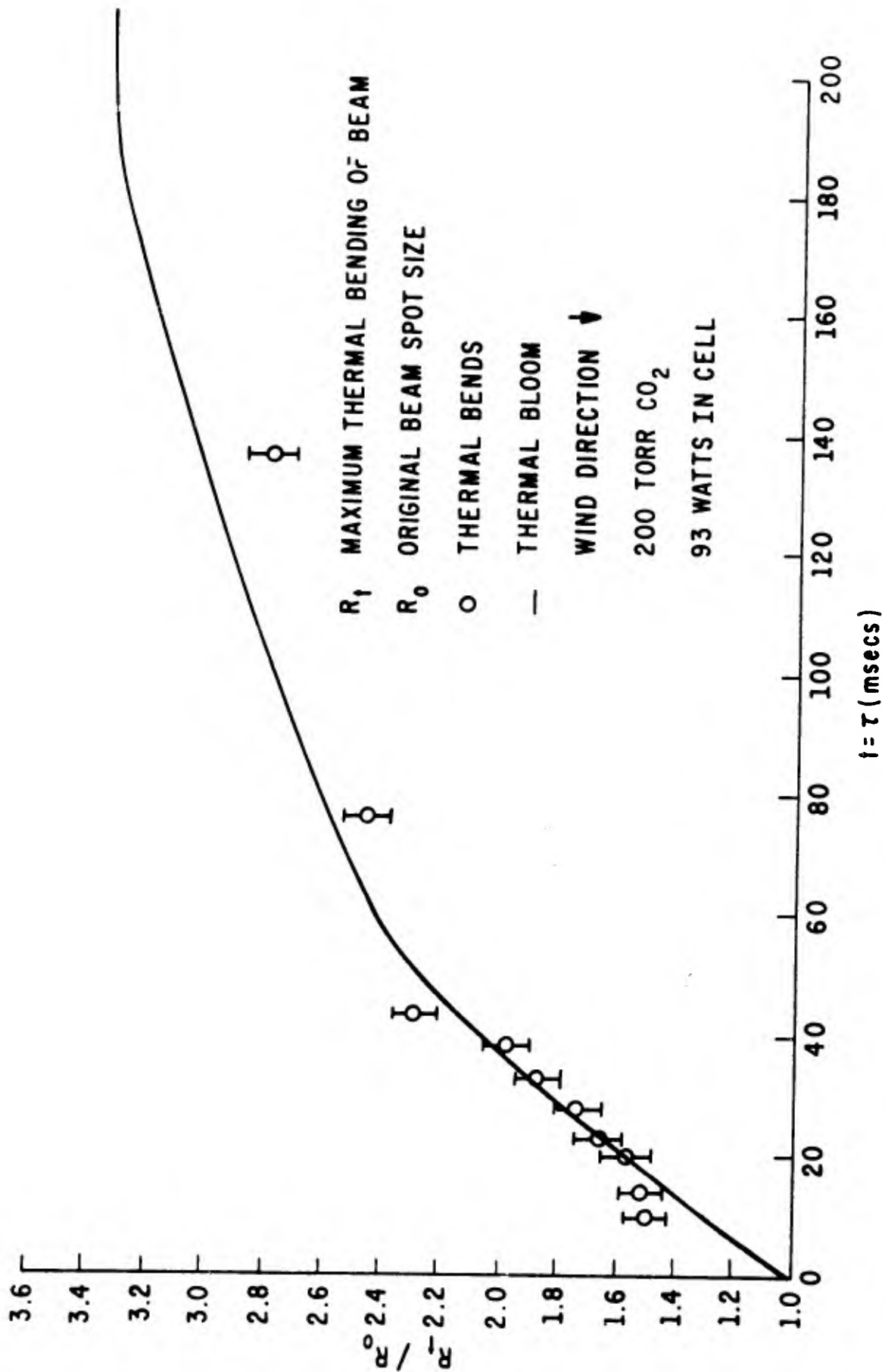


Figure 4. Comparison of Beam Bending and Beam Blooming as a Function of Characteristic Time.

function of time with the degree of bending observed for various wind velocities as a function of the characteristic time calculated using equation (9). In Figure 5, the degree of bending (again represented as the ratio of the maximum extent of the bent beams to the original spot size) for both wind directions investigated is plotted as a function of the wind speed.

### Conclusion

In summary we have shown the relationship between thermal blooming and thermal bending. We have represented the results of thermal bending experimentation which used a beam translator to simulate the wind velocities. Theory and experiment are in good agreement.

### REFERENCES

1. Tucker, J. W., Hancock, H., The Effect of Wind on the Development of Thermal Blooming, NRL Report 7096, 12 August 1970.
2. Kenemuth, J. R., Hogge, C. B., Avizonis, P. V., "Thermal Blooming of a 10.6 $\mu$  Laser Beam in CO<sub>2</sub>," Appl. Phys. Letters 17, No. 5, pp. 220-223, September 1970.
3. Kleiman, H., O'Neil, R. W., "Deflection of a CO<sub>2</sub>-Laser Beam in an Absorbing Gas," Jour. Optical Soc. Amer. 61, No. 1, pp. 12-15, January 1971.



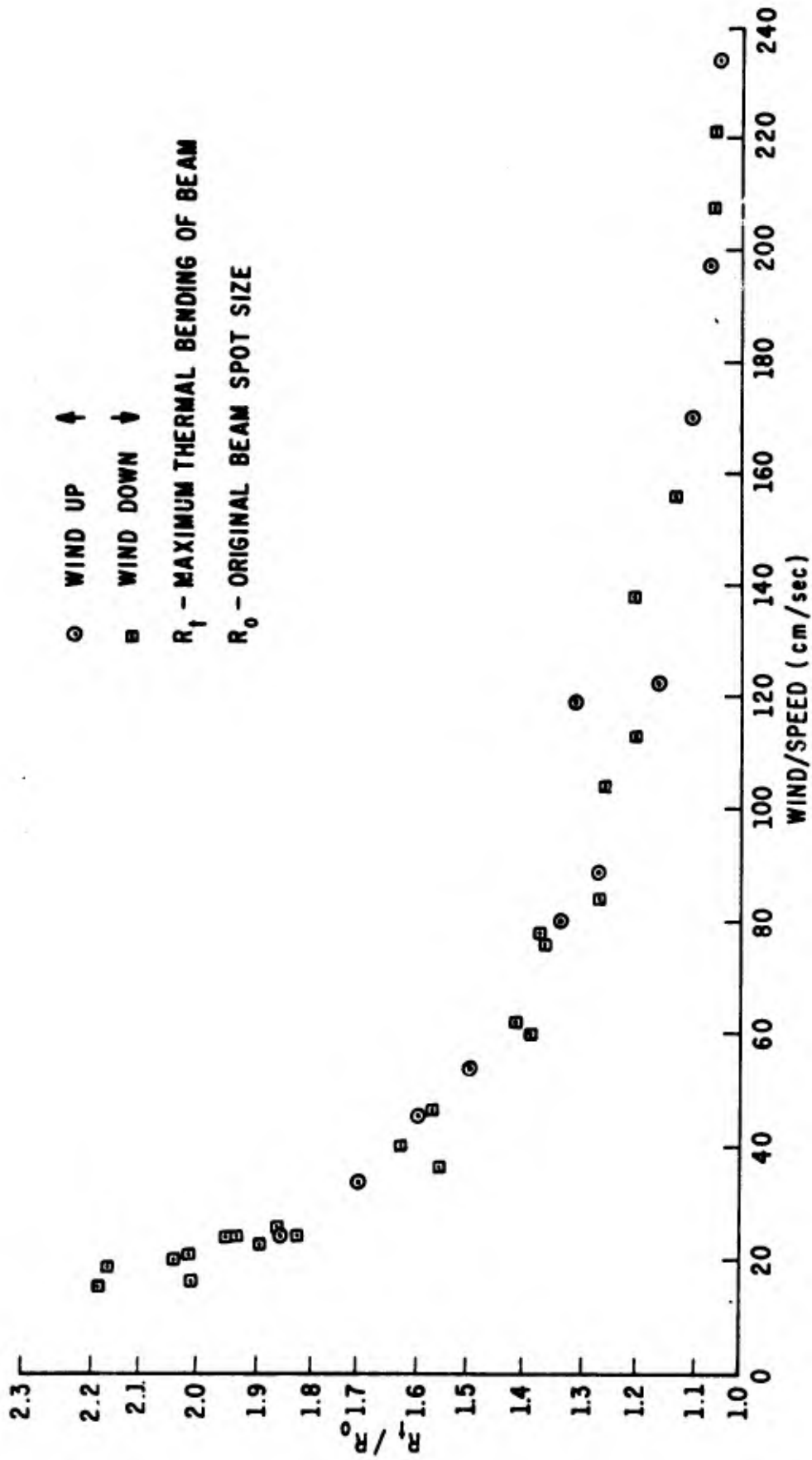


Figure 5. Beam Bending as a Function of Wind Speed.

## PROBLEMS ASSOCIATED WITH PROPAGATION IN AN AERODYNAMIC ENVIRONMENT

W. L. Visinsky and C. B. Hogge

Laser systems designed for use in aerodynamic environments will encounter many problems. Aircraft in flight generate local disturbances in the atmosphere which in addition to the normal atmospheric turbulence must be considered in the laser propagation models. In what follows, we will discuss wake turbulence, boundary layers, jet exhausts, clear air turbulence, and shock waves on laser beam propagation.

### Wake Turbulence

Wake turbulence is generated by flying aircraft. The effect is caused by the normal generation of lift on the aircraft wings and can be characterized by two counter-rotating vortices which extend some distance behind the aircraft. It has been stated<sup>1</sup> that the vortices from jumbo jets might persist to a distance of 14 nm behind the aircraft and that at 9.5 nm this wake turbulence could possibly invert an F-104 in 1 sec at accelerations approaching 15 radians/sec<sup>2</sup>. Under normal atmospheric conditions these contained "tornadoes" could be located at the flight altitude of the aircraft or below.

Laser beam propagation through the vortices of the aircraft wake would be detrimental. The basic interaction is a refractive bending of the laser beam and a subsequent spreading of the radiation due to fluctuations in the refractive index. Scattering off of the wake turbulence as well as the jet exhaust turbulence entrained in the vortices would also be present.<sup>2</sup>

### Boundary Layer

Boundary layers around aircraft surfaces may be either turbulent or laminar. The effect of a turbulent boundary layer on beam wave propagation is probably the most difficult to analyze. In a turbulent boundary layer the important parameters are the thickness of the boundary layer, the size of the turbulent eddies and the strength of the turbulence.

A few experimental measurements have been made of the degradation to optical resolution experienced when "looking" through turbulent boundary layers

surrounding airplanes in flight. For example, a 10.6- $\mu$  imaging system with 8- $\mu$ radian resolution suffered a degradation to 20  $\mu$  radians when operated at 35,000 feet at subsonic speed.\*

On the other hand there is a proliferation of theoretical analysis (of questionable value) on this subject. For example, Liepmann<sup>3</sup> estimated a theoretical limiting resolution (at visible wavelengths) for a Mach-2 sea-level flight of  $4 \times 10^{-4}$  radians. Hufnagel,<sup>4,5</sup> on the other hand, estimated for the same conditions a limiting resolution of  $4 \times 10^{-5}$  radians.

It is readily apparent that there is some disagreement on the extent of boundary layer effects and many more experimental measurements need to be made before a really useful analysis can be performed.

#### Jet Engine Exhaust

The degrading effects of jet engine exhaust on laser beam propagation preclude the operation of any high resolution system in their environment. Measurements of the degree of turbulence in the jet exhaust have been made and the effects on 0.628- $\mu$  and 10.6- $\mu$  laser beams have been evaluated. Maximum turbulence in the jet exhaust is about two orders of magnitude higher than very strong atmospheric turbulence. With such strong turbulence, the spreading of even 10.6- $\mu$  beams can be very substantial at any reasonable distance. For example, a 10.6- $\mu$  beam propagating through 1 meter of jet exhaust turbulence and focused at 500 meters would be spread to approximately three times the unperturbed focal spot size.<sup>6</sup>

#### Clear Air Turbulence

The same turbulence which unexpectedly buffets aircraft in flight, usually called clear air turbulence (CAT), can have strongly deleterious effects on laser beam propagation. These pockets of turbulence, often 10 to 100 miles wide horizontally but only a few thousand feet thick vertically, exhibit turbulence levels that are one to two orders of magnitude more severe than the surrounding air space. As an example, the peak intensity of a laser beam focused at 3 km in a CAT pocket whose turbulence is characterized as intermediate would suffer a 20 percent reduction. Clearly, avoidance of CAT is highly desirable.

---

\*D, Ross, private communication.

## Shock Waves

In supersonic flight, and to some extent at subsonic speeds, aircraft generate shock waves. The predominate effect of these shocks is to induce an almost uniform refractive effect on optical waves passing through them. Thus, if a tracking and illuminating system operates at the same wavelength, the detrimental effect of shock waves should be minimal. Experimental observation of supersonic shock wave refractive effects are difficult to perform, but preliminary data indicate a bending upper limit of 50  $\mu$ rad (at 6328 Å). This number is believed to be very conservative.

## Refractive Effects

The high-speed passage of an aircraft through an otherwise quiescent atmosphere will produce a locally nonuniform average density gradient. As a result, an optical beam propagated to or from the airplane will experience a net refractive effect similar to a prism. This prism effect will depend strongly on the "looking" direction relative to the aircraft.

Various opinions on the severity of these effects range from very minimal to completely debilitating. We hope that within a year experimental numbers will be available to evaluate the true severity of this problem. It should be noted that the effect will surely become more pronounced the faster and lower that the aircraft flies.

## Weather

While adverse weather conditions can strongly effect the usefulness of a high resolution laser system, such conditions will effect both ground based and airborne based systems. Researchers have been studying for many years the gross effects of numerous weather conditions on laser beam propagation. Generally speaking, as a laser rule of thumb, one can say that when "seeing" is good (in the meteorological sense), conditions will be good for a high resolution optical system.

Of particular interest to airborne systems are the effects of large thunderstorms on imaging systems. Propagation through such storms is clearly impossible, and is therefore really not of interest to us here. Of more interest, however, is the fact that the stronger convective activity associated with the disturbance will greatly increase the probability for clear air turbulence for many miles around the storm itself. As already discussed, CAT can have significant effects on otherwise ideal propagating conditions.

## Conclusions

Airborne optical systems will encounter numerous physical effects which will tend to degrade the total performance characteristics. Of particular importance will be the self-induced effects such as wake and jet exhaust turbulence, boundary layer turbulence, and average refractive effects. The extent of these degrading conditions will probably place certain restrictions on operating configurations. It is hoped that within the next 6 months additional experimental data will be available to help evaluate the true severity of these problems.

CAT and naturally occurring weather are conditions about which little can be done. It is desirable, of course, to avoid air space regions affected by these disturbances. Clearly, then, especially for CAT, meaningful tactical positions could be achieved if some means of locating and mapping these disturbances were possible.

## REFERENCES

1. Krier, G. E., Letter to the Editor, Aviation Week, 20 April 1970.
2. McCormick, B. W., "Aircraft Wakes: A Survey of the Problem," presented at FAA Symposium on Turbulence, Washington, DC, 22-24 March 1971.
3. Liepmann, H. W., Deflection and Diffusion of a Light Ray Passing through a Boundary Layer, Douglas Aircraft Corp. Report SM-14397, Santa Monica Division, May 1952.
4. Hufnagel, R. E., "Random Wavefront Effects," The Practical Application of Modulation Transfer Functions, Perkin-Elmer Corp., March 1963.
5. Veed, A. M., Tuttle, J. W., Derivation of an Optical Modulation Transfer Function for Turbulent Boundary Layers, General Dynamics Report ERR-FW-347, 1964.
6. Hogge, C. B., Visinsky, W. L., "Laser Beam Probing of Jet Exhaust Turbulence," Appl. Optics 10, 4, 1971.
7. Loving, N. V., "Highlights of CAT Test Programs," presented at FAA Symposium on Turbulence, Washington, DC 22-24 March 1971.

## PROPAGATION THROUGH A SHOCK WAVE

W. L. Visinsky

An experiment was conducted at the Holloman AFB test track facility to determine the effect of shock waves on laser beam propagation. The experiment was run in conjunction with an 8000-foot-per-second rocket sled test conducted by the Electronics Division of the Air Force Weapons Laboratory.

A He-Ne laser beam was used to investigate the effect of the shock wave. The beam, as indicated in Figure 1, was propagated from Blockhouse Alpha to Blockhouse Dog where two high-speed cameras (50 and 200 frames/sec) were used to record the overall effects on the beam. The total propagation path was 3000 feet. The rocket sled took 2.1 sec to travel to Blockhouse Dog and had reached a velocity of 3470 feet/sec at that point. Sonic velocity was reached somewhere between 500 and 800 feet down track or 1 to 1.25 seconds after firing.\*

The film records clearly show the start of the run and the light from the rocket as it passes Blockhouse Dog. There is some vibration of the spot as the sound wave from the rocket firing reaches the laser but this clears up in a few frames. The lighting of the second stage at approximately 500 feet down the track is also clearly visible. The major effect of the shock wave on the beam appears to be a decrease in intensity or, in other words, a spreading in the spot size. Bending of the beam is not apparent in the film and, from the argument that a bend of half the beam diameter should be discernible in the film strip, an upper limit on the bending would be approximately  $100 \mu\text{rad}$ . The net bending should be much less than this and would seem to emphasize the fact that the true bending is a function of the total thickness of density change. When one considers that the shock wave has thickness, the net change in bend is much less than when the shock wave is assumed to be an abrupt change. With thickness included one sees that the ray path will bend back toward the original path or, in other words, the angle of bend induced by the shock will not be as great as for the case of the abrupt, instantaneous change. See Figure 2. For an abrupt change, the degree of bending would be calculated as  $5 \times 10^{-3}$  radians or 50 times as great as the upper limit mentioned above.

\*Hugh Southall, private communication.

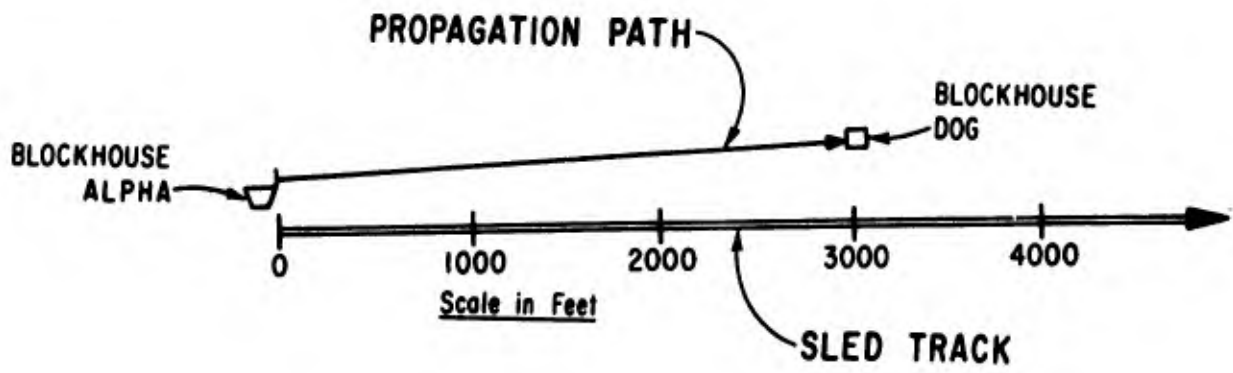


Figure 1. Holloman AFB Test Track and Laser Propagation Path.

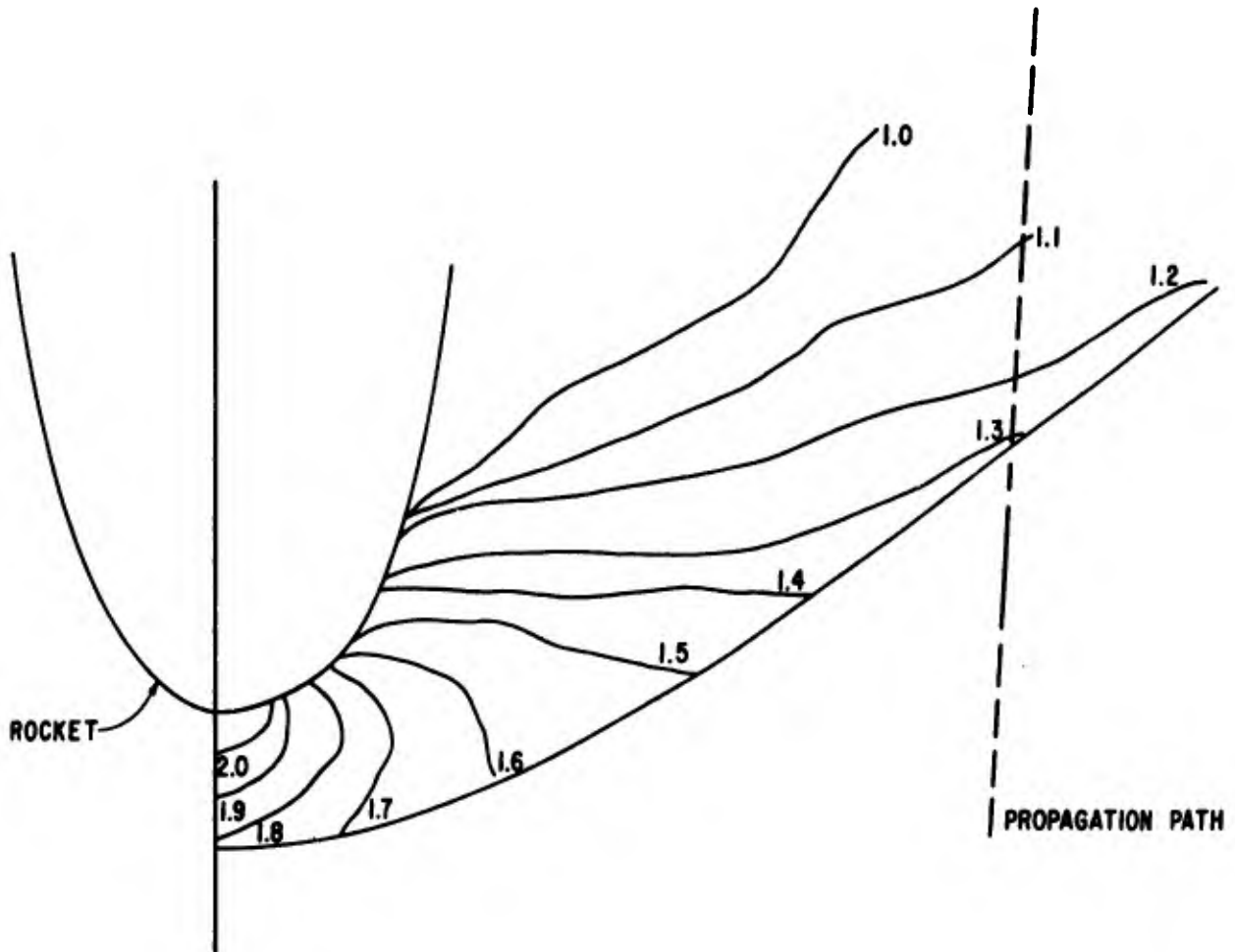


Figure 2. Contours of Constant Ratio of Density to Free Stream Density (Idealized)

MODELING PROPAGATION THROUGH TURBULENT BOUNDARY LAYERS  
BY THIN RANDOM PHASE SCREENS

C. B. Hogge and W. L. Visinsky

If the self-induced turbulence around an aircraft in flight is sufficiently localized relative to the entire propagation path length of interest, one may investigate the average degrading effects of this boundary turbulence by modeling the random atmospheric index of refraction fluctuations as a thin random phase screen. The problem is trivial if one knows the covariance function of the resulting phase fluctuations across an otherwise perfect optical beam. Let  $\phi(\bar{r})$  be the relative phase (in wave numbers) at  $\bar{r}$  of an optical beam after it has traversed the turbulent layer. Then the covariance function is

$$C_{\phi}(\bar{\rho}) = \langle (\phi(\bar{r}) - \langle \phi \rangle) (\phi(\bar{r} + \bar{\rho}) - \langle \phi \rangle) \rangle \quad (1)$$

where the  $\langle \rangle$  brackets denote in theory an ensemble average, but in practice a time average.

$$\begin{aligned} C_{\phi}(\bar{\rho}) &= \langle \phi(\bar{r}) \phi(\bar{r} + \bar{\rho}) \rangle + \langle \phi \rangle^2 - 2\langle \phi \rangle^2 \\ &= \langle \phi(\bar{r}) \phi(\bar{r} + \bar{\rho}) \rangle - \langle \phi \rangle^2 \end{aligned} \quad (2)$$

If  $\langle \phi \rangle = 0$ , which we will assume is true in our case,

$$C_{\phi}(\bar{\rho}) = \langle \phi(\bar{r}) \phi(\bar{r} + \bar{\rho}) \rangle \quad (3)$$

when  $\bar{\rho} = \bar{0}$

$$C_{\phi}(0) = \langle \phi^2 \rangle = \sigma^2 \quad (4)$$

where  $\sigma^2$  is the variance of the phase fluctuations. We are assuming here that the phase degradation is spatially and temporally stationary.



For an ideal Gaussian beam focused at  $z = F$ , the field strength  $u(\bar{r})$  on axis ( $\bar{r} = 0$ ) in the focal plane is given by the cylindrically symmetric Fresnel integral.

$$u(0,F) = \sqrt{\frac{2P_T}{\pi\omega_1^2}} \frac{n_o k_o e^{i\pi/2}}{F} \int_0^\infty dr' r' \left[ \exp\left(-r'^2/\omega_1^2\right) \right] \quad (5)$$

where the quantity in the brackets [ ] is the amplitude distribution at the transmitter plane. The other parameters are  $P_T$ , the total output laser power;  $n_o$ , the atmospheric average index of refraction;  $k_o$ , the wave number ( $k_o$  is  $2\pi/\lambda$ , where  $\lambda$  is the optical wavelength);  $\omega_1$ , the transmitted beam spot size (or radius); and  $F$ , the distance to the focal plane. Because the beam is assumed to be focused at  $z = F$  and because we are also observing the field in that plane, the phase term reflecting the focusing property of the beam has "cancelled out." To include the effect of the local turbulence on the beam, we select one member of the ensemble of phase distributions  $\phi(F)$  across the beam. While the beam actually must propagate a finite distance toward the receiver before it experiences this phase degradation, we assume this distance is very short compared to  $F$  and therefore treat the beam as if it had this phase distribution when it left the exit aperture of the optical system. Hence the analogy to the "thin phase screen." The field distribution becomes

$$u(0,F) = \sqrt{\frac{2P_T}{\pi\omega_1^2}} \frac{n_o k_o i}{F} \int_0^\infty dr' r' \exp\left(-r'^2/\omega_1^2\right) \exp\left(i2\pi\phi(r')\right) \quad (6)$$

The on-axis intensity in the focal plane is given by

$$I(0,F) = u(0,F) * u(0,F) \quad (7)$$

$$I(0,F) = \frac{2P_T}{\pi\omega_1^2} \left(\frac{n_o k_o}{F}\right)^2 \int_0^\infty \int_0^\infty dr' dr'' r' r'' \exp\left[-\frac{1}{\omega_1^2}(r'^2+r''^2)\right] \cdot \exp\left[i2\pi(\phi(r')-\phi(r''))\right] \quad (8)$$

The average intensity is then

$$\begin{aligned} \langle I(0, F) \rangle &= \frac{2P_T}{\pi\omega_1^2} \left( \frac{n_o k_o}{F} \right)^2 \int_0^\infty \int_0^\infty dr' dr'' r' r'' \exp \left[ -\frac{1}{\omega_1^2} (r'^2 + r''^2) \right] \\ &\cdot \langle \exp \left[ i2\pi (\phi(r') - \phi(r'')) \right] \rangle \end{aligned} \quad (9)$$

Note that the averaging operation only affects the phase terms, the remaining terms being deterministic.

Now by a very simple geometrical optics argument, and the Central Limit Theorem of statistics, one can show that, for any member of the phase distribution ensemble considered, the phase variations represent a Gaussian stochastic process. Therefore, the quantity  $(\phi(\bar{r}') - \phi(\bar{r}''))$  when considered as a new random variable of time can be shown to be normally distributed. Hence, one can show that

$$\langle \exp \left[ i2\pi (\phi(\bar{r}') - \phi(\bar{r}'')) \right] \rangle = \exp \left[ -\frac{(2\pi)^2}{2} \langle (\phi(\bar{r}') - \phi(\bar{r}''))^2 \rangle \right] \quad (10)$$

The averaging here being taken with respect to time. Expanding we get

$$= \exp \left[ -4\pi^2 \left( \langle \phi^2 \rangle - \langle \phi(\bar{r}') \phi(\bar{r}'') \rangle \right) \right] \quad (11)$$

We have assumed that the stochastic process is stationary in both time and space, so that  $\langle \phi(\bar{r}') \phi(\bar{r}'') \rangle$  is only a function of  $|\bar{r}' - \bar{r}''| = \rho$ . Hence,

$$= \exp \left[ -4\pi^2 \left( \sigma^2 - C_\phi(|r' - r''|) \right) \right] \quad (12)$$

Thus for the intensity,

$$\begin{aligned} I(0, F) &= \frac{2P_T}{\pi\omega_1^2} \left( \frac{n_o k_o}{F} \right)^2 \int_0^\infty \int_0^\infty dr' dr'' r' r'' \exp \left[ -\frac{1}{\omega_1^2} (r'^2 + r''^2) \right] \\ &\cdot \exp \left[ -4\pi^2 \left( \sigma^2 - C_\phi(|r' - r''|) \right) \right] \end{aligned} \quad (13)$$

where  $\rho = r' - r''$ .

We pause here to indicate the fallacious reasoning in the preceding derivation. In equation (5) we have assumed radial symmetry of the illuminating source. Hence

$$r' = |\bar{r}'|$$

The random phase distribution, written in equation (6), however, should be a function of both Cartesian coordinates,  $x'$  and  $y'$ . Thus it is a function of the vector  $\bar{r}'$ . We have treated it, however, simply as a function of the magnitude of  $\bar{r}'$  in the derivation presented here and to be rigorous, this is not true. One can show, however, that the correct formulation does produce exactly the same results as equation (13). Because no improved insight is gained by the formally correct derivation, and because the principles involved are much more transparent in this slightly fallacious derivation, we will simply assert here that equation (13) is correct and no longer belabor the point.

Continuing with equation (13), we now make a change of variables. Let

$$\begin{aligned} \rho' &= 1/2(r' - r'') \\ R' &= 1/2(r' + r'') \end{aligned} \tag{14}$$

so that

$$\begin{aligned} r' &= R' + \rho' \\ r'' &= R' - \rho' \end{aligned} \tag{15}$$

Equation (13) becomes

$$\begin{aligned} \langle I(0, F) \rangle &= \left\{ \frac{2P_T}{\pi\omega_1^2} \left( \frac{n_o k_o}{F} \right)^2 \right\} 2 \cdot \int_0^\infty \int_{-R'}^{+R'} dR' d\rho' (R'^2 - \rho'^2) \exp \left[ -\frac{1}{\omega_1^2} (R'^2 + \rho'^2) \right] \\ &\cdot \exp \left[ -4\pi^2 (\sigma^2 - C_\phi (2\rho')) \right] \end{aligned} \tag{16}$$

Letting

$$R = \sqrt{2} R' / \omega_1$$

$$\rho = \sqrt{2} \rho' / \omega_1 \quad (17)$$

so that

$$\langle I(0, F) \rangle = \left\{ \frac{2P_T}{\pi\omega_1^2} \left( \frac{n_o k_o}{F} \right)^2 \right\} \frac{2 \cdot \omega_1^4}{4} \int_0^\infty 2 \int_0^R dR d\rho (R^2 - \rho^2) \exp[-(R^2 + \rho^2)]$$

$$\cdot \exp \left[ -4\pi^2 \left( \sigma^2 - C_\phi(\sqrt{2} \omega_1 \rho) \right) \right] \quad (18)$$

One can readily show that when  $\sigma^2 = 0$ , the constant phase case reduces to

$$\langle I(0, F) \rangle = I(0, F) = \left( \frac{2P_T}{\pi\omega_1^2} \left( \frac{n_o k_o}{F} \right)^2 \right) \frac{\omega_1^4}{4} = I_o \quad (19)$$

so that

$$\frac{\langle I(0, F) \rangle}{I_o} = 4 \int_0^\infty \int_0^R dR d\rho (R^2 - \rho^2) e^{-(R^2 + \rho^2)} e^{-4\pi^2 \left( \sigma^2 - C_\phi(\sqrt{2} \omega_1 \rho) \right)} \quad (20)$$

Equation (20) describes how the peak focused intensity (relative to the peak focused intensity when there are no random phase fluctuations) varies as a function of the covariance of the phase variations.

The form of  $C_\phi(x)$  is yet to be specified. We have no experimental indications of form of this function. As a result, we have chosen the frequently used Gaussian form

$$C_\phi(x) = \sigma^2 \exp\{x^2/\ell^2\} \quad (21)$$

where  $\ell$  is a parameter characterizing the transverse correlation length of the phase fluctuations. As we will show, the relative size of  $\ell$  to the transmitter radius strongly affects the focusing ability of the optical system. Defining  $\ell/\omega_1 = f$ , equation (20) becomes

$$\frac{\langle I(0,F) \rangle}{I_0} = 4 \int_0^\infty \int_0^R dR d\rho (R^2 - \rho^2) \exp \left\{ - \left[ R^2 + \rho^2 + 4\pi^2 \sigma^2 \left( 1 - e^{-2\rho^2/f^2} \right) \right] \right\} \quad (22)$$

Case I:  $f \ll 1$

Equation (22) becomes approximately

$$\frac{\langle I(0,F) \rangle}{I_0} \Big|_{f \ll 1} = e^{-4\pi^2 \sigma^2} \cdot 4 \int_0^\infty \int_0^R dR d\rho (R^2 - \rho^2) e^{-(R^2 + \rho^2)} = e^{-4\pi^2 \sigma^2} \quad (23)$$

Thus, for the case of phase fluctuation which have a very small spatial coherence length, the peak intensity is degraded like the variance of the phase fluctuations. This limiting case is most frequently used as a "worst case" estimate of the degradation suffered by a random phase distorted optical system.

Case II:  $f \gg 1$

With a minimum of algebraic manipulation, one can easily show (the expected result) that in this limit, the peak intensity is not degraded.

$$\frac{\langle I(0,F) \rangle}{I_0} \Big|_{f \gg 1} \approx 1 \quad (24)$$

### Results

Equation (22) has been programmed on the CDC 6600. In Figure 1 we have plotted  $\frac{\langle I(0,F) \rangle}{I_0}$  versus  $f$  for a phase variance of one-tenth of a wave ( $\sigma = 0.1$ ). The transmitter spot size (radius) is 50 cm. Note that these results are independent of the focal distance.

Equation (23) was tabulated and is shown in Figure 2. Of particular importance we note the extremely rapid decrease in the relative peak intensity  $\frac{\langle I(0,F) \rangle}{I_0}$  for phase variances larger than one-tenth of a wave ( $\sigma = 0.1$ ).

### Conclusions

In the formalism developed here, we are treating the localized boundary layer turbulence as a source of phase degradation very much like a random thin phase screen. This analogy is probably very good whenever the thickness of the

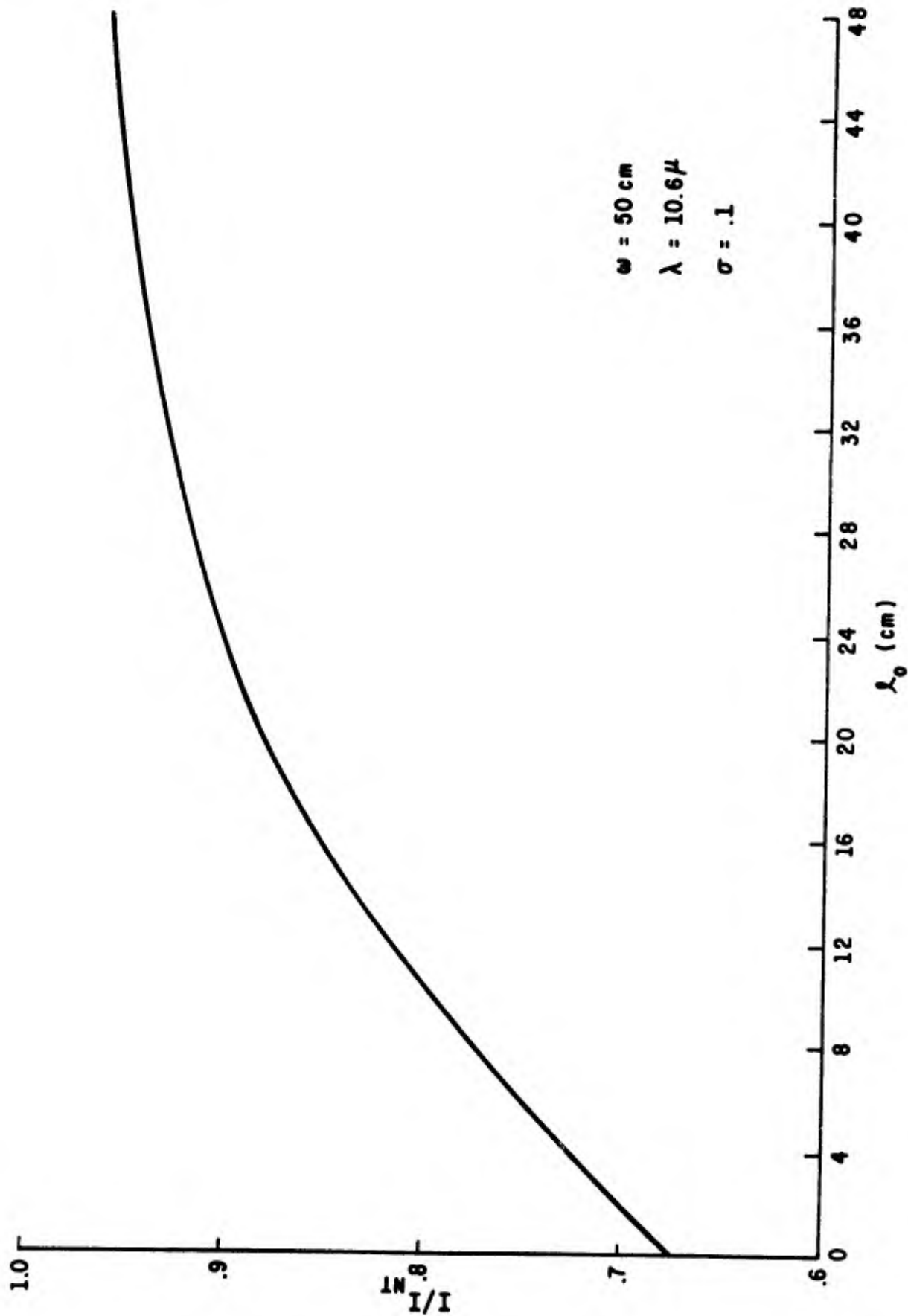


Figure 1. Degradation of average on-axis focal plane intensity as a function of the correlation length of the phase fluctuations.

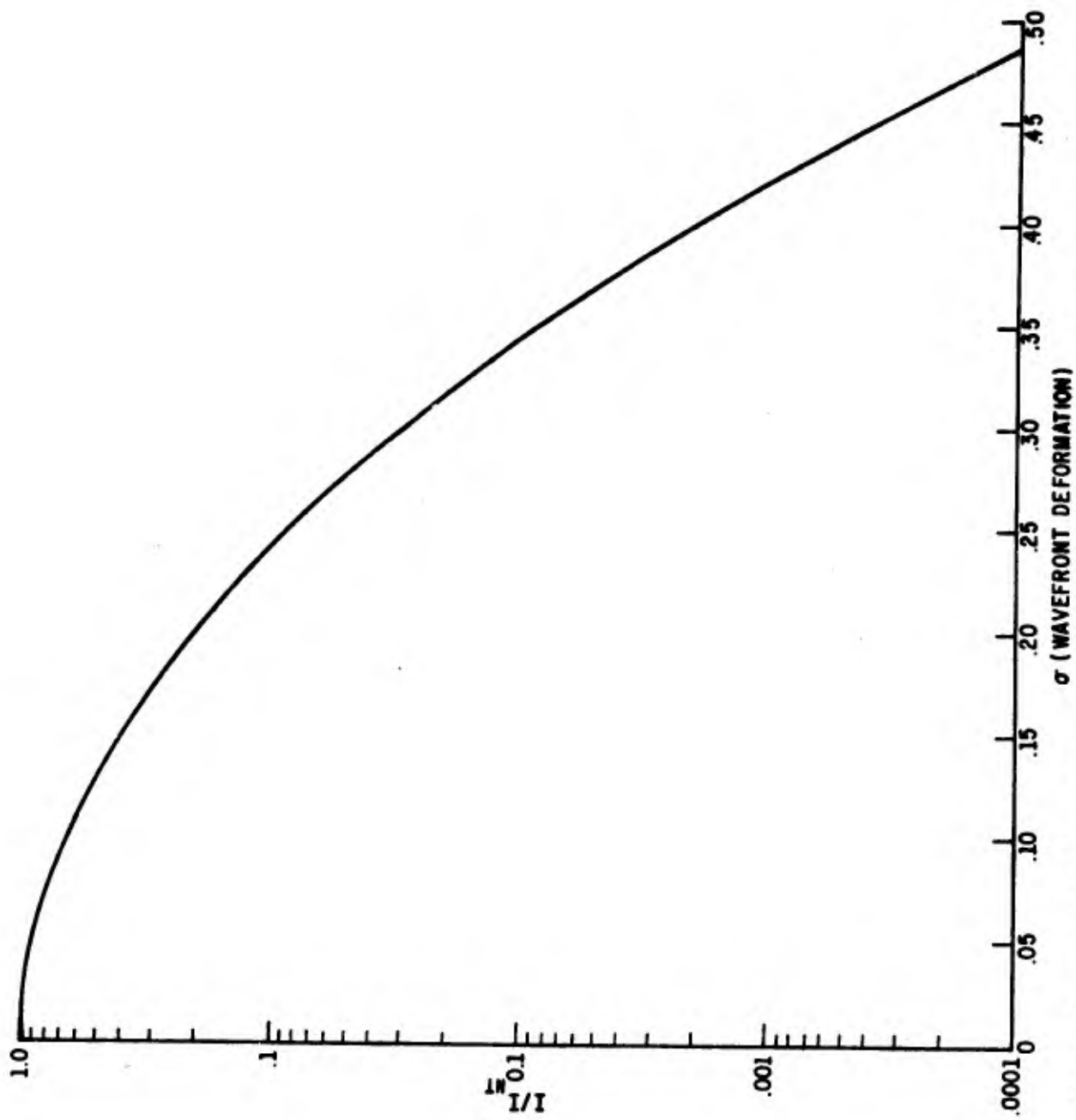


Figure 2. Degradation of on-axis focal plane intensity as a function of the variance of the phase fluctuations.

boundary layer turbulence is small compared to the total propagation path of interest. In addition to this, we were motivated also by the fact that much of the experimental data available in the literature on propagation through turbulent boundary layers describes experiments performed to measure the RMS phase distortion of optical beams. While the method presented here assumes that no further degradation is experienced by the optical beam as it propagates to the focal plane, it is not difficult to incorporate an ambient turbulent atmosphere in the problem.



## TURBULENCE DEGRADATION OF FOCUSED GAUSSIAN BEAMS

C. B. Hogge

In the past years, a number of interesting papers have been published which attempt to treat the problem of a beam wave propagating in a turbulent atmosphere. Unfortunately, most of the methods lack sufficient generality to treat the more meaningful and realistic problems of interest. Lutomirski,<sup>1</sup> however, has developed a method from first principles which treats the general beam wave propagation problem. To apply the method, one need only know the atmospheric Modulation Transfer Functions for a spherical wave when taken at the transmitter for a point source at the receiver. The MTF\* may be estimated from theoretical considerations, or it may be measured directly. The latter situation circumvents the often undesirable feature of having to make any assumptions about the nature of the turbulence.

In this paper, we will consider one particular aspect of the propagation of beam waves: How well can an optical system (transmitter size and optical wavelength) deliver energy to a target? In particular, we will only consider systems which are focused (in the geometrical sense) at the targets, and then ask the question: What is the value of the maximum intensity on target? We will impose a number of assumptions to simplify the calculations.

(1) Assume that the transmitted beam resembles the perfect Gaussian beam usually described for ideal, single-mode lasers. While such beams are theoretically infinite in extent, we will define a beam radius (at the transmitter output it will be given by  $\omega_0$ ) which defines the point on the intensity profile where the intensity is equal to  $1/e^2$  its maximum value. The initial beam therefore has cylindrical symmetry.

(2) Assume that the turbulent atmosphere is homogeneous and isotropic, so that its statistical properties (in particular its structure constant  $C_n$ ) are constant as a function position. Therefore, by symmetry arguments, the average beam profile in the focal plan will also be cylindrically symmetric. Furthermore, the MTF will have cylindrical symmetry as well.

\*Henceforth, "MTF" will always refer to the atmospheric Modulation Transfer Function unless otherwise noted.

(3) In the usual developments of Fresnel and Fraunhofer diffraction theory, small angle assumptions are made. For the development here, the same approximations are assumed.

(4) By the symmetry in the problem, we will assume that the maximum intensity at the target will still occur along the optical axis of the system. By assumption (1), this is clearly true at the transmitter plane.

### Generalized Intensity Distribution

Following Lutomirski's formalism, one can show, using assumptions (2) and (3) and the assumption of cylindrical symmetry in (1), that the time average intensity at any point\* ( $\underline{p}, z$ ) along the beam is given by

$$\langle I(\underline{p}, z) \rangle = \frac{1}{(z\lambda)^2} \left\{ \int_{\underline{\rho}} d^2 \underline{\rho} M_g(\rho, z) e^{-\left(\frac{ik}{z}\right) \underline{p} \cdot \underline{\rho}} \cdot \left[ \int_{\underline{x}} u(\underline{x} + \underline{\rho}/2) \cdot u^*(\underline{x} - \underline{\rho}/2) e^{\left(\frac{ik}{z}\right) \underline{\rho} \cdot \underline{x}} d^2 \underline{x} \right] \right\} \quad (1)$$

where  $M_g(\rho, z)$  is the spherical wave MTF,\*\* and where  $\lambda$  is optical wavelength,  $k = 2\pi/\lambda$  is the wave number and where  $\rho = |\underline{\rho}|$ .  $u(\underline{x})$  is the field distribution at the exit pupil of the optical system; for the case considered here,

$$u(\underline{x}) = \sqrt{\frac{2P_t}{\pi\omega_0^2}} \exp \left\{ -\left( \frac{1}{\omega_0^2} + \frac{ik}{2F} \right) \underline{x} \cdot \underline{x} \right\} \quad (2)$$

where  $F$  is the focal distance and where  $P_t$  is total power leaving the optical system. We get that

$$u(\underline{x} + \underline{\rho}/2) = \sqrt{\frac{2P_t}{\pi\omega_0^2}} \exp \left\{ -\left( \frac{1}{\omega_0^2} + \frac{ik}{2F} \right) (\underline{x} \cdot \underline{x} + \underline{\rho} \cdot \underline{\rho}/4 + \underline{x} \cdot \underline{\rho}) \right\} \quad (3)$$

---

\*The vector  $\underline{p}$  describes the radial position in a cylindrically symmetric system;  $z$  is the linear distance of vector  $\underline{p}$  from the transmitter plane.

\*\*By symmetry, the MTF is only a function of the magnitude of  $|\underline{\rho}|$ .

$$u^*(\underline{r} - \underline{\rho}/2) = \sqrt{\frac{2P_t}{\pi\omega_0^2}} \exp \left\{ - \left( \frac{1}{\omega_0^2} + \frac{ik}{2F} \right) (\underline{r} \cdot \underline{r} + \underline{\rho} \cdot \underline{\rho}/4 - \underline{r} \cdot \underline{\rho}) \right\} \quad (4)$$

$$u^*(\underline{r} - \underline{\rho}/2)u(\underline{r} + \underline{\rho}/2) = \frac{2P_t}{\pi\omega_0^2} \exp \left\{ - \frac{2}{\omega_0^2} (r^2 + \rho^2/4) - i\frac{k}{F} \underline{r} \cdot \underline{\rho} \right\} \quad (5)$$

where  $r = |\underline{r}|$  and  $\rho = |\underline{\rho}|$ .

The integral in the square brackets in equation (1) (call it  $L_1$ ) will become

$$L_1 = \frac{2P_t}{\pi\omega_0^2} e^{-(\rho^2/2\omega_0^2)} \int_0^{2\pi} \int_0^\infty e^{-(2r^2/\omega_0^2)} e^{ik\left(\frac{1}{z} - \frac{1}{F}\right)\underline{r} \cdot \underline{\rho}} r dr d\theta \quad (6)$$

Because  $e^{-2r^2/\omega_0^2}$  is an even function, equation (6) can be written as

$$L_1 = \frac{2P_t}{\pi\omega_0^2} e^{-(\rho^2/2\omega_0^2)} \int_0^{2\pi} \int_0^\infty e^{-(2r^2/\omega_0^2)} \cos \left[ kr\rho \cos\theta \left( \frac{1}{z} - \frac{1}{F} \right) \right] r dr d\theta \quad (7)$$

Performing the  $\theta$  - integration,

$$L_1 = \frac{2P_t}{\pi\omega_0^2} e^{-(\rho^2/2\omega_0^2)} 2\pi \int_0^\infty e^{-(2r^2/\omega_0^2)} J_0 \left( kr\rho \left[ \frac{1}{z} - \frac{1}{F} \right] r dr \right) \quad (8)$$

The  $r$  - integration produces

$$L_1 = P_t \exp \left\{ - \left[ \frac{1}{2\omega_0^2} + \frac{k^2\omega_0^2}{8} \left( \frac{1}{z} - \frac{1}{F} \right)^2 \right] \rho^2 \right\} \quad (9)$$

Equation (1) can now be written as

$$\langle I(\underline{p}, z) \rangle = \frac{P_t}{(z\lambda)^2} \int_0^{2\pi} \int_0^\infty \rho d\rho d\theta M_s(\rho, z) \cdot e^{-i\frac{k}{z} \underline{p} \cdot \underline{\rho} \cos\theta} e^{-Q\rho^2} \quad (10)$$

where

$$Q = \frac{1}{2\omega_o^2} + \frac{k^2\omega_o^2}{8} \left( \frac{1}{z} - \frac{1}{F} \right) \quad (11)$$

Performing the  $\theta$  - integration,

$$\langle I(\underline{p}, z) \rangle = \frac{2\pi P_t}{(z\lambda)^2} \int_0^\infty \rho d\rho M_s(\rho, z) e^{-Q\rho^2} J_0\left(\frac{k}{z} p\rho\right) \quad (12)$$

Equation (12) describes the average intensity distribution at any point along the path of propagation in terms of the atmospheric MTF as viewed at the transmitter from a point source located on the observation plane at  $z$ .

To simplify the problem we will limit our investigation of the intensity to its value at  $\underline{p} = 0$ ; i.e., on-axis. By assumption (4), and clearly from equation (12), the maximum intensity in any  $z$ -plane will occur for this value of  $\underline{p}$ . Equation (12) becomes

$$\langle I(o, z) \rangle = \frac{2\pi P_t}{(z\lambda)^2} \int_0^\infty \rho d\rho M_s(\rho, z) e^{-Q\rho^2} \quad (13)$$

Finally, we choose to investigate the intensity only in the focal plane; i.e.,  $z = F$ . Hence,  $Q = \frac{1}{2\omega_o^2}$ , and equation (13) becomes

$$\langle I(o, z) \rangle = \frac{2\pi P_t}{(z\lambda)^2} \int_0^\infty \rho d\rho M_s(\rho, z) e^{-\left(\rho^2/2\omega_o^2\right)} \quad (14)$$

This result is the fundamental equation used in this paper. Before its properties are investigated, we will consider briefly the atmospheric MTF.

#### Atmospheric Modulation Transfer Function

Consider the following situation: Place a point source at  $z = 0$ . In a plane located at  $z = L$  place a collecting lens of diameter  $D$ . Assume that there is a turbulent medium between  $z = 0$  and  $z = L$ . Defining the combination of the turbulent medium and the collecting lens as an image forming system, one can show that its Modulation Transfer Function is given by the normalized

two-dimensional (spatial) Fourier transformation of the intensity distribution in the image plane. Let  $v(\underline{r})$  be the complex quantity which describes a wave that deviates (not grossly) in amplitude and phase from a spherical wave. Assume that the collecting lens is diffraction-limited so that on the image side of the lens the field can be written as

$$v(\underline{r}) = w(\underline{r}) q(\underline{r}) \quad (15)$$

where

$$w(\underline{r}) = \begin{cases} 1 & \text{if } |\underline{r}| \leq D/2 \\ 0 & \text{if } |\underline{r}| > D/2 \end{cases}$$

and where  $q(\underline{r})$  describes the deviation of the wave from an ideal spherical wave. Then, for the case where a long time average is taken, one can show that<sup>2</sup>

$$\text{MTF} \Big|_{\text{system}} = \text{MTF} \Big|_{\text{diffraction limited lens}} \cdot \langle q(\underline{r}') \cdot q^*(\underline{r}'') \rangle \quad (16)$$

where  $q^*(\underline{r}'')$  is the complex field conjugate to  $q(\underline{r}'')$ .

Now the total field on the object side of the lens can be written as a spherical wave times its deviation. Hence,

$$\frac{e^{ik(|\underline{r}'| - |\underline{r}''|)}}{|\underline{r}'||\underline{r}''|} \cdot \langle q(\underline{r}') \cdot q^*(\underline{r}'') \rangle$$

is the cross-correlation of the complex fields at  $\underline{r}'$  and  $\underline{r}''$  and can be measured experimentally in a number of ways. The cross-correlation of the deviations ( $\langle q(\underline{r}') \cdot q^*(\underline{r}'') \rangle$ ) can readily be determined from the knowledge of this quantity; therefore, its importance to image forming optical systems is clear.

In general lens design theory, one finds that the MTF of a system can frequently be represented by a product of the system's component MTF's. In this vein then, the quantity in the brackets of equation (16) is defined as the Modulation Transfer Function of the atmosphere.

Now, if one defines

$$u(\underline{r}) = e^{\left(\ell(\underline{r}) + i\phi(\underline{r})\right)} \quad (17)$$

where  $\ell(\underline{r})$  and  $\phi(\underline{r})$  are the log amplitude and phase fluctuations of an otherwise perfectly coherent point source, then one can show\* that <sup>2</sup>

$$\langle q(\underline{r}')q(\underline{r}'') \rangle = \exp \left\{ -\frac{1}{2} D(|\underline{r}' - \underline{r}''|) \right\} = M_s(\rho, z) \quad (18)$$

where  $D(\rho)$ \*\* is called the wave structure function <sup>4</sup> and is defined as

$$D(\rho) = D_\ell(\rho) + D_\phi(\rho) \quad (19)$$

where  $D_\ell(\rho)$  and  $D_\phi(\rho)$  are the log amplitude and phase structure functions. These functions are defined as

$$\begin{aligned} D_\ell(\rho) &= \langle [\ell(\underline{r}') - \ell(\underline{r}'')]^2 \rangle \\ D_\phi(\rho) &= \langle [\phi(\underline{r}') - \phi(\underline{r}'')]^2 \rangle \end{aligned} \quad (20)$$

where, under the assumption of locally homogeneous and isotropic turbulence, one can show that  $D_\ell$  and  $D_\phi$  depend only on  $\rho = |\underline{r}' - \underline{r}''|$ . For a spherical wave (point source) Fried<sup>3</sup> shows that  $D(\rho)$  is

$$D(\rho, z) = 8\pi^2 k^2 \int_0^z dz' \int_0^\infty K dK \left[ 1 - J_0\left(\frac{K\rho z'}{L}\right) \right] \Phi_n(z', K) \quad (21)$$

where  $J_0(x)$  is the 0<sup>th</sup> order Bessel function of the first kind and where  $\Phi_n(z, K)$  is the power spectrum of the atmospheric index of refraction fluctuations. Equation (21) is completely general and can treat any locally homogeneous power spectrum. In practice, one normally selects a spectrum which has an

---

\*Certain assumptions are required, which do not violate any of the assumptions made here.

\*\*If a lens is used to define this function, then some nonessential scaling coordinate parameters will appear.

inertial<sup>4</sup> subrange that varies as\*  $K^{-11/3}$ , although frequently people<sup>5,6</sup> have used other more mathematically convenient forms. The simplest type spectrum, often called the Kolmogorov spectrum, is

$$\Phi_n(K, z) = 0.033C_n^2(z)K^{-11/3} \quad (22)$$

where  $C_n^2(z)$  is the atmospheric structure constant and is the only measure of the degree of turbulence when this form of the spectrum is used. While experimentally this spectrum has been shown to be valid (under good turbulent mixing conditions) for spectral wave numbers,  $K$ , in the inertial subrange, it has been noted that at either limit ( $K \rightarrow \infty$  and  $K \rightarrow 0$ ) disagreements have been observed. In fact, it is clear that at the lower limit ( $K \rightarrow 0$ ) the spectrum becomes meaningless in that it predicts an infinite amount of energy in turbulent eddies with wave number\*\*  $K = 0$ . While this mathematical singularity is bothersome on physical grounds,  $\Phi_n(K, z)$  normally appears in integrals which still remain bounded when both the  $K$  and  $z$  integrations are performed. Furthermore, for many applications, the form of the spectrum for large and small wave numbers has often been shown to be of little consequence to the final results. Just the same, however, for some problems people have been forced to modify the Kolmogorov spectrum. Tatarski<sup>4</sup> used the following form for the refractive index power spectrum:

$$\Phi_n(z, K) = 0.033C_n^2(z)K^{-11/3}e^{-\left(K/K_m\right)^2} \quad (23)$$

It modifies the Kolmogorov spectrum for<sup>7</sup>  $K > K_m = 5.92/\ell_0$ , where  $\ell_0$  is called the inner scale of turbulence, and, in so doing, attempts to account for the viscous damping effects experienced by the smallest turbulent eddies. Von Karman suggested a spectrum of the form<sup>1</sup>

$$\Phi_n(z, K) = \frac{0.033C_n^2(z)e^{-\left(K/K_m\right)^2}}{\left(K^2 + \left(2\pi/L_0\right)^2\right)^{11/6}} \quad (24)$$

---

\*This general form of the spectrum was derived on the basis of physical grounds and dimensional analysis.<sup>4</sup>

\*\*One can easily convince himself that the energy in the wave numbers  $K - (dK/2)$  to  $K + (dK/2)$  may be that thought of as the energy in the turbulent eddies of size  $L = 2\pi/K$ .

This form not only modifies the spectrum for viscous effects, but also accounts for the finite energy requirements of the very small wave numbers.  $L_0$  is called the integral scale\* of turbulence and provides a length measurement over which the index of refraction fluctuations remain correlated.<sup>8</sup> Lutomirski<sup>1</sup> has shown that the relative size of  $L_0$  to the transmitting aperture diameter can have significant effects on the focusing characteristics of an optical system. While this may be true, the use of equation (24) for the spectrum only serves for our calculations to complicate the mathematics, and does not add to the understanding of the physical processes which are occurring. Thus we choose to use equation (22) for the power spectrum of the refractive index fluctuations, not because it more correctly represents the turbulence characteristics (which it does not), but because it simplifies and clarifies the analysis to be performed, and, in addition, yields numerical results which tend to be conservative when compared to the results obtained for the power spectrum of equation (24).

Using equation (22) in equation (21), the K-integration yields

$$D(\rho, F) = 2.91 k^2 \rho^{5/3} \int_0^F C_n^2(z) \left(\frac{z}{F}\right)^{5/3} ds \quad (25)$$

where we have set  $z = F$ .

We next assume that the turbulence is stationary over the path of propagation. (See assumption (2).) As a result, we will let

$$C_n^2(z) = C_n^2$$

where  $C_n^2$  is a constant independent of  $z$ . The final integration in equation (25) can now be performed. We get

$$D(\rho, F) = (2.91) \left(\frac{3}{8}\right) k^2 \left(F C_n^2\right) \rho^{5/3} \quad (26)$$

---

\*There is some disagreement (or confusion) about the definition of  $L_0$  as used for this spectrum. Tatarski defines this parameter as the integral scale of turbulence, whereas Lutomirski defines it as the outer scale.



Defining

$$R(\lambda, F C_n^2) = \left(\frac{2.91}{2}\right)\left(\frac{3}{8}\right)k^2(F C_n^2) \quad (27)$$

the spherical wave MTF (equation (18)) becomes

$$M_s(\rho, F) = e^{-R(\lambda, F C_n^2)\rho^{5/3}} \quad (28)$$

### Parametric Studies of Focused Gaussian Beams in Turbulence

Combining equations (28) and (14), one obtains an expression for the peak, on-axis intensity of a perfect Gaussian beam focused through spatially stationary homogeneous and isotropic turbulence.

$$\langle I(0, F) \rangle = \frac{2\pi P_T}{(\lambda F)^2} \int_0^\infty \rho d\rho e^{-R\rho^{5/3}} e^{-\rho^2/2\omega_0^2} \quad (29)$$

A change of variables will produce a slightly more convenient form. Let  $x = \rho/\omega_0$ ; then equation (29) becomes

$$\langle I(0, F) \rangle = \frac{2\pi P_T}{(\lambda F)^2} \omega_0^2 \int_0^\infty x dx e^{-R\omega_0^{5/3}x^{5/3}} e^{-x^2/2} \quad (30)$$

Defining\*  $N = R\omega_0^{5/3}$ , we get

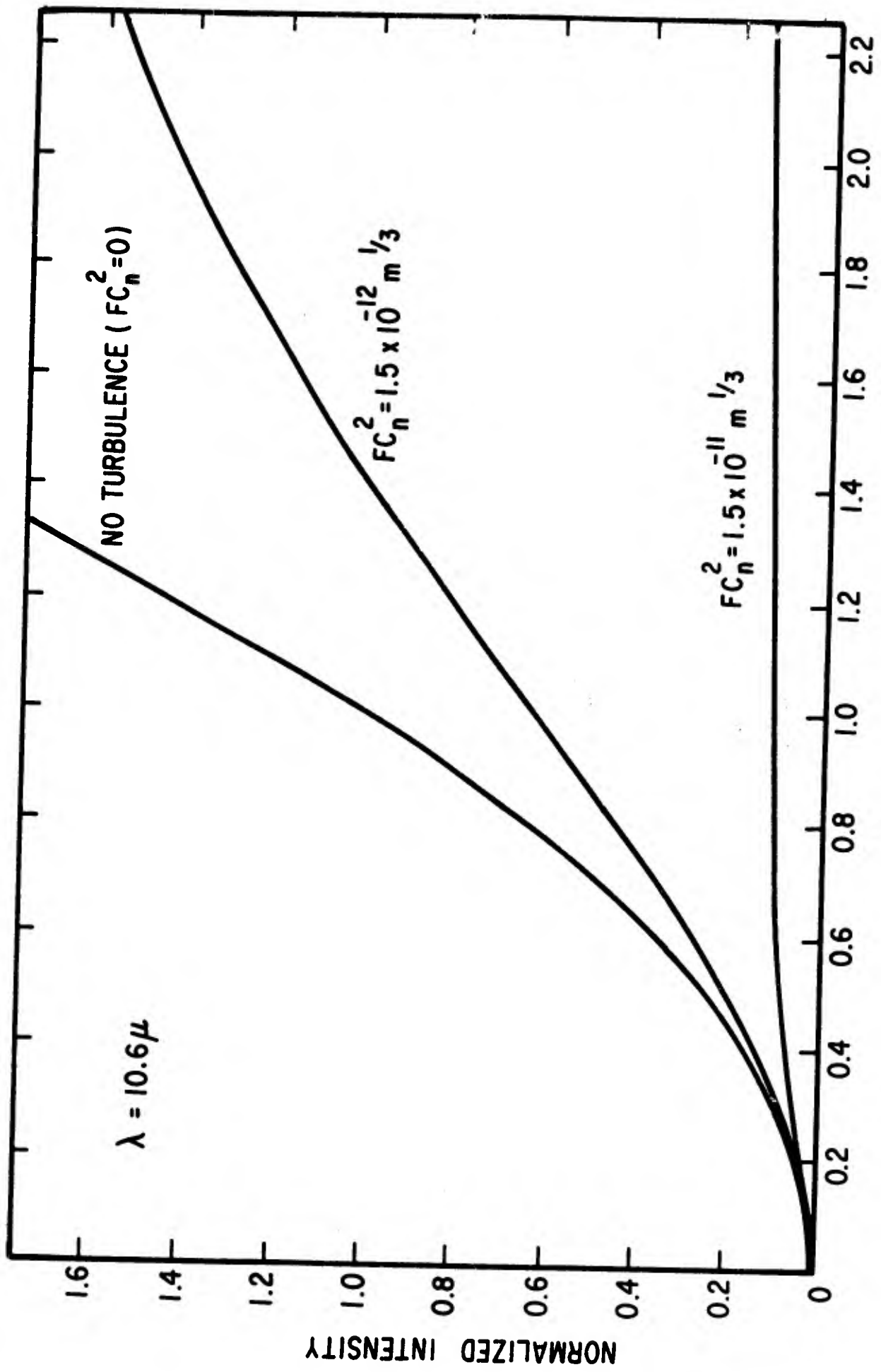
$$\langle I(0, F) \rangle = \frac{2\pi \omega_0^2 P_T}{(\lambda F)^2} \int_0^\infty x dx e^{-Nx^{5/3}} e^{-x^2/2} \quad (31)$$

To familiarize the reader with the general behavior of beams focused in a turbulent media, we show in Figure 1 a plot of

$$\langle I(0, F) \rangle / \left[ 2\pi P_T / (\lambda F)^2 \right] \text{ versus } \omega_0$$

---

\*See appendix for nomograph to determine N.



$\omega_0$  TRANSMITTER RADIUS ( METERS )

Figure 1. Characteristic Saturation of Peak Focal Point Intensity in the Presence of Turbulence.

for numerous values of  $F C_n^2$ . Note that for the case of no turbulence, an increasing  $\omega_0$  produces a continuously increasing intensity. This represents the ideal diffraction limited case. In practice, however, for propagation paths in the atmosphere, turbulent conditions do exist with the subsequent result that the focused peak intensity always tends to saturate with increasing  $\omega_0$ . This limit depends on both  $\lambda$ , and  $F C_n^2$  and its value will be discussed in more detail at a later time.

We now will investigate several properties of equation (31) with the thought of providing some guidelines for optimizing an optical system of the type considered in this paper. It is of interest to point out that this entire analysis can equally as well be applied to systems designed to image incoherent sources viewed through a turbulent atmosphere.\*<sup>2</sup>

Normalized to the No-Turbulence Case. If the atmosphere were a perfect transmission medium completely free of turbulence, then  $C_n^2 \equiv 0$ ; hence  $N = 0$ . Letting  $I_{NT} = \langle I(0,F) \rangle$  for this case, we get from equation (31),

$$I_{NT} = \frac{2\pi \omega_0^2 PT}{(\lambda F)^2} \quad (32)$$

Thus, equation (31) can be written as

$$\langle I(0,F) \rangle = I_{NT} \cdot \int_0^{\infty} x dx e^{-Nx^{5/3}} e^{-x^2/2} \quad (33)$$

In Figure 2 we have plotted  $\langle I(0,F) \rangle / I_{NT}$  versus  $N$ . We observe that for larger  $N$ , i.e., larger  $(F C_n^2)$ 's, larger  $\omega_0$ 's, and smaller  $\lambda$ 's, the optical system performs less and less like the ideal system. Clearly then, one might want to specify a value of  $N$  in design criteria to ensure that the system operate in excess of some specified performance level (often specified in number of diffraction limits which might be defined here to be  $[\langle I(0,F) \rangle / I_{NT}]^{1/2}$ ).

Normalized to the Intensity Limit for Large Transmitting Apertures. Next consider the effect of increasing without limit the size of the transmitter radius. By equation (29) it is clear that the intensity becomes

---

\*Some distinctions must be made when the turbulence is only locally homogeneous and isotropic.

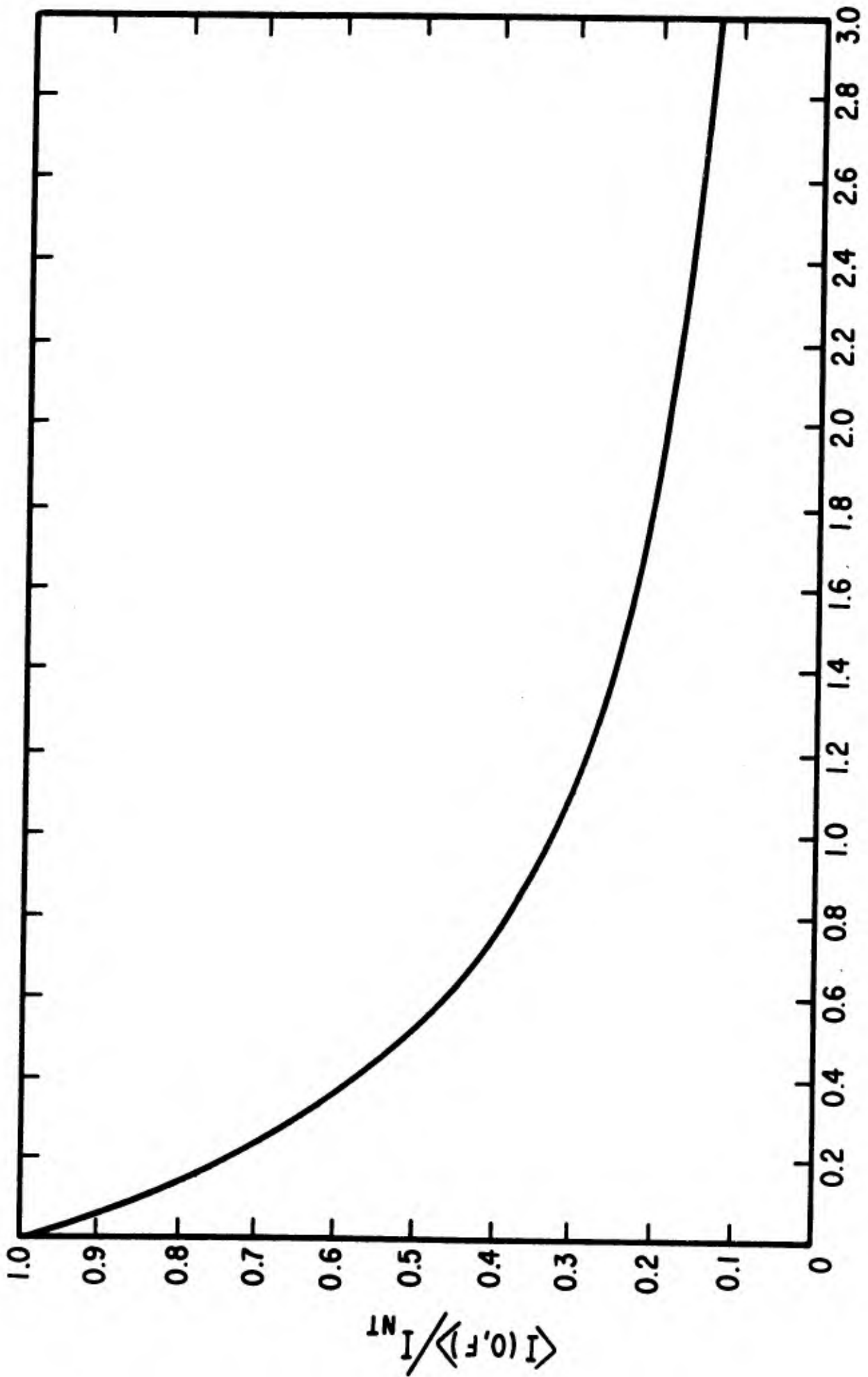


Figure 2. Ratio of Intensity in Turbulence to the Ideal Intensity in the Absence of Turbulence versus the System Parameter  $N$ .

$$\langle I(0,F) \rangle \Big|_{\omega_0 \rightarrow \infty} = I_L = \frac{2\pi P_T}{(\lambda F)^2} \cdot \int_0^{\infty} \rho d\rho e^{-R\rho^{5/3}} \quad (34)$$

Integrating equation (34) we get

$$I_L = \frac{2\pi P_T}{(\lambda F)^2} \frac{3}{5} \frac{\Gamma(6/5)}{R^{6/5}} \quad (35)$$

Now, in the classical limit of no turbulence (equation (31)), the intensity increases without bound as  $\omega_0 \rightarrow \infty$ . We observe, however, that whenever any degree of turbulence is present (this means  $R \neq 0$ ), there is a limit to the maximum intensity. Using equation (27), we see that

$$I_L = \frac{(0.087) P_T \lambda^{2/5}}{F^{16/5} (C_n^2)^{6/5}} \quad (36)$$

Of particular interest in equation (36) is the fact that  $I_L$  increases for longer wavelengths; the dependence on  $F$  and  $C_n^2$  is not unexpected, and deserves no comment other than to note a rather strong dependence on the focal length.

Dividing equation (31) by equation (35), we get

$$\frac{\langle I(0,F) \rangle}{I_L} = \frac{5}{3\Gamma(6/5)} \cdot N^{6/5} \cdot \int_0^{\infty} x dx e^{-Nx^{5/3}} e^{-x^2/2} \quad (37)$$

In Figure 3 we have plotted  $\langle I(0,F) \rangle / I_L$  versus  $N$ . We note that as  $N$  increases (that is for larger  $F C_n^2$ , larger  $\omega_0$ 's, and smaller  $\lambda$ 's) the optical system approaches its limit of performance. Clearly, then, we do not wish to design a system which is approaching its limit capacity, and as a result again we would probably wish to choose an upper limit for  $N$ .

An Upper Limit for the Transmitter Aperture Size. If equation (37) is plotted as a function of  $(\omega_0^2)$ , a family of curves will result (for different  $F C_n^2$ 's and  $\lambda$ 's). The general shape of the curve would, however, be as shown in Figure 4.

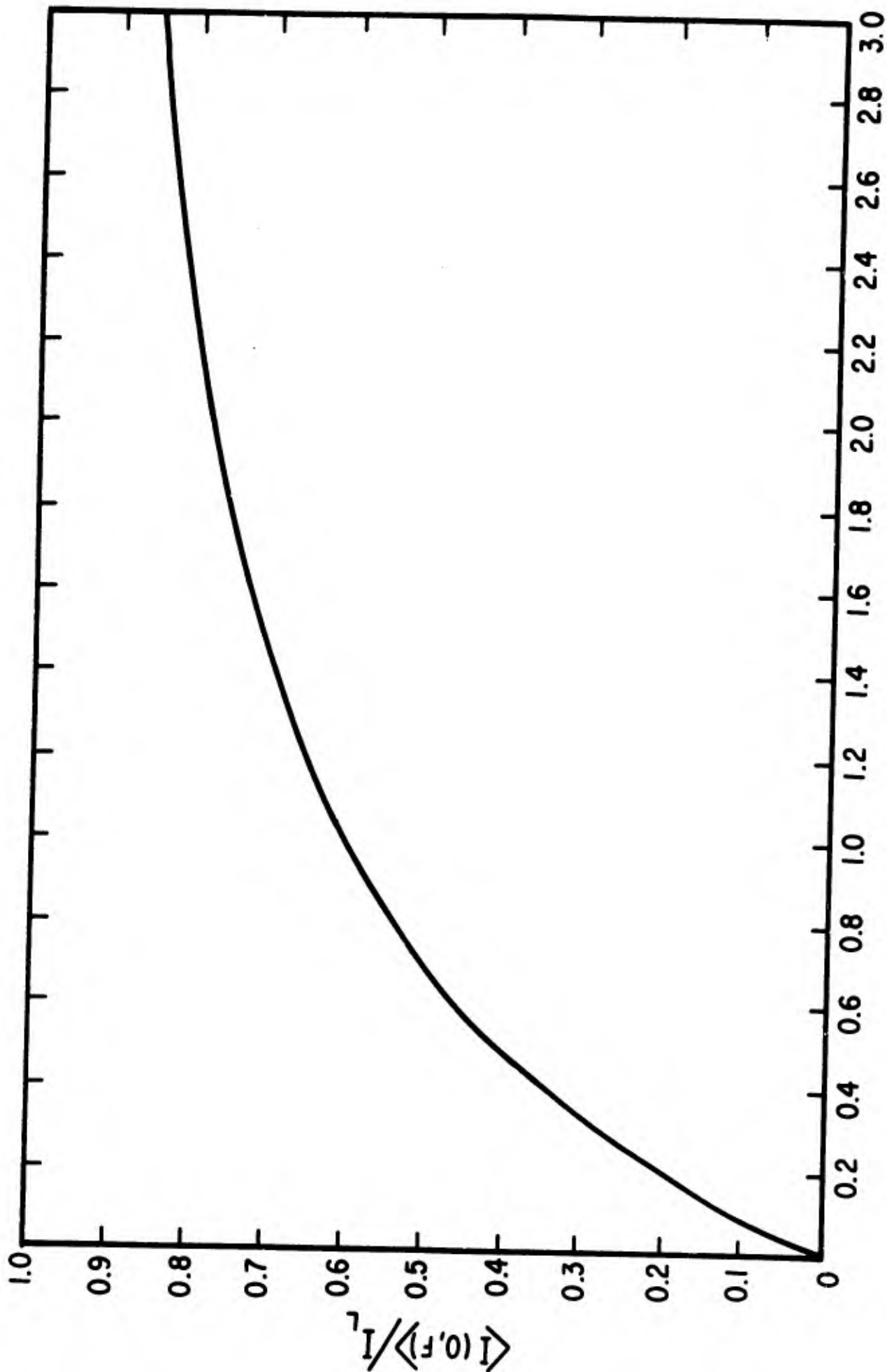


Figure 3. Ratio of Intensity in Turbulence to the Saturated Intensity for an Infinitely Large Transmitting Radius versus the System Parameter  $N$ .

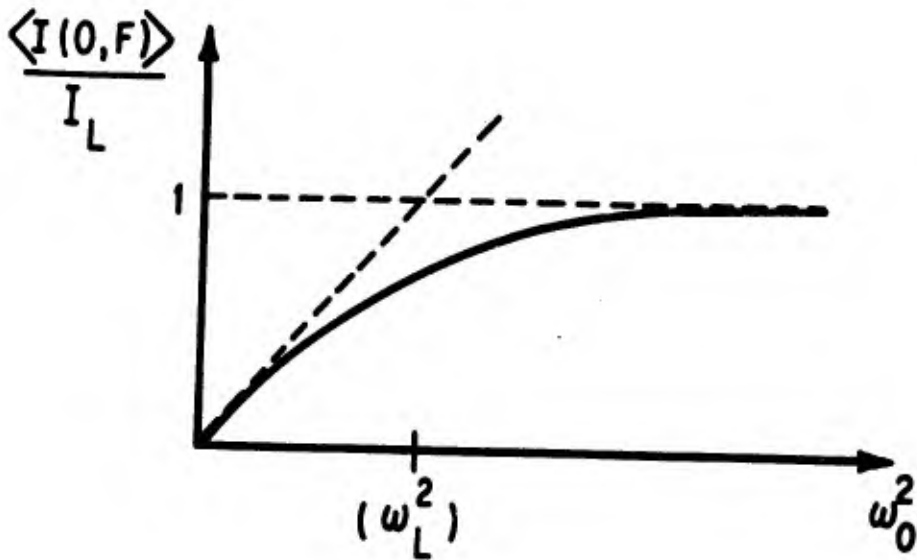


Figure 4. Ratio of Intensity in Turbulence to Saturated Intensity as a Function of the Transmitting Radius.

In the limit as  $\omega_0^2 \rightarrow 0$ , equation (37) becomes

$$\left. \frac{\langle I(0,F) \rangle}{I_L} \right|_{\omega_0^2 \rightarrow 0} = \frac{5}{3} \frac{R^{6/5}}{\Gamma(6/5)} (\omega_0^2)$$

so that a straight line drawn tangent to the curve at  $\omega_0^2 = 0$  will have a slope  $m = \frac{5}{3} \frac{R^{6/5}}{\Gamma(6/5)}$ . We now arbitrarily define a limiting aperture,  $\omega_L$ , as the  $\omega_0^2$  corresponding to the intersection of the tangent line and the limit line of  $\frac{\langle I(0,F) \rangle}{I_L} = 1$ . We get that

$$\omega_L = 0.118 \frac{\lambda^{6/5}}{(F C_n^2)^{3/5}} \quad (38)$$

which corresponds to  $N = \left[ \frac{3}{5} \Gamma(6/5) \right]^{5/6} = 0.608$ , and  $\frac{\langle I(0,F) \rangle}{I_L} \approx 0.465$ .

While this definition appears rather arbitrary, we point out that this value for  $N$  corresponds to the intersection of curves in Figures 2 and 3 and mathematically implies that

$$\frac{\langle I(0,F) \rangle}{I_{NT}} = \frac{\langle I(0,F) \rangle}{I_L}$$

Thus, in some sense a balance has been set between the quality of operation achieved as compared to the ideal case where there is no turbulence, and the more realistic case of a very large transmitting aperture in the presence of turbulence.

In Figure 5 we have plotted  $\omega_L$  versus  $F C_n^2$  for numerous values of  $\lambda$ .

System Wavelength Dependence. Again consider an ideal system with no turbulence. From equation (32) we see that if we specify  $P_T$  and  $F$ , then there is a continuum of combinations of  $\omega_0$  and  $\lambda$  which will produce exactly the same  $I_{NT}$ . Suppose we start with  $\omega_0 = a$  and  $\lambda = b$ . Then

$$I_{NT}(a,b) = \left( \frac{2\pi P_T}{F^2} \right) \left( \frac{a}{b} \right)^2$$

Requiring  $I_{NT}(\omega'_0, \lambda') = I_{NT}(a,b)$ , we get the combination of  $\omega'_0$ , and  $\lambda'$  must satisfy

$$\frac{\omega'_0}{\lambda'} = \frac{a}{b}$$

or

$$\lambda' = \left( \frac{b}{a} \right) \omega'_0 \quad (39)$$

Choosing  $a = 0.25$  m and  $b = 10.6\mu$ , equation (39) plots as the straight (dotted) line in Figure 6.

Let us now return to the problem of a turbulent transmission medium, and again ask the same question: If  $P_T$  and  $F$  are specified, beforehand (and held fixed throughout) and if the corresponding intensity,  $\langle I(0,F) \rangle$ , is set by selecting  $\omega_0 = a = 0.25$  m and  $\lambda = b = 10.6\mu$ , what other combinations of  $(\omega'_0, \lambda')$  will produce the same intensity? Using equation (31), one can readily show that the combination  $(\omega'_0, \lambda')$  will be specified by the integral-transcendental relation

$$\lambda' = \left( \frac{b}{a} \right) \cdot \left[ \frac{G(N_2)}{G(N_1)} \right]^{1/2} \cdot \omega' \quad (40)$$



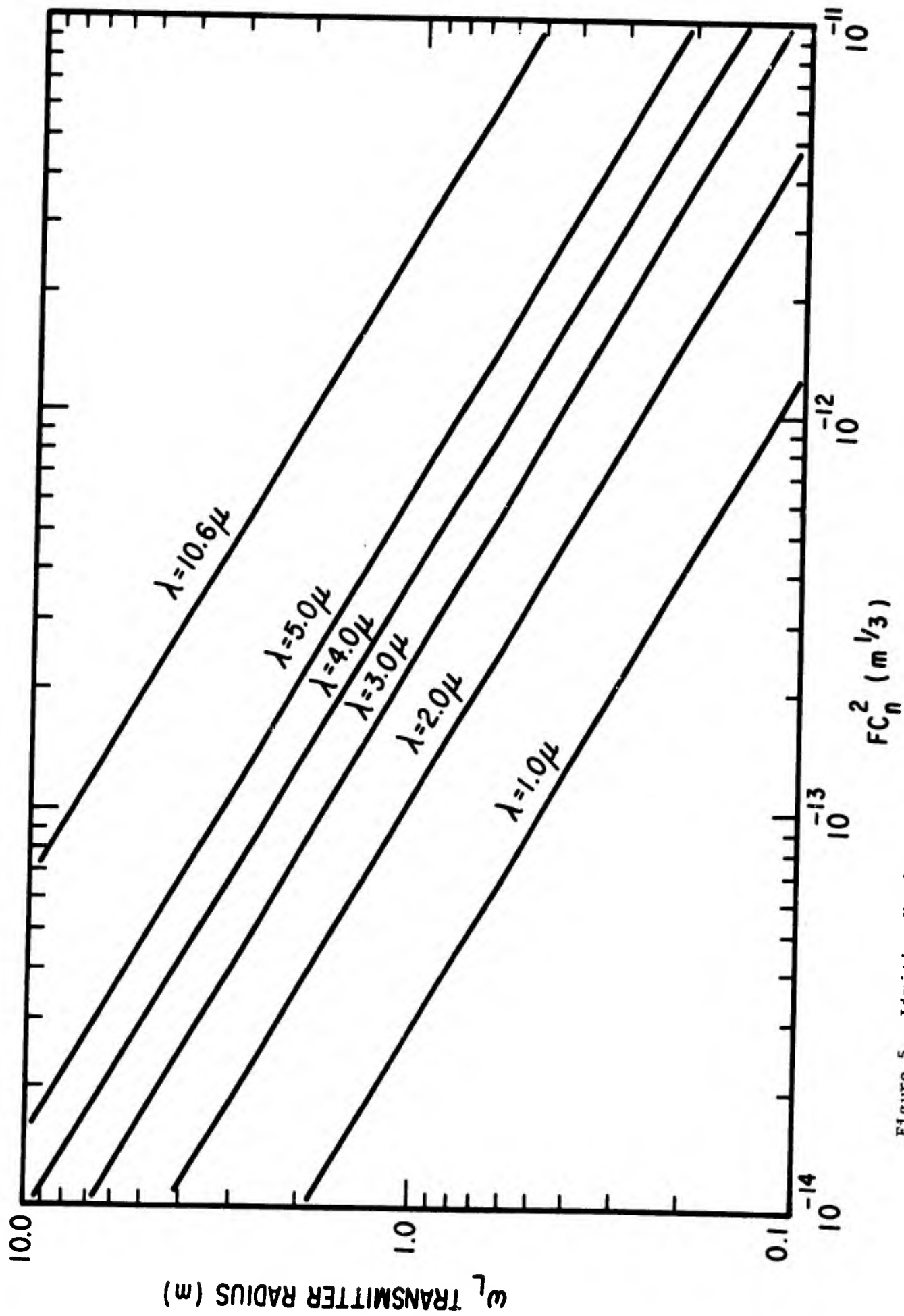
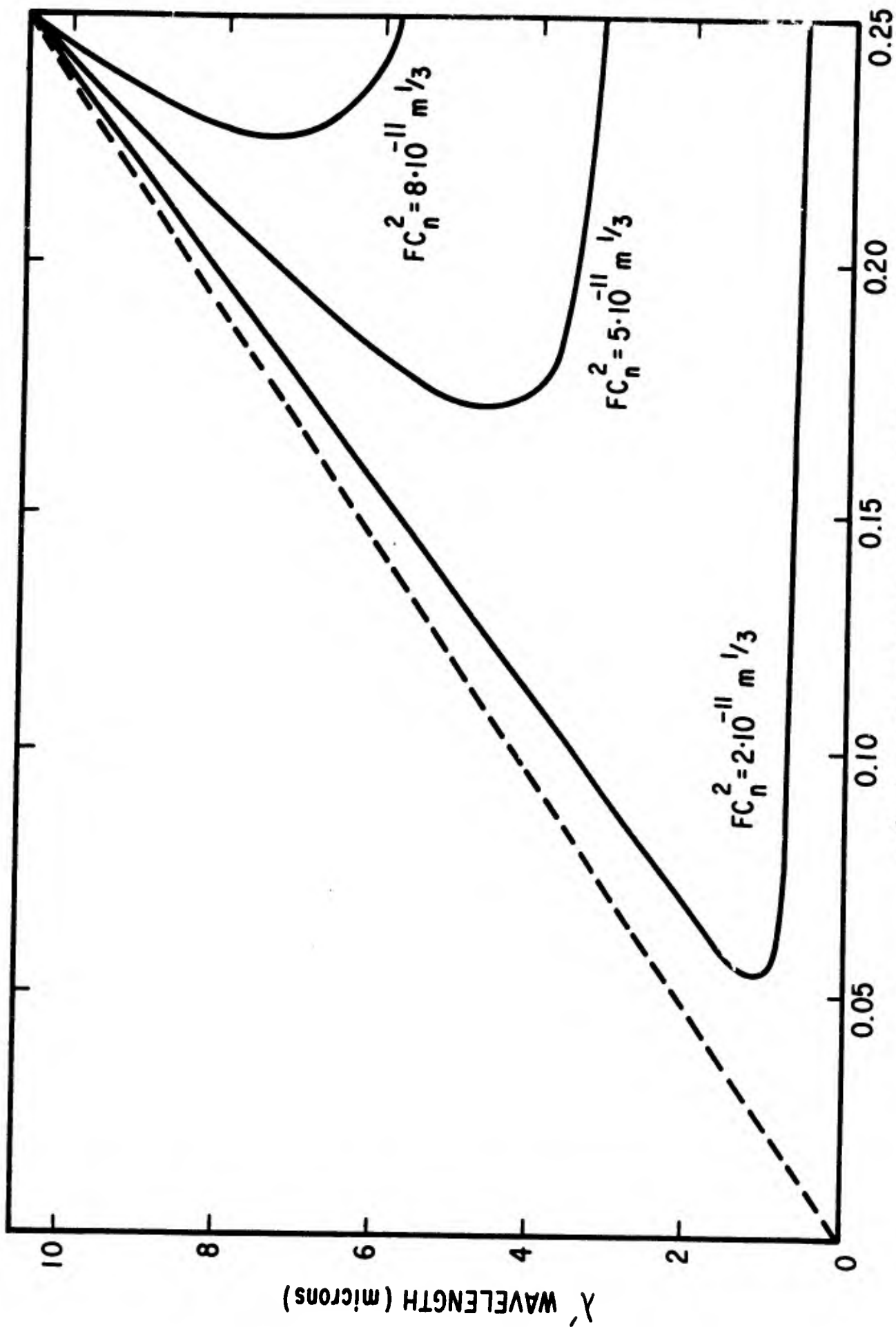


Figure 5. Limiting Useful Transmitted Aperture in the Presence of Turbulence.



$\omega'_0$  TRANSMITTER RADIUS (METERS)

Figure 6. Equivalent Constant Intensity Optical Systems (referenced to  $\omega'_0 = 0.25 \text{ m}$  and  $\lambda = 10.6 \mu$ ).

where

$$N_1 = \left(\frac{2.91}{2}\right) \left(\frac{3}{8}\right) \frac{4\pi^2}{b^2} (F C_n^2) a^{5/3} \quad (41)$$

$$N_2 = \left(\frac{2.91}{2}\right) \left(\frac{3}{8}\right) \frac{4\pi^2}{(\lambda')^2} (F C_n^2) (\omega')^{5/3} \quad (42)$$

$$G(N) = \int_0^{\infty} x \, dx \, e^{-Nx^{5/3}} e^{-x^2/2} \quad (43)$$

In the case of no turbulence ( $C_n^2 \equiv 0$ ) equation (40) is readily seen to reduce to equation (39). Otherwise, the ratio  $G(N_2)/G(N_1)$ , which is seen to be a function of  $a$ ,  $b$ ,  $\lambda'$ , and  $\omega'$  will alter the ideal case as represented by equation (39). We have solved equation (40) for several values of  $F C_n^2$  and the results are plotted in Figure 6. Several things are worth noting, all of which are a result of the fact that shorter wavelength radiation is affected more by turbulence than longer wavelength radiation.

First we see that for all values of  $\lambda' < 10.6\mu$  the transcendental curves lie below the dashed line representing the ideal (no turbulence) case. Hence, for a given wavelength ( $<10.6\mu$ ) one must transmit a beam whose radius is larger than the corresponding ideal beam radius. This directly supports the above statement that the turbulence affects the shorter wavelengths more.

Secondly, note that each curve approaches an asymptotic value of  $\lambda' (<10.6\mu)$  as  $\omega'_0 \rightarrow \infty$ . The reason for this is clear if we recall equation (36).

$$I_L = 0.087 \frac{P_T \lambda^{2/5}}{F^{16/5} (C_n^2)^{6/5}} \quad (36)$$

Keeping  $P_T$ ,  $F$ , and  $C_n^2$  fixed, and decreasing  $\lambda$ , we decrease the limiting intensity which an optical system with an infinitely large transmitting aperture can achieve. With  $\lambda = 10.6\mu$  and  $\omega_0 = 0.25 \text{ m}$  inserted in equation (30), we will obtain some value for  $\langle I(0,F) \rangle$ . Now, when  $\lambda'$  becomes so small in equation (36) that

$$\langle I(0,F) \rangle \left| \begin{array}{l} \omega_0 = 0.25 \text{ m} \\ \lambda = 10.6\mu \end{array} \right. > I_L(\lambda')$$

we see that one is physically unable to satisfy the constant intensity requirement. Hence there is a limiting value of  $\lambda_L$ , for each value of  $F C_n^2$ ; such that for all  $\lambda' < \lambda_L$  one cannot possibly construct an equivalent optical system capable of focusing to the same peak intensity even if an infinitely large transmitting aperture could be used.

Curves such as these in Figure 6 might be used in performing cost-effective analyses. For instance, if the operating turbulence characteristics and focal range are known with reasonable certainty, one might design the transmitting optics near the knee of the appropriate  $F C_n^2$  curve. In so doing, the cost of constructing as small a telescope as possible would be achieved.

We must point out here that these parametric curves are a function of the reference wavelength and transmitting aperture chosen. If one prefers, other pairs of parameters  $(\omega_0, \lambda)$  could be chosen as a reference. Likewise, similar curves can be obtained if one simply assigns a numerical value to the minimum peak intensity required\* (for a specific task) and the corresponding pairs of  $(\omega_0', \lambda')$  then determined from equation (31). However, as long as we require  $P_T$  to be the same for both optical systems, one can easily convince himself that this latter procedure is exactly the same as what we have done, the only difference being the choice of the reference  $\omega_0$  and  $\lambda$ .

This last remark suggests yet another parametric curve of interest. Suppose we have an optical system with a fixed transmitting aperture diameter. The variables of interest now are the total power,  $P_T$ , and the wavelength. Again we will require the peak intensities for the two optical systems to be the same.

In the case of no turbulence we get that

$$P_T(\lambda') = \left( \frac{P_T(\lambda)}{\lambda^2} \right) (\lambda')^2 \quad (44)$$

where we indicate that the total power is a function of the wavelength. In the presence of turbulence, this equation becomes

---

\* $P_T$  must be specified also if this approach is to be taken.

$$P_T(\lambda') = \left( \frac{P_T(\lambda)}{\lambda^2} \right) \left[ \frac{G(N_1')}{G(N_2')} \right] (\lambda')^2 \quad (45)$$

where

$$N_1' = \left( \frac{2.91}{2} \right) \left( \frac{3}{8} \right) \frac{4\pi^2}{\lambda^2} (F C_n^2) \omega_o^{5/3} \quad (46)$$

$$N_2' = \left( \frac{2.91}{2} \right) \left( \frac{3}{8} \right) \frac{4\pi^2}{(\lambda')^2} (F C_n^2) \omega_o^{5/3} \quad (47)$$

We did not compute the results of equation (45) for this report, though it will be done in the future.

### Conclusions

In the preceding analysis we have tried to illustrate some of the calculations which are possible with the mathematical formalism developed by Lutomirski to treat the propagation of beam waves in turbulent media. While we have treated the simplest possible problem of a focused Gaussian beam in the presence of stationary turbulence (described by the Kolmogorov spectrum), one may reproduce the preceding analysis with any degree of complication desired. In any event, the results presented here should be an upper limit to the actual physical problem.

### Acknowledgement

We wish to express our appreciation to R. Butts for his many helpful discussions and his frequent computational support. Thanks also to M. Burlakoff for his computer support with this analysis.

### APPENDIX: Nomograph for Evaluation of the System Parameter N

The nomograph shown in Figure 7 facilitates a rapid computation of the system parameter, N, used in Figures 2 and 3. One must specify  $F C_n^2$ ,  $\omega_o$ , and  $\lambda$ . Beginning with the proper value on the  $F C_n^2$  axis, one then draws a straight line through the specified value on the  $\omega_o$  axis, noting the intersection of this line with the "intermediate variable" axis. One then draws a straight line between this intermediate variable and the required value on the  $\lambda$  axis, this time noting the intersection of the line with the N axis. The required system parameter variable N is given by this intersection.

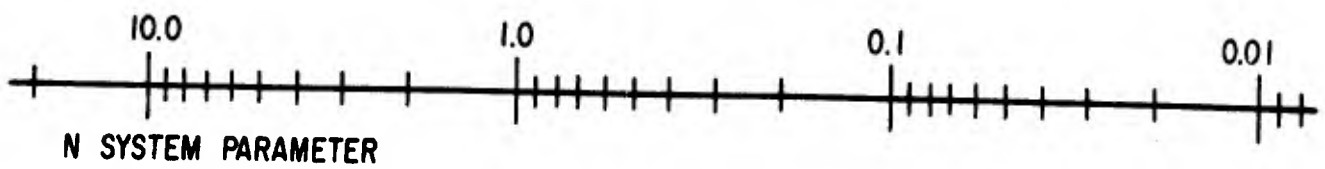
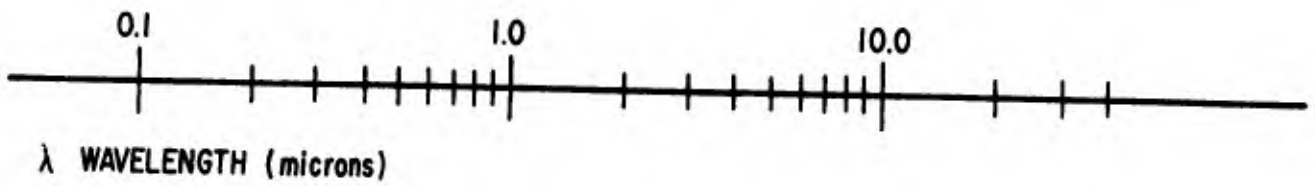
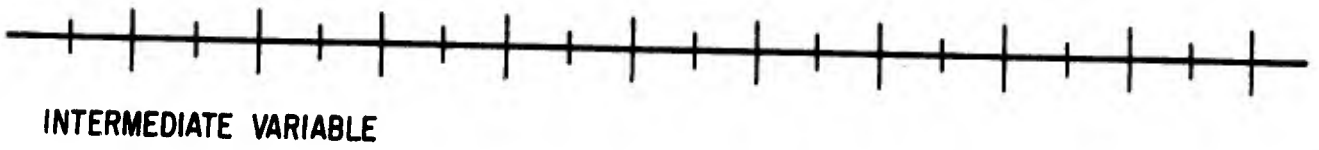
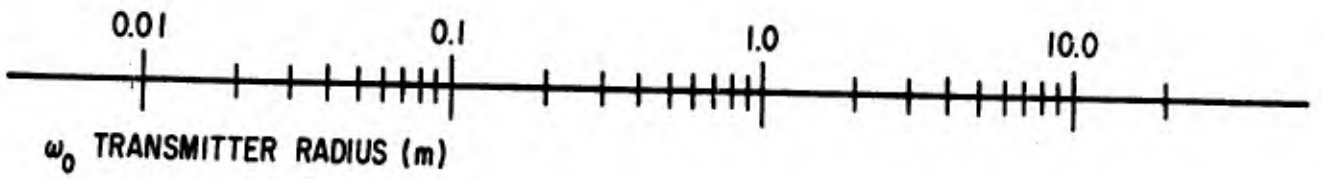
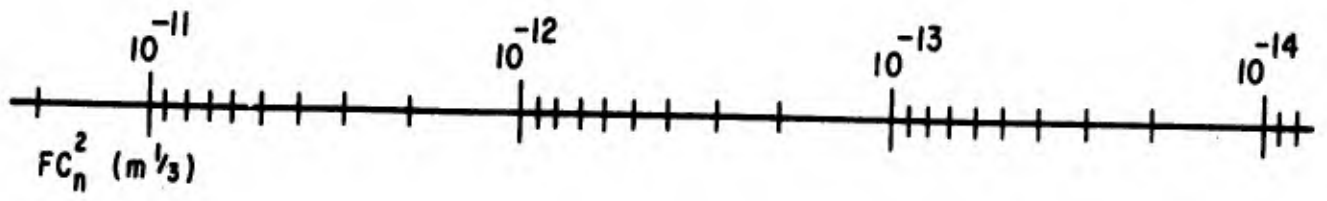


Figure 7. Nomograph for Evaluation of System Parameter N.

## REFERENCES

1. Lutomirski, R. F., Propagation of a Finite Optical Beam in an Inhomogeneous Medium, ARPA Memorandum RM-6055-ARPA, April 1970.
2. Fried, D. L., "Optical Resolution through a Randomly Inhomogeneous Medium for Very Long and Very Short Exposures," J. Opt. Soc. Amer., 56, 10, pp. 1372-1379, October 1966.
3. Fried, D. L., "Limiting Resolution Looking Down through the Atmosphere," J. Opt. Soc. Amer., 56, 10, pp. 1380-1384, October 1966.
4. Tatarski, V. I., Wave Propagation in a Turbulent Medium, trans. by R. A. Silverman, Dover Publications, Inc., New York, 1967.
5. Whitman, A. M., Beran, M. J., "Beam Spread of Laser Light Propagating in a Random Medium," J. Opt. Soc. Amer., 60, 12, pp. 1595-1602, December 1970.
6. Asakura, T., Kinoshita, Y., "Fluctuation Distribution of Collimated and Focused Gaussian Beams Propagated through a Random Medium," Jap. J. Appl. Phys., 8, 2, pp. 260-267, February 1969.
7. Strohbehn, J. W., "Line-of-Sight Wave Propagation through the Turbulent Atmosphere," Proc. IEEE, 56, 8, pp. 1301-1318, August 1968.
8. Lutomirski, R. F., Shapiro, A. R., Yura, H. T., Experiments on Turbulence Effects in Laser Propagation, ARPA Working Note WN-7063-ARPA, pp. 12-13, September 1970.

## COMPUTER SIMULATION OF BOUNDARY LAYER TURBULENCE

C. B. Hogge and W. L. Visinsky

The turbulence generated in aerodynamic boundary layers may cause significant laser propagation problems. Experimental data of the temperature and hence, density fluctuations in an aerodynamic boundary layer is virtually nonexistent, although some information may be gleaned from experimental hot-wire anemometry. Experimental information indicates that velocity fluctuations in a turbulent boundary layer are 4 to 10 percent of the local mean velocity. This same source<sup>1</sup> indicates values of 30 to 60 percent for turbulent jets and 2 to 5 percent for turbulent wakes. We can, perhaps, relate these data to experimental information on  $C_n$  (the structure constant of the refractive index fluctuations) in a jet engine exhaust.<sup>2</sup> Taking a value of  $C_n = 3 \times 10^{-5} \text{m}^{-1/3}$  as typical for the turbulent jet exhaust would lead one to conclude that  $C_n$  values for the turbulent boundary layer might be approximately  $5 \times 10^{-6} \text{m}^{-1/3}$ .

One can use existing propagation theories to try to predict the degrading effect of the boundary layer turbulence on an idealized laser beam focused at arbitrary distances from the aircraft. This involves defining (or assuming) a form for the index of refraction structure constant ( $C_n$ ) which varies with position away from the aircraft. Two things must be made clear. First, the form for  $C_n(z)$ , where  $z$  is the parameter specifying distance away from the aircraft, is a pure guess fabricated to model what is thought to be the behavior of the turbulence in the vicinity of the airplane. There is no experimental evidence why this (or for that matter any other) model is more preferable or correct. However, the numerical results for the degradation do appear to be somewhat insensitive to the choice of the form of  $C_n(z)$ , depending only on the general property that  $C_n(z)$  decreases as one moves away from the airplane.

Secondly, all theories of beam wave propagation in locally homogeneous and isotropic media require that the turbulent characteristics ( $C_n(z)$ ) change "slowly" with position. The question of "how slowly" is still open to discussion, but surely for strongly local boundary layer effects, the assumption of locally homogeneous and isotropic turbulence must fail. (One could perhaps argue that to be locally homogeneous and isotropic, the turbulence characteristics must



not change over a beam diameter in the transverse direction and over a couple of beam diameters in the longitudinal direction. Clearly, for 50-cm transmitting optics, one could easily violate the assumption of local homogeneity and isotropy.) To the extent to which this assumption is violated, one must judge the validity of the calculations presented here.

It should be pointed out that if the intense turbulent boundary layer is found to be extremely small (much less than a beam diameter), one might get a better estimate of focal distribution degradation by treating the layer as a thin, random phase screen. We have investigated this approach to the problem in a cursory fashion, and some of the initial results are presented in another article in this digest.

Finally, we indicate that one can treat the boundary layer turbulence as a thin phase screen and also include the remaining intervening turbulence in the problem. We have only just begun work on this approach and it is reported briefly in a short article in the digest.

In view of the preceding discussion, we will assume that the refractive structure constant  $C_n$  varies as follows:

$$C_n^2(z) = U \left( 1 + V e^{-[(1-z/L)^2/M]} \right)$$

where  $U$  is the limiting value of turbulence far away from the aircraft,  $V$  is an arbitrary parameter designed to greatly increase the turbulence structure constant for points near the aircraft,  $L$  is the distance from the aircraft to the focal plane, and  $M$  is an arbitrary parameter designed to adjust the rate in the reduction of turbulence as one moves away from the aircraft.

Using the theory of Lutomirski,<sup>3</sup> we can show that the average maximum intensity of a perfect Gaussian beam focused at distance  $L$  in the presence of turbulence is given by

$$\langle I(0, z=L) \rangle = \frac{2\pi P_T}{(L\lambda)^2} \int_0^\infty \rho M_s(\rho, z) e^{-\rho^2/2\omega_1^2} d\rho$$

where  $\omega_1$  is the transmitted beam spot size,  $\lambda$  is the wavelength,  $P_T$  is the total power in the beam, and  $M_s(\rho, z)$  is the spherical wave MTF as seen at the

transmitter from a point source located at the receiver. Assuming a Kolmogorov spectrum of turbulence, one can then show that

$$M_s(\rho, z) = \exp \left\{ -1.45 k^2 \rho^{5/3} \int_0^L dz \left( \frac{z}{L} \right)^{5/3} C_n^2(L-z) \right\}$$

where  $k = 2\pi/\lambda$ . In the absence of turbulence,  $M_s(\rho, z) \equiv 1$ , the peak intensity of a focused Gaussian beam is

$$I(0, L) = \frac{2\pi\omega_1^2 P_T}{(\lambda L)^2} = I_0$$

In the parametric analysis which follows, we have computed  $\frac{\langle I(0, L) \rangle}{I_0}$  versus  $V$ ,  $M$ , and  $L$ . We have set  $\lambda = 10.6$  microns,  $U = 5 \times 10^{-16} \text{m}^{-2/3}$ ,\* and  $\omega_t = 0.25$  m for all cases. The parameter  $n$  shown in the Tables is related to  $(ML^2)$  and expresses a distance (in meters) from the aircraft at which the turbulence level has dropped to  $1/e^2$  of its initial value ( $C_n^2(0) = UV$ ). For example, if the boundary layer thickness was 10 cm and we were focused at 1000 m our intensity from Table III would be degraded to 0.9 of its original value. This value would be associated with a maximum turbulence in the boundary layer of  $5 \times 10^{-11} \text{m}^{-2/3}$ , or approximately the figure quoted earlier for the boundary layer turbulence from velocity considerations.

#### REFERENCES

1. "Advances in Hot-Wire Anemometry," Proc. Inter. Symp. on Hot Wire Anemometry, University of Maryland, 20-21 March 1967.
2. Hogge, C. B., Visinsky, W. L., "Laser Beam Probing of Jet Exhaust Turbulence," Appl. Opt., 10, No. 4, April 1971.
3. Lutomirski, R. F., Propagation of a Finite Optical Beam in an Inhomogeneous Atmosphere, RAND Corp. Report, RM-6055, April 1970.

---

\*This limiting value of  $C_n^2$  is characteristic of intermediate to weak turbulence.

Table I

## INTENSITY DEGRADATION FOR BOUNDARY LAYER TURBULENCE

$$V = 1 \times 10^3$$

<u>Range to focus (m)</u>	<u>n(m)</u>	<u>I/I<sub>NT</sub>*</u>
500 	0.050	0.991
	0.158	0.982
	0.500	0.966
	1.58	0.914
1000 	0.100	0.983
	0.316	0.965
	1.0	0.934
	3.16	0.841
2000 	0.20	0.966
	0.632	0.931
	2.0	0.875
	6.32	0.720
3000 	0.30	0.950
	0.948	0.900
	3.0	0.822
	9.48	0.627
4000 	0.400	0.935
	1.264	0.870
	4.0	0.775
	12.64	0.553

Table II

## INTENSITY DEGRADATION FOR BOUNDARY LAYER TURBULENCE

$$V = 1 \times 10^4$$

<u>Range to focus (m)</u>	<u>n(m)</u>	<u>I/I<sub>NT</sub>*</u>
500 	0.050	0.987
	0.158	0.900
	0.500	0.777
	1.58	0.515
1000 	0.100	0.975
	0.316	0.816
	1.0	0.628
	3.16	0.331
2000 	0.20	0.951
	0.632	0.684
	2.0	0.444
	6.32	0.184
3000 	0.30	0.927
	0.948	0.585
	3.0	0.338
	9.48	0.123

Table II (cont'd)

<u>Range to focus (m)</u>	<u>n(m)</u>	<u>I/I<sub>NT</sub>*</u>
4000 	0.400	0.905
	1.264	0.508
	4.0	0.270
	12.64	0.092

Table III

## INTENSITY DEGRADATION FOR BOUNDARY LAYER TURBULENCE

$$V = 1 \times 10^5$$

<u>Range to focus (m)</u>	<u>n(m)</u>	<u>I/I<sub>NT</sub>*</u>
500 	0.050	0.947
	0.158	0.467
	0.500	0.228
	1.58	0.072
1000 	0.100	0.899
	0.316	0.288
	1.000	0.117
	3.16	0.033
2000 	0.20	0.814
	0.632	0.154
	2.0	0.055
	6.32	0.015
3000 	0.30	0.742
	0.948	0.102
	3.0	0.035
	9.48	0.009
4000 	0.400	0.681
	1.26	0.075
	4.00	0.025
	12.64	0.006

---

\*I<sub>NT</sub> = intensity with no turbulence.

## PROPAGATION IN EXTREME TURBULENCE

C. B. Hogge and W. L. Visinsky

In a previous paper, the authors reported on the use of a He-Ne laser to probe the extreme turbulence of a jet engine exhaust.<sup>1</sup> Measuring the amount of spreading induced on collimated and focused beams and then using the theory of Gebhardt and Collins,<sup>2</sup> we determined an index of refraction structure constant (usually denoted by  $C_n$ ) characteristic of the turbulence in the exhaust. While the numbers for structure constant determined in this manner agreed fairly well with other measurement techniques, we must point out that the validity of the approximations made in the Gebhardt and Collins theory, in particular for the focused beam case, are positively violated. In fact, it appears that for most focused beam problems of interest, their assumption is violated.

One can show that for the collimated beam case, the particular assumption of concern requires that<sup>2</sup>

$$\Omega \gg \pi \quad (1)$$

where  $\Omega$  is the Fresnel number of the aperture

$$\left( \Omega = \frac{\pi \omega_1^2}{\lambda z} \right)$$

and where

$\omega_1$  is transmitted beam spot size

$\lambda$  is wavelength

$z$  is distance to the observation plane

Thus, as long as one is well within the near field of the transmitting aperture,  $\omega_1$ , this requirement will be satisfied.

For the case of a beam focused at  $z = F$ , where  $F$  is less than the Rayleigh range of the transmitting spot size, the requirement becomes

$$\frac{\omega_1^2}{\lambda z \Omega^2} \gg 1$$

$$\frac{1}{\Omega} \gg \pi \quad (2)$$

However, if, as assumed, one is focused well within the near field of the transmitting aperture, then  $\Omega \gg 1$ , and clearly, condition (2) cannot possibly be satisfied. While this is true in general (and in particular in our case), Gebhardt and Collins state that they still feel that their results should yield "good estimates" of the physical situation. The results of our analysis of our data appear to substantiate their beliefs.

This contradiction in the validity of the assumptions used for our earlier analysis has lead us to review further our beam spreading data with two other theoretical models. While many theories are becoming available,<sup>3,4</sup> we have confined our analysis to the work of Ishimaru<sup>5</sup> and Lutomirski.<sup>6</sup> We choose to investigate these two particular theories because of their markedly different approach to the problem of beam spreading in turbulent environments.

With the assumption that the original Gaussian-profile beam will remain, on the average, Gaussian in shape, one can readily show from Ishimaru's theories that

$$\left(\frac{\omega_t}{\omega_o}\right)^2 = 1 - \langle X^2(z, o) \rangle + \langle X^2(z, \omega) \rangle$$

where  $\omega_t$  is the average spot size of the beam at the observation plane after traversing the turbulence,  $\omega_o$  is the theoretical spot size of the beam at the observation plane in the absence of turbulence, and  $\langle X^2(z, \omega) \rangle$  is the mean square log amplitude fluctuations at a distance  $z$  from the transmitter plane and a radial distant  $\omega$  from the center of the beam. According to Ishimaru,

$$\langle X^2(z, \omega) \rangle = 0.033\pi^2 k^{7/6} z^{11/16} \left[ -\Gamma\left(-\frac{5}{6}\right) \right] \int_0^1 dx C_n^2(zx) G_A(x)$$

The spatial filter function  $G_A(x)$  is a function of  $\omega$  as well as the normalized distance  $x$ . It is a weighting function which emphasizes or de-emphasizes the effect of the turbulence along the path. The transcendental equation given

above may be solved for the beam-spread ratio for both collimated and focused beams with the proper substitutions in the weighting function.

Lutomirski's theory basically concerns the determination of the spherical wave modulation transfer function in the presence of turbulence. While being able to treat generalized aperture problems, the formalism is significantly less cumbersome for the case of a perfect Gaussian beam. For a focused Gaussian beam observed in its focal plane,

$$\left(\frac{\omega_o}{\omega_t}\right)^2 = \frac{1}{\omega_1^2} \int_0^\infty \rho e^{-R\rho^{5/3}} e^{-\rho^2/2\omega_1^2} d\rho$$

where  $\omega_t$  and  $\omega_o$  were defined before and where  $\omega_1$  is the transmitted beam spot size.

$$R = 1.455 k^2 z \int_0^1 C_n^2 [z(1-x)] x^{5/3} dx$$

For a collimated Gaussian beam, Lutomirski's theory yields

$$\left(\frac{\omega_o}{\omega_t}\right)^2 = \frac{1}{\omega_1^2} \left[ 1 + \left( \frac{\pi\omega_1^2}{\lambda z} \right)^2 \right] \int_0^\infty \rho e^{-R\rho^{5/3}} e^{-Q\rho^2} d\rho$$

where

$$Q = \left( \frac{1}{2\omega_1^2} + \frac{k^2\omega_1^2}{8z^2} \right)$$

These equations have been programmed on the CDC 6600. To simplify the analysis, we have assumed that the structure constant does not vary over the width of the engine exhaust.

### Collimated Beam Results

In Figure 1 the computer results of Ishimaru's and Lutomirski's theories are plotted for a  $z = 12.4$  meters. In Figure 2 their results are plotted for  $z = 16.8$  meters. On both graphs we have reproduced the data of Table 2, reference (1), using Gebhardt and Collins' theory. Note that for these points we used the measured values of the collimated beam spot size. If one similarly uses the measured values of  $\omega_1$  to determine  $(\omega_0/\omega_t)^2$  in the present analysis, we see that excellent agreement results. Of particular interest is the fact that the Gebhardt and Collins points always fall between Ishimaru's and Lutomirski's curves. We think this is to be expected, however, since the Gebhardt and Collins theory is a modified version of Ishimaru's theory. The latter theory calculates the variance of the scintillation of the log amplitude "off-axis" for an ideal Gaussian beam. It is well known that the Rytov approximation begins to fail for points sufficiently far "off-axis." We feel that for degrees of turbulence sufficient to spread the beam (either focused or collimated) by a factor of two or more, Ishimaru's theory is no longer valid. Notice the rapid drop, without an apparent limit of Ishimaru's curve. This curve actually begins dropping very fast for a beam spread much less than a factor of two and suggests that Ishimaru's theory may be failing even sooner.

The Gebhardt and Collins theory predicts a beam spread simply from the log amplitude scintillation occurring at the center of the beam. Thus it does not suffer from the same problems encountered by Ishimaru's theory. There are, however, other differences between these two theories which make a complete comparison difficult.

The Lutomirski theory also does not suffer from instabilities for points for off-axis. Because the theory is developed around the atmospheric MTF, the results remain well bounded as long as the form of the MTF remains bounded. Using the Kolmogorov Spectrum, the MTF does remain bounded and hence the theory plotted in Figures 1 and 2 show a well behaved shape.

### Focused Beam Results

We observed experiments that for the degrees of turbulence present in a jet engine exhaust, a focused spot will spread on the order of seven times its original diameter. As a result, in view of the preceding discussion, it is clear that Ishimaru's theory cannot be applied to these cases. Thus in Figures 3 and 4 we have plotted the results of Lutomirski's theory for the range of  $C_n^2$ 's



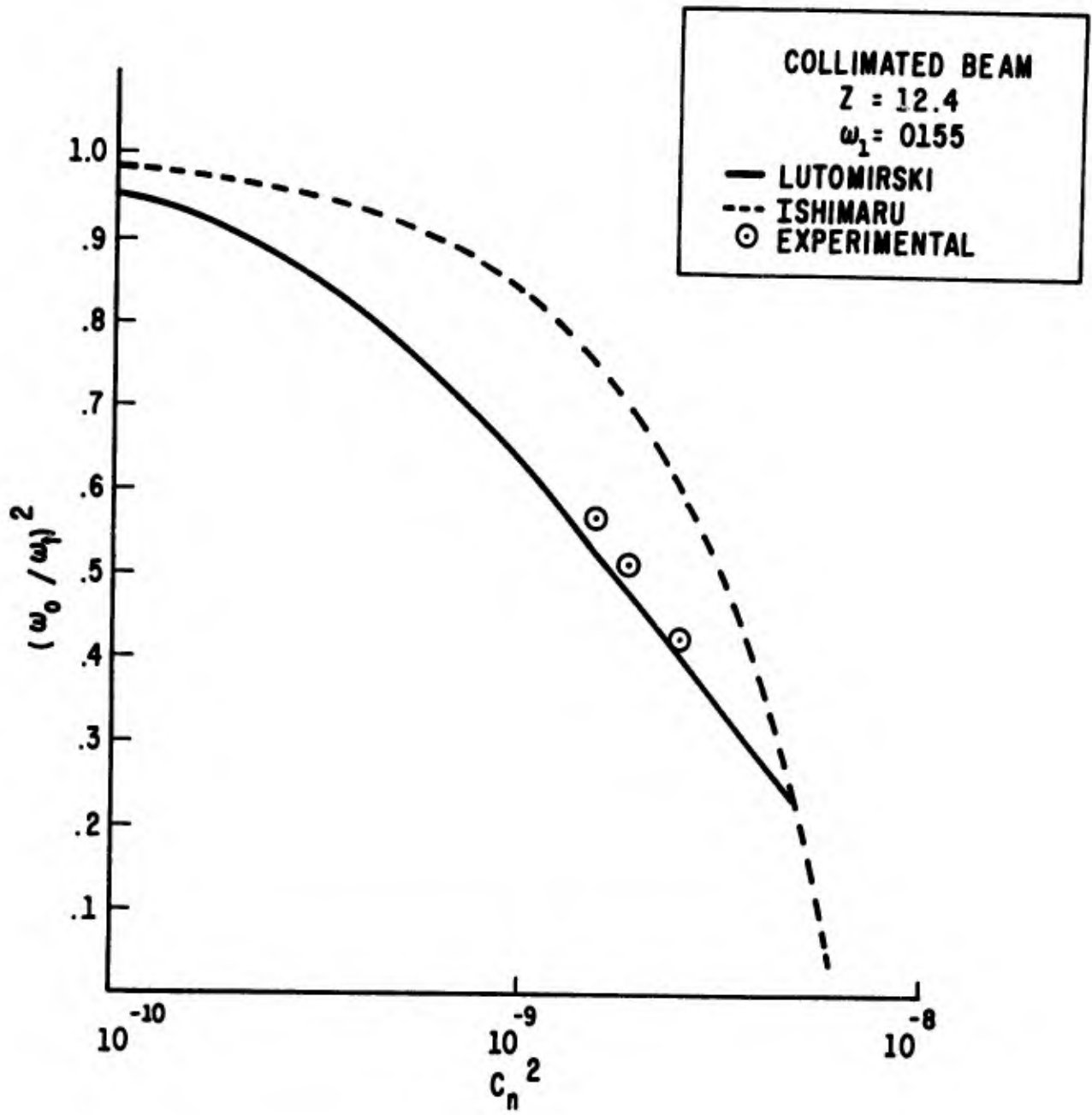


Figure 1. Intensity degradation for a collimated beam. Propagation path is 12.4 meters.

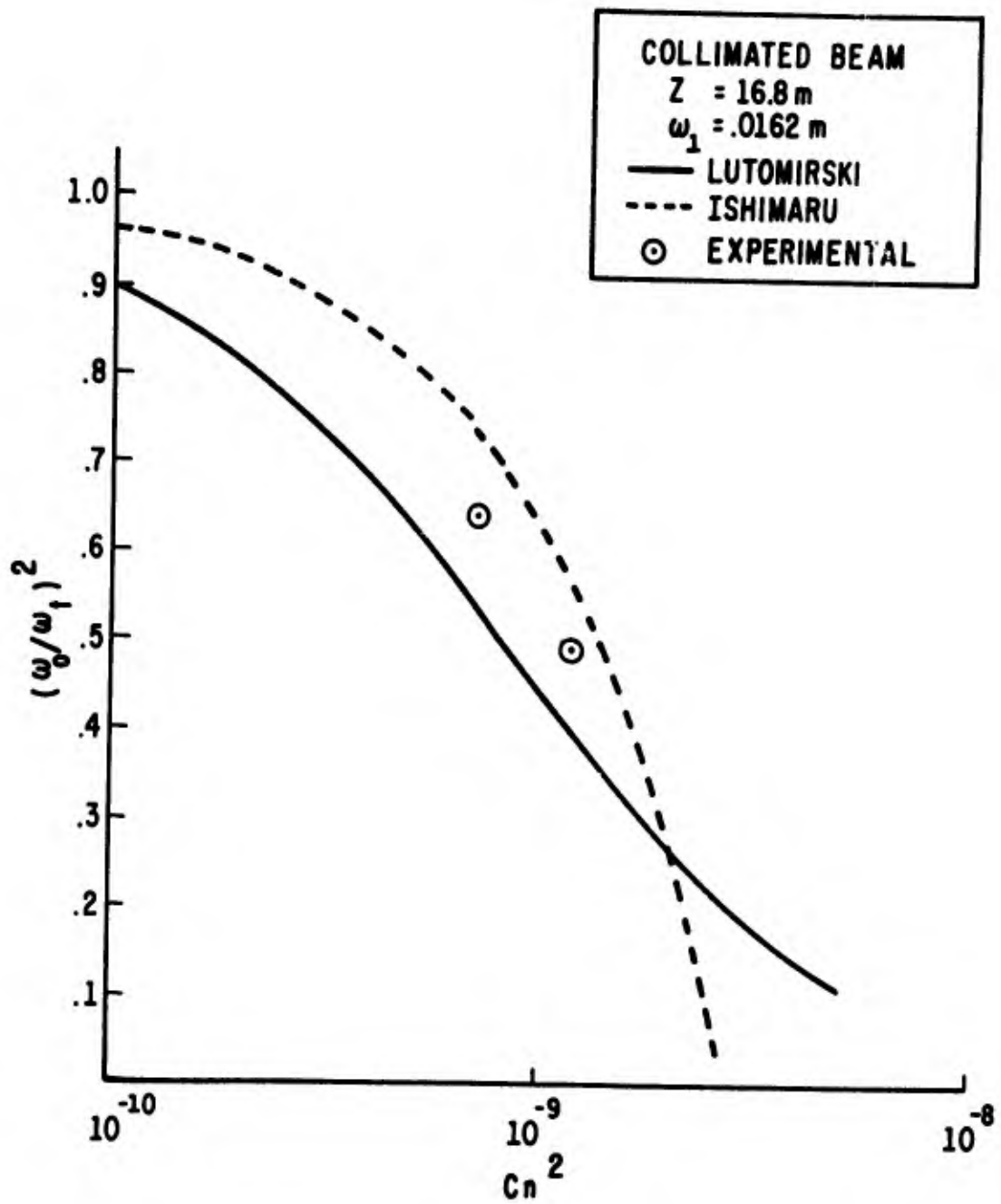


Figure 2. Intensity degradation for a collimated beam. Propagation path is 16.8 meters.

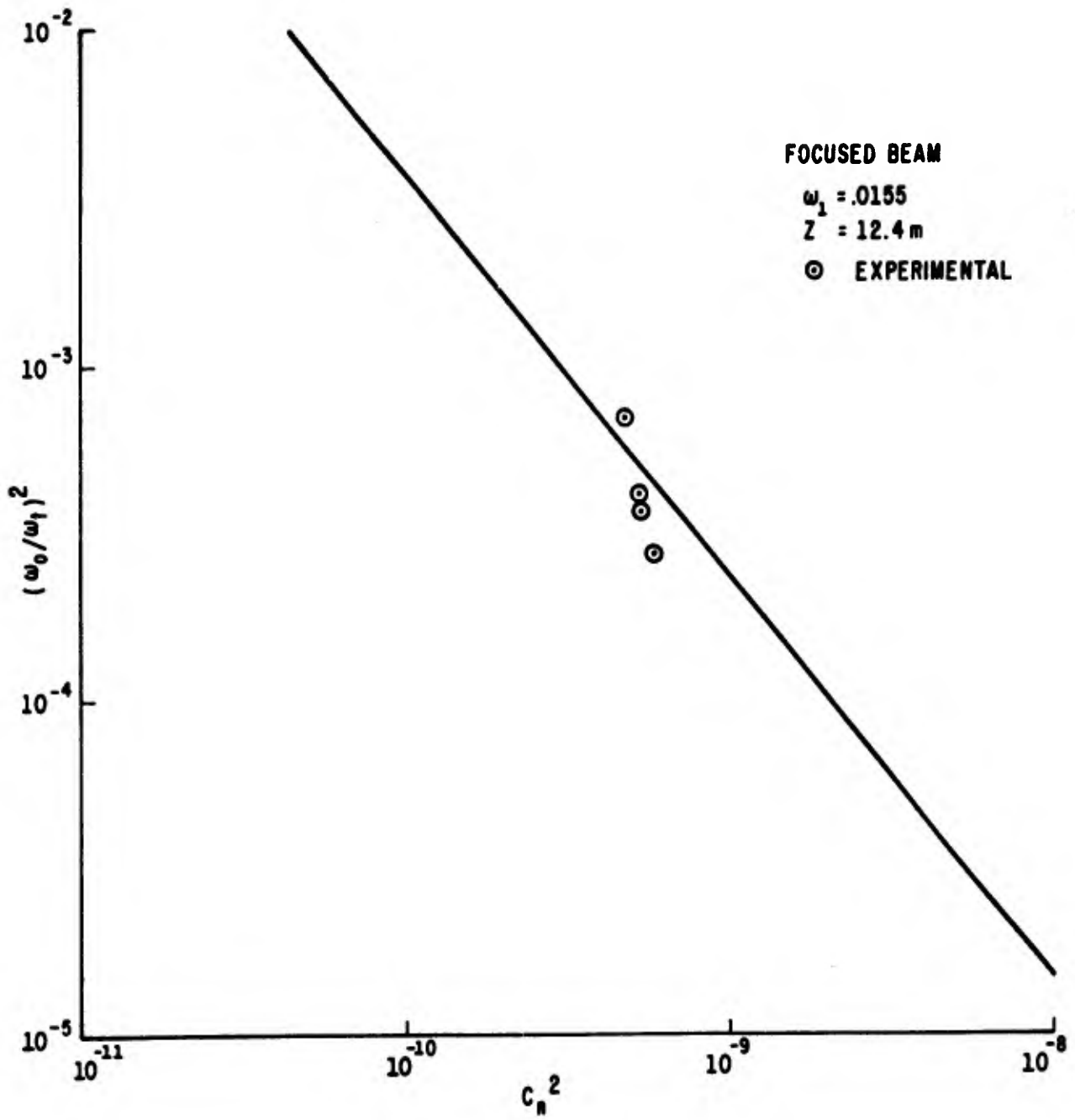


Figure 3. Intensity degradation for a focused beam. Propagation path is 12.4 meters.

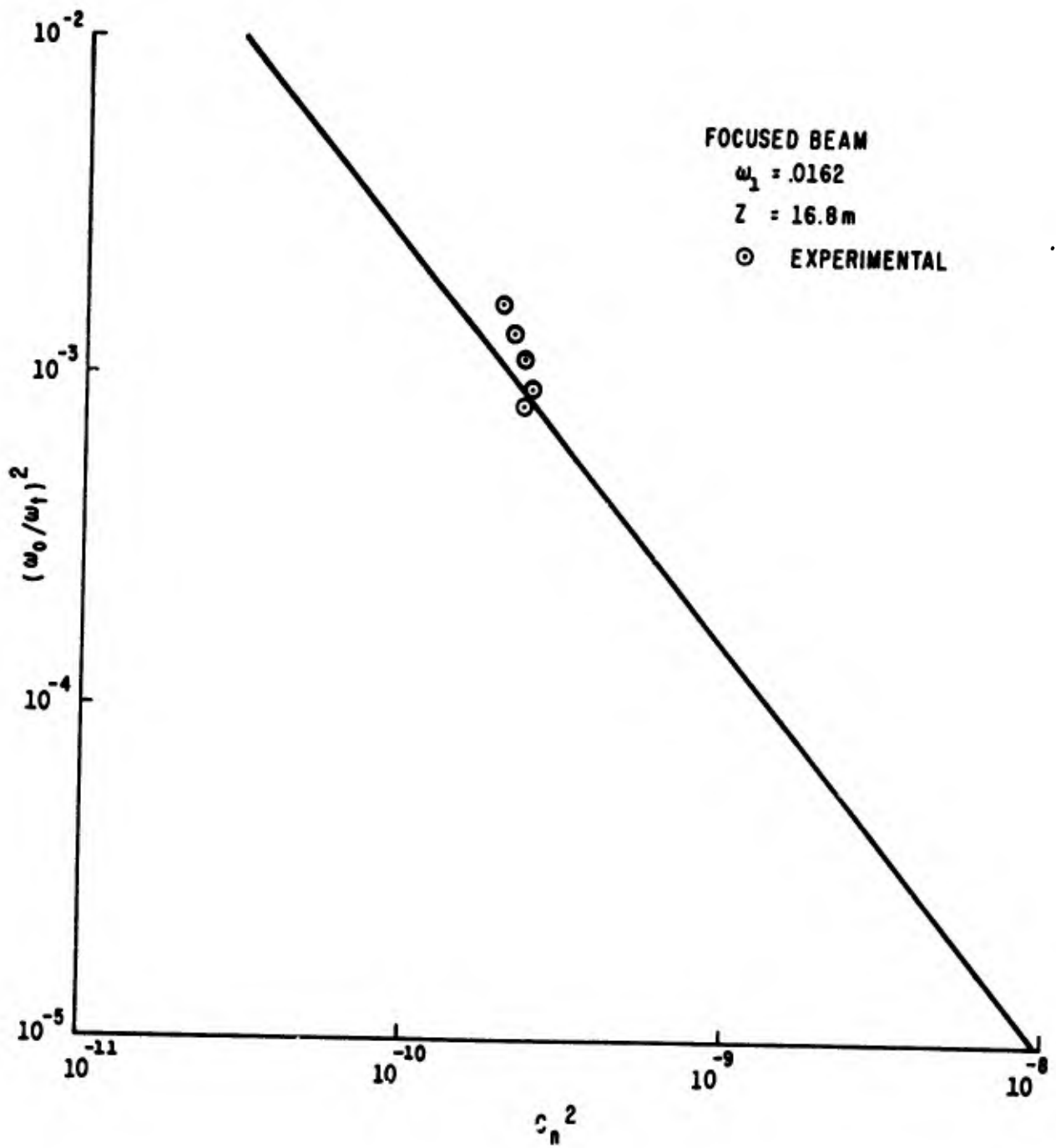


Figure 4. Intensity degradation for a focused beam. Propagation path is 16.8 meters.

of interest. Also plotted are Gebhardt and Collins' results, once again using the measured spot sizes (see Table 3, reference 1). Note that even though the assumption used in the Gebhardt and Collins theory for the focused beam is violated (as discussed earlier), their results agree reasonably well with Lutomirski's if the experimentally measured spot sizes are used.\*

### Conclusions

In summary, Lutomirski's method seems to be ideally suited for most applications of beam spread or turbulence degradation in turbulence. Methods which are inherently dependent on the radial form of the Rytov approximation may develop problems for those high degrees of turbulence or long ranges where the beam spread would be approximately two times the original beam size (an intensity degradation to 1/4 the original value).

We have presented our results of the comparison of three methods of beam wave propagation in turbulence. Our treatment is not meant as a condemnation of any of the methods nor an ultimate statement of fact. We do feel, however, that more thorough investigations of other regions of the turbulence spectrum are warranted before any final decisions are made.

### REFERENCES

1. Hogge, C. B., Visinsky, W. L., "Laser Beam Probing of Jet Exhaust Turbulence," Appl. Opt., 10, No. 4, April 1971.
2. Gebhardt, F. G., Collins, S. A., Jr., "Log-Amplitude Mean for Laser-Beam Propagation in the Atmosphere," J. Opt. Soc. Amer., 59, No. 9, September 1959.
3. Ho, T. L., "Coherence Degradation of Gaussian Beams in a Turbulent Atmosphere," J. Opt. Soc. Amer., 60, No. 5, May 1970.
4. Beran, M. J., "Propagation of a Spherically Symmetric Mutual Coherence Function through a Random Medium," IEEE Transactions on Antennas and Propagation, AP-15, No. 1, January 1967.
5. Ishimaru, A., "Fluctuations of a Beam Wave Propagating through a Locally Homogeneous Medium," Radio Sci., 4, No. 4, April 1969.
6. Lutomirski, R. F., Propagation of a Finite Optical Beam in an Inhomogeneous Atmosphere, RAND Corp. Report, RM-6055-ARPA, April 1970.

---

\*In reference 1 we describe an alternate method of analyzing the data, which uses theoretical spot sizes in the absence of turbulence rather than measured spot sizes as described here.

## LASER BEAM PROPAGATION THROUGH JET EXHAUSTS

K. G. Gilbert, C. B. Hogge, and W. L. Visinsky

### ABSTRACT\*

CO<sub>2</sub> (10.5 micron) and He-Ne (6328 Å) laser beams were passed through the highly turbulent region in the exhaust of a jet engine (J-57 with afterburner). Experimental information was obtained on the absorption, scattering and turbulence effects of the jet exhaust on both laser beams for various propagation paths. Estimates of a structure constant that would characterize the turbulence in the exhaust are made from the beam spread of focused and collimated beams. The structure constant obtained in this manner is then compared with the structure constant determined from scintillation measurements on the CO<sub>2</sub> and with the results of hot-wire anemometer readings in the exhaust. The various methods yield results for the structure constant that are in good agreement (typically a structure constant of the order of  $3 \times 10^{-5} \text{m}^{-1/3}$ ).

---

\*This report has been published as AFWL-TR-70-128, December 1970.

## CO<sub>2</sub> LASER AIR BREAKDOWN CALCULATIONS

G. H. Canavan and S. D. Rockwood

The calculations reported here test the validity of interpolating between microwave<sup>1</sup> and optical frequency<sup>2</sup> theory and experiments to predict a breakdown field of  $E = E_{th} = 1.5_6 [\approx 1.5 \times 10^6]$  volt/cm (peak) for a large diameter CO<sub>2</sub> 10.6-micron laser beam in air. The number density,  $n_e$  (cm<sup>-3</sup>), and thermal energy density,  $E_T$  (eV/cm<sup>3</sup>), of Maxwellian electrons of temperature  $T_e$  (eV) interacting with air of density  $n_n$  (molecules/cm<sup>3</sup>) obey

$$\dot{n}_e = (R_i/I - R_a n_n) n_n n_e \quad (1)$$

$$\dot{E}_T = \frac{3}{2} k (\dot{n}_e T_e + n_e \dot{T}_e) = \left( F - R_i - R_v - \sum_{\lambda=1}^5 R_\lambda - \frac{3}{2} k T_e R_a n_n \right) n_n n_e \quad (2)$$

where  $I =$  ionization potential of air = 15 eV,

$$R_a \text{ (cm}^6\text{/sec)} = \left( 2.8_{-30} (0.026/T_e) e^{-0.052/T_e} + 8_{-32} \right)$$

is the three-body rate of electron attachment to O<sub>2</sub>,<sup>3,4</sup> and the explicit temperature dependence of the terms on the right-hand side of equation (2) is shown in Figure 1.  $F$  (eV-cm<sup>3</sup>/sec) =  $e^2 E^2 (\nu/n_n) / (2m_e (\nu^2 + \omega^2))$  is the microwave laser input<sup>2</sup> plotted for  $E = E_{th}$  and scaling vertically on  $(E/E_{th})^2$  for other fluxes. The collision frequency,  $\nu = 1.3_{-7} T_{eV}^{1/2} n_n$ , was obtained from the data of Englehardt et al.,<sup>5</sup> and Phelps.<sup>6</sup>  $R_i$  (eV-cm<sup>3</sup>/sec) is the loss rate due to impact ionization<sup>7</sup> and is plotted together with the energy needed to thermalize the new cold electron produced with each ionization.  $R_v$  (eV-cm<sup>3</sup>/sec) is the energy lost in vibrationally exciting N<sub>2</sub> molecules with a rate based on the cross sections measured by Schulz.<sup>8</sup>  $R_\lambda$  (eV-cm<sup>3</sup>/sec),  $\lambda = 1-5$ , are the energy loss rates for impact excitation of the A<sup>3</sup>Σ, a<sup>1</sup>π, and C<sup>3</sup>π states of N<sub>2</sub> (Ref. 5) and the A<sup>3</sup>Σ and B<sup>3</sup>Σ states of O<sub>2</sub> (Ref. 9).

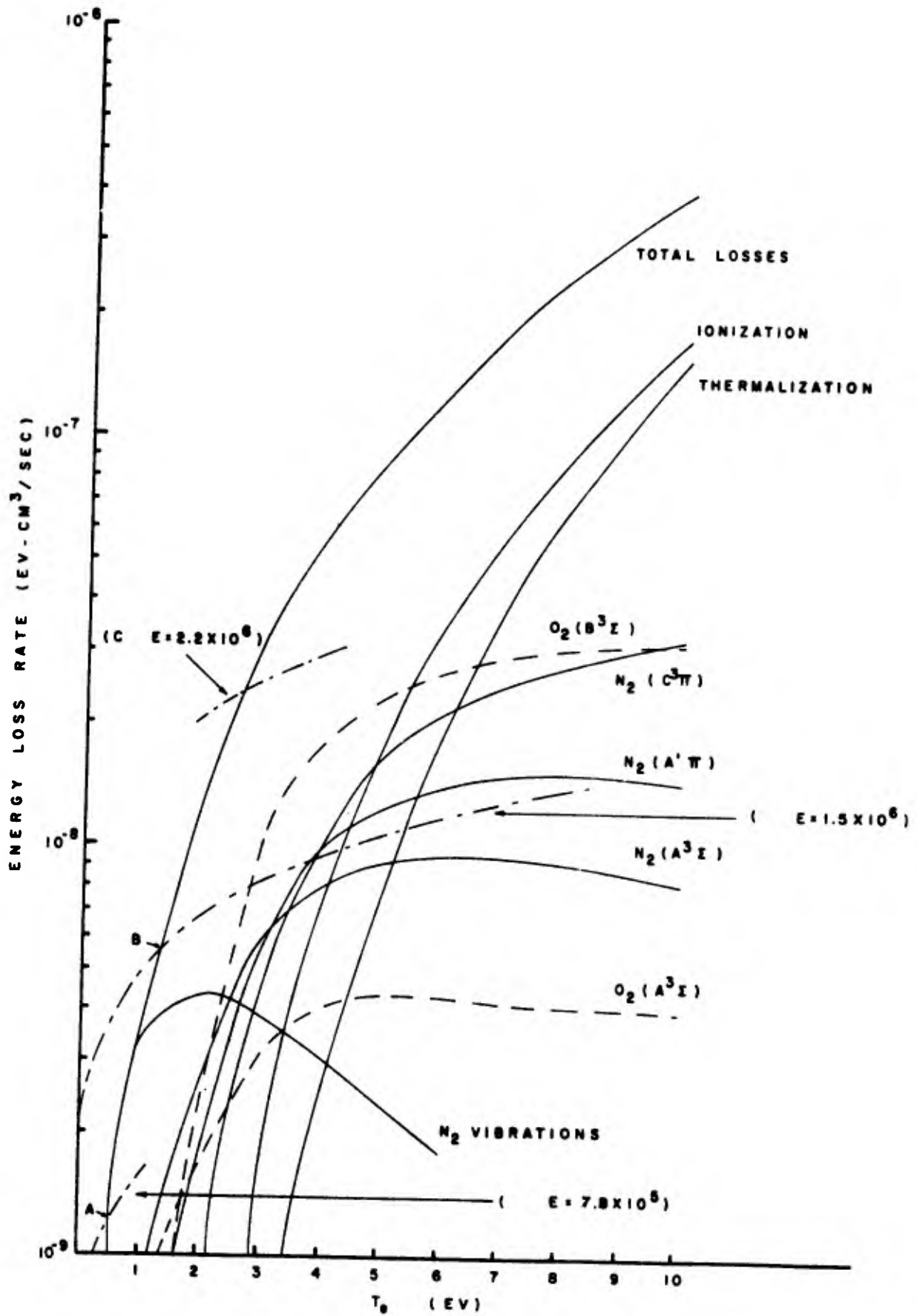


Figure 1. Energy loss rate of Maxwellian electrons interacting with air.



After a brief transient, the electron temperature stabilizes at a quasi-equilibrium value,  $T_q$ , where the laser input is balanced by the sum of the loss terms. Thus Figure 1 contains the graphical solution of equation (2) for  $T_q(E^2)$  which is plotted in Figure 2 along with the time constant for electron growth,

$$t_b = \left\{ \left( R_i/I - R_a n_n \right) n_n \right\}^{-1} \text{ for } n_n = 3_{19} \text{ cm}^{-3}$$

As an example of the use of Figure 2, let  $E^2 = 3_{12} \text{ (volt/cm)}^2$ , point  $B_o$ . Read vertically from  $B_o$  to B to find  $T_q = 2.4 \text{ eV}$ ; read horizontally from B to the intersection with the positive branch at B\*; then read vertically to  $t_b = 1_{.9} \text{ sec}$  for  $n_n = 3_{19} \text{ cm}^{-3}$ . Owing to the strong exponential behavior of  $R_i$  on  $T_e$ , the quantity  $(R_i/I - R_a n_n)$  switches rapidly from a large negative value to a large positive value as  $T_e$  passes through  $T_{th} = 1.9 \text{ eV}$ , which determines the cw threshold field  $E_{th} = 1.5_6 \text{ volt/cm}$  needed to break down STP air. Since

$$R_i/I \approx R_I e^{-I/T_e} = 1.1_{-8} e^{-I/T_e}$$

and

$$R_a \approx R_A = 1.2_{-31}$$

the cw threshold

$$E_{cw}^2 \propto T_{cw} = I / \ln(R_I / R_A n_n) \quad (3)$$

is but weakly dependent on  $n_n$  and is insensitive to diffusion so long as  $R_a n_n^2 \gg D/L^2$ ; e.g.,  $cE_{th}^2 / 8\pi = 2.3_9 \text{ watt/cm}^2$ , independent of diffusion lengths  $L \gg 1_{.3} \text{ cm}$ . Thus, for  $E < 1.5_6 \text{ volt/cm}$ , balance with vibrational losses occurs at  $T_q < 1.9 \text{ eV}$ ; e.g., point A of Figure 1, where  $R_a n_n \gg R_i/I$ , so that  $n_e(t) = n_e(0) \exp(-R_a(T_q) n_n^2 t)$ . For  $E \gg 1.5_6 \text{ volt/cm}$ , balance with ionization losses results at  $T_q \gg 1.9 \text{ eV}$  (i.e., point C) so that for  $t > 1.1_{21} T_q^{1/2} / (n_n E^2)$  sec,  $n_e(t) = n_e(0) \exp[R_i(T_q) n_n t]$ .

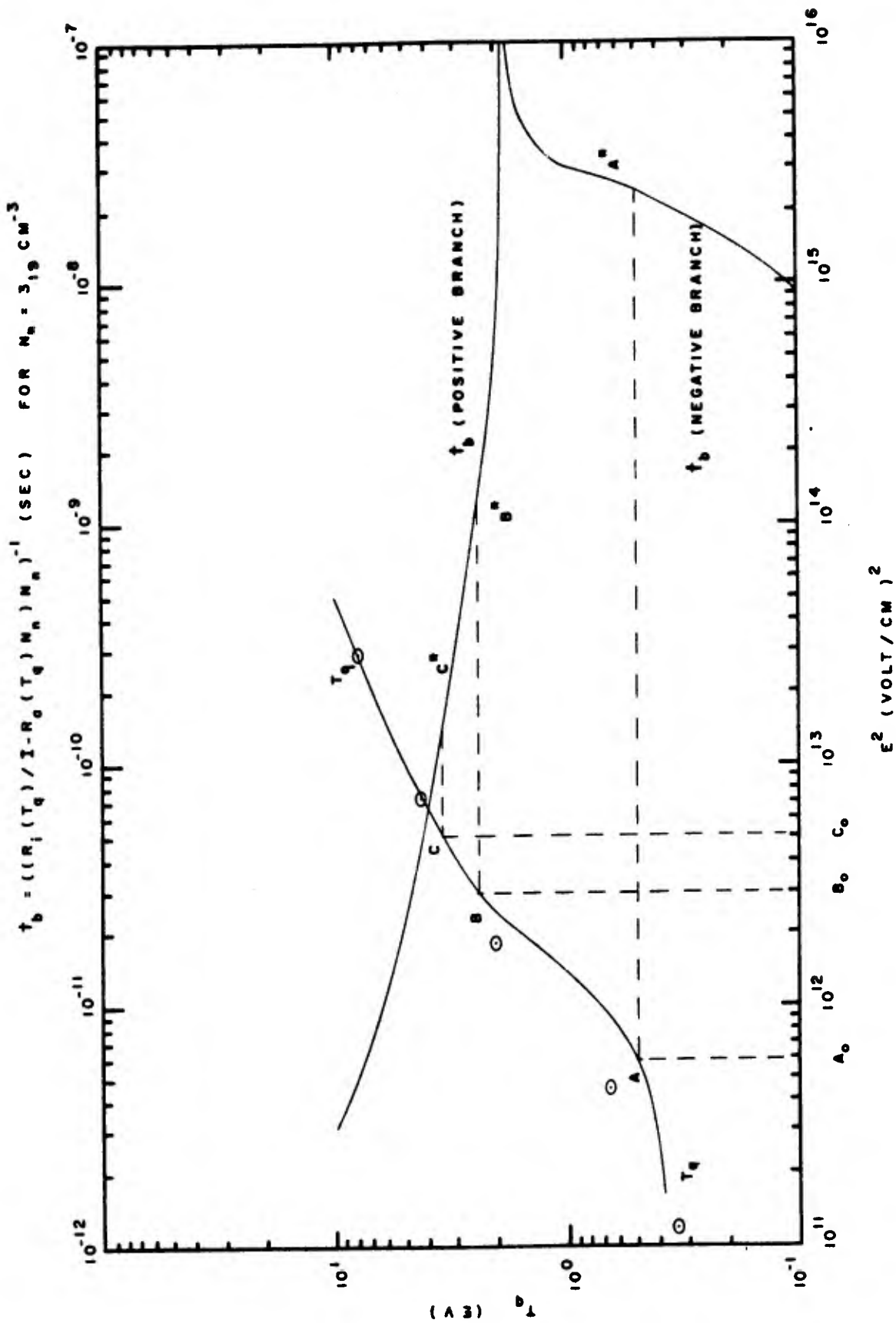


Figure 2. Equilibrium electron temperature as a function of the square of the electric field. Upper axis,  $t_b$ , is the time constant for electron growth at an air density of  $3 \times 10^{19} \text{ cm}^{-3}$ . Circled points are taken from reference 11.

Even for  $E$  such that  $\dot{n}_e > 0$ , breakdown occurs during a square pulse of length  $t_p$  only if  $t_b < t_p/N$  where  $N = \ln n_n/n_e(0)$ . Locate this value of  $t_b$  on the positive branch in Figure 2, read horizontally to find  $T_q$ , and vertically downward to find  $E^2$ . This value of  $E^2$  yields the energy flux,  $cE^2/8\pi$ , and energy fluence,  $t_p cE^2/8\pi$ , necessary to produce  $n_e(0)e^N$  electrons during the pulse  $t_p$  as plotted in Figure 3 for  $N = 44$ , STP air. For  $2_{-11} < t_p < 1_{-9}$  sec, a large  $R_1(T_q)$  is necessary to produce breakdown, which implies  $E \gg E_{th}$ , so that essentially all of the laser energy absorbed goes into ionization as at point C of Figure 1, yielding an energy fluence dependent threshold of 10 joules/cm<sup>2</sup>. As  $t_p$  increases for a given energy fluence,  $E$  decreases, wasting an ever increasing fraction of the absorbed energy in vibrational and electronic excitations, so that the threshold energy fluence increases slowly as  $t_p$  increases from  $2_{-9}$  to  $1_{-8}$  sec. For longer pulses the fluence threshold increases linearly with  $t_p$  in order to maintain  $E \geq E_{th}$ , and the actual threshold becomes an energy flux of 2.39 watt/cm<sup>2</sup>. Since this threshold scales on  $(E/\omega)^2$ , the 1.06-micron measurements of Smith and Tomlinson<sup>10</sup> were reduced by a factor of 100 for comparison. Smith's point,\* however, was actually obtained with a CO<sub>2</sub> 10.6-micron laser in air and is strong evidence for the correctness of our results. Approximating the breakdown flux by equating  $F$  and  $R_1$  in equation (2) to obtain

$$cE^2/8\pi - m_e \omega^2 INc/4\pi e^2 t_p \nu$$

for  $t_p \ll N/R_A n_n^2$ , and as the cw value from equation (3) for longer pulses, is well borne out by the exact solutions shown in Figure 3.

The assumption that the electrons have a Maxwellian distribution is justified by calculations<sup>11,12</sup> which solve the quantum mechanical kinetic equation<sup>2</sup> for the time evolution of the distribution function of electrons interacting with a quantized 10.6-micron radiation field and cold nitrogen molecules, producing near Maxwellian distributions with temperatures indicated by the points on Figure 2 which are in excellent agreement with the predictions of the analytic model presented here.

The authors wish to express their gratitude to Major W. A. Whitaker for many helpful discussions during this work.

---

\*D. C. Smith, private communication.

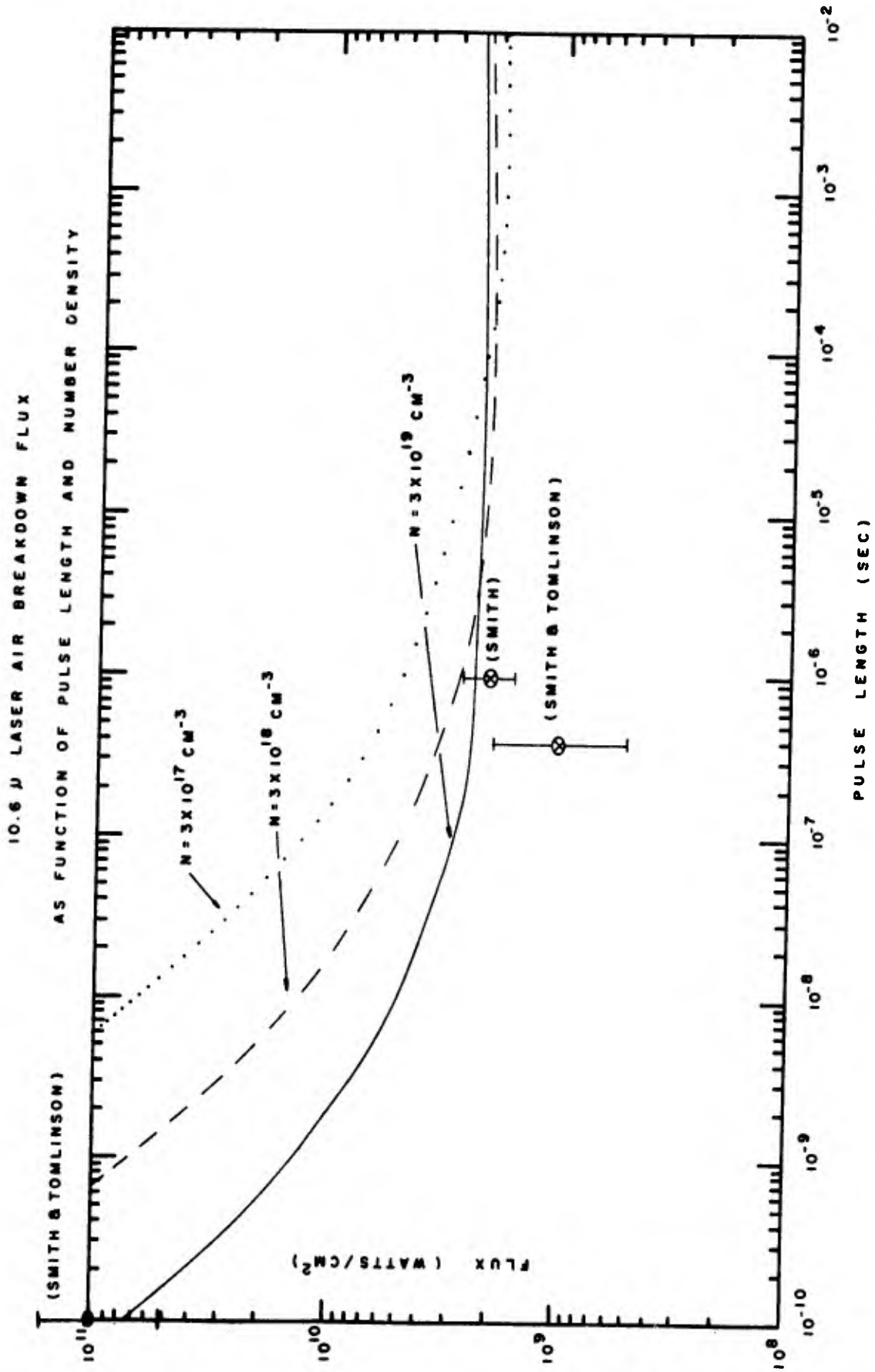


Figure 3. Air breakdown threshold for flux of 10.6- $\mu$  laser radiation as a function of pulse length and number density.

## REFERENCES

1. Brown, S. C., "Gas Discharges, II," Handbuch der Physik Vol XXII, S. Flugge (ed.), Springer-Verlag, Berlin, 1956.
2. Raizer, Y. P., "Heating of a Gas by a Powerful Light Pulse," Zh. Eksperim. Teor. Fiz., 48, 1508, 1965 [English transl.: Soviet Physics--JETP 21, 1009, 1965].
3. Pack, J. L., Phelps, A. V., "Electron Attachment and Detachment: I, Pure O<sub>2</sub> at Low Energy," J. Chem. Phys., 44, 1870, 1966.
4. van Lint, V. A. J., Wikner, E. G., Trueblood, P. L., "Thermal Electron Attachment in Oxygen and Oxygen-Containing Mixtures," Bull. Amer. Phys. Soc., 5, 122, 1960.
5. Englehardt, A. G., Phelps, A. V., Risk, C. G., "Determination of Momentum Transfer and Inelastic Cross Sections for Electrons in Nitrogen Using Transport Coefficients," Phys. Rev., 135, A1566, 1964.
6. Phelps, A. V., "Propagation Constants for Electromagnetic Waves in Weakly Ionized, Dry Air," J. Appl. Phys., 31, 1273, 1960.
7. Tate, J. T., Smith, P. T., "The Efficiencies of Ionization and Ionization Potentials of Various Gases under Electron Impact," Phys. Rev., 39, 270, 1932.
8. Schulz, G. J., "Vibrational Excitation of N<sub>2</sub>, CO, and H<sub>2</sub> by Electron Impact," Phys. Rev., 135, A988, 1964.
9. Hake, R. D., Phelps, A. V., "Momentum-Transfer and Inelastic Cross Sections for Electrons in O<sub>2</sub>, CO, and CO<sub>2</sub>," Phys. Rev., 158, 70, 1968.
10. Smith, D. C., Tomlinson, R. G., "Effects of Mode Beating in Laser-Produced Gas Breakdown," Appl. Phys. Letters, 11, 73, 1967.
11. Nielson, P. E., Rockwood, S. D., Canavan, G. H., "Breakdown of N<sub>2</sub> with a CO<sub>2</sub> Laser," AFWL (SYT) Note, 20 January 1971.
12. Nielson, P. E., Canavan, G. H., Rockwood, S. D., "Breakdown of Deuterium with a Ruby Laser," Proc. IEEE, Special Issue on Atomic and Molecular Physics, April 1971.

## INTERACTION OF HIGH-INTENSITY LASERS WITH OPTICALLY THIN AEROSOLS

P. E. Nielsen and G. H. Canavan

Atmospheric aerosols which are optically thin to a laser, whose intensity is sufficiently great that the particle's energy loss through thermal conductivity is negligible, heat rapidly and uniformly, vaporizing in place. There are two mechanisms whereby the breakdown threshold might be lowered by the expanding vapor of such particles. First, the vapor might heat sufficiently that thermal ionization could become significant, leading to strong free-free absorption and subsequent breakdown. Second, the vapor might expand into the air with sufficient velocity to shock-heat the air, producing a thin strongly absorbing region of large thermal ionization, and leading to a radiation-supported shock wave.<sup>1</sup> The first of these mechanisms depends upon the maximum temperature the vapor reaches and the ionization potential for the material under consideration, while the second depends upon the limiting velocity reached by the expanding vapor. These phenomena are conveniently investigated within the framework of a Sedov<sup>2</sup> model, in which the density,  $\rho$ , and temperature,  $T$ , of the expanding vapor are assumed uniform, with the velocity,  $v$ , varying linearly with radius from the center to the edge at  $r$ . The equations for conservation of vapor mass, momentum, and energy are

$$\frac{4}{3} \pi \rho r^3 = M = \text{Const} \quad (1)$$

$$p \ 4\pi \ r^2 \ \frac{dr}{dt} = \frac{1}{2} \left( \frac{3}{5} M \right) \frac{d}{dt} v^2 \quad (2)$$

and

$$\frac{3}{2} Nk \ \frac{dT}{dt} = -4\pi p r^2 v + W \quad (3)$$

where  $k$  is Boltzmann's constant,  $W$  the rate of energy input from the laser, and  $N$  and  $p$  are the total number of particles and pressure within the vapor. Use of the equation of state

$$p = \frac{3NkT}{4\pi r^3} \quad (4)$$

converts equations (1) through (3) into those for the time development of the radius, velocity of expansion, and temperature of the vapor

$$\dot{r} = v \quad (5)$$

$$\dot{v} = \frac{5kT}{m} \frac{1}{r} \quad (6)$$

and

$$\dot{T} = \frac{2Tv}{r} + \frac{2W}{3Nk} \quad (7)$$

where  $m = M/N$ . Equations (5) through (7) are easily solved numerically, once a functional form has been assigned to the laser heating term  $W$ . In general

$$W = \mu \rho f \left( \frac{4}{3} \pi r^3 \right) = \mu M f \quad (8)$$

where  $\mu$  is the mass absorption coefficient in the vapor and  $f$  is the laser flux. We expect that as the vapor expands the mass absorption coefficient will decrease, and we assume it to vary as a power of the density

$$\mu = \mu_0 \left( \rho / \rho_0 \right)^{n-1} = \mu_0 \left( r_0 / r \right)^{3n-3} \quad (9)$$

where  $\mu_0$  is the mass absorption coefficient in the solid. If  $n = 1$ , the vapor continues to absorb like the solid, a clearly unrealistic case, while as  $n \rightarrow \infty$  absorption in the vapor rapidly ceases as it expands. The theory of pressure broadening within the vapor would predict  $n = 2$ , and this value is often assumed in estimating vapor opacities.<sup>3</sup>

It is convenient to write equations (5) through (7) in terms of the dimensionless variables  $r = xr_0$ ,  $v = yv_0$ , and  $T = ZT_0$ .

$$\frac{dx}{dw} = y \quad (10)$$

$$\frac{dy}{dw} = \left( \frac{5k}{m} \frac{T_0}{v_0^2} \right) \frac{z}{x} \quad (11)$$

and

$$\frac{dz}{dw} = -\frac{2zy}{x} + \left[ \frac{2}{3} m \frac{f\mu_o}{k} \frac{r_o}{v_o T_o} \right] \left( \frac{1}{x} \right)^{3n-3} \quad (12)$$

where  $w = tv_o/r_o$  and we have made explicit use of equations (8) and (9) for  $W$ . Thus, the solutions for  $r$ ,  $v$ , and  $T$  as a function of time depend upon  $n$  and the dimensionless combinations  $\alpha = 2mf\mu_o r_o/3kv_o T_o$  and  $\beta = 5kT_o/mv_o^2$ , of the initial radius, velocity, and temperature of the vapor. Numerical calculations demonstrate that the solutions are in fact insensitive to  $\alpha$  and  $\beta$  individually, depending rather upon  $\alpha^2/\beta$ , a quantity which is independent of  $v_o$ , the only parameter in equations (1) through (12) which is undetermined for any particular particle and incident laser flux. This is demonstrated in Figure 1, where we show the maximum value reached by  $Z$ , denoted  $Z_{\max}$ , as a function of  $\alpha^2/\beta$ . The "error bars" show the amount by which the solutions vary for different  $\alpha$  and  $\beta$  which have the same value of  $\alpha^2/\beta$ . It will also be noted that the dependence of the solution upon  $n$  is likewise a weak one. The quantity  $Z_{\max}$  is the parameter which determines whether or not the mechanism of thermal ionization within the vapor can occur and lower the breakdown threshold, for such ionization will occur in significant amounts only if the temperature of the vapor approaches approximately  $I/10$ , where  $I$  is the ionization potential. Thus, we must have  $kT_{\max} = I/10$ , or  $Z_{\max} = I/10kT_o \equiv Z_{\text{cr}}$ . For any material we can determine  $Z_{\text{cr}}$ , and determine from Figure 1 the value of  $\alpha^2/\beta$  at which  $Z_{\max}$  will reach this critical value, implying significant thermal ionization. For example, carbon has an ionization potential  $I$  of 11 eV, and a vaporization temperature  $T_o$  of 5100°K, so that  $Z_{\text{cr}}(c) = 2.5$ . Entering Figure 1 at  $Z_{\text{cr}}(c)$ , we find the value of  $\alpha^2/\beta$  at which  $Z_{\max} = Z_{\text{cr}}$  to be given by  $(\alpha^2/\beta)_{\text{cr}} \approx 55$ . From equations (11) and (12), we note

$$\frac{\alpha^2}{\beta} = \frac{4}{45} \left( \frac{m}{kT_o} \right)^3 \left( \frac{f}{\rho_o} \right)^2 (\mu_o r_o \rho_o)^2 \quad (13)$$

and solving equation (13) for  $f^2$ , we find  $\alpha^2/\beta$  exceeds 55 for  $f > 3.6 \times 10^{17}$  erg/cm<sup>2</sup>/sec, if  $\mu_o r_o \rho_o = 1$  (its upper limit if this model is to retain its validity). It is of interest to note that over the range of interest,

$$Z_{\max} \approx \frac{1}{2} (\alpha^2/\beta)^{1/3}$$



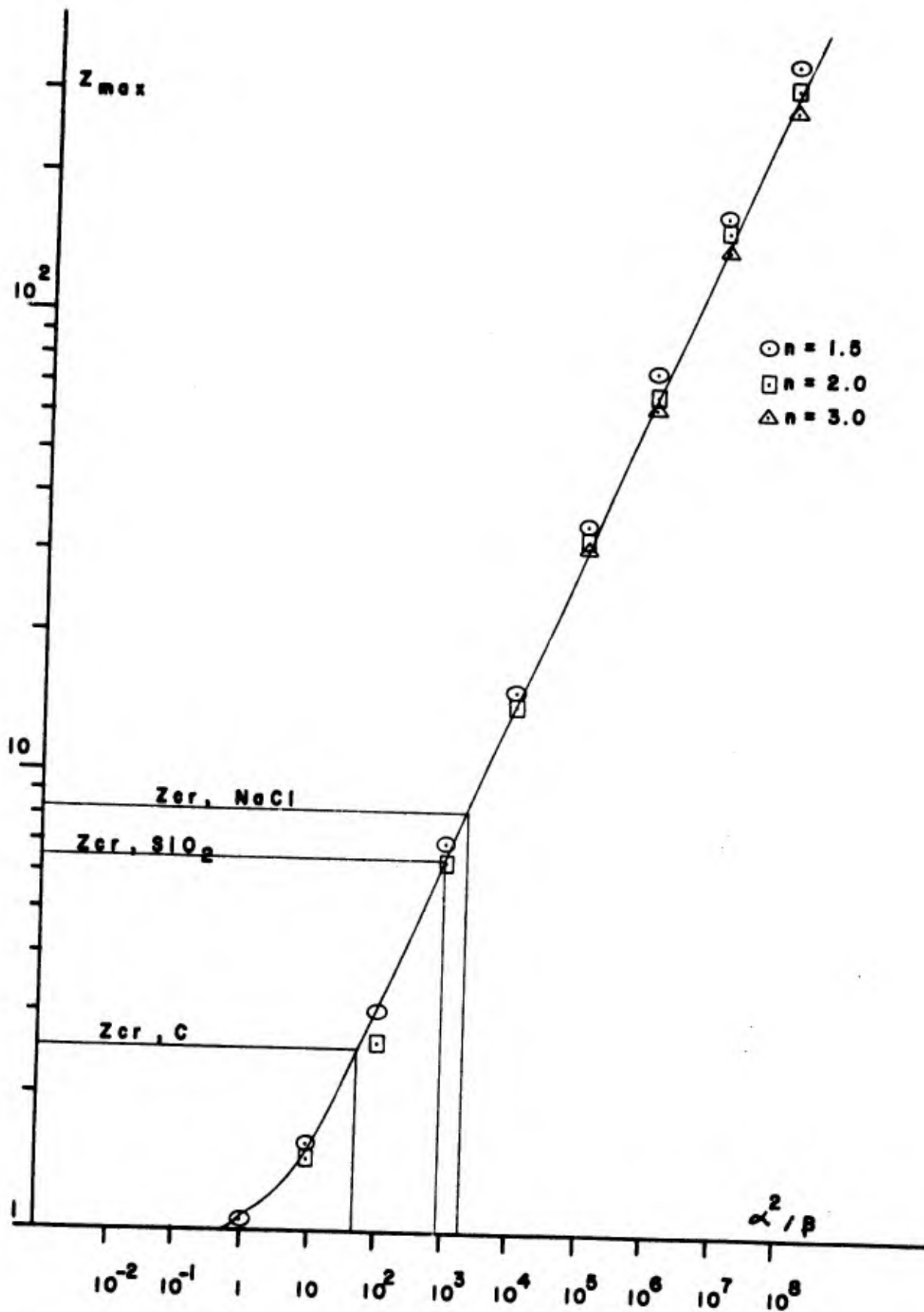


Figure 1. Maximum vapor temperature versus the square of the incident laser flux, in dimensionless units. The critical value at which thermal ionization in the vapor is expected to be important, and the corresponding flux at which that temperature might be achieved, are indicated for several possible aerosols.

so that one may obtain an approximate analytic expression for the critical flux for thermal ionization as a function of material-dependent parameters by setting

$$2Z_{cr} = \frac{I}{5kT_o} = \left[ \frac{4}{45} \left( \frac{m}{kT_o} \right)^3 \left( \frac{f}{\rho_o} \right)^2 \left( \mu_o r_o \rho_o \right)^2 \right]^{1/3}$$

or

$$f \geq \rho_o \left( \frac{2I}{5m} \right)^{3/2} \quad (14)$$

For carbon, equation (14) yields  $f_o \geq 4.6 \times 10^{17}$  erg/cm<sup>2</sup>/sec, which agrees well with the graphical solution obtained from Figure 1. In a similar way, critical fluxes for SiO<sub>2</sub> and NaCl have been determined as outlined on Figure 1, and the results are summarized in Table I.

Table I

FLUXES FOR BREAKDOWN OF AEROSOL LADEN AIR

$f_1$  = flux for thermal ionization

$f_2$  = flux for shock heating

Aerosol	$T_o$ (K)	I (eV)	$Z_{cr}$	$f_1$ (erg/cm <sup>2</sup> /sec)	$y_{\infty}/\beta^{1/2}$ cr	$f_2$ (erg/cm <sup>2</sup> /sec)
SiO <sub>2</sub>	2500	14	6.5	$4.7 \times 10^{16}$	5.03	$8.1 \times 10^{16}$
C	5100	11	2.5	$3.6 \times 10^{17}$	1.57	$6.1 \times 10^{16}$
NaCl	1686	12	8.3	$4.3 \times 10^{16}$	6.05	$9.4 \times 10^{16}$

The second mechanism which could lead to a lowering of the air breakdown threshold, that of shock-heating the surrounding air, depends upon the limiting velocity achieved by the expanding vapor, which we denote  $v_{\infty}$ . The dimensionless parameter corresponding to this is  $y_{\infty} = v_{\infty}/v_o$ , but it is more convenient to focus attention upon

$$y_{\infty}/\beta^{1/2} = v_{\infty}/(5kT_o/m)^{1/2}$$

which is independent of any initial velocity and which has a simple physical interpretation as the ratio of the final velocity to that corresponding to the initial temperature of the vapor. In Figure 2 we show  $y_{\infty}/\beta^{1/2}$  as a function of

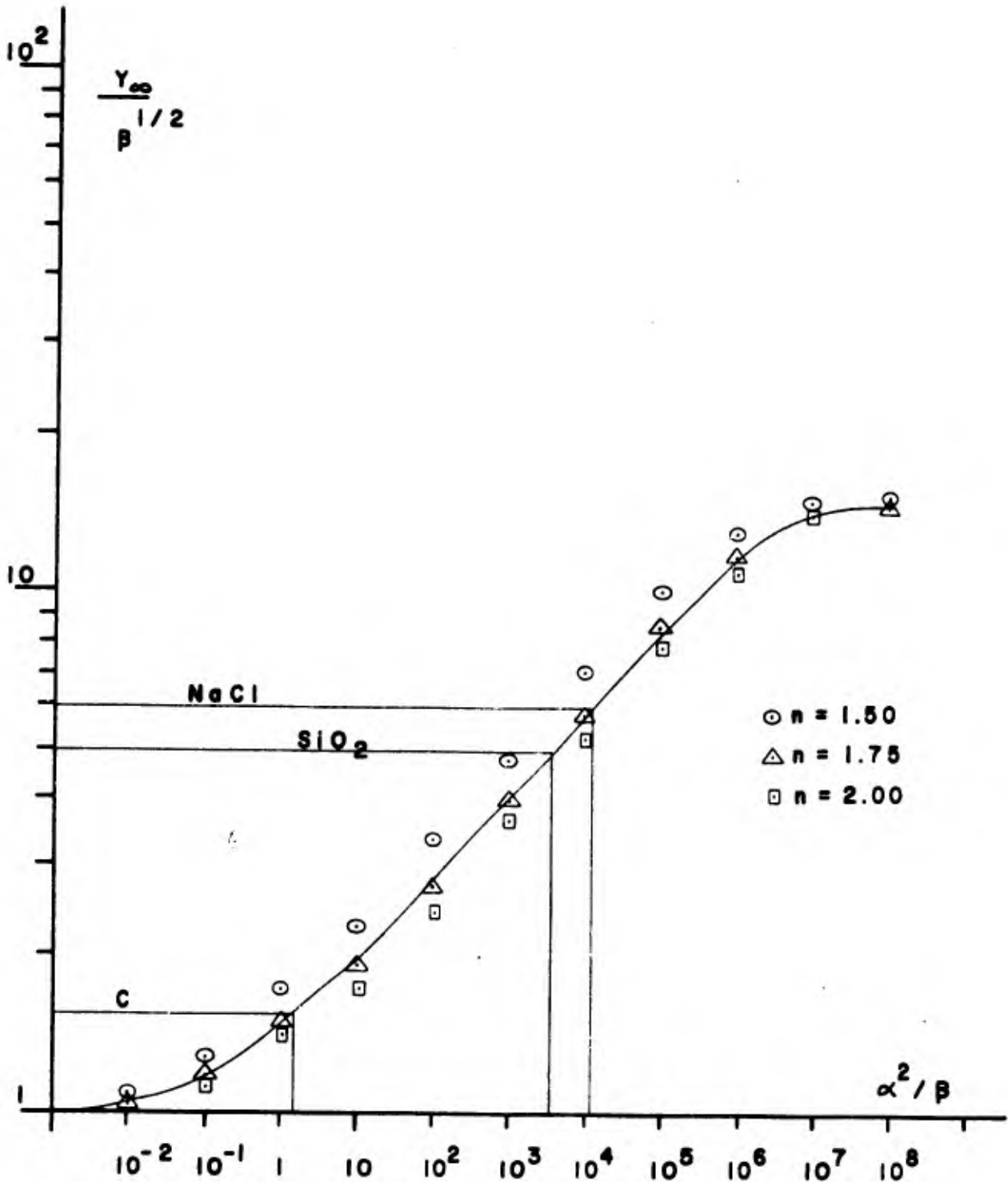


Figure 2. Maximum velocity of expanding vapor sphere versus the square of the incident laser flux, in dimensionless units. This velocity determines the temperature to which ambient air will be shock-heated; critical fluxes at which the expanding vapors of various aerosols are predicted to cause strongly absorbing shock fronts are indicated.

$\alpha^2/\beta$ , and note that as in the case of  $Z_{\max}$ , the results are only weakly dependent upon  $n$  and the individual values of  $\alpha$  and  $\beta$ . Shock-heated air will achieve a temperature of about 1 eV and be significantly ionized if  $v_{\infty} \approx 20C_s$ ,\* where  $C_s$  is the speed of sound in STP air. This relation allows us to determine a critical value

$$y_{\infty}/\beta^{1/2})_{cr} = 20C_s / (5kT_o/m)^{1/2}$$

at which shock heating will be important. Again using the example of carbon, we find

$$y_{\infty}/\beta^{1/2})_{cr} = 1.6$$

which by Figure 2 corresponds to a value of  $\alpha^2/\beta \approx 1.5$ , or  $f = 5.9 \times 10^{16}$  erg/cm<sup>2</sup>/sec. Again we note that within the range of interest

$$y_{\infty}/\beta^{1/2} \approx \frac{3}{2} (\alpha^2/\beta)^{1/6}$$

from which we derive an approximate expression for the critical flux for shock heating,

$$f > 7 \times 10^2 \rho_o C_s^3 \quad (15)$$

which for carbon gives the result  $f > 5.5 \times 10^{16}$  erg/cm<sup>2</sup>/sec. Graphical solutions for critical shock-heating fluxes for SiO<sub>2</sub> and NaCl have also been obtained, and are outlined in Figure 2 and summarized in Table I.

We note that in all cases the fields at which the breakdown mechanisms of thermal ionization and shock heating are expected to become significant are above the clean air breakdown threshold<sup>5</sup> of  $2 \times 10^{16}$  erg/cm<sup>2</sup>/sec at 10.6 $\mu$ . However, these results are independent of frequency, so that while optically thin particles pose no additional threat to the transmission of CO<sub>2</sub> laser radiation, thresholds for higher frequency lasers may be substantially reduced.

---

\*This relation can be estimated from reference 4.

## REFERENCES

1. Raizer, Y. P., "Heating of a Gas by a Powerful Light Pulse," Zh. Eksperim. Teor. Fiz., 48, 1508, 1965 [English transl.: Soviet Physics--JETP 21, 1009, 1965].
2. Sedov, L. I., Similarity and Dimensional Methods in Mechanics, Academic Press, New York, 1959.
3. Chang, D. B., Drummond, J. E., Hall, R. B., "High-Power Laser Radiation Interaction with Quartz," J. Appl. Phys., 41, 4851, 1970.
4. Gilmore, F. R., "Equilibrium Composition and Thermodynamic Properties of Air to 24,000°K," RAND Corp. Report RM-1543, 1955.
5. Rockwood, S. D., Canavan, G. H., "CO<sub>2</sub> Laser Air Breakdown Calculations," AFWL Laser Division Digest, LRD-71-1, June 1971.

HYDRODYNAMIC CALCULATIONS OF LASER INTERACTION  
WITH ATMOSPHERIC AEROSOLS

P. E. Nielsen and C. H. Canavan

There are two mechanisms by which the threshold for the laser-induced breakdown of air might be lowered through interaction with aerosols. First, the aerosol vapor itself might heat sufficiently to become thermally ionized, leading to strong free-free absorption and subsequent breakdown. Second, the shock which is driven into the air might heat it sufficiently to produce strong absorption within the thin layer of the shock wave, leading to a radiation-driven shock.<sup>1</sup>

In order to determine the extent to which the threshold for air breakdown by intense laser radiation is likely to be lowered by the presence of particulate contaminants, we have investigated the heating, vaporization, and subsequent development of atmospheric aerosols within the framework of a one-dimensional Lagrangian hydrodynamic computer code. The position,  $x$ , velocity,  $v$ , density,  $\rho$ , and pressure,  $p$ , of each Lagrangian cell develop in time according to the equations

$$\frac{dx}{dt} = v \quad (1)$$

$$\frac{dv}{dt} = -\frac{1}{\rho} \text{grad} (p+q) \quad (2)$$

$$\frac{d\rho}{dt} = -\rho \text{div } \underline{v} \quad (3)$$

and

$$\frac{dp}{dt} = -\gamma(p+q) \text{div } \underline{v} - (\gamma-1) \text{div } \underline{u} + (\gamma-1) Q \quad (4)$$

where  $q$  is an artificial pressure<sup>2</sup> designed to enable the numerical treatment of shock waves,  $\underline{u} = -K\nabla T$ , with  $K$  the thermal conductivity, is the heat flux,  $Q$  is heating due to the laser, and we have assumed the equation of state

$$P = (\gamma - 1) \rho e \quad (5)$$

with  $e$  the specific internal energy.

Initially, the first  $N$  of  $M$  spherically symmetric cells are taken to be solid, with density  $\rho_0$ , temperature  $T_0$ , and a mass absorption coefficient to the incident laser radiation of  $\mu_0$ . The remaining cells are taken to be air at standard temperature and pressure, and are assumed to be transparent to the laser radiation. A solid cell is released and becomes a vapor cell with an initial energy of  $CT_v$  when the total energy deposited within that cell is equal to  $L + CT_v$ , where  $L$  is the heat of vaporization,  $C$  the specific heat, and  $T_v$  the vaporization temperature. In the vapor phase, the mass absorption coefficient is taken to be  $\mu_0 \left(\rho/\rho_0\right)^{n-1}$ , where  $n$  is a parameter most commonly<sup>3</sup> taken to be 2. For  $1 < n < \infty$ , one obtains absorption in the vapor intermediate between the unphysical extremes of absorption as strong as in the solid and no absorption at all. As we shall see, the results are insensitive to the choice of this parameter, if  $n \geq 1.5$ .

In Figure 1 we show density, velocity, and pressure profiles just after vaporization for an optically thin particle whose linear absorption coefficient is  $10^3 \text{ cm}^{-1}$  and whose radius is  $10^{-4} \text{ cm}$ . As would be expected, such particles heat uniformly, vaporizing in place. In their subsequent development, as can be seen in Figure 1, the pressure and density are approximately uniform throughout the vapor, and the velocity increases linearly from the center to the edge. These features are characteristic of a Sedov<sup>4</sup> model for vapor expansion and heating. Accordingly, we have performed an exhaustive analysis of the interaction of lasers and optically thin particles within the framework of this model. These results are presented in a separate report,<sup>5</sup> and the conclusion reached is that such particles cannot lower the threshold for air breakdown at  $10.6\mu$  below that of clean air.

In Figure 2 we show density, velocity, and pressure profiles just prior to complete vaporization for an optically thick particle, with a linear absorption coefficient of  $10^4 \text{ cm}^{-1}$  and a radius of  $10^{-3} \text{ cm}$ . It will be noted that the optically thick particle vaporizes in a way which is qualitatively different from that of the thin particle. The thick particle vaporizes over an extended period, during which time there is a more or less nondivergent mass flux in the vapor boiling off the surface. The vapor expands at supersonic velocities, ultimately shocking into the surrounding air and going subsonic when it has

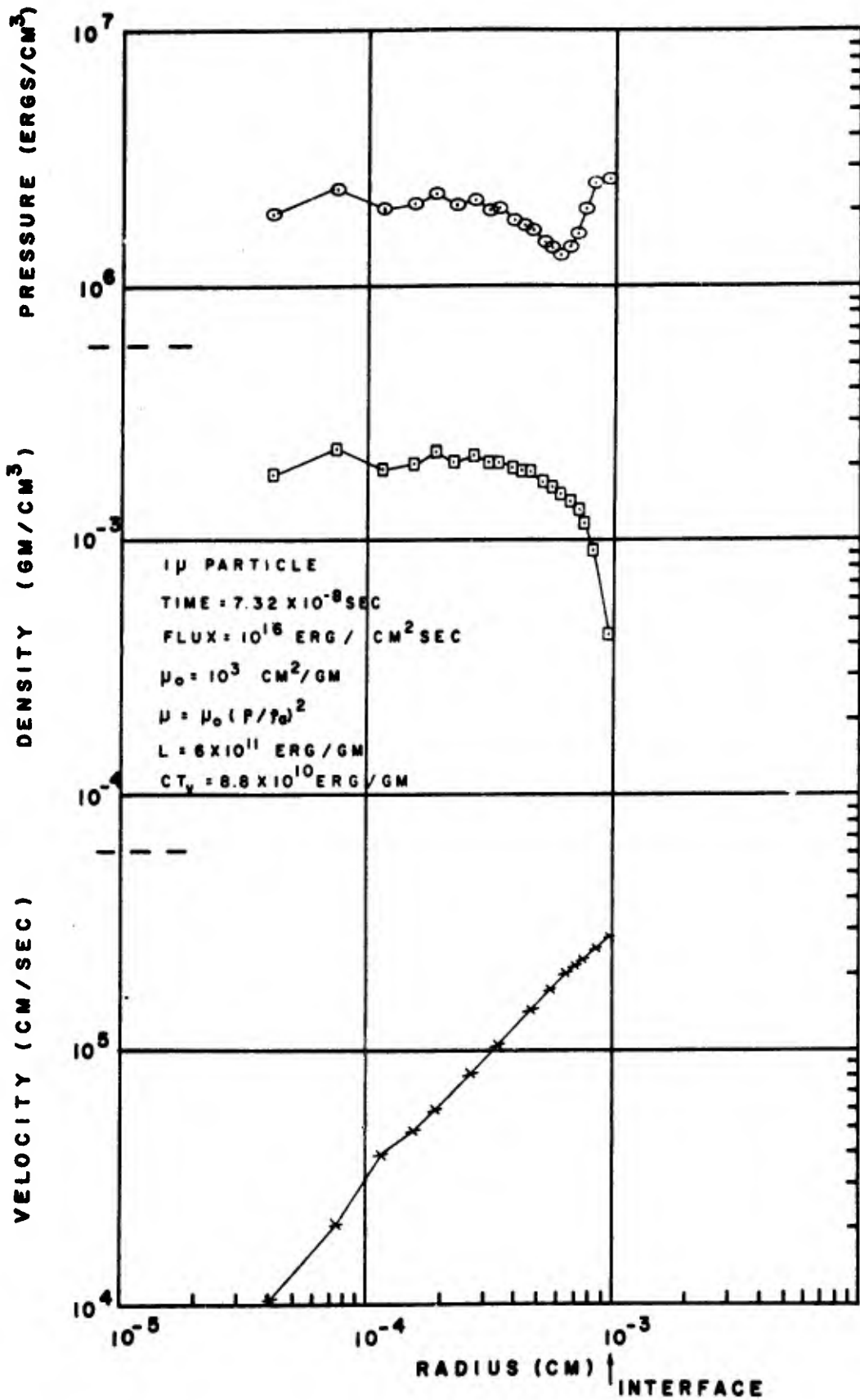


Figure 1. Velocity, density, and pressure profiles of an optically thin aerosol.



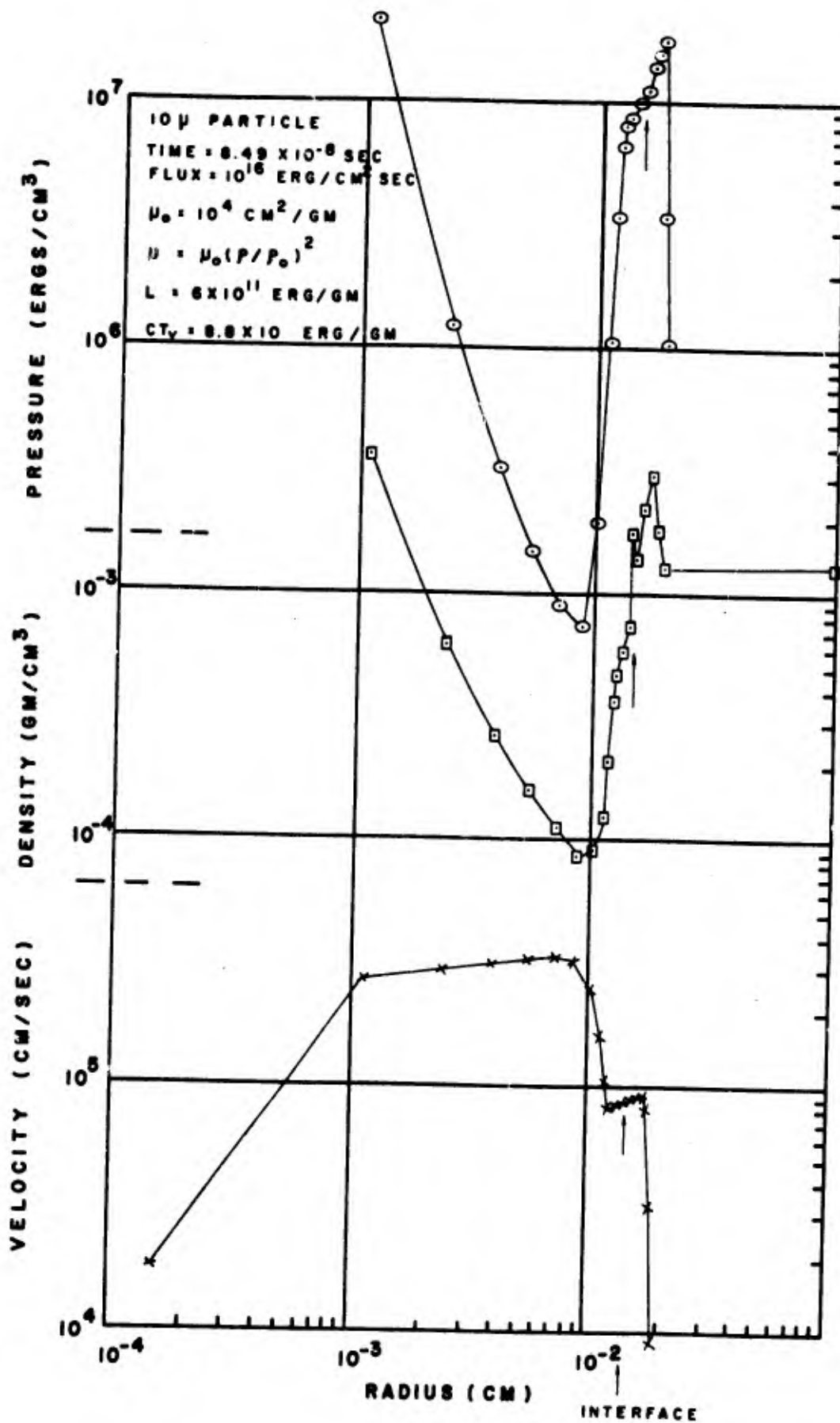


Figure 2. Velocity, density, and pressure profiles of an optically thick aerosol.

reached a distance of roughly ten times the initial radius of the particle. In the example of Figure 2 the shock formed in the air is about three times overdense, at a temperature of about 2000°K, and the blow-off vapor is at a temperature of about 2400°K.

We have performed calculations for a variety of laser flux strengths and absorption coefficients. In Figures 3 and 4 we show the maximum temperature reached by the blow-off vapor and shock-heated air for a typical particle as a function of the assumed mass absorption coefficient for different values of incident laser flux. It will be noted that as the mass absorption coefficient goes to infinity, the temperature achieved at a constant flux approaches a limiting value. This effect is due to the increased self-shielding of the aerosol by the blow-off vapor, and allows us to plot a maximum achievable vapor and air temperature as a function of laser flux, which we do in Figure 5. If we assume that the air will be largely ionized and broken down at a temperature of  $10^4$ °K, we see from Figure 5 that for aerosols with the indicated material parameters and an arbitrarily large optical thickness, the threshold flux for breakdown is about  $2 \times 10^{15}$  erg/cm<sup>2</sup>/sec, an order of magnitude below the threshold for clean air.

In order to extend our results to cover all conceivable aerosols, we have recast the hydrodynamic equations (1) through (4) in dimensionless form. This analysis reveals that the solution to these equations depends primarily upon the following dimensionless parameters, which we present in their order of importance:

$$\alpha = f_0 / \rho_0 (CT_v)^{3/2}$$

$$\lambda = \mu_0 \rho_0 r_0 = \text{optical thickness of aerosol}$$

$$\xi = L / CT_v$$

$$\delta = (K/C) / r_0 c_0 (CT_v)^{1/2}$$

$$\eta = \rho_{\text{air}} / \rho_0$$

$$T_v / T_0$$

The value of such an analysis is shown in Figure 6, where we plot  $Z_{\text{max}}$ , the ratio of maximum temperature achieved as  $\lambda \rightarrow \infty$  to vaporization temperature, as a function of  $\alpha$ , for both the blow-off vapor and the shock-heated air. For any material, a critical  $Z$  for thermal ionization is defined by  $I/10T_v$ , and for shock heating by  $1 \text{ eV}/T_v$ , where  $I$  is the ionization potential and we take  $I/10$

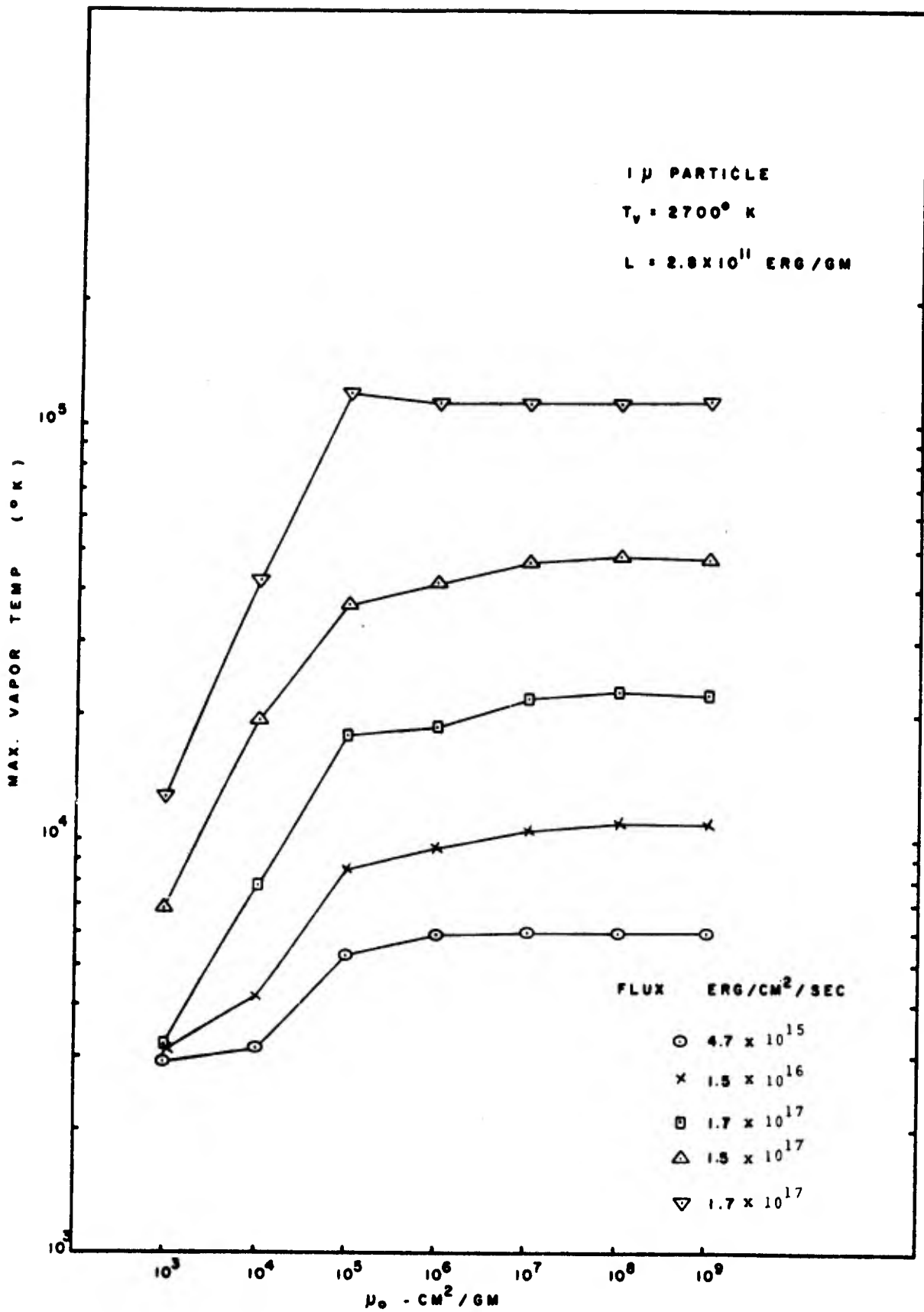


Figure 3. Maximum temperature of aerosol vapor as a function of absorption coefficient for various fluxes.

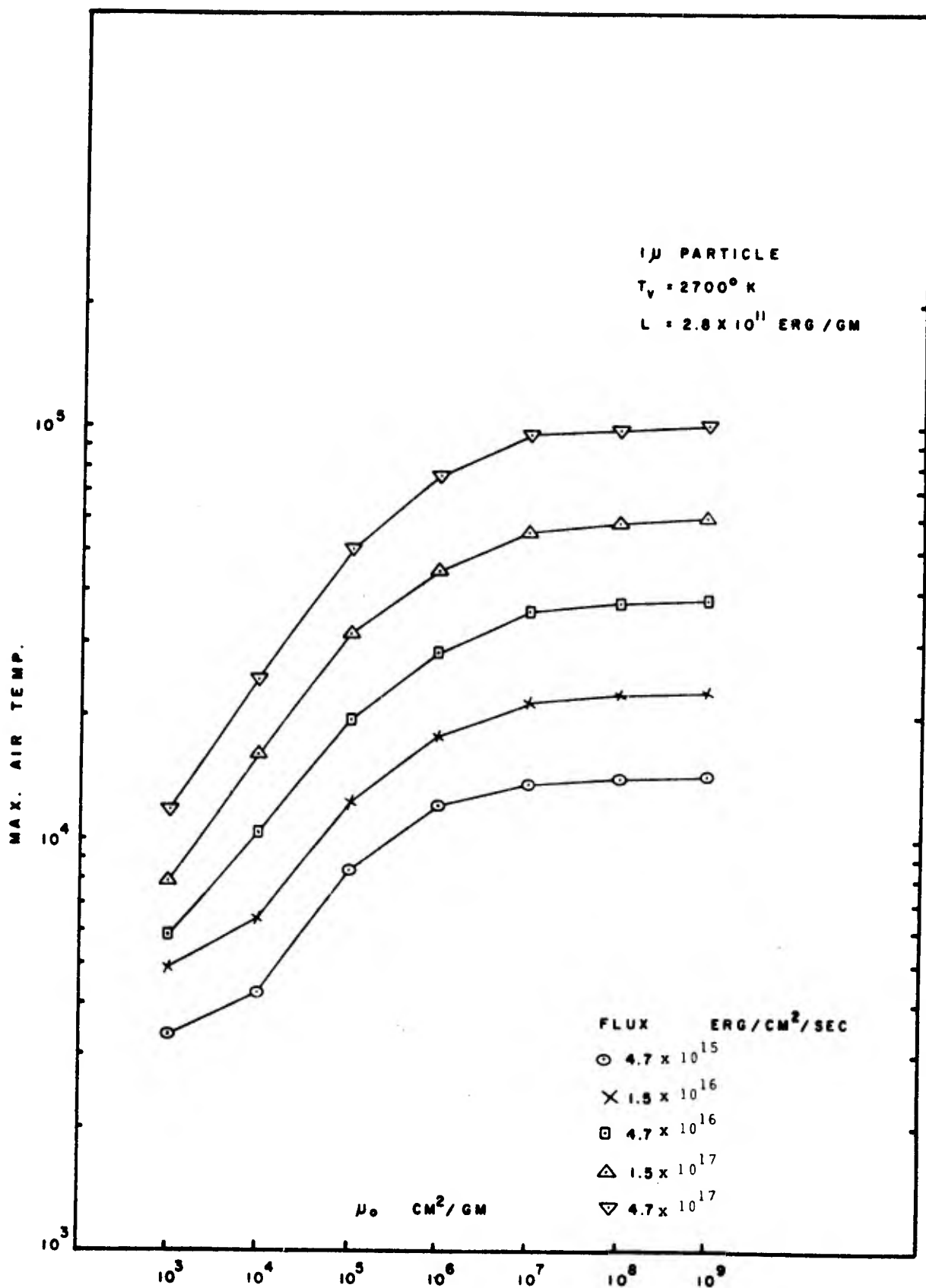


Figure 4. Maximum temperature of shock-heated air as a function of absorption coefficient for various fluxes.

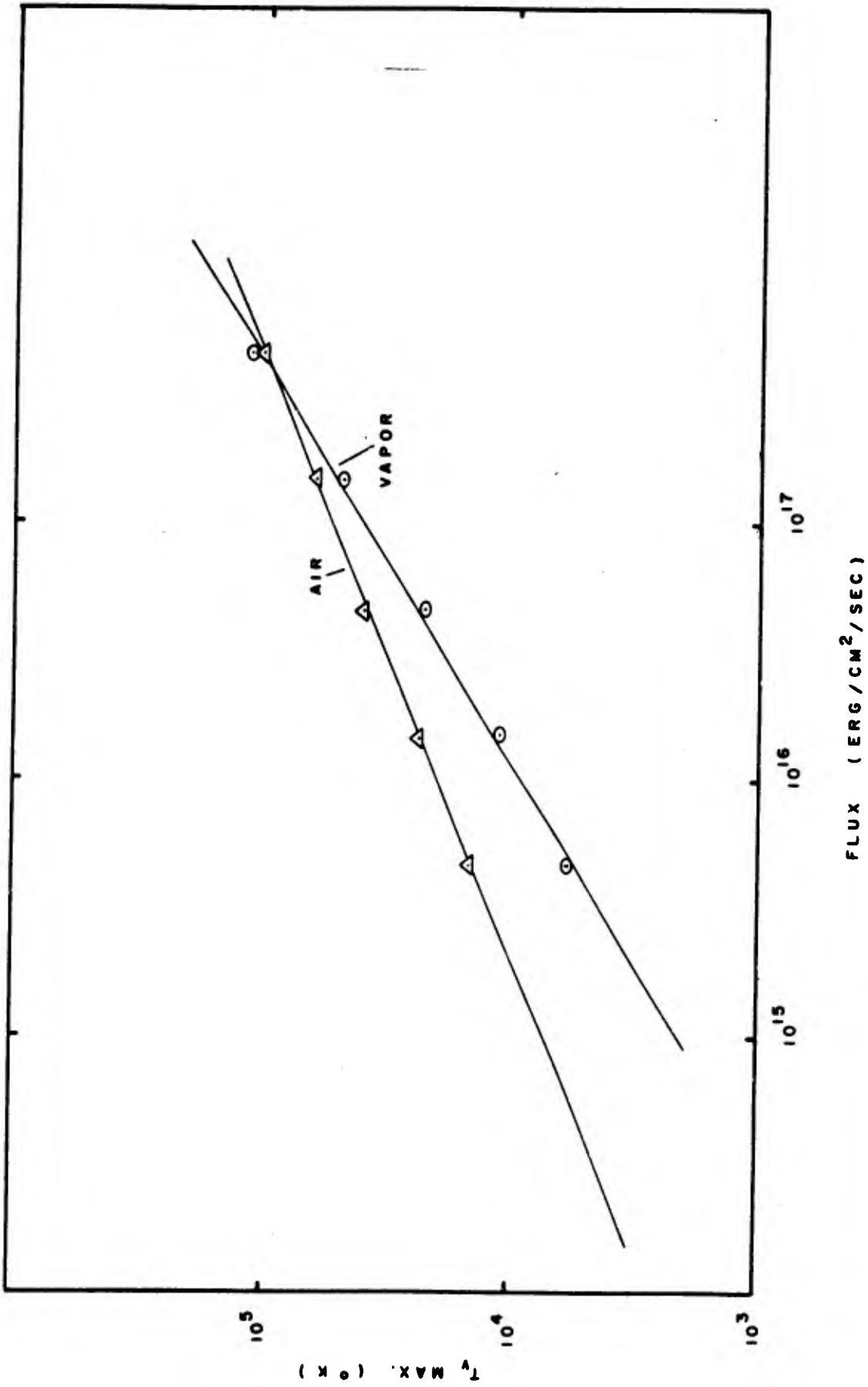


Figure 5. Maximum temperature of vapor and shock-heated air for a typical optically thick aerosol as a function of incident flux.

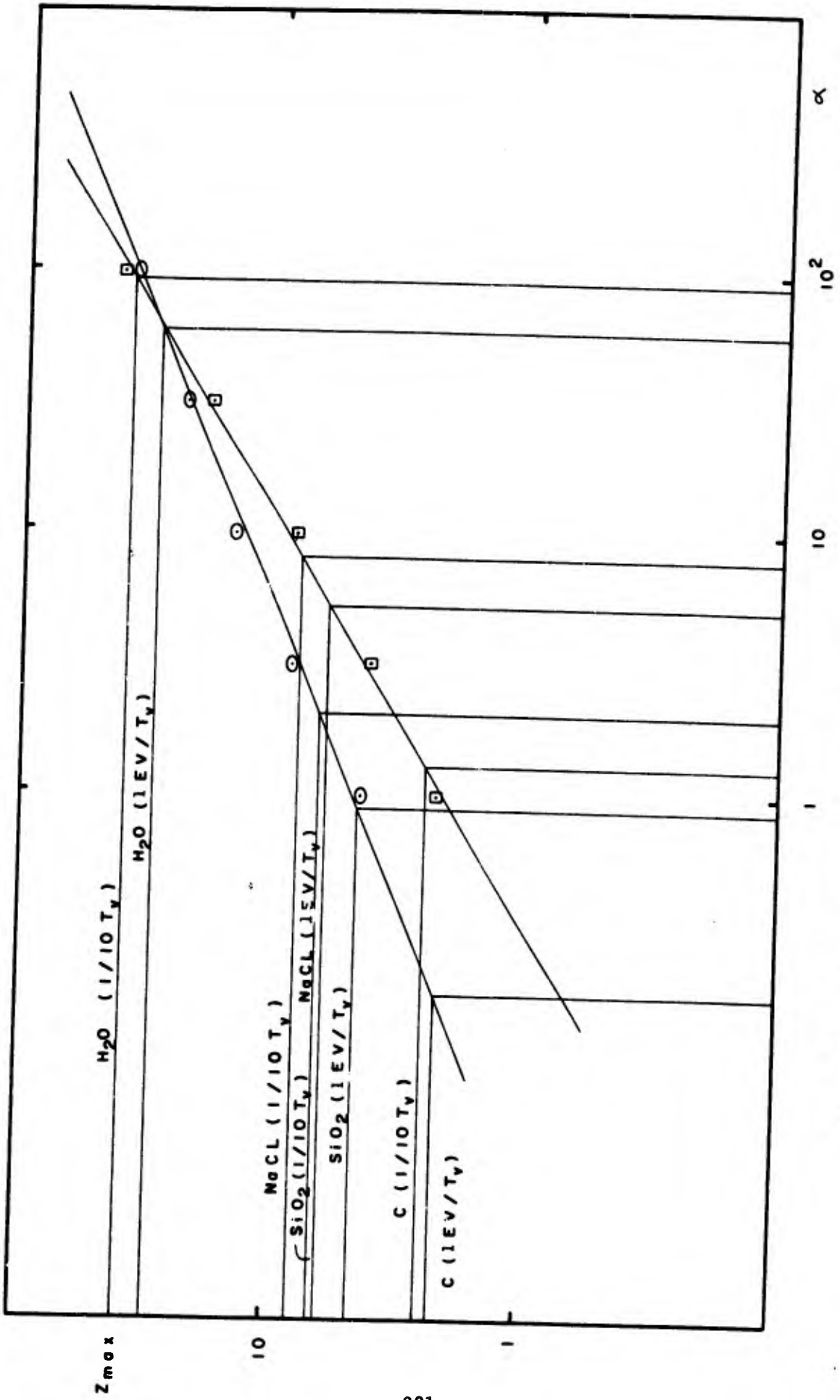


Figure 6. The maximum temperature of aerosol vapor and shock-heated air versus laser flux for optically thick aerosols.

and 1 eV to be the temperatures at which vapor and air respectively are ionized sufficiently to breakdown. We show these critical values of  $Z$ , and the fluxes at which they would be achieved, in Figure 6 and Table I for several common aerosols. The examples given span a reasonable range of material parameters, and we therefore conclude that the presence of atmospheric aerosols can lower the threshold for air breakdown up to two orders of magnitude below the  $10.6\mu$  threshold for clean air. It is of interest to note that these results are independent of laser frequency, except in the frequency dependence of the absorption coefficient. As we have taken the limit of this coefficient going to infinity, our results determine a threshold at all frequencies.

Table I

FLUXES FOR BREAKDOWN OF AEROSOL LADEN AIR

$f$  = flux for thermal ionization of aerosol vapor

$f$  = flux for shock heating of surrounding air

Aerosol	$T_v$ (K)	I (eV)	$CT_v$ (erg/gm)	$f_1$ (erg/cm <sup>2</sup> /sec)	$f_2$ (erg/cm <sup>2</sup> /sec)
NaCl	1686	12	$2.38 \times 10^9$	$2.04 \times 10^{15}$	$5.36 \times 10^{14}$
SiO <sub>2</sub>	2500	14	$3.44 \times 10^9$	$2.40 \times 10^{15}$	$3.99 \times 10^{14}$
C	5100	11	$3.50 \times 10^{10}$	$1.87 \times 10^{16}$	$2.59 \times 10^{15}$
H <sub>2</sub> O	373	12.6	$1.57 \times 10^{10}$	$1.77 \times 10^{17}$	$1.18 \times 10^{17}$

REFERENCES

1. Raizer, Y. P., "Heating of a Gas by a Powerful light pulse," Zh. Eksperim. Teor. Fiz., 48, 1508, 1965 [English transl.: Soviet Physics--JETP-21, 1009, 1965].
2. Richtmyer, R. D., Morton, K. W., Difference Methods for Initial-Value Problems, Interscience, New York, 1967.
3. Chang, D. B., Drummond, J. E., Hall, R. B., "High-Power Laser Radiation Interaction with Quartz," J. Appl. Phys., 41, 4851, 1970.
4. Sedov, L. I., Similarity and Dimensional Methods in Mechanics, Academic Press, New York, 1959.
5. Nielsen, P. E., Canavan, G. H., "Interaction of High-Intensity Lasers with Optically Thin Aerosols," AFWL Laser Division Digest, LRD-71-1, June 1971.

# THREE-MICRON LASER WINDOW ABSORPTION COEFFICIENTS

K. G. GILBERT

## Introduction

Even miniscule absorption of laser radiation by a window can cause significant degradation in far-field beam quality. When a non-uniform high-power beam traverses a window material, various thermal gradients appear. If the beam profile is center-peaked, the resultant gradient between the window center and edge causes a center budging; a lens forms, and the effective system focal length decreases. An important result of this total thermo-optical distortion is a reduced brightness at the original focal plane. The extreme sensitivity of this lensing effect is made clear by noting that an induced optical path difference of just 4 microns in length between the center and the edge of a 15-cm-radius aluminum oxide ( $\text{Al}_2\text{O}_3$ ) window can cause the recession of 2-km focal plane to approximately 1 km. The "distorted" intensity at 2 km has now decreased nine-fold from its original value.

Laser absorption of eight candidate window materials has been measured calorimetrically in the 2.8-micron ( $\mu$ ) regime. Thermally-induced window lensing and aberration were also studied by observing the transmitted energy on a thermally-deactivated fluorescent screen. The laser used for these experiments was the Aerospace Corporation continuous hydrogen-fluoride system. The beam profile was found to be nearly Gaussian, with a peak intensity and total power of approximately  $2.3 \text{ kW/cm}^2$  and 0.75 kW, respectively.

Most of the windows evaluated exhibit 2.8  $\mu$  absorption coefficients well below  $0.01 \text{ cm}^{-1}$ . Thermal fracture is generally not the limiting feature of these materials. A secondary window effect is stress-induced birefringence, causing polarization-dependent optical paths. The thermal lensing effect, however, is generally more important.

## Experiment

Figure 1 shows the experiment. Samples are mounted behind a 1-cm graphite aperture; this restricts the near-normal incident laser energy to the window's central portion. Energy reflected from the two window surfaces enters a thermopile. A three-point mount with rubber tips thermally isolates the window yet



SECTION V

LASER EFFECTS

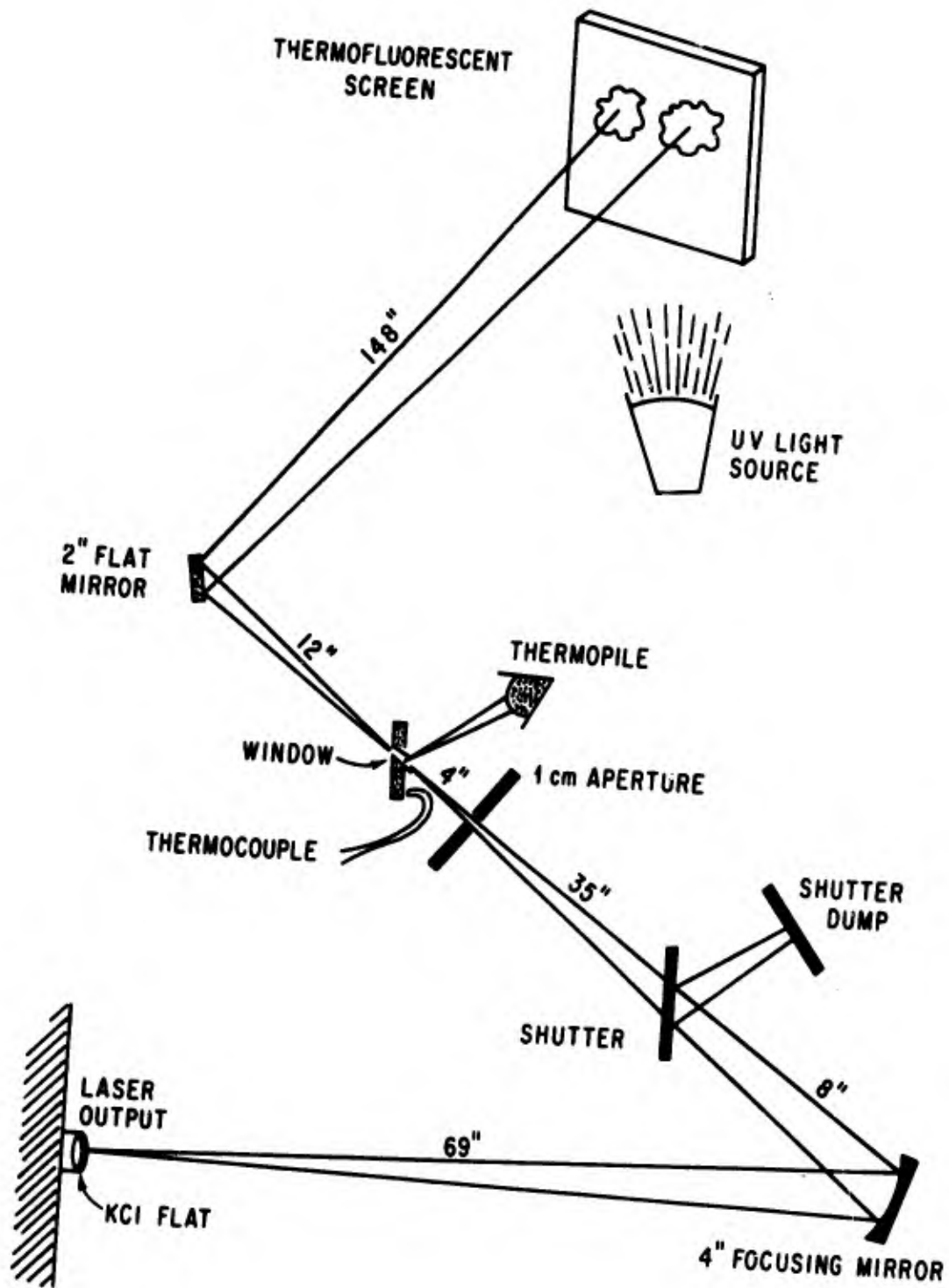


Figure 1. Experiment.

leaves it essentially unconstrained. A single thermocouple is attached to the front surface of each window at a distance of 1.1 cm from the window center, or about 0.6 cm outside the laser energy path. A trace of thermally conducting epoxy is used to bond each thermocouple to its window. Transmitted energy continues against a flat turning mirror and is displayed on a thermofluorescent screen. A nearly-colinear helium neon beam also traverses the heated portion of the window and is viewed on a screen. Framing cameras (30 fps) record both images. The overall accuracy of the temperature measurement is about 5 percent.

Approximately 750 watts of laser energy are incident on the windows. The beam profile was determined by transmitting energy through a variable-diameter iris located at the beam focal plane. A Gaussian profile with a  $1/e^2$  radius of 0.44 cm fits the data well. The peak intensity was obtained by measuring surface recession rates in linear ablaters. The agreement with the peak intensity obtained by extrapolating power-measurement data on a very small-diameter iris was good.

The Aerospace Corporation hydrogen-fluoride laser emits primarily at 2.79  $\mu$ , 2.71  $\mu$ , and 2.83  $\mu$ , although eight vibration-rotation transitions contribute between 2.64  $\mu$  and 2.87  $\mu$ <sup>1</sup>. The output coupler used in this series of experiments was a slit device with a KCl window. The laser beam at the exit slit was composed of two lobes. Total power output was about 900 watts for constituent flows:  $\dot{m}_{N_2} = 7$  gm/sec,  $\dot{m}_{SF_6} = 1$  gm/sec,  $\dot{m}_{H_2} = 1$  gm/sec. Run times were limited only by gas supply; two minutes of continuous operation were typical.

## Results

Window absorption coefficients are inferred from the radial thermocouple response. A three-dimensional heat transport program first calculates the necessary central energy absorption (joules/cm) to yield the observed radial response. Uniform bulk absorption is assumed. The material absorption coefficient follows from this result. Next a window-center temperature response is tabulated. This latter calculation establishes the important thermal gradient which drives the lensing mechanism. Window reflectivity is measured directly by means of a thermopile. Sample irradiation times range from 12 to 75 seconds.

Figure 2 shows a recorded radial thermal response for a magnesium fluoride window. The smooth curve in Figure 2 is the inferred temperature response at the central window position. Notice a temperature difference of approximately 5°C is established between the window center and edge in 4 seconds. The

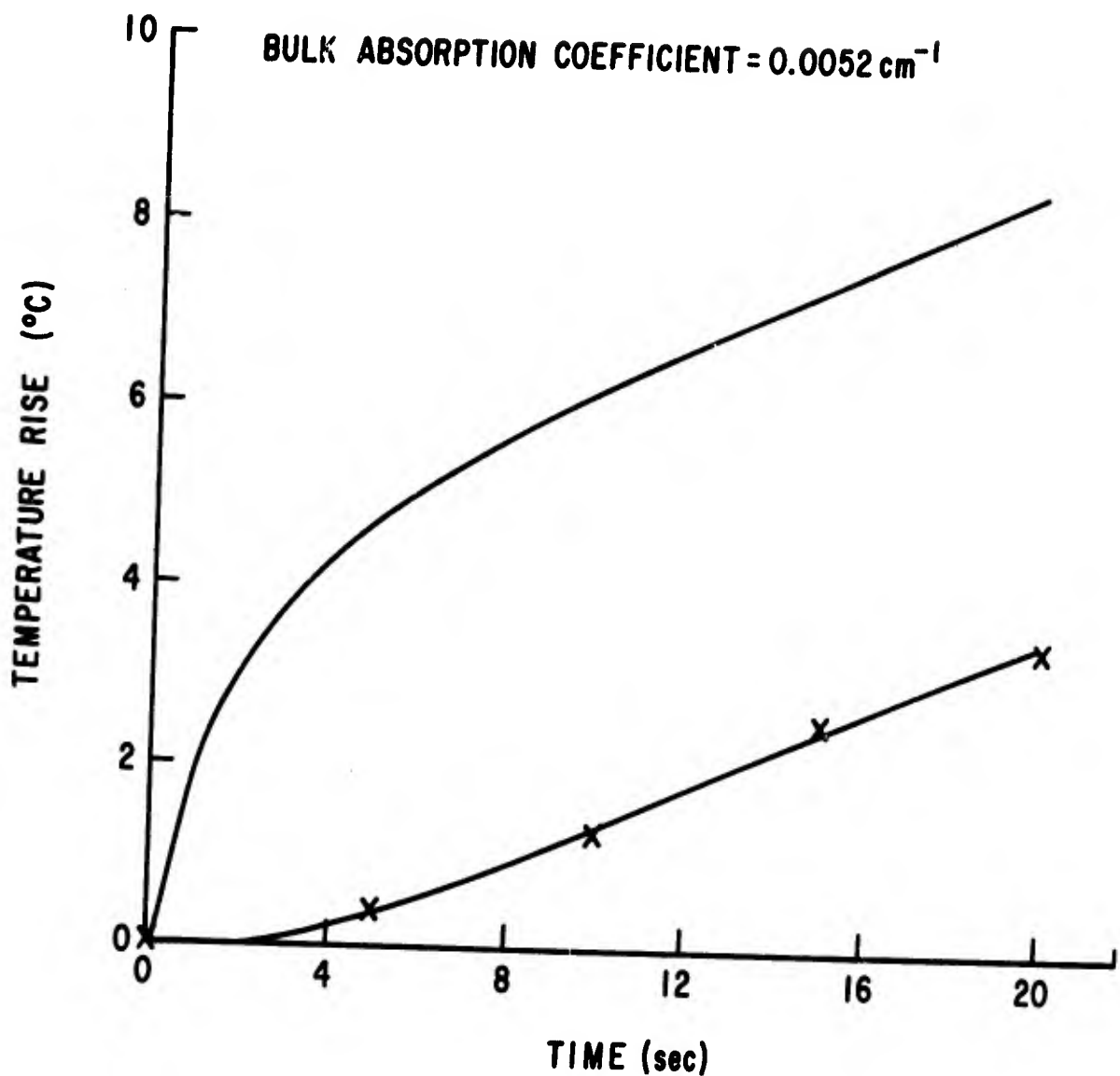


Figure 2. Magnesium fluoride temperature response. Lower curve is a fit to the experimental points measured at the edge of the window. Upper curve is the calculated response of the center of the window.

calculated average absorbed energy is 3.92 watts/cm of window thickness and since the total incident power is 750 watts, the resulting absorption coefficient is approximately  $\alpha = 3.92/750 = 0.0052 \text{ cm}^{-1}$ .

Table I describes material thermal parameters together with all measured absorption coefficients and reflectivities. Columns 2 through 4 show room temperature values of the thermal conductivity, material density, and specific heat. Column 5 lists the measured surface reflectivity (both faces), while the final column gives the absorption coefficients. Multiple values of this latter parameter are given whenever several measurements were made on one window.

Table I

RESULTS OF 2.8  $\mu$  LASER ABSORPTION MEASUREMENTS

Material	Thermal Conductivity K(j/cm sec <sup>o</sup> K)	Material Density $\rho$ (gm/cm <sup>3</sup> )	Specific Heat C <sub>p</sub> (j/gm <sup>o</sup> K)	Surface Reflectivity R(%)	Absorption Coefficient $\alpha$ (cm <sup>-1</sup> )
Al <sub>2</sub> O <sub>3</sub>	0.45	3.98	0.75	12.2	0.0034 0.0036
LiF	0.11	2.60	1.56	5.8	0.0042 0.0034
MgF <sub>2</sub>	0.15	3.00	1.19	5.3	0.0052 0.0058
CaF <sub>2</sub>	0.09	3.18	0.86	6.7	0.0025
SrF <sub>2</sub>	0.10	4.25	0.60	7.0	0.0034
BaF <sub>2</sub>	0.12	4.83	0.40	6.4	0.0030
Si	1.48	2.42	0.76	45.0	0.0085
Fused Quartz	0.014	2.20	0.71	3.6 (4.8)	0.0152 0.0120

Films of the transmitted beam projected on a thermofluorescent screen show detectable distortion only for fused quartz. The transmitted helium neon laser beam also displayed marked interference patterns indicative of optical distortion of the fused quartz. Far-field distortion in other materials was not observable due to inherent spatial and temporal fluctuations in the beam together with atmospheric degradation. This latter absorption is very evident, as the wavelengths in this lasing spectrum overlap the strong  $2.8 \mu$   $H_2O$  vibrational band.

### Discussion

A steady state temperature gradient between the center and edge of the windows is achieved in a characteristic time required for heat to flow to the sample edge,  $t \sim r^2/4D$ , with  $r$  the distance from beam edge to sample edge and  $D$  the material thermal diffusivity. Measured steady state temperature differences range from 0.75 and 1.0°C for silicon and aluminum oxide, respectively, to 3.8 to 5.2°C for the fluoride crystals. Fused silica was unique, in that its center reached an annealing temperature ( $\sim 1150^\circ C$ ) after 50 seconds of irradiation, while its edge never exceeded 100°C.

The effective focal length of a thermo-lensed window can be shown to be

$$f = \frac{R^2}{4(n-1)\Delta X} \quad (1)$$

Here  $R$  is the window radius,  $n$  is the material refractive index, and  $\Delta X$  is the established optical path difference across the window. Furthermore, if the original focal distance of the optical train is  $f_o$ , then the focal length after heating,  $f_{TH}$ , follows from:

$$\frac{1}{f_{TH}} = \frac{1}{f_o} + \frac{1}{f} \quad (2)$$

The real importance of focal plane recession is the concomitant reduction in beam brightness in the original focal plane. This intensity reduction can be estimated from the above two equations. For example, if one were to operate the Aerospace Corporation hydrogen-fluoride laser with a window of 10-cm radius and an initial system focal length of 5 km, assuming the incident beam has a Gaussian profile, then the predicted intensities at 5 km will be diminished in

amounts ranging from 3 percent ( $\text{Al}_2\text{O}_3$ ) to 11 percent ( $\text{CaF}_2$ ) and 58 percent (Si). The fused silica of course shows a considerably greater brightness degradation than any of these values.

### Conclusion

Absorption coefficients can be measured calorimetrically for candidate chemical laser window materials, with an overall accuracy of about 10 percent. At the same time, sufficient information could be obtained about the thermal gradients present in the windows during irradiation to estimate the thermo-optical distortion as well as its effect on the far-field brightness.

### REFERENCES

1. Kwok, M. A., Giedt, R. R., and Gross, R. W. F., "Comparison of HF and DF Chemical Lasers: II Spectroscopy," Appl. Phys. Letters, 16, p. 386, 1970.

UNSTEADY-STATE HEATING OF A FINITE DISC  
BY LASER RADIATION

W. T. LAUGHLIN AND J. S. SHABERMAN

The investigation of the effects of both pulsed and continuous laser beams on materials has brought about a renewed effort to solve a particular class of heat flow problems. Although the heating of materials by a laser can sometimes be represented approximately by one-dimensional heat flow analyses, for most laser effects experiments it is desirable to account for the heat conducted both into the depth of the sample as well as radially away from the irradiated spot. Also most heat transfer solutions available in the literature apply to semi-infinite solids. As larger lasers are developed and the size of the irradiated spot increases relative to convenient, small sample dimensions, it becomes extremely useful to have temperature solutions for bodies of finite radius and especially of finite thickness.

General analytical solutions to a series of heat flow problems of direct interest for a finite right circular cylinder with azimuthal symmetry have been obtained by N. Y. Olcer<sup>1, 2</sup>. From his results a particular solution has been derived and applied to the unsteady-state heating of materials by pulsed or continuous laser radiation. The solution finds the temperature,  $T(r, z, t)$ , in a finite right circular cylinder with azimuthal symmetry of radius  $0 \leq r \leq a$  and thickness  $-b \leq z \leq b$ , which obeys the heat conduction equation

$$\nabla^2 T = \frac{1}{\kappa} \frac{\partial T}{\partial t} \quad (1)$$

subject to the initial condition that the temperature of the cylinder be uniform throughout:

$$T(r, z, 0) = T_0 \quad (2)$$

The disc is heated symmetrically on one face by the laser beam and reradiation occurs from all surfaces, so the boundary conditions are

$$K \frac{\partial T}{\partial n} + hT = 0 \quad \text{at } r = a \text{ and } z = -b \quad (3)$$



and

$$\kappa \frac{\partial T}{\partial n} + hT = f(r,t) \quad \text{at } z = +b$$

where  $n$  is the outward pointing normal to a surface. The thermal diffusivity,  $\kappa$ , and the thermal conductivity,  $K$ , are treated as two independent properties, and are assumed to be independent of temperature. The energy being reradiated,  $hT$ , used in the boundary condition equations, is an approximation to the Stefan-Boltzmann radiation law .

$$\dot{Q} = \epsilon \sigma_0 T^4 \quad (4)$$

where the coefficient,  $h$ , is defined as

$$h = 4\epsilon \sigma_0 T^3 \quad (5)$$

where

$\epsilon$  = surface emissivity

$\sigma_0$  = Stefan-Boltzmann constant.

It should be noted that the flux entering the disc's front surface,  $f(r,t)$ , can be a function of both radius (radially symmetric) and time. This rather flexible boundary condition insures that the actual solution will be applicable to a wide variety of laser heating problems. The temperature solution is a series-eigenvalue expression, is complex algebraically, and must be evaluated by computer. Two applications will be shown here to illustrate how it can predict the temperature history in a laser-irradiated sample.

(a) Unpainted 2024 Aluminum Plate

The continuous 10.6-micron beam intensity profile is represented by a Gaussian so that  $f(r,t)$  in equation (3) is

$$f(r) = I_{\max} \exp(-r^2/2\sigma^2) \quad (6)$$

where  $I_{\max}$  is the maximum intensity at the beam center. Figure 1 shows a comparison of the form of the temperature solution with experimental temperature rise data from a thermocouple attached to the center rear surface of the sample. Here the computer program made a "best fit" to the experimental data and solved for a surface absorption coefficient,  $\alpha$ , of about 7 percent for this aluminum sample.

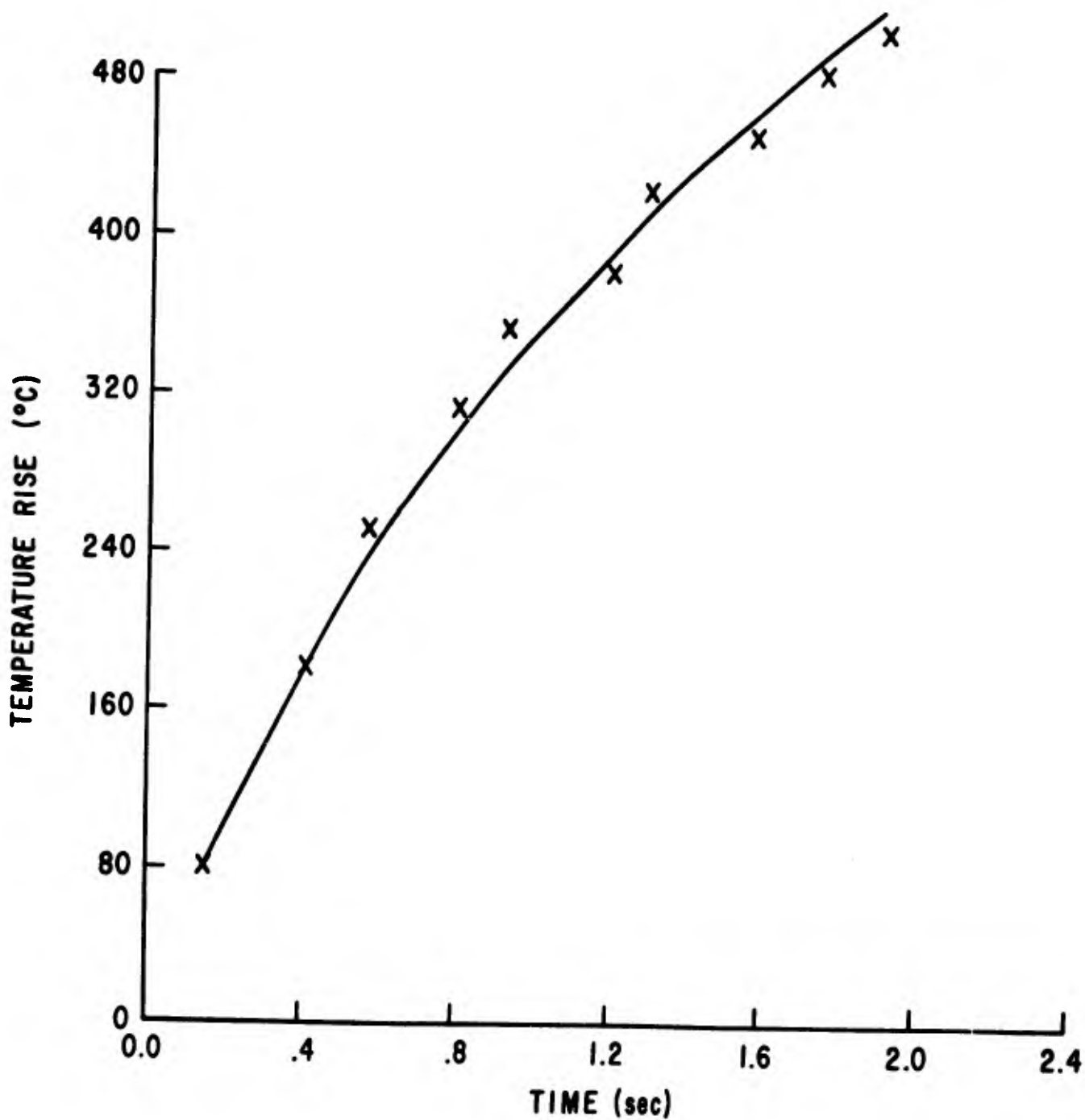


Figure 1. Theoretical and experimental temperature rise in unpainted 2024 aluminum. Maximum intensity -  $2 \text{ kW/cm}^2$ ; sample thickness - 0.10 cm; laser spot size ( $\sigma$ ) - 1.0 cm.

(b) Single-Crystal Barium Fluoride Window

The continuous 2.8-micron beam was represented by a Gaussian intensity profile. The temperature solution was modified to model uniform absorption throughout the bulk of the window by using an extremely thin sample, suppressing conduction along the window axis, but maintaining the correct flux per unit volume of sample. The program was then used to fit experimental temperature rise data at long irradiation times from a radially distant thermocouple. Figure 2 shows the good agreement in the form of the predicted temperature history with the data. A bulk absorption coefficient of 0.0003 cm for the window material is thus obtained directly by the computer program. Figure 2 also gives the corresponding calculated temperature history of the center of the window.

REFERENCES

1. Ölcer, N. Y., "On the Theory of Conductive Heat Transfer in Finite Regions," Int. J. Heat Mass Transfer, 7, pp. 307-314, 1964.
2. Ölcer, N. Y., "General Solutions to a Class of Heat Flow Problems in a Finite Circular Cylinder," Brit. J. Appl. Phys., 18, pp. 89-105, 1967.

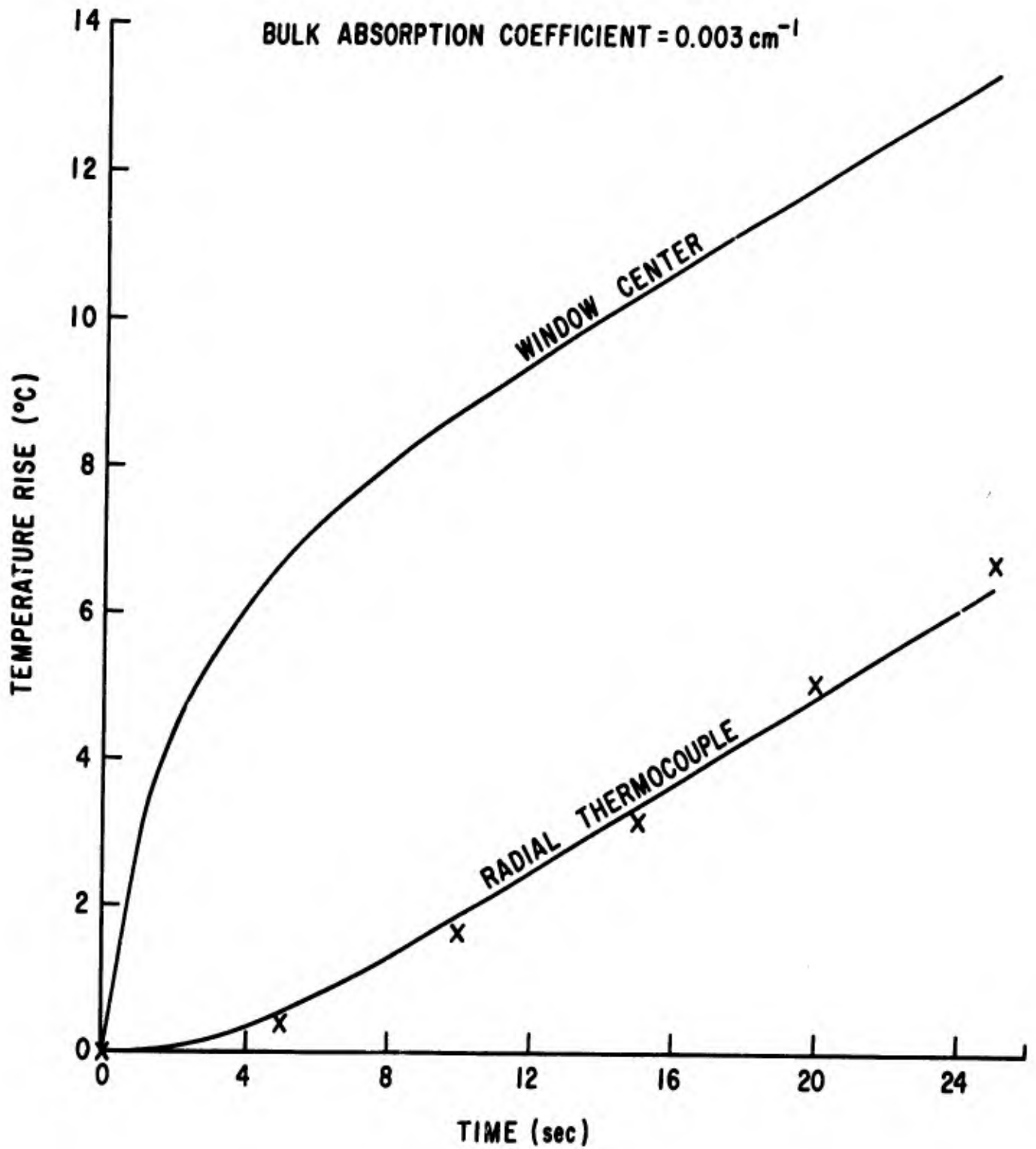


Figure 2. Temperature rise in barium fluoride

UNCLASSIFIED

Security Classification

## DOCUMENT CONTROL DATA - R &amp; D

*(Security classification of title, body of abstract and indexing annotation must be entered when the overall report is classified)*

1. ORIGINATING ACTIVITY (Corporate author) Air Force Weapons Laboratory (LR) Kirtland Air Force Base, New Mexico 87117		2a. REPORT SECURITY CLASSIFICATION UNCLASSIFIED	
		2b. GROUP	
3. REPORT TITLE LASER DIVISION DIGEST			
4. DESCRIPTIVE NOTES (Type of report and inclusive dates) Semiannual Technical Summary--1 November 1970 through 1 May 1971			
5. AUTHOR(S) (First name, middle initial, last name)			
6. REPORT DATE June 1971		7a. TOTAL NO. OF PAGES 304	7b. NO. OF REFS 100
8a. CONTRACT OR GRANT NO.		9a. ORIGINATOR'S REPORT NUMBER(S) LRD-71-1	
b. PROJECT NO. 644A, 3326, 0313, 1256		9b. OTHER REPORT NO(S) (Any other numbers that may be assigned this report)	
c.			
d.			
10. DISTRIBUTION STATEMENT Each transmittal of this document outside the agencies of the US Government must have prior approval of AFWL (LR), Kirtland AFB, NM 87117. Distribution is limited because of the technology discussed in the report.			
11. SUPPLEMENTARY NOTES		12. SPONSORING MILITARY ACTIVITY AFWL (LR) Kirtland AFB, NM 87117	
13. ABSTRACT (Distribution Limitation Statement No. 3) This digest covers the unclassified high-energy laser research performed at the Air Force Weapons Laboratory during the 6 months ending 1 May 1971. This report includes individual technical contributions in the specific areas of laser systems and devices, optics, optical systems, propagation, and laser effects.			

DD FORM 1 NOV 65 1473

UNCLASSIFIED  
Security Classification

UNCLASSIFIED

Security Classification

14.

KEY WORDS

LINK A		LINK B		LINK C	
ROLE	WT	ROLE	WT	ROLE	WT

Lasers  
Electro-aerodynamic laser  
Optics  
Optical systems  
Propagation  
Laser effects  
Air breakdown

UNCLASSIFIED

Security Classification